

Universidade do Minho
Escola de Engenharia

Mateus Antônio Nogueira Oliveira

A Multi-Physics Approach Applied to Masonry
Structures with Non-Hydraulic Lime Mortars



Universidade do Minho
Escola de Engenharia

Mateus Antônio Nogueira Oliveira

A Multi-Physics Approach Applied to Masonry
Structures with Non-Hydraulic Lime Mortars

Tese de Doutoramento
Engenharia Civil – Engenharia de Estruturas

Trabalho efectuado sob a orientação do
Professor Doutor Paulo J. B. B. Lourenço
Professor Doutor Miguel A. D. Azenha

STATEMENT OF INTEGRITY

I hereby declare having conducted my thesis with integrity. I confirm that I have not used plagiarism or any form of falsification of results in the process of the thesis elaboration.

I further declare that I have fully acknowledged the Code of Ethical Conduct of the University of Minho.

University of Minho, Guimarães, 11/12/2015

Full name: Mateus António Nogueira Oliveira

Signature:

This thesis is dedicated to my parents Silvana and Antônio, my eternal gratitude would not be sufficient to thank you for everything.

ABSTRACT

The structural safety of historic buildings is an important issue. These constructions frequently have cultural value, they are usually constructed with masonry. In ancient masonry structures mortar generally only represents a small (or moderate) part of the structure volume. Nonetheless, mortar has been acknowledged as the principal cause for deformations or movements. This fact justifies the necessity for a detailed analysis of the role of mortar within the scope of the structural behavior of historic masonry construction. These studies of ancient masonry structures are demanded by the society and frequently supported by governmental funding agencies.

In Portugal, as well as Europe in general, there is a significant quantity of historic constructions comprehending binders based on aerial lime mortars. The current work is focused in this binder. Aerial lime is one of the most ancient binders discovered and used. The aerial lime is produced from relatively pure limestone in kilns with high temperatures. Mortars based in such binder, after placement, harden gradually from the surface to their interior, due to reaction with carbon dioxide present in atmosphere, reaction usually denominated as carbonation. The carbonation is a natural process and occurs in different materials, such as different mortars or cementitious based material. For aerial lime mortar, this process has important structural effects, modifying the material mechanical properties. Nowadays, with the continued interest of the governmental agencies and the society in the conservation and restoration of the built heritage and because of its compatibility with traditional materials, the necessity of a detailed study about the material became even more important.

Considering this growing interest, in this thesis an experimental and numerical approach have been adopted in the studying of aerial lime mortar, in view of multi-physics modeling. For this purpose a hygro-carbo-mechanical model has been developed. For the numerical aspects, a software capable to simulate the coupled hygro-carbo fields over time has been implemented using the Finite Difference Method (FDM). The obtained results are then exported for a recognized software based in the Finite Element Method (TNO-DIANA[®]) that processes the mechanical analyses varying the elastic modulus over time. This framework is considered important, because such kind of structures last for long ages, and the mechanical analysis by itself may not be enough to reproduce the complicated behavior of them.

In terms of experiments, the drying process has been investigated through specific measurements. Mechanical properties have been measured since early ages and coupled with considerations regarding the evolution of carbonation. The evolution of carbonation (reaction field) has been investigated using thermogravimetric analysis and phenolphthalein indicator.

From the set of experiments and simulations, continuing with the study, and using the previous acquired experience, the different experiments are simulated. Numerical simulations are done to obtain the set of parameter to reproduce the experimental data, from the simplest to the most complex modeling. The first simulation is related to the humidity field. The experiments of humidity diffusion process are simulated with the decoupled humidity model. A unified pair of diffusivity and boundary coefficients is obtained. With these parameters, which best reproduce the experimental data in terms of humidity results, the carbonation process is in sequence simulated. Finally, the hygro-carbo model is coupled with TNO-DIANA[®] to simulate the evolution of elastic modulus experiments. A mathematical formulation that correlates the reaction (carbonation) and the humidity with the increase of elastic modulus is proposed.

This work shows that numerical models could reproduce reasonably well the experimental behavior. Experimentally, some innovative procedures regarding the tests in aerial lime mortar are done. The work presented herein can be considered in several aspects introductory and also seminal, due to the scarce of literature information about the study of aerial lime mortar.

RESUMO

A segurança estrutural de edifícios históricos é uma questão importante. Estas construções frequentemente possuem valor cultural, e as mesmas são geralmente construídas com alvenaria. Em estruturas de alvenaria antiga a argamassa geralmente representa apenas uma pequena (ou moderada) parte do volume da estrutura. No entanto, a argamassa é reconhecida como a principal causa para as deformações ou movimentos. Este facto justifica a necessidade de uma análise detalhada do papel da argamassa dentro do âmbito do comportamento estrutural de construções históricas em alvenaria. Estes estudos de estruturas em alvenaria antiga são exigidos pela sociedade e frequentemente apoiados por agências de financiamento governamentais.

Em Portugal, bem como na Europa em geral, há uma quantidade significativa de construções históricas com argamassas a base de cal aérea. O presente trabalho está focado neste ligante. A cal aérea é um dos mais antigos ligantes descobertos e usados. A cal aérea é produzida a partir de calcário relativamente puro em fornos com altas temperaturas. Argamassas baseadas nesse ligante, após a aplicação, endurecem gradualmente a partir da superfície para o interior, devido à reação com o dióxido de carbono presente na atmosfera, reação habitualmente denominada como carbonatação. A carbonatação é um processo natural e ocorre em diferentes materiais, tais como argamassas ou materiais à base de cimento. Para argamassas de cal aérea, esse processo tem importantes efeitos estruturais, modificando as propriedades mecânicas do material. Hoje em dia, com o contínuo interesse dos órgãos governamentais e da sociedade na conservação e restauro do património construído e por causa de sua compatibilidade com materiais tradicionais, a necessidade de um estudo detalhado sobre o material tornou-se ainda mais importante.

Considerando esse interesse crescente, nesta tese, abordagens experimentais e numéricas foram adotadas no estudo das argamassas de cal aérea, em vista da modelagem multi-física. Para este efeito, um modelo de higro-carbo-mecânico foi desenvolvido. Para os aspetos numéricos, um programa capaz de simular os campos higro-carbo acoplados ao longo do tempo foi implementado utilizando o Método das Diferenças Finitas (MDF). Os resultados obtidos são em sequência exportados para um programa reconhecido baseado no Método dos Elementos Finitos (TNO-DIANA[®]) que realiza as análises mecânicas e o estudo da variação do módulo elástico ao longo do tempo. Este quadro é considerado importante,

porque esse tipo de estrutura tende a existir por séculos, e a simples análise estrutural por si só, pode não ser suficiente para reproduzir o comportamento complexo dessas estruturas.

Em termos de ensaios, o processo de difusão da humidade foi estudado através de medições específicas. As propriedades mecânicas foram medidas desde as primeiras idades, juntamente com considerações sobre a evolução da carbonatação. A evolução da carbonatação (campo de reação) foi investigada utilizando análises termogravimétrica e fenolftaleína.

A partir do conjunto de experimentos e simulações, continuando com o estudo, e utilizando a experiência adquirida anteriormente, os diferentes ensaios são simulados. Simulações numéricas são feitas para obter o conjunto de parâmetros para reproduzir os dados experimentais, desde o mais simples ao mais complexo. A primeira simulação está relacionada com o campo de humidade. Os experimentos referentes ao processo de difusão são simulados com o modelo de humidade desacoplado de outros campos. Um par unificado de difusividade e coeficiente de fronteira é obtido. Com esses parâmetros, que melhor reproduziram os dados experimentais em termos dos resultados de humidade, o processo de carbonatação é em sequência simulado. Por fim, o modelo de higró-carbo é acoplado com TNO-DIANA[®] para simular os ensaios sobre a evolução do módulo de elasticidade. Uma formulação matemática que relaciona a reação (carbonatação) e a humidade com o aumento do módulo de elasticidade é proposta.

Este trabalho mostra que os modelos numéricos puderam reproduzir razoavelmente o comportamento experimental. Alguns procedimentos inovadores em relação aos testes em argamassa de cal aérea estão apresentados. O trabalho aqui presente pode ser considerado em diferentes aspetos pioneiros, mas também é introdutório, devido à escassez de informações na literatura sobre o estudo de argamassas à base de cal aérea.

ACKNOWLEDGEMENTS

Firstly, I would like to humbly acknowledge to God for his generosity, benevolence and infinite patience.

This research was supported by the Brazilian National Counsel of Technological and Scientific Development (CNPQ) under the program “*Ciência sem Fronteira*” and additional financial support by FCT (Portuguese Foundation for Science) which are gratefully acknowledged.

The research was performed under the direct auspices of Prof. Paulo Lourenço, who provided this opportunity, supported the work, had the patience and believed in the project, including Prof. Miguel Azenha, for his valued support, patience, grateful discussion and essential assistance.

Prof. Roberto Márcio from the Federal University of Minas Gerais had a key role of importance in this thesis, by providing me with opportunity and support on many occasions during the research.

I would also like to thank the technicians of the laboratory of the Civil Engineering Department of University of Minho (LEST), especially Mr. Marco, Matos, Mr. Carlos, Mr. Fernando Pokee and Mr. Gonçalves for their efforts and assistance during the experiments. I am grateful to all my colleagues from the ISISE Group, especially Dr. Bahman, for his support and interesting discussions, Erika Guimarães and Anna Meneghini, for the essential support during the experimental work, Prof. Rodrigo Lameiras, Prof. Glaucia and Dr. Nuno Mendes. I would like to express also my deep gratitude to Prof. Fernando Castro, and Mr. Miguel of the Mechanical Department from the University of Minho, for their presence during the tests, and assessment of the results obtained from thermogravimetric data. I continue the acknowledgements to Mr. Joel (Department of Industrial Electronics at University of Minho), Professor Daniele Ferretti from University of Parma, and to Lusical for providing the aerial lime. Many people have been included in for the development of this work, especially thanks to Prof. Ana Lydia, Prof. Gustavo Simões, Prof. Edgar Carrasco and Prof. Judy (Federal University of Minas Gerais) and my dear friend Prof. Luiz Henrique who gave me professional support several times.

An essential person in my research journey is dear Prof. Estevão Bicalho. I would like also to thank Dr. Eduardo Barbosa and all his team, and Mr. Geraldo César for their friendship.

Included are my dear friends, who have an essential contribution, especially: Willian, Plinio, Aliciane, Felipe Marques, Vitor Lages, Silvia Pucci, Anna Sophia, María Paula, Filomena & Célio, Mardônio Girão, Rodrigo Barichello, Carlos Bruno, Leandro, Hyggor, Alex, Aline, Nicola Donato, Paulina, Paulo Rogério, Anna Javashvili, João Herdeiro, Driano and all the friends that I had the pleasure to meet, from many different countries.

I would like to express my deep gratitude to my special brothers: Samih Eisa, Prof. Bernardo Neto and his lovely family, Mohamed Sabet and Rafael Brandão for sharing the experience and to care me.

Finally, I would like to thank all my family, especially my parents Silvana and Antônio, for their love, incredible patience and support, even more through all the difficulties that we experienced during this difficult period.

TABLE OF CONTENTS

LIST OF SYMBOLS AND ABBREVIATIONS	17
1 INTRODUCTION	21
1.1 Scope and motivation	21
1.2 Objectives	23
1.3 Chapters outline.....	24
2 MASONRY STRUCTURES AND AERIAL LIME.....	27
2.1 Introduction	27
2.2 Masonry structures.....	28
2.2.1 Brief history	28
2.2.2 Modeling strategies	29
2.2.3 Ancient masonry structures	31
2.2.4 Long term behavior	32
2.2.5 Failure examples	33
2.3 Lime	36
2.3.1 Introduction	36
2.3.2 Aerial lime and its cycle.....	37
2.3.3 Classification of aerial lime.....	39
2.3.4 Brief history of aerial lime application.....	42
2.4 Mortars.....	44
2.4.1 Introduction	44
2.4.2 Deterioration and restoration.....	45
2.4.3 Composition in ancient buildings and recent research	48
2.5 Carbonation process.....	49
2.5.1 General aspects.....	49
2.5.2 Influence of relative humidity	56
2.5.3 Diffusion of CO ₂	58
2.5.4 Pore structure changes during the carbonation and the diffusion of CO ₂	62
2.5.5 Measurement techniques	67
2.6 Mechanical properties.....	77
3 NUMERICAL MODELS FOR MOISTURE AND CARBONATION.....	81
3.1 Introduction	81
3.2 Moisture transport in porous material	82
3.2.1 General remarks about the moisture diffusion process.....	82
3.2.2 Drying process.....	84
3.2.3 Numerical simulation of the moisture field	87
3.2.4 General considerations for thermodynamic model for moisture transport and equilibrium	89
3.2.5 Thermo-hygro-mechanical model	90

3.2.6	General considerations and governing equations in terms of humidity.....	91
3.2.7	Integrated discussion of the moisture modeling	100
3.3	Multi-physics models for simulation of carbonation	101
3.3.1	General remarks	101
3.3.2	Simple diffusion equations	101
3.3.3	Model of ion transport in porous media - Poisson-Nernst-Planck model.....	108
3.3.4	Phase equilibrium model	110
3.3.5	Mass transport coupled model.....	112
3.3.6	Other multi-physics carbonation models	113
3.3.7	Discussion	113
4	NUMERICAL IMPLEMENTATION	115
4.1	Introduction	115
4.1.2	Numerical implementation in axisymmetric conditions.....	119
4.1.3	Humidity implementation in 2D.....	122
4.2	Sensitivity analyses	124
4.2.1	General considerations	124
4.2.2	Sensitivity analyses regarding f_{boundary}	125
4.2.3	Sensitivity analyses regarding D_1	126
4.3	Applications in concrete - Simulation of 1D specimens.....	128
4.4	Multi-physics model implementation.....	136
4.4.1	Program verification and preliminary analyses	140
5	EXPERIMENTAL PROGRAM FOR HUMIDITY FLUX STUDY.....	157
5.1	Introduction	157
5.2	Characterization of raw materials	158
5.2.1	General aspects.....	158
5.2.2	Lime	160
5.2.3	Aggregates	161
5.3	Mortar composition and preparation	163
5.4	Casting and curing conditions	166
5.5	Experiments to study the humidity diffusion process.....	167
5.5.1	Introduction	167
5.5.2	Prismatic specimens - 5.0 thickness	168
5.5.3	Cylindrical specimens	173
5.5.4	A comparative method to measure the humidity	180
6	EXPERIMENTAL PROGRAM FOR CARBONATION AND MECHANICAL PROPERTIES	183
6.1	Introduction	183
6.2	Specimens types and initial curing conditions.....	185

6.3	TGA: Data analysis and experimental methodology	190
6.3.1	General information	190
6.3.2	Data analysis	190
6.3.3	Experimental methodology	192
6.4	Testing program for carbonation process	196
6.4.1	Introduction	196
6.4.2	Time effect	196
6.4.3	Environmental effect in discs	211
6.4.4	Effect of the size of the specimens	214
6.4.5	TGA in lime paste	217
6.5	Testing program for evolution of mechanical properties	219
6.5.1	General aspects.....	219
6.5.2	Preliminary measurement of e-modulus evolution over time – Part A	219
6.5.3	Elastic modulus in cylinders with sealed top and bottom faces (part B)	227
6.5.4	Evolution of compressive strength	231
6.5.5	Evolution of compressive strength in standard and high humidity environments	235
7	NUMERICAL SIMULATIONS OF EXPERIMENTS	237
7.1	Introduction	237
7.2	Humidity field	239
7.3	Carbonation	242
7.3.1	General aspects.....	242
7.3.2	Simulation of the TGA results :Parameters and proposals for model modification	243
7.3.3	Simulations of carbonation results from phenolphthalein indicator, effect of the size of the specimens	249
7.4	Elastic modulus	255
7.4.1	General considerations	255
7.4.2	Proposed model for e-modulus evolution.....	256
7.4.3	Multi-physics numerical modelling.....	262
7.4.4	Calculated strain fields	263
7.4.5	Calculated stress fields	264
7.4.6	Evolution of elastic modulus	269
8	CONCLUSIONS AND RECOMMENDATIONS FOR FURTHER WORK	273
8.1	Conclusions.....	273
8.2	Further work.....	280
	REFERENCES.....	285
	ANNEX A	325

LIST OF SYMBOLS AND ABBREVIATIONS

For the sake of clarity, the description of each notation or symbol is made upon its first appearance in the text. The following list is presented in alphabetic order and does not include symbols or notations of a secondary nature.

Roman Letters

A	Transversal area / the impact number
c	Carbon dioxide concentration / Carbon dioxide field
C_i	The concentration of species i
c_n	Represents the carbon dioxide vector multi-physics model
c_{max}	Maximum CO ₂ concentration
c_s	The average molecular speed
$C-S-H$	Calcium silicate hydrate
C_w	Diffusivity of water
$C_{w,rif}$	Diffusivity in standard conditions for water
d	Molecular number
d_p	Pore diameters
D	Diffusion coefficient
D_c	Diffusivity of CO ₂
D_{CO_2}	The diffusion coefficient of CO ₂ in concrete
$D_{c,rif}$	Diffusivity of CO ₂ in standard conditions
D_h, D_h^*	Humidity diffusion coefficients
D_0, D_1	The minimum and maximum values for D_h
D_∞	The aggressive species diffusion coefficient at time = infinity
D_{28}	The aggressive species diffusion coefficient at 28 days
DSC	Differential scanning calorimetry
DTA	Differential thermal analysis
E	Elastic modulus
E_a	The activation energy
E_{final}	Final elastic modulus

F	Faraday's constant
f_i	Function related with the calculation of the carbon dioxide and humidity fields ($i = 1, 2, 3$ and 4)
F_i^R	Function related with the calculation of the reaction field ($i = 1, 2, 3$ and 4)
F_y	Force in y direction
f_{cm}	Mean compressive concrete strength
$f_{boundary}$	Proportionality factor used to simulate the boundary effect
h	Internal relative humidity
h_c	Relative humidity for which $D_h = 0.5 \times D_l$
h_{en}	Environmental humidity
h_s	Internal humidity decrease associated with concrete hydration – self-desiccation
h_{surf}	Concrete humidity in the surface
H_n	Humidity vector in multi-physics model
i	Denotes the analyzed node/The current density applied to the pore solution/species
J / J_i	Flux (in general) / The flux of species i
k	The air permeability of concrete
k_c	Factor related with carbonation process
K_H	Henry's constant
K_p	Thermodynamic equilibrium constant
$LVDT$	Linear Variable Differential Transformer
M	Molar mass
\dot{m}_{hydr}	Mass source of skeleton
\dot{m}_{vap}	The vapor mass source caused by the liquid water evaporation or desorption
N	Avogadro number
n	Exponent used to calculate D_h / n^{th} time step / An exponent related with carbonation process
$n_{i,g}$	The stoichiometric coefficient of the aqueous species i in the dissolution equation
p	Radius in axisymmetric formulation
p_v	The pressure of water vapor
p_w	The pressure in water

P	Pressure.
P_g	The partial pressure of gas component calculated using activities in the aqueous phase
P_k	The partial carbon dioxide pressure
pH	Negative logarithm of concentration of hydrogen ion
r	Capillary radius
Q	The sink term corresponding to water consumption due to hydration
R	Reaction field, or reaction degree / Gas constant
R_{max}	Maximum reaction degree
R_n	Reaction vector in multi-physics model
$R_{normalized}$	Normalized reaction degree
Rhc	Vector with reaction, humidity and carbon dioxide fields
S	The degree of saturation of pores
t	Time
T	Temperature
TGA	Thermogravimetric analysis
W	Total water concentration
W_e	Evaporable water concentration
W_n	Non-evaporable water concentration
w/c	Water/cement ratio
x	Cartesian coordinate / Abscissa along the Finite Difference Method in 1D model; vector normal to the boundary / carbonation depth
XRF	X-ray fluorescence
y	Cartesian coordinate, ordinate
z_i	Charge number of the ionic species i
$[]$	Bracket symbols stands for concentration in general, for instance $[CO_2]$ is the carbon dioxide (CO ₂) concentration

Greek Letters

α	Parameter used to calculate the diffusion coefficient D_0 / D_I (Model Code 2010 and Model Code 1990 approaches)
α_i ,	Parameters that vary according to the characteristics of the concrete or mortar and reagents ($i = 1, 2, 3$ and 4)
Δt	Time difference
λ	Mean free path
∇	Nabla operator
$\nabla \theta$	Angular variation
ζ	Parameter related with the porosity reduction
ε	Deformation
$\hat{\psi}$	Residual vector
φ	Porosity
φ_v	Electrical potential
γ_i	The activity coefficient
ρ	Specific mass (mass per unit volume)
ρ_d	Concentration of dissolved carbon dioxide in pore water
ρ_g	Concentration of gaseous carbon dioxide
ρ_l	The density of liquid water
θ_w	The mass of moisture in a unit volume of concrete
v	Specific volume of water
Σ	Sigma notation, product notation
Π	Pi notation, product notation

1 INTRODUCTION

1.1 Scope and motivation

According to United Nations World Tourism Organization (UNWTO, 2014), the European Union (EU) is the major tourist destination, with five of its Member States among the world's top 10 destinations in 2013 (E.C., 2014). The tourist industry has become a key sector of the European economy, generating over 10% of EU Gross Domestic Product (GDP) (directly or indirectly), and employing 9.7 million citizens in 1.8 millions of business (Wood, 2015). In Europe the tourism is directly linked with the history, cultural aspects, and its architecture (Richards, 2002). In this scenario, historical masonry structures have important cultural, social, archaeological, aesthetic, economic, political, architectural and technical aspects that should be considered. In this sense, the preservation of historical constructions is of major importance for society and for future generations (Warren, 2000). These constructions have significant tourism potential (Lourenço *et al.*, 2006, Adriano *et al.*, 2009). These facts make the conservation and study of ancient structures an important task (Lourenço, 2004). A historical construction is complex, where the structural features are combined with the visual image and the architectural style, and all of these elements are significant parts (Oliveira, 2002). The age and the history of ancient buildings are other important aspects that also carry cultural significance (Agnew, 2010, Oliveira, 2002).

Historical constructions suffer damage over time, such as earthquakes, soil settlements, material degradation and lack of maintenance (Oliveira, 2002). These phenomena are some of the main reasons for structural damage (Macchi, 1998). Accordingly, careful and periodic inspections may be considered necessary in order to evaluate the actual structural safety of this kind of construction (Rabun, 2000, Oliveira, 2002). However, performing the structural analysis of a historical masonry construction is, generally, a complex task (Lourenço, 2001, Lourenço *et al.*, 2011), since structural engineering is just one of the necessary disciplines of a multidisciplinary task that should be constituted within a general plan of intervention for a determined historical construction and several uncertainties may be involved (Oliveira, 2002, Rabun, 2000). In this sense, the different components of a historical construction must be considered when the structural safety is analyzed (Friedman, 2010).

Many of the remaining ancient structures around the world are in vulnerable condition to upcoming effects and for the continuity of their presence, structural conservation or

strengthening applications are necessary (Rabun, 2000, Binda *et al.*, 2000b, Valluzzi *et al.*, 2005, D'Ayala and Fodde, 2008, Oliveira, 2002). Therefore, besides the structural intervention, both image and substance of historical constructions are required to be preserved after the structural intervention (Langenbach, 1994, Oliveira, 2002).

The historical structures with mortar based on aerial lime have even more complexity because the material properties change significantly over time due to the carbonation process (Arizzi and Cultrone, 2013, Lanas *et al.*, 2005, Ferretti and Bažant, 2006a, Glasser *et al.*, 2008, Houst and Wittmann, 1994, Huang *et al.*, 2012, Johannesson and Utgenannt, 2001). Several mechanisms are involved and coupled during the carbonation (Ferretti and Bažant, 2006b, Ferretti and Bažant, 2006a, Lawrence, 2006). To quantify the extension and the evolution of this phenomenon is essential to understand the physical, chemical and mechanical properties of mortar and consequently the structure performance (Arizzi and Cultrone, 2013, Lanas *et al.*, 2005, Lawrence *et al.*, 2007, Lawrence, 2006). The carbonation rate depends largely on the diffusivity of the material (Jung *et al.*, 2011). The process of CO₂ diffusion through the mortar depends of the carbonation reaction, the pore structure, the humidity and other aspects (Lawrence, 2006, Ferretti and Bažant, 2006a, Van Balen and Van Gemert, 1994).

Even with this mentioned complexity, design and practice often considers structural analysis, simplifying or even disregarding, the above mentioned phenomena. Another factor that limits our knowledge, when compared with cement based materials, is that studies about aerial lime mortars are scarce in the literature (Colleparidi, 1990). Beyond the understanding of these structures, their repair and conservation strongly relies on aerial lime mortars since, according to Faria *et al.* (2008) they are usually referred as presenting the necessary compatibility with ancient masonries, also cited by Croci (1998).

In a different context, the use of aerial lime for new constructions is aligned with modern eco-efficient construction. In recent years, the need for low embodied energy materials has become increasingly recognized (Cabeza *et al.*, 2013, Scannell *et al.*, 2014). Government targets aim to decrease carbon emissions by 80% before 2050 (E.C., 2015). The construction industry has been responsible for approximately 50% for carbon emissions in UK and an increase use of low energy materials (such as aerial lime) could provide an important contribution to achieve this target (Scannell *et al.*, 2014).

From the considerations above, the subject of this reason is important, not only for the study of ancient structures but in the context of modern construction.

Therefore, the fundamental purpose of this work is to establish a methodology for numerical modeling the behavior of masonry structures based on aerial lime mortar, with the explicit account for a set of physical and chemical processes. In terms of experiments, different techniques with feasibility already recognized in literature are adopted, such as phenolphthalein and thermogravimetric analysis to evaluate the carbonation process. Other specific developments for the experimental work are also presented here. The experimental program is pioneer in the experimental simulation of aerial lime mortar with the objective to test the material behavior and to support the multi-physics modeling strategy. The work also presents an integration with the data obtained from the experiments and the numerical models. This integration is important for a more precise achievement of parameters specific for aerial lime mortar. As a final result, a hygro-carbo-mechanical model is presented.

1.2 Objectives

The present work has two major contributions: numerical and experimental. Regarding the numerical modeling, the objective is to obtain a model capable to simulate the multi-physics fields for aerial lime, and understand the main phenomena involved.

These processes are not usually studied together in the analysis of the performance of real scale structures. For numerical models, one of the reasons that may be assumed as the indicator for the feasibility of the research reported in this work is the availability of computational capacity for the intended simulations.

A coupled model capable to simulate the hygro-carbo behavior is implemented here. An emphasis on the experimental characterization of the material is also developed for this propose.

Regarding the experimental part, the objective is a systematic study on the effects of the main variables in the carbonation process, developing and validating novel experimental approaches.

Other objectives of this work are: to apply and study the coupled model (hygro-carbo) by simulating the carbonation process with experimental data in different conditions; and to study the interaction of carbonation with mechanical aspects.

1.3 Chapters outline

The conducted research reported in this thesis is organized in eight Chapters (including the present introduction chapter).

Chapter 2 presents the literature review and the main aspects related to the current work. Initially concepts about the masonry structures are presented, followed by some information about aerial lime, mortar and general concepts about the carbonation process and its measurement.

Chapter 3 addresses models in literature to simulate the moisture flux in a porous material with special consideration for cementitious materials. Special attention is dedicated to the *fib* Model Code formulation (CEB–FIP, 2010, CEB–FIP, 1993) to simulate the humidity field. In this chapter, numerical multi-physics models to simulate the carbonation process are also summarized. The model proposed by Ferretti and Bažant (2006a) is described with more details, because of its relevance for the current work.

Chapter 4 shows the implementation of the humidity field in the Finite Difference Method (FDM). The implemented model is used to make sensitivity analyses and it is used to simulate experimental data from literature (simulation of 1D flux in concrete). Also in Chapter 4, a multi-physics model (hygro-carbo) to simulate the coupled carbonation process is implemented.

Chapter 5 starts with the experimental campaign, namely with the raw material characterization (lime and sand) and the definition of a suitable mix. The humidity flux in aerial lime mortar is also studied. In order to study the phenomenon, two different geometry of humidity molds (experimental setups) are adopted.

In Chapter 6, the experimental campaign is focused in the study of carbonation and mechanical properties evolution. The carbonation process is evaluated with two techniques, phenolphthalein indicator and thermogravimetric analysis. The evolution of mechanical properties is investigated with the study of two parameters, the elastic modulus and the compressive strength. Two different environments are also studied in order to analyze its influence in carbonation process.

In Chapter 7, the obtained experimental data in previous chapters is numerically simulated with the developed model. First, the humidity results are simulated with the software presented in Chapter 4. With the set of parameters, obtained from these simulations, the carbonation experiments are then simulated with the coupled software (hygro-carbo model).

At the end of chapter, mechanical elastic modulus results are simulated for different ages, integrating the mechanical field with the hygro-carbo model.

Finally, the main conclusions of this thesis are summarized in Chapter 8, together with some suggestions for possible extensions of the performed research.

The summary of the thesis outline is presented in Figure 1-1.

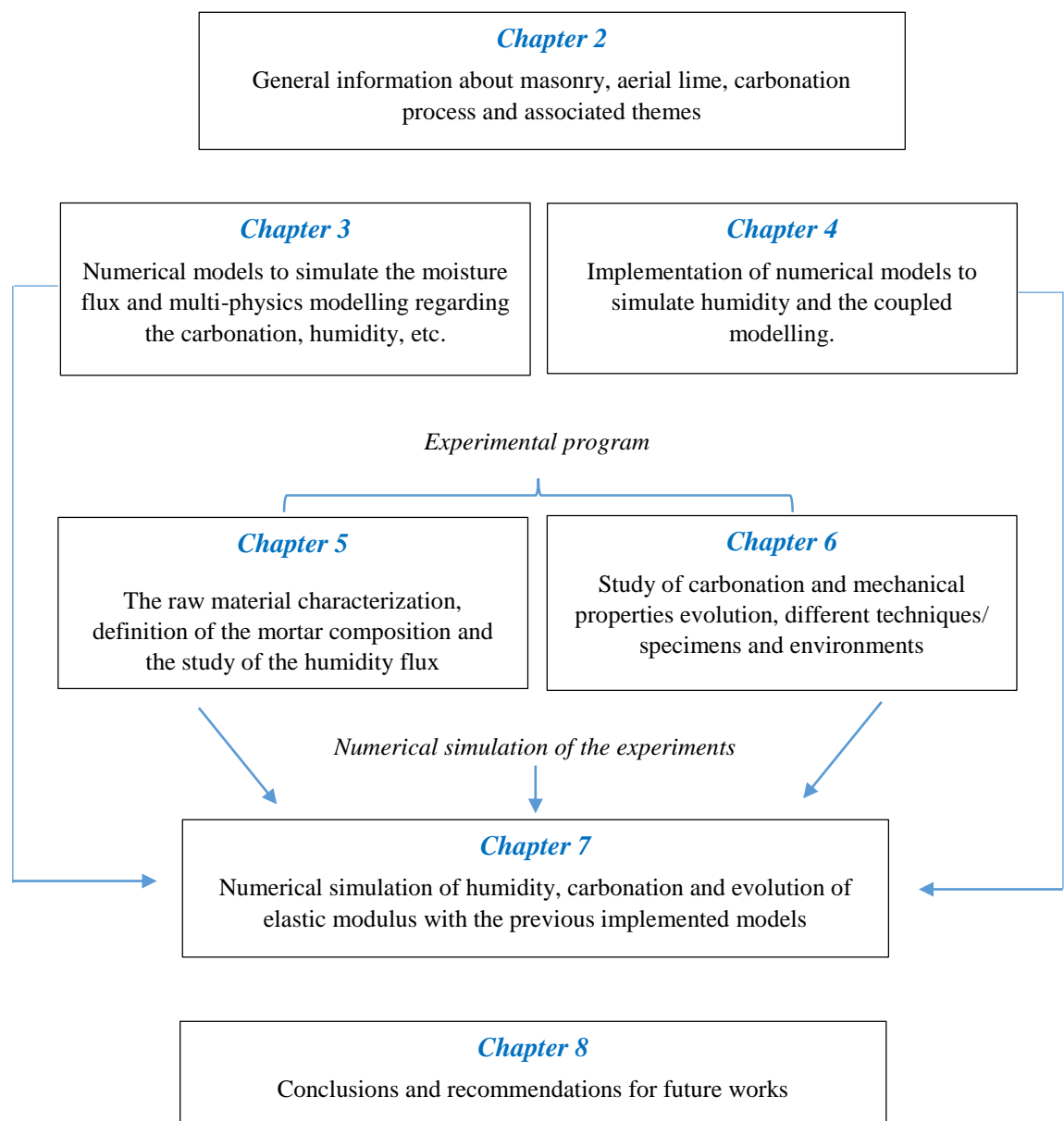


Figure 1-1 – Summary of thesis outline

2 **MASONRY STRUCTURES AND AERIAL LIME**

2.1 *Introduction*

This is an introductory chapter, where general concepts about ancient masonry structures, historic mortars and aerial lime are presented.

Masonry is considered one of the oldest and the most used structural systems (Lourenço, 1996). Ancient structures require special attention and monitoring (Lourenço, 2002) since they are complex. Given their societal and economic importance a detailed characterization can be necessary (Oliveira, 2002).

Some historical constructions collapsed over the years for different reasons (Gimbert, 2008, Binda *et al.*, 2001, Anzani *et al.*, 2002). A particular case is the accident in 1989, after eight centuries of construction, the Civic Tower of Pavia, Italy collapsed (Binda *et al.*, 2001). It failed suddenly (see Figure 2-1), with imperceptible warning signals (Binda *et al.*, 1992, Binda *et al.*, 2001, Macchi, 1998). This event was only the last in a series of failures of masonry towers built in Europe between the 11th and 14th centuries (Ferretti and Bažant, 2006a, Ferretti and Bažant, 2006b) (more examples and details will be given in Section 2.2).



Figure 2-1 – Civic Tower of Pavia before and after the collapse (images from Garavaglia *et al.* (2006) and Anzani *et al.* (2009))

This accident illustrates the importance of the study and monitoring for ancient masonry structures. For masonry structures, the understanding of the mortar properties is an important aspect (Brooks and Bakar, 2004, van Zijl *et al.*, 2001). In terms of mortar, the study herein is focused in materials based in aerial lime. The use of aerial lime mortars in masonry structures is present all around the world, namely in European context (Moropoulou *et al.*, 2005, Andrejkovicova *et al.*, 2012, Pesce, 2014). These mortars present properties that

change over time by different phenomena, which are coupled and are complex (Lanas *et al.*, 2004a, Guimarães, 2014, Lanas and Alvarez, 2003).

This chapter also addresses general concepts about the use of aerial lime as binder for preparation of mortars and different phenomena involved in carbonation, which is a chemical process (Arandigoyen *et al.*, 2004, Moorehead, 1986, Lawrence *et al.*, 2006a, Lawrence *et al.*, 2007, Cultrone *et al.*, 2005). Carbonation process is a natural phenomenon and modifies the material properties (Lanas *et al.*, 2005, Arizzi and Cultrone, 2013). Due to the lack of knowledge about the behavior of aerial lime mortars (Lanas and Alvarez, 2003, Cultrone *et al.*, 2005), often the behavior of cementitious based material are adopted as reference.

2.2 *Masonry structures*

2.2.1 *Brief history*

About the years 9000-7000 BC, with the earliest civilizations, the history of architecture begins and simultaneously appeared masonry as a construction technique (Lourenço, 1996). Constructions were made empirically, mostly based on intuition about how the loads should be carried by the resistant elements to the ground (D'Ayala and Fodde, 2008, Friedman, 2010). Using this technique, important monuments were built, such as the Colosseum of Rome (~ 82 BC), where the theater was supported by arches, which were supported on pillars (Friedman, 2010, Sear, 1983).

Independent of the material components or technique, masonry was around the time and the globe one of the most common construction methods (Lourenço, 1996, Pfeifer, 2001).

An important point in the history of masonry is the era of the Industrial Revolution as described by Elliot (1992) and cited by (Lourenço, 1996). Due to the expansion of the industrial activity, traditional handwork procedures were replaced by machinery (Lourenço, 1996).

The reduction of the masonry use as a structural material began in the early twentieth century (Rocha, 2013). In the years 1920-40, in Europe and United States, the study on the behavior of masonry subjected to all kinds of efforts started with laboratory experiments, which gave foundation to the modern theory of structural masonry design (Biggs, 2007). Since then, buildings whose walls were exorbitantly thick, at the end of the nineteenth century, gave way to more slender walls (MacLaughlin and Estrada, 2009, Randall, 1949). The advent of

steel and concrete have allowed designers to use new structural forms, leaving masonry as a system to small buildings (Biggs, 2007, Rocha, 2013). Still, on the 1950s masonry was partly reborn as a structural system, after numerous experimental studies (Rocha, 2013). From this point on, many buildings were built around the world (Biggs, 2007, Rocha, 2013), mostly for housing. Masonry has become recognized as a rational structural system, emerging in this period the first documents that established limitations for building design (Oliveira, 2002, Lourenço, 1996).

Currently, masonry is a construction system widely used, depending on the building markets (Robertson and Naka, 1980, Lourenço, 1996), and different materials and shapes, different types of mortar and different techniques may be found (Lourenço, 1996). More information about the use of masonry may be found in e.g. Hendry (1981) Lourenço (1996), Heyman (1997) and Como (2012).

2.2.2 *Modeling strategies*

As stated in literature, the use of masonry with a structural function is not recent (Lourenço, 1996). Masonry does presents distinct directional properties due to the mortar joints which act as planes of weakness (Lourenço, 1996). Depending on the level of accuracy and the simplicity desired, in general it is possible to use the following modeling strategies (see Figure 2-2) (Lourenço, 1996):

- Detailed micro-modeling - units and mortar in the joints are represented by continuum elements whereas the unit-mortar interface is represented by discontinuous elements;
- Simplified micro-modeling - expanded units are represented by continuum elements whereas the behavior of the mortar joints and unit-mortar interface is lumped in discontinuous elements;
- Macro-modeling - units, mortar and unit-mortar interface are smeared out in the continuum.

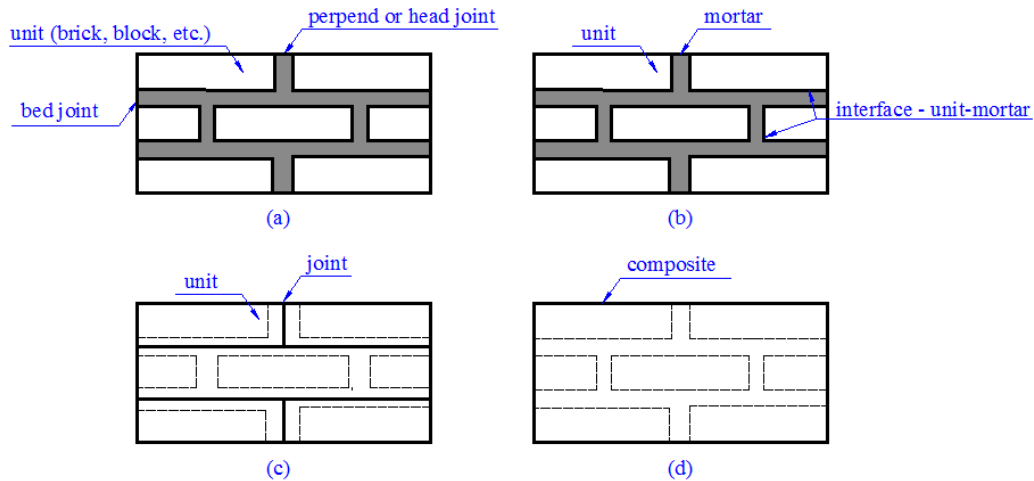


Figure 2-2 – Modeling strategies for ancient masonry structures: (a) ancient masonry sample; (b) detailed micro-modeling; (c) simplified micro-modeling; (d) macro-modeling (adapted from Lourenço (1996))

According to Lourenço (1996) in the detailed micro-modelling approach, Young’s modulus, Poisson’s ratio and, optionally other properties such as inelastic properties of both unit and mortar are taken into account, while the interface represents a potential crack/slip plane. This strategy enables the combined action of unit (brick, block, etc.), mortar and interface to be studied in details. In the cited second approach, each joint, consisting of mortar and the two unit-mortar interfaces, is lumped into an “average” interface (Lourenço *et al.*, 2010, Lourenço, 1996). While the units are expanded in order to keep the geometry unchanged. In this fashion, masonry is considered as a set of elastic blocks bonded by potential fracture/slip lines at the joints (Zucchini and Lourenço, 2004, Lourenço, 1996). Finally, the third approach (macro-modeling) does not make a distinction between individual units and joints but treats masonry as a homogeneous anisotropic continuum (Lourenço *et al.*, 2010, Lourenço, 1996).

In this sense, according to Lourenço (1996) one modeling strategy cannot be preferred over the other, because different application fields exist for micro and macro-models (Lourenço *et al.*, 2010, Lourenço, 1996). Micro-modeling studies are generally adopted to give a better understanding about the local behavior of masonry structures (Lourenço, 1998, Lourenço, 1996). The macro-modeling is more practice oriented due to the reduced time and memory requirements as well as a user-friendly mesh generation (Lourenço, 1998, Lourenço, 1996). A precise micro or macro-modeling of masonry structures requires a thorough experimental description of the material (Lourenço, 1998, Lourenço, 1996).

The properties of masonry are influenced by a large number of factors, for instance, the material properties of the units and mortar, arrangement of bed and head joints, anisotropy of units, dimension of units, joint width, quality of workmanship, degree of curing, environment and age (Lourenço, 1998, Lourenço, 1996).

2.2.3 *Ancient masonry structures*

Structures may be classified as historical when they become part of the built heritage (Oliveira, 2003). Historical buildings carry cultural significance attached not only to the formal architectural aspects, but also to specific structural features, applied materials and building techniques and, by being old, they become also been a part of human history (Friedman, 2010). Therefore, considering the complexity of the analyses, different technical skills are necessary to apply the knowledge at the service of culture and history, in order to respect the historical value of the heritage and to guarantee appropriate safety levels (D'Ayala and Fodde, 2008).

The analysis of historical masonry structures present an even bigger challenge, when compared to regular modern masonry or other types of ordinary structures (Lourenço *et al.*, 2011). Aspects as geometry data or characterization of mechanical properties of used materials are, most of the times, inexistent or difficult to find (Lourenço, 2002, Oliveira, 2002). Accordingly, a large variability is usually found, due to workmanship and use of natural materials, as well as to the existence of unknown damage in the structure (Oliveira, 2002, Padura, 2001). In addition to these challenges, existing standards or codes are in general non-applicable to the safety assessment of historical masonry structures (Lourenço, 2002, Holický *et al.*, 2013).

An important point to understand historic masonry behavior is to study specifically the mortar (Lourenço, 2002). For instance, in a historic mortar based in aerial lime, the degree that the aerial lime (quicklime form) would have converted to Ca(OH)_2 would depend upon the quantity of water and duration of slaking (Forster, 2004a, Forster, 2004b). Since the carbonation process depends on the available Ca(OH)_2 , the amount of water also has implication on the development of mortar properties (Forster, 2004a, Forster, 2004b). This illustrates, how an initial aspect (amount of water adopted in the mortar preparation) may affect the structure behavior over time.

Still regarding the mortar, the knowledge of its behavior is important, because despite occupying less than 15% of the total volume of the masonry, mortar joints are the main

source of the movements of such kind of structure (Brooks and Bakar, 2004, van Zijl *et al.*, 2001).

Therefore, studies in the subject of historical masonry buildings and their elements are essentials to understand their specificities and unique behavior (Oliveira, 2002, Lourenço, 2004). These studies are fundamental to define reliable and consistent approaches to assess the safety level and to design potential retrofitting measures (Oliveira, 2002).

2.2.4 Long term behavior

As stated before, the mechanical behavior of ancient masonry structures, is complex and depends on many factors including the age of the mortar composition, binder type, environmental conditions and others (Brooks and Bakar, 2004). Damage and collapses of monumental buildings, over the last years, have produced records noting the measurements of internal movement in masonry, mainly in cases where the stability of the foundation is known to remain intact (Gimbert, 2008, Anzani *et al.*, 2005, Anzani and Binda, 2013).

The long term behavior of masonry can have important consequences, particularly with respect to historical buildings (van Zijl, 2000, Gimbert, 2008). Masonry structures under persistent loading over relatively long periods of time may potentially collapse at lower stress values, around 45-50% of the nominal strength (Binda *et al.*, 2001). And due to the creep process, internal stresses are continuously redistributed throughout the loaded masonry structure (Binda *et al.*, 2001, Anzani *et al.*, 2002, Binda *et al.*, 2000b). Additionally, an associated redistribution of stress from external loads is possible (Scherer, 2006). When combined with this secondary reduction in strength, an increase in the stress may also result in the structural collapse (Papa *et al.*, 1994).

The time influence on the deformation on historical masonry became even more clearly and important after the sudden failure of the Civic Tower of Pavia on March 17, 1989 (Binda *et al.*, 1992, Binda *et al.*, 2000b). These authors related the failure of the tower to the time-dependent behavior (long-term), likely coupled with synergistic cyclic loads. Tall and heavy buildings, like towers, or heavily loaded structural elements, like piers, are greatly influenced by the high compressive stresses due to dead loads (Binda *et al.*, 2001). Other examples indicate similar structural aspects, where damages could be potentially induced from time dependent behavior (Anzani and Binda, 2013, Gimbert, 2008).

The stress distribution in ancient masonry structures is in general complex (Binda and Saisi, 2002, Anzani and Binda, 2013). The literature described cases often cited structural damage

caused by compression, mainly caused by heavy persistent dead loads (Binda *et al.*, 2001, Anzani *et al.*, 2002, Gimbert, 2008, Roca, 2001). Moreover, collected specimens after the failure are found to have high concentrations of stress due to non-uniform distributions of the internal forces (Binda *et al.*, 1992, Binda *et al.*, 2001).

As stated before, another aspect important is the fatigue effects due to cyclic actions, induced by temperature variation and wind, which can as well cause synergetic damage effects (Binda *et al.*, 2000b). The damage manifestation are thin or large vertical cracks which tend to propagate their dimension with time (Binda *et al.*, 2000b). The characteristics of long-term behavior are still being understood; there is however no disagreement on the extensive damage state seen in several historical masonry buildings nowadays (Gimbert, 2008, Anzani *et al.*, 2002, Roca, 2001). As an example of study about historical structures, Anzani *et al.* (2002) have investigated approximately sixty (60) ancient Italian towers to collect information about the degradation cases, particularly taking in to account the crack patterns.

2.2.5 Failure examples

In order to illustrate the possibly problems faced in ancient constructions related to long term loading, basic information about five failures/damage in important ancient masonry structures are presented next.

The Cathedral of Noto, Italy - The accident occurred in 1996 at Noto, Italy (Tobriner, 2003, Binda *et al.*, 2003). The identification of spalling and pre-existing diffuse vertical cracks indicated serious progressive damage (Tobriner, 2003, Binda *et al.*, 2003). Additionally, the internal rubble structure of the piers had substantially decreased in strength (Binda *et al.*, 2003, Garavaglia *et al.*, 2003, Binda, 2003). One picture after the collapse of structure is presented in Figure 2-3.



Figure 2-3 – The Cathedral of Noto after the collapse (Binda *et al.*, 2001)

Mallorca Cathedral (Mallorca, Spain) - The cathedral could be considered one of the most imposing Gothic buildings of the Mediterranean area (Roca *et al.*, 2012). It presented large cracks and deformations; and the arch nave collapsed in 1490; then there were the reconstruction of vaults (17th and 18th centuries) (Roca *et al.*, 2012). Nowadays, the structure presents large deformations in the piers showing curvature and lateral displacement longitudinally and transversally. Also it presents vertical cracks at the base of some piers (Roca *et al.*, 2012, Lourenço, 2001).

The Church of SS. Crocifisso (Noto, Italy) - Constructed around, 1715, the Sicilian church was damaged from the 1990 earthquake (Binda and Saisi, 2001). The transept, dome and vaults of the lateral nave sustained heavy deterioration and, at the time, were supported by a provisional structure (Gimbert, 2008). During the diagnostics, surface plaster not associated with the original construction was removed from piers that appeared unaltered (Binda and Saisi, 2004, Gimbert, 2008). Nonetheless, the investigation exposed a series of complex vertical cracks (Binda, 2003).

The Church of SS. Annunziata (Ispica, Italy) - The church was started in 1703, and it has survived over some events that have induced damage (Milne *et al.*, 2003). Particularly, in 1727 an earthquake shifted the piers of the main arcade out of plumb and the repairs did not occurred (Milne *et al.*, 2003, Gimbert, 2008). In 1869, the façade collapsed and recently the 1990 earthquake caused further damage (Milne *et al.*, 2003, Gimbert, 2008).

The Civic Tower of Pavia (Pavia, Italy) - Prior to collapse, the tower presented vertical capillary cracks (Anzani *et al.*, 2002). Studies carried out after the collapse of the tower showed that the mortar exhibits good compactness and satisfactory mechanical properties (Gimbert, 2008, Anzani *et al.*, 2002). Further investigation on the piers determined poor consistency in the morphology of the internal core where the mortar and its adhesion to the stone developed weakly (Gimbert, 2008, Anzani *et al.*, 2002). This situation according to Anzani *et al.* (2002) was, however, less critical than the material coherence observed at the Cathedral of Noto. Figure 2-4 presents a picture after the structure collapse.



Figure 2-4 – The Civic Tower of Pavia after collapse (Binda *et al.*, 2000a)

More details about this case is briefly presented, due to its importance to this work. According to Binda *et al.* (2001), the chemical and mineralogical characterization of the Pavia Civic Tower was performed in 22 samples of mortar. The chemical analyses indicate that the mortar during the first building phase consisted mostly of lime putty and the aggregate was mainly siliceous (Binda *et al.*, 2001). The binder/aggregate ratio varied from 1:3 to 1:5 (in terms of volume), similar values were obtained from the mortar of second and third building phases (Binda *et al.*, 2001). In order to analyze the collapse, many mechanical tests on the recovered masonry were conducted. The researchers performed fatigue and monotonic tests, creep and pseudo-creep tests, uniaxial unloading/reloading cyclical tests (Binda *et al.*, 1992, Binda *et al.*, 2000b). The high levels of stress found in the ruins could be attributed to the considerable dead load, and the tests defined three phases of creep behavior (Binda *et al.*, 2001).

Two other recent examples are the collapse of the bell tower of the Sint-Willibrordus Church at Meldert and the Medieval Maagden tower at Zichem both in Belgium, which occurred in 2006 (Verstrynghe *et al.*, 2011, Verstrynghe, 2010).

Herein, for sake of brevity, just an overall view with brief information about five cases was presented. Further details about damages/accidents in ancient masonry structures may be found in literature (Gimbert, 2008, Binda *et al.*, 1992, Pavía and Treacy, 2006, Binda *et al.*, 2001, Macchi, 1998, Anzani *et al.*, 2002, Roca *et al.*, 2012, Binda *et al.*, 2003, Milne *et al.*, 2003, Binda, 2008).

2.3 Lime

2.3.1 Introduction

Lime has been often used for construction purposes, because it presents good features, including high plasticity and water-retention capacity (Boynton, 1984, Swenson and Sereda, 1968). The term lime has been used for centuries to describe a broad group of inorganic binders mainly composed by calcium oxides and/or hydroxides (Pesce, 2014).

Natural limestones are the most important sources of raw materials to obtain the lime. These are sedimentary rocks, mainly composed by calcite (CaCO_3), and magnesite (MgCO_2) (Boynton, 1984, Holmes and Wingate, 1997). There are four different mineralogical limestones forms, which are: calcite and aragonite (CaCO_3), and magnesite and dolomite ($\text{CaMg}(\text{CO}_3)_2$) (Boynton, 1984, Holmes and Wingate, 1997). Limestone is found in the massive forms of these minerals in nature. The properties of the limestones are the main factors that affect the quality and properties of the lime material (Boynton, 1984, Holmes and Wingate, 1997).

In terms of source, there are two main groups of limestone, organic and inorganic (Boynton, 1984, Holmes and Wingate, 1997). Organic limestone occurs in nature from the accumulation of shells, corals and the remains of organisms layers in the oceans, seas and lakes (Boynton, 1984). Inorganic limestones are formed by chemical reactions with precipitation of calcium carbonate ions (Boynton, 1984). From different material sources, as cited before, a wide range of lime compositions may be obtained (Carran *et al.*, 2011). This diversity is then present in many structures around the world and the history (Boynton, 1984, Holmes and Wingate, 1997).

Because of this high number of materials compositions, a precise definition of lime is important. According to EN 459-1 (CEN, 2010a), lime may be defined as covering any material physical and chemical forms under which it may appear, namely calcium CaO and magnesium oxides MgO , and/or hydroxides $\text{Ca}(\text{OH})_2$ and $\text{Mg}(\text{OH})_2$.

Another relevant aspect is the lime production technique, which leads to different crystal sizes, depending on factors such as burning temperature, particle reactivity and slaking conditions (Pavía and Treacy, 2006). In the present work, the focus is on the study of aerial lime, as addressed next.

2.3.2 Aerial lime and its cycle

Aerial lime is also denominated non-hydraulic lime or quicklime (Valek *et al.*, 2012, Lawrence, 2006, Groot *et al.*, 2007). Aerial lime is composed mostly of calcium oxides or hydroxides of calcium/magnesium (Lawrence, 2006, Groot *et al.*, 2007).

The properties of aerial lime usually include high permeability, flexibility and plasticity, tendency to shrink in early stages of hardening, solubility in water and relatively low mechanical strength (Vicat, 1997, Holmes and Wingate, 1997, Cowper, 1998). Currently, in civil engineering area, aerial lime is used, for example, mixed with gypsum, in manufacture of plasters (Ashurst and Ashurst, 1988), mixed with pozzolans constituting hydraulic binders, together with cement or hydraulic lime in mortar for plaster and in the form of slurry white washing the walls, and also for soil stabilization, and others (Lawrence, 2006, BLA, 2015).

In terms of applicability, the use of aerial lime is not restricted to civil engineering. As examples of past studies, the chemical water treatment has also contributed to the modeling of the reaction between lime and water (Roques and Girou, 1974). Researches on gas treatment such as desulphurization (Shih *et al.*, 1999) have dealt with the reaction of gaseous phases with lime (Van Balen, 2005).

Aerial lime is obtained from the thermal decomposition, called calcination, of limestone. Calcination of calcium carbonate (CaCO_3) is a highly endothermic reaction (Oates, 1998, Rackley, 2009). The reaction only begins when the temperature is above the dissociation temperature of the carbonates in limestone or lime mud (Oates, 1998, Elert *et al.*, 2002). This is typically between 780 °C and 1340 °C (Moffat and Walmsley, 2006). Smaller stones of calcine dissociate faster and provide a greater surface for heat transference, while larger stones require more time, and often higher temperatures (Elert *et al.*, 2002). Once the reaction starts, the temperature must be maintained above the dissociation temperature (Elert *et al.*, 2002). Dissociation of the calcium carbonate proceeds gradually from the outer surface of the particle inwards (Elert *et al.*, 2002, Moffat and Walmsley, 2006).

Moropoulou *et al.* (2001) states that the reactivity is related to the calcination temperature and the specific surface area. The greatest surface area is obtained for limestone calcined at around 900 °C, which was the temperature performed in traditional kilns (Elert *et al.*, 2002). Other researchers (Elert *et al.*, 2002) claim that lime exhibiting the highest surface area is not necessarily the most reactive, since water access might be restricted by small pores. The optimum calcination parameters vary for the different types of limestone, and they are

influenced by chemical and textural characteristics of the raw material (Elert *et al.*, 2002, Okonkwo and Adefila, 2012).

Under severe calcining conditions the lime might become hard-burned or even dead-burned when sintering temperatures are reached (Elert *et al.*, 2002, Boynton, 1984). In these conditions the stone shrinks to 25-50% of its original size, resulting in a densification and a reduction of the surface area and chemical reactivity (Elert *et al.*, 2002, Boynton, 1984). The sintering processes (Angelo and Subramanian, 2008, Kingery *et al.*, 1976), as the effect of temperature progresses, lead to an increase in apparent density and a decrease in the specific internal surface area of the lime and therefore retard the slaking reaction of the lime (Hogewoning *et al.*, 2008, Chen *et al.*, 2006). Sintering (Angelo and Subramanian, 2008, Kingery *et al.*, 1976) starts when the relevant area has been calcined (Hogewoning *et al.*, 2008). The calcination zone advances as a front towards the center of the piece and leaves behind a calcined outer zone in which the temperature rises (Hogewoning *et al.*, 2008). Sintering of the sample can therefore take place in this zone although the core is not yet fully dissociated (Hogewoning *et al.*, 2008).

Burned lime, exposed to temperatures of around 1400 °C, shows a dark color and might have a porosity of only about 8-12% (Elert *et al.*, 2002, Swallow and Carrington, 1995). On the other hand, soft-burned lime, calcined at low temperature, has a porosity up to 50% and a greater chemical reactivity (Boynton, 1984, Elert *et al.*, 2002). A soft-burned lime pebble is full of small hair-like cracks where CO₂ has escaped from the limestone during the calcination process (Hassibi 2009).

The color of soft-burned lime is typically white, even if some impurities can result in grey, brown or yellow tint (Elert *et al.*, 2002). After the calcination is completed, air exposure of the quicklime must be kept to a minimum to avoid air-slaking, a process whereby the aerial reacts with the carbon dioxide and moisture in the atmosphere to become partially hydrated and carbonated (Elert *et al.*, 2002). The use of high purity lime is even suggested, since the impurities may obstruct the pores making the surface more impervious to water and slaking process lower (Elert *et al.*, 2002, Harrison, 1993).

After this general explanation about aerial lime, with emphasis on how the material is obtained/produced (calcination), a schematic representation of its cycle is presented in Figure 2-5. Each process involved in the lime cycle, slaking/hydration and carbonation will be presented with more details next.

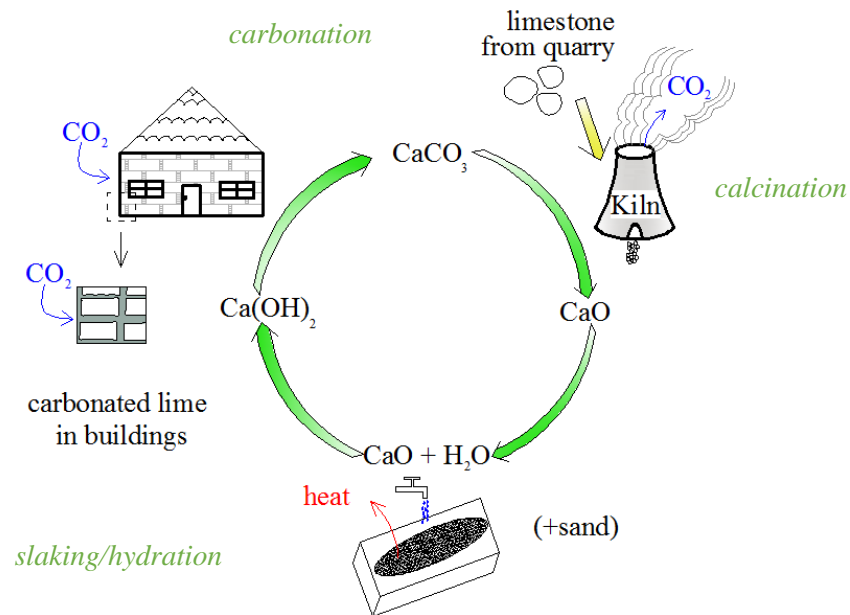


Figure 2-5 – Aerial lime cycle (adapted from Lawrence (2006))

The hydration process generally causes an increase in surface area and volume of hydrated lime compared to the aerial lime (Oates, 1998). A dry hydrate is produced by mixing one part by weight of quicklime with about 0.5 to 0.75 parts of water, depending on the reactivity of aerial lime (Miller, 1960, Elert *et al.*, 2002). The water quality also has influence on the final hydrated lime (Elert *et al.*, 2002).

The last stage presented in Figure 2-5 is the carbonation, after placement the aerial lime mortar in the presence of the atmospheric CO_2 (Arizzi and Cultrone, 2013, Lawrence *et al.*, 2006a, Lawrence, 2006, Carran *et al.*, 2011). Mortars based on non-hydraulic lime, do not harden the water, because they have no hydraulic properties (CEN, 2010a, Lawrence, 2006). The study of the carbonation is one of the focus of the present work, in this sense, a more detailed description will be presented during the development of the thesis.

2.3.3 Classification of aerial lime

In this section, information about the classification of aerial lime is presented. In a simplified classification, aerial lime can be divided in two groups (Adam, 2005):

a – fat or rich lime, containing 0.1 to 1 percent of clay;

b – poor or lean lime resulting from calcination and slaking of limestone containing 2 to 8 per cent clay.

In terms of international regulations, two different standards are cited, the first related to the European Standard, and the second according to the American Society for Testing and Materials (ASTM, 2011). According to EN 459-1 (CEN, 2010a) aerial lime can be classified in three designation as shown in Table 2-1. This norm classifies the material as CL 90, CL 80 and CL 70 (CEN, 2010a).

Table 2-1 – Designation of limes (EN 459-1 (CEN, 2010a))

Designation	Notation
Calcium lime 90	CL 90
Calcium lime 80	CL 80
Calcium lime 70	CL 70
In addition, calcium lime is classified according to the form of the product, quicklime (Q), hydrated lime (S), lime putty (S PL) or milk lime (S ML)	

The standard EN 459-1 (CEN, 2010a) classifies aerial lime according to the percentage values presented in Table 2-2. Here, the values for CaO + MgO, MgO, CO₂ and SO₃ are applicable to all forms of calcium lime. For quicklime, these values correspond to the finished product and, for all other forms of lime (hydrated lime, lime putty and milk of lime), the values are based on the product after subtraction of its free water and bound water content. The values for available lime (calcium oxide for quicklime, calcium hydroxide for hydrated lime) refer to the product when tested in accordance with EN 459-2.

Table 2-2 – Compositions of aerial limes

Type of calcium lime	Values given as mass fraction in percentage				
	CaO+MgO	MgO	CO ₂	SO ₃	Available lime
CL90	≥90	≤5	≤4	≤2	≥80
CL80	≥80	≤5	≤7	≤2	≥65
CL70	≥70	≤5	≤12	≤2	≥55
a MgO content up to 7% is permitted if the soundness test in accordance with EN 459 is passed. b A higher content of CO ₂ is permitted, if all other chemical requirements in Table 2 (EN 459) are satisfied and the test frequency satisfies the requirements in Table 7 (EN 459). c Higher values of available lime may be requested.					

Another parameter that characterizes the aerial lime is the reactivity (CEN, 2010b). Aerial lime on slaking process presents an increase in temperature, which occurs because the exothermic reaction with water, the reactivity is measured as a function of the reaction time (wet slaking curve) (Gambhir and Jamwal, 2014). An example of a typical wet slaking curve is presented in Figure 2-6.

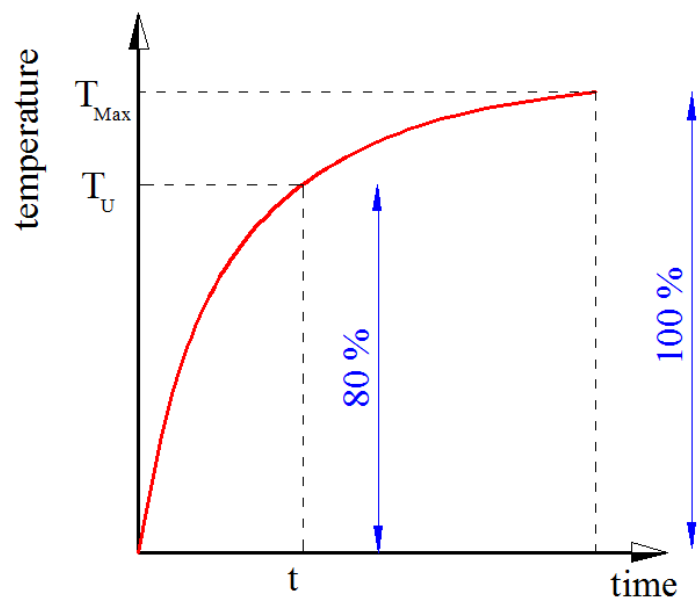


Figure 2-6 – Typical reactivity curve for aerial lime (CEN, 2010b)

The reactivity of the material is described by the parameter t_{60° or t_u , according to EN 459-2 (CEN, 2010b). The slaking reaction of the lime is assumed to be 100% complete at the time when the maximum temperature has been reached (Zacharopoulou, 2013). The first parameter t_{60° corresponds to the time necessary to reach a required temperature T (for instance, 60°C), while the second parameter indicates the time required for the hydration reaction to be 80% complete (CEN, 2010b).

Oates (1998) presents a relation between t_{60° and t_u , which is the time to hydrate 80% of lime (see Figure 2-6). Both the parameters are defined according to EN 459-2 (CEN, 2010b).

In continuity with the study of aerial lime, in another normative reference, the ASTM standard C51-11 (ASTM, 2011) classifies aerial lime according to the size of the cluster, as explained in Table 2-3.

Table 2-3 – Classification of aerial (ASTM, 2011)

Denomination	Classifying parameter
Large lumps	Diameter \leq 8 in. (20.32 cm)
Crushed/pebble lime	2.5 in. (6.35 cm) \leq diameter \leq 0.25 in. (0.64 cm)
Ground lime	Diameter \leq 0.25 in. (0.64 cm)
Pulverized lime	Maximum grain size passes through 0.033 in. (8.4 mm) sieve
Pelletized lime/briquettes	Grain average dimension : 1 in. (2.5 cm)

2.3.4 Brief history of aerial lime application

Lime-based mortar has been widely used as a structural and finishing material for at least the past 10000 years (Bentur, 2002, Lawrence, 2006). A considerable portion of the worldwide architectural heritage is constructed with clay bricks or stone blocks bound together with mortars based in lime, especially in Europe, America, North Africa and West Asia (Arizzi and Cultrone, 2013, Pesce, 2014). The most ancient archaeological examples of lime and gypsum mortars have been found in the cities of Yftah (Israel) and Catalhoyük (Turkey) (7000-6000 BC) and in the Egyptian pyramids (4000-2000 BC) (Arizzi and Cultrone, 2013). In Europe, the greatest examples of the ample range of construction ability achieved with mortars date back to Greek and Roman times (Arizzi and Cultrone, 2012, Arizzi and Cultrone, 2013). Furthermore, mortars are often applied as finishing or decoration layers to provide a protective, smooth and attractive finish (Groot, 2010, Veiga *et al.*, 2010b). As examples of ornamental mortars, it is worth mentioning the stuccos of the Mayan and Inca civilizations (AD 300-900), and the gypsum plasters of Spain (14th century, Spain) (Arizzi and Cultrone, 2013, Carran *et al.*, 2011).

As mentioned, aerial lime, which had already been used by Egyptians, started to be largely used by Romans (Arizzi and Cultrone, 2013, Thirumalini and Sekar, 2013). From the 3rd century BC, Romans used lime with pozzolans and caementa (aggregates from volcanic rocks and limestone) to make the well-known “*Opus Caementicium*” (Dodge, 1984, Kourkoulis, 2006, Brandon *et al.*, 2014). Pozzolans had a great importance as additive, in fact it gives to the mix the ability to set under water (Festa and Colombo, 2006).

Continuing with the history, during the Middle Ages, with the fall of Roman Empire, the abilities in preparing lime mortars achieved by Romans in several aspects were lost (Zawawi, 2010, Silva *et al.*, 2005). Lime and artefacts quality became very poor, also because of the

low quality of furnaces, which were not able to guarantee the thermal decomposition of all the limestone (Arizzi and Cultrone, 2012, Arizzi and Cultrone, 2013).

In Portuguese context, air lime-based mortars are present in ancient buildings, in different types of application (Faria and Martins, 2013, Veiga *et al.*, 2008). The most common uses in ancient buildings are as renders, plasters, ceramic glazed tiles bond layers and masonry joint mortars (Faria and Martins, 2013).

The industrial production of hydraulic lime started in the 18th century (Christidis, 2011, Bartos *et al.*, 2000). Then Vicat (1818) patented a type of hydraulic lime made from calcination of limestone and clay (Lawrence, 2006, Bartos *et al.*, 2000). Other patents based on the mixture of Vicat had followed (Dobbs, Frost) before 1824 (when the modern Portland cement was invented by Aspdin) (Lawrence, 2006, Hewlett, 2003).

The use of aerial lime in construction was recurrent until the 19th century (Lawrence, 2006, Langenbach, 2010). In the 19th century, the development of Portland cement led to a considerable fall in aerial lime use (Callebaut *et al.*, 2001, Cultrone *et al.*, 2005, Pesce, 2014) because cement offered advantages such as fast setting and high mechanical strength (Radonjic *et al.*, 2001b, Cultrone *et al.*, 2005). Modern construction techniques have benefited from this speed (Baccaro *et al.*, 2000, Alvarez De Buergo *et al.*, 1994, Radonjic *et al.*, 2001a).

The way to prepare the aerial lime mortar may affect the material performance and properties (Forster, 2004a, Forster, 2004b), and a schematic representation of different possibilities are shown in Figure 2-7.

In Figure 2-7 the general name of lime putty has been adopted. But depending on the amount of water added several products can be produced from the slaking process of quicklime (Pesce, 2014, Boynton, 1984). From the most to the least rich in water, the available products are (Pesce, 2014, Boynton, 1984):

- *Lime water*: a saturated or unsaturated solution of Ca(OH)_2 without solid phase;
- *Milk of lime*: (or whitewash) an aqueous colloidal suspension with Ca(OH)_2 particles which the solid ranges are between 1 and 20%.
- *Lime slurry*: a colloidal suspension of Ca(OH)_2 characterized by the consistency of a thick cream without body or plasticity with Ca(OH)_2 content between 20 and 35%.

- *Lime putty*: a plastic moldable pasta, sometimes also described as a colloidal gel that contains $\text{Ca}(\text{OH})_2$ between 30 and 40%.

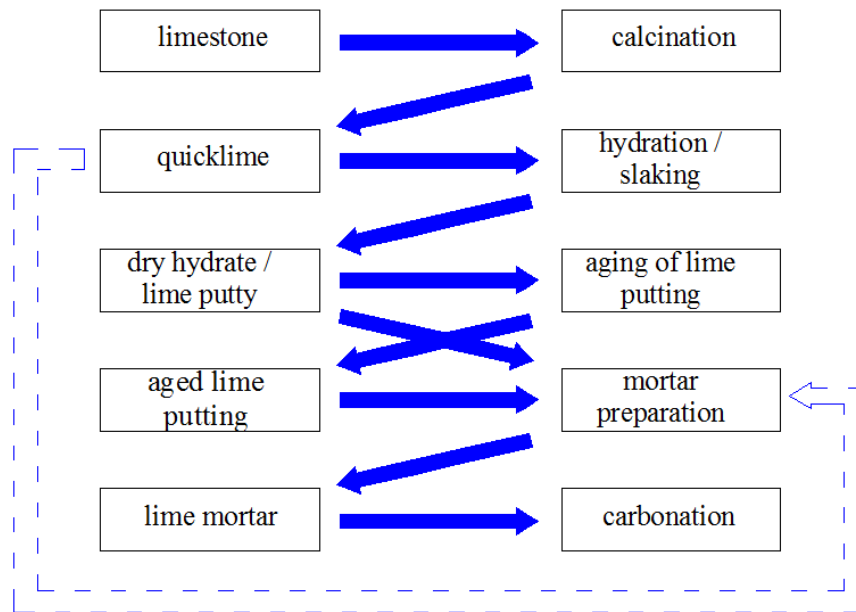


Figure 2-7 – Processing of lime and resulting material (adapted from Elert *et al.* (2002))

Lime putty, in particular, is obtained by adding water in excess to the necessary amount to hydrate lime (DOI, 2004) This product can be aged, improving some characteristics (Cizer *et al.*, 2012, Ruiz-Agudo and Rodriguez-Navarro, 2010). A traditional method cited in literature was to slake lime with sand (hot lime mix) (Forster, 2004a, Forster, 2004b), by adding quicklime to sand in a pre-defined volume proportion (Margalha *et al.*, 2011, Válek and Matas, 2010, Malinowski and Hansen, 2011, Moropoulou *et al.*, 1996) and water (simple represented by the dashed line in Figure 2-7). This method is adopted in the experimental part of the present work (Chapters 5 and 6).

2.4 Mortars

2.4.1 Introduction

Mortars are constituted by a binder (such as lime or cement) and an aggregate such as sand. A wide variety of mortars (Elert *et al.*, 2002) was used in the construction of historical monuments and other structures. The mortars based on lime are the most commonly used in

historic context (Maravelaki-Kalaitzaki *et al.*, 2003, Moropoulou *et al.*, 2005, Bianchini *et al.*, 2004). Historically, examples of early applications of lime mortar include buildings in Palestine and Turkey dating from 12000 BC (Kingery, 1988, Landsberg, 1992, Maravelaki-Kalaitzaki *et al.*, 2003, Genestar and Pons, 2003, Degryse *et al.*, 2002).

As mentioned, in the 19th century, the advent of Portland cement led to a significant reduction in the utilization of the material (Callebaut *et al.*, 2001, Cultrone *et al.*, 2005, Pesce, 2014). Recently the interest in lime-based mortars is increasing because of the study and restoration of historic buildings, as they are compatible with traditional building materials (Moropoulou *et al.*, 2005, Cultrone *et al.*, 2005), with which Portland cement shows low chemical and physical affinity (Binda *et al.*, 2000b, Cultrone *et al.*, 2005, Lanas and Alvarez, 2003). Characterization of historic lime mortars became an important subject in the second half of the 20th century (Böke *et al.*, 2008, Cowan, 1978). The studies on historic lime mortars and plasters are compiled by Moropoulou *et al.* (1995), Elert *et al.* (2002) and Hansen *et al.* (2005) in an extensive bibliography. In the Portuguese context, reference is made to the works presented by Silva *et al.* (2006), Magalhães and Veiga (2009) and Adriano *et al.* (2009).

2.4.2 *Deterioration and restoration*

The degradation of masonry walls of historical buildings depends on original traditional building materials used (stone, brick, mortar, etc.), environmental loads and the materials used in subsequent conservation and restoration interventions (limestone, plaster, cement, lime, polymer materials, and others) (Moropoulou *et al.*, 2005, Ngoma, 2009).

Atmospheric pollution and acid deposition on materials are recognized as some of the most important and common causes of decay endangering the built heritage (Lanas and Alvarez, 2003, Lanas *et al.*, 2005, Price, 1996, Pérez Bernal and Bello López, 2004). The physical cause of degradation can be related to the content variations of water within the masonry (evaporation, capillary flow or ice formation and others) or chemical attack (sulfate, alkali-silica reaction, the formation of ettringite expansion, and products such as thaumasite) (Moropoulou *et al.*, 2005, Collepardi, 1990).

The processes of transference of pollutants from the atmosphere to surfaces are divided into two groups: deposition "*dry*" and "*wet*" (Lewis and McConchie, 1994). The "*dry deposition*" is the direct collection of gases, aerosols and particulate species in a dry or wet, whereas the "*wet deposition*" includes the incorporation of pollutants in cloud droplets ("*rainout*"),

removal by deposition of precipitation ("*washout*") and deposit the resulting liquid on the surface (Lewis and McConchie, 1994). In order to predict the damage from acid deposition it is necessary to know how decomposition rates are related quantitatively to the concentration of pollutants and meteorological parameters (Lewis and McConchie, 1994). The mathematical formulation used in these expressions is usually called "*Damage function*" (Lewis and McConchie, 1994). The deterioration of real structures, in the absence of known and controlled conditions is complex due to several mechanisms and because various circumstances can occur simultaneously: the materials used may vary and are often unknown (Moriconi *et al.*, 1994).

Knowledge about durability is still a critical aspect for historic mortars (Lanas *et al.*, 2005, Lanas *et al.*, 2006). Different authors have been testing mortar samples under different environmental conditions, and the various aspects of durability that were considered include: external exposure to urban atmosphere (Zappia *et al.*, 1994, Boutin and Bromblet, 2000a, Boutin and Bromblet, 2000b) and pollutants (SO₂) (Sabbioni *et al.*, 2002, Sabbioni *et al.*, 2001, Martínez-Ramírez *et al.*, 2002), weathering cycles (in a climatic chamber) (Laycock, 2002), or freeze-thaw cycles (Klemm and Klemm, 1997, Shao *et al.*, 1997).

As mentioned before, for adequate restoration and conservation works, the knowledge of the material properties is essential (Collepari, 1990). There are numerous techniques for the mortars characterization (Jedrzejewska, 1960, Frizot, 1981, Dupas, 1981, Cliver, 1974, Moropoulou *et al.*, 1995). For historic buildings (subject to restrictions of public authorities), diagnostic implies additional difficulties due to the limited number of samples collected, when this is allowed at all (Moriconi *et al.*, 1994, Binda and Saisi, 2009). In addition, for historic buildings the problem of diagnosis is usually more complex than for modern concrete structures (Moriconi *et al.*, 1994). These difficulties occur because historic buildings are subjected to longer exposures, with changing and often unknown environmental conditions (micro-climate and urban) (Moriconi *et al.*, 1994, Binda and Saisi, 2009).

In recent decades, few researches have been carried out in aerial lime mortars (Cultrone *et al.*, 2005, Collepari, 1990). In addition the literature reports that the problem of degradation and restoration of masonry walls, especially in historic buildings (Elert *et al.*, 2002, Cazalla *et al.*, 2000, Collepari, 1990, Lawrence, 2006). Restoration interventions may include significant errors and cause acceleration of damage to buildings with authentic material and structures (Teutonico *et al.*, 1993, Moropoulou *et al.*, 2005). However, the long-term compatibility between materials is often not clearly yet understood (Martinez and Carro,

2007, Torgal *et al.*, 2012, Sasse and Snethlage, 1997). Moreover, the assessment of compatibility is based on experimental results in laboratory conditions, which may differ significantly from reality (Lawrence, 2006). This assessment cannot be considered a safe and reliable way to estimate the compatibility of such composite systems. In the research presented by Moropoulou *et al.* (2005), the authors studied restoration mortars with similar chemical composition of binders, aggregates and minerals (Moropoulou *et al.*, 1996, Moropoulou *et al.*, 2005). In Moropoulou *et al.* (2005) various mixtures were tested in laboratory, and their chemical and mechanical properties were investigated. Furthermore, the authors attempted to estimate the cure time required for reaching the maximum strength, and for reaching physical and chemical stability of the system's compounds.

Different authorities have published guidelines which are useful to deal with restoration of historic mortars (South Somerset District Council, 1996; English Heritage, 1997; Scottish Lime Centre, 2003). Other useful publications include (Schofield, 1997) and some articles in "*Lime News*" the "*Journal of the Building Limes Forum*" (Lawrence, 2006). Another important example is "*The Smeaton Project*" (Teutonico *et al.*, 1993). It was a joint research programme of ICCROM¹ (International Centre for the Study of the Preservation and Restoration of Cultural Property) (ICCROM, 2014), a range of hydraulic and non-hydraulic lime mortars over several years were tested (Lawrence, 2006).

It seems, therefore, that the study and production of more suitable "*traditional*" mortars is being encouraged. The production of repair mortars, nevertheless, presents a considerable task for construction industry, because of a series of aspects that difficult an appropriate re-establishment of the materials used in the past (Lawrence, 2006). There are no standards referring to the production of lime mortars and this makes replication more complicated at an industrial level (Cazalla *et al.*, 2000, Lawrence, 2006).

Considering that aerial lime mortars have proved over the centuries to be compatible of long duration under severe mechanical and environmental loads, the materials for restoration should be able to replicate the behavior of historical materials as close as possible (Moropoulou *et al.*, 2005, Paiva *et al.*, 2006, Lawrence, 2006). More information about techniques and the use of lime for the restoration of ancient constructions can be found in Carran *et al.* (2011), Elsen (2006), Winfield (2006), Moropoulou *et al.* (2005) and Degryse *et al.* (2002).

¹ ICCROM is an intergovernmental organization dedicated to the conservation of cultural heritage.

2.4.3 *Composition in ancient buildings and recent research*

The composition of mortars varies greatly due to the types and quantities of aggregates, forms of binder and also additives that can be mixed. Analysis of traditional mortars indicates that they tend to be binder rich, sometimes in the region of 1:1 to 1:2.5 (binder to aggregate respectively, in volume) and have a quantity of whitish-colored, unmixed lumps of binder known as lime inclusions (Lawrence, 2006, Forster, 2004b, Forster, 2004a). Lime inclusions may appear as unmixed dry powder, unmixed lime putty, reprecipitated lime, or hot-lime inclusions (Lawrence, 2006, Forster, 2004b, Forster, 2004a). Several organic and inorganic additives were also added for preparing mortar over the history, and an extensive description of historical mortar composition can be found in Gimbert (2008) and Sickels (1988).

Regarding the mixing procedure, hot limes are made by mixing aggregates with quick-lime and hydrating the lime during the mixing process (Veiga *et al.*, 2010a, Margalha *et al.*, 2011, Lawrence *et al.*, 2006a). Hot limes have been used in ancient and historic masonry constructions in Europe, in different ways and construction situations (Martínez *et al.*, 2013, Forster, 2004a, Forster, 2004b). An extensive study about the properties of mortar produced from hot lime method can be found in Malinowski and Hansen (2011), Foster (2004a) and Foster (2004b).

In recent studies, varying proportions of raw materials were considered in order to describe how the binder:aggregate ratio affects mortar properties. As examples of compositions, Teutonico *et al.* (1993) used the ratios of 1:2.5 and 1:3 (binder/aggregate). Baronio *et al.* (1999) initially tried an unsuccessful ratio of 1:5, thus changing to 1:3 (binder/aggregate). Lanás and Alvarez (2003) on the other hand, tried lower aggregate proportions (1:1, 1:2, 1:3 and 1:4) (binder/aggregate), which did not presented casting issues. Moropoulou *et al.* (2005) used 1:1.5 and 1:3 (binder/aggregate). Lawrence (2006) repeated the three first ratios adopted by Lanás and Alvarez (2003). Válek and Matas (2010) performed 1:0.9 and also 1:3 ratios. Margalha *et al.* (2011) differently from the previous references adopted the composition in terms of weight instead of volume, and two different binder/aggregate ratios were selected (1:5 and 1:13).

Lawrence *et al.* (2006a) stated that the composition 1:3 (lime/aggregate) is the most common adopted in research.

Also, different forms of aerial lime have been used and a summary is presented in Table 2-4.

Table 2-4 – Type of binder used by different researchers

Author	Type of binder
Teutonico <i>et al.</i> (1993)	lime putty
Baronio <i>et al.</i> (1999)	pieces of quicklime
Lanas and Alvarez (2003)	dry hydrated lime
Moropoulou <i>et al.</i> (2005)	dry hydrated lime
Van Balen (2005)	lime putty, putty extra water, dry hydrated lime
Lawrence (2006a)	4 month-old lime putty, 20 year-old lime putty, kibbled high purity quicklime, dry hydrate lime
Válek and Matas (2010)	lime putty, quicklime
Margalha <i>et al.</i> (2011)	micronized quicklime

2.5 Carbonation process

2.5.1 General aspects

Carbonation may be considered a natural process (Erdly and Schwartz, 2004). The estimation of the carbonation progress is of great importance, for instance in concrete structures, as the calculation of the carbonation depth is essential for the estimation of the service life for concrete components (Chang and Chen, 2006, Pacheco Torgal *et al.*, 2012). For aerial lime, the process has also importance, because of the modifications in the material properties in time (Lawrence *et al.*, 2007, Lawrence, 2006). Research has been focused on the study of carbonation of cement-based materials such as concrete (Papadakis *et al.*, 1991a, Papadakis *et al.*, 1989, Steffens *et al.*, 2002, Shih *et al.*, 1999, Hobbs, 2001, Kobayashi *et al.*, 1994, Kamiya *et al.*, 1986) or cement-based waste deposits (Venhuis and Reardon, 2003) considering its long-term behavior (Liu *et al.*, 2003). Mathematical models with different complexity for carbonation have been proposed (Saetta *et al.*, 1993a, Saetta and Vitaliani, 2005, Steffens *et al.*, 2002, Papadakis *et al.*, 1991a, Papadakis *et al.*, 1989) (cement) and Van Balen (2005) (lime). More details about the models will be given in Chapter 4.

The experimental study of the carbonation process in lime based material has been done by different researches (Lanas *et al.*, 2005, Arizzi and Cultrone, 2013, Van Balen and Van Gemert, 1994, Lawrence *et al.*, 2006a, Lawrence, 2006, Lawrence *et al.*, 2007, Lanas *et al.*,

2004b, Cizer *et al.*, 2012, Cazalla *et al.*, 2000). As in concrete, aerial lime mortar reacts with atmospheric carbon dioxide (CO₂) and forms calcium carbonate (Lawrence, 2006). Calcium oxide, hydroxide and carbonate make up a significant proportion of the chemistry of ordinary Portland cement (OPC) (Saetta *et al.*, 1993a, Saetta, 1992) and of aerial lime, therefore the general behavior of both materials in terms of carbonation may be assumed as similar (Ferretti and Bažant, 2006a). Because of this similarity, carbonation of lime mortar was often studied in the past to investigate carbonation of Portland cement mortar and vice versa (Ferretti and Bažant, 2006a). Different authors (Van Balen and Van Gemert, 1994, Papadakis *et al.*, 1992) suggest using the same mathematical models for carbonation of both materials (Ferretti and Bažant, 2006a).

The carbonation occurs from external to internal part (Lawrence, 2006, Arizzi *et al.*, 2011). The carbonation process may be described overall by the chemical processes (Holmes and Wingate, 1997, Lawrence *et al.*, 2007, Lawrence, 2006, Van Balen and Van Gemert, 1994, Van Balen, 2005, Moorehead, 1986). For carbonation to occur the presence of water is essential, since it requires also the dissolution of CO₂ (Van Balen and Van Gemert, 1994, Lawrence, 2006). The CO₂ in atmosphere dissolves in the water present in the mortar (Van Balen and Van Gemert, 1994, Lawrence *et al.*, 2006a). The dissolution of carbon dioxide in water depends on the mass transfer coefficient between water and air (Van Balen and Van Gemert, 1994, Lawrence *et al.*, 2006a). This coefficient is unknown, but from a set of equilibrium conditions, there is a relationship between the concentration of carbon dioxide in water and partial pressure in air (Van Balen and Van Gemert, 1994):

$$\begin{cases} [CO_2]_w = K_H P_k \\ [CO_2]_w = K_H RT [CO_2] \end{cases} \quad 2.1$$

where: $[CO_2]$ is the carbon dioxide concentration (mol/m³); $[CO_2]_w$ is the carbon dioxide concentration in water (mol/m³); K_H is the Henry's constant (mol/L×atm); and P_k is the partial carbon dioxide pressure (Pa) (Van Balen and Van Gemert, 1994).

The calcium hydroxide (Ca(OH)₂) is accessed by the CO₂ in its dissolved state (Johannesson and Utgenannt, 2001). However, there are five main stages involved in the carbonation process of mortar made with aerial lime (Lawrence, 2006, Lawrence *et al.*, 2006a, Andrejkovicova *et al.*, 2012):

1. diffusion of gaseous CO₂ through the pores of the mortar;

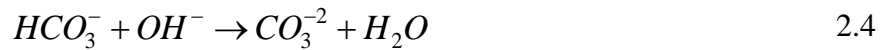
2. dissolution of the CO_2 in the pore water;



3. dissolution of $\text{Ca}(\text{OH})_2$ in the pore water;



4. chemical equilibrium of dissolved CO_2 in the pore water;



5. precipitation of CaCO_3 .

Considering these five main stages, a schematic representation of components during the carbonation process is shown in Figure 2-8. The percentage of each component depends on the evolution of the carbonation process Moorehead (1986) (Lawrence, 2006).

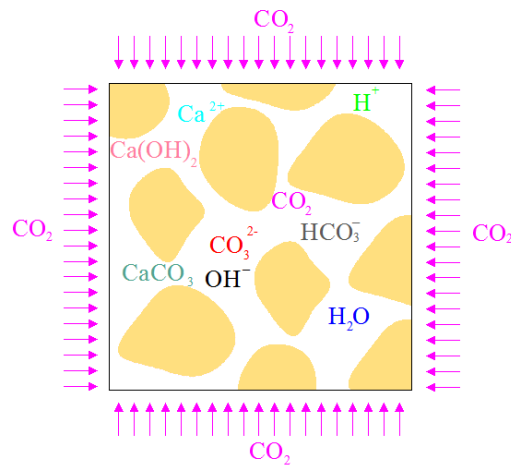


Figure 2-8 – Components presents in aerial lime mortar during the carbonation (adapted from Cizer *et al.* (n. d))

The dissolution of CO_2 in water creates an acid environment with a pH equilibrium (in an environment with $20\text{ }^\circ\text{C}$ and CO_2 concentration $\approx 0.03\%$) around 5.6 (value calculated with

PHREEQC²). In opposition to the previous phenomenon, the dissolution of $\text{Ca}(\text{OH})_2$ in water solution generates a basic environment, with a pH equilibrium at 20 °C around 12.6 (value calculated with PHREEQC²).

The final compound of the carbonation process is CaCO_3 , which usually presents a smaller pH than $\text{Ca}(\text{OH})_2$ (Pesce, 2014). Due to the chemical modifications, either using cement and lime as binders, carbonation can modify the microstructure and microstructural properties, namely porosity, pore size distribution, and specific surface area (Arandigoyen *et al.*, 2006, Johannesson and Utgenannt, 2001, Cultrone *et al.*, 2005). Within the carbonation process there is a non-uniform distribution of material compounds over time and space, schematically represented in Figure 2-9 in time.

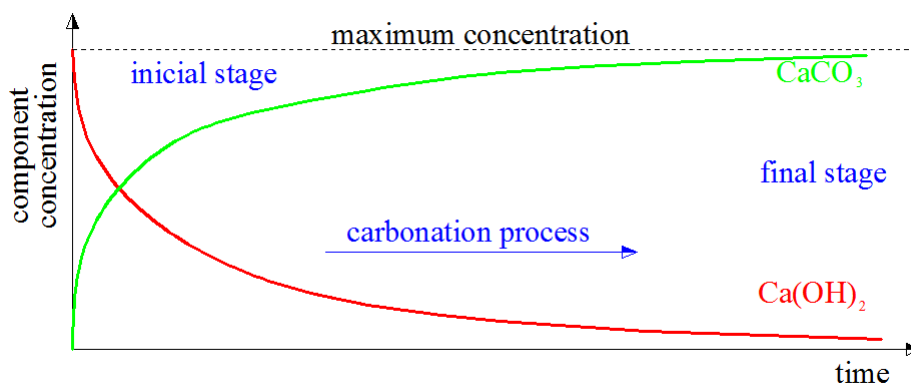


Figure 2-9 – Components concentration in aerial lime mortar during the carbonation process

The carbonation rate depends on several factors, for instance, CO_2 concentration, air pressure and moisture content of lime, relative humidity and other factors (Arizzi and Cultrone, 2013, Lawrence, 2006). In terms of carbon dioxide concentration, air consists mainly of four gases: nitrogen, oxygen, argon and carbon dioxide. The proportional volume of these gases in dry air are about 80% nitrogen, 20% oxygen, 1% argon and <0.1% carbon dioxide (Sisomphon, 2004). The concentration of CO_2 in air is an environmental parameter that can affect the rate

² PHREEQC is a computer program for speciation, reaction-path, advective transport, and inverse geochemical calculations (Parkhurst, 1995). According to Pesce (2014), it is an accurate and powerful tool to investigate lime based materials. For the calculations, the *llnd* databased was used. The software uses an iterative process, in order to find the solution equilibrium, because of the non-linearity involved. More information about the model will be presented in Chapter 3. The calculations were done considering the set of parameters used by Pesce (2014).

of carbonation. Table 2-5 gives the CO₂ values measured in different environments, in terms of volumetric concentration (Saetta and Vitaliani, 2004).

In terms of cementitious based materials, there are very few experimental works, in which the authors directly compare results of accelerated tests with those under natural conditions (Muntean *et al.*, 2005). Sanjuán *et al.* (2003) compare the carbonation of a set of concrete samples under natural and accelerated (5% and 100% CO₂) testing conditions. They obtained a propagation of the carbonation depth which is 5 and 40 times faster than in the natural case, respectively. The authors (Sanjuán *et al.*, 2003) conclude that experimental results with 4-5% CO₂ concentration cannot be simply extrapolated to larger values of CO₂ (Muntean *et al.*, 2005, Sanjuán *et al.*, 2003). Similar effects have been observed by Ishida *et al.* (2004) by means of numerical simulations. These authors (Ishida *et al.*, 2004) investigate the behavior of their model under different CO₂ concentrations and also with different additions in the concrete. Ishida *et al.* (2004) conclude also that accelerated and natural tests may not be always analogous results.

Table 2-5 – Typical CO₂ concentration in different conditions (adapted from Saetta and Vitaliani (2004))

Sample from	CO ₂ concentration (%)
Open country	0.015
City center	0.036
Industrial zone	0.045
Well-ventilated stable	0.046
Stable	0.075
Motor car exhaust	16.7
Human breath	3.6

The result of the carbonation process is calcium carbonate crystals. Carbonation process with high concentration of carbon dioxide leads to the formation of crystals of aragonite (Roques and Girou, 1974). This has been observed in samples carbonated in an atmosphere with a 100% CO₂ concentration (Roques and Girou, 1974). The presence of other gases, can also affect the carbonation, for instance SO₂ may retard the carbonation reaction (Sada *et al.*, 1977). Still in respect to the concentration of carbon dioxide in the surrounding environment, Moorehead (1986) states that increasing values would lead to an increasing amount of calcite, as in a saturated CO₂ atmosphere. Experiments carried out by Shin (2009) and by

Van Balen (2005) show opposite results, though. Both authors state that it is actually the availability of moisture which guides the process, and carbonation proceeds at a rate independent from the carbon dioxide concentration.

Dehilly *et al.* (2002) demonstrated that the carbon dioxide concentration is important during carbonation process in lime paste. The authors observed that lime paste underwent a rapid and complete reaction in a carbonic atmosphere, while in a low CO₂ atmosphere carbonation took twice as long (Cultrone *et al.*, 2005, Dheilly *et al.*, 2002).

The exposure duration/time of the material in the environment in the presence of CO₂ affects directly the carbonated depth (Van Balen and Van Gemert, 1994). Experimentally different authors measured the progress of the carbonation depth over time, for both materials: concrete (Papadakis *et al.*, 1991a, Chang and Chen, 2006, Villain *et al.*, 2007, Thiery *et al.*, 2007) and for aerial lime (Lawrence, 2006, Lawrence *et al.*, 2007, Lawrence *et al.*, 2006a, Guimarães, 2014, Meneghini, 2014, Arizzi and Cultrone, 2013).

Two simple models, which directly consider the time, for the calculation of the carbonation depth are briefly presented next. As in many problems of diffusion, the carbonation process can be, in simplified way, expressed as (Van Balen and Van Gemert, 1994):

$$x = k_c \sqrt{t} \text{ or } x = e + k_c \sqrt{t} \quad 2.5$$

where: x is the carbonation depth; k_c is the carbonation factor (in general experimentally determined); t is the time and e is a constant.

Another simple formulation to calculate the carbonation depth is proposed by Parrott (1994). The author has developed an equation that takes into account the humidity (h) to predict the carbonation depth (x), as:

$$x = ak^{0.4} \left(\frac{t^n}{CaO^{0.5}} \right) \quad 2.6$$

where: a is a constant ($a = 64$); k is the air permeability of concrete; t is the exposure time; CaO is the CaO content, and n is an exponent (Parrott, 1994).

The exponent, n is typically about 0.5, but decreases for h greater than 70% (Parrott, 1994). The equation presented in Parrott (1994) for the power exponent, n is related to the h by:

$$n = 0.02536 + 0.01785(h) - 0.0001623(h)^2 \quad 2.7$$

The previous equations (Eqs. 2.5, 2.6 and 2.7) presented simplified formulations and several phenomena are not considered. The environmental pH is another aspect that affects the carbonation and the precipitation of CaCO₃. Few data is available about this (Pesce, 2014) and more information can be found in Ma *et al.* (2010), Sheng Han *et al.* (2006) and Tai and Chen (1998). Temperature also can be a factor affecting the carbonation reaction (Pesce, 2014). In concrete, for instance, the increasing of carbonation observed for poorly cured concretes cast at low temperatures is due to the retardation of the hydration of Portland cement and pozzolanic reactions (Neville, 1995). In a simple way the activation energy measures the influence of temperature in one phenomenon (Poole *et al.*, 2007, Carino and Lew, 1984).

For the numerical modeling presented by Ferretti and Bažant (2006a), the activation energy is also adopted as a parameter (Ferretti and Bažant, 2006a). These authors adopted an Arrhenius's law-equation (Masel, 1996) in the numerical modeling for this purpose (Ferretti and Bažant, 2006a). Still, scarce data is available in literature for this parameter even if the diffusion of CO₂ is affected by the activation energy (Tian and Jiang, 2012). The activation energy (E_{a,co_2}) for CO₂ diffusing in concrete was experimentally determined by Saeki *et al.* (1991). These authors obtained a value about 39 kJ/mol, which was used by Talukdar *et al.* (2012) to simulate the carbonation process. A similar value was obtained by Khunthongkeaw and Tangtermsirikul (2005). For aerial lime, Nikulshina *et al.* (2007) and Montes-Hernandez *et al.* (2012) used thermogravimetric analyses and obtained relatively low values, namely $E_a = 5.9-17.44$ kJ/mol for CaO and Ca(OH)₂ particles.

The mortar composition (Arizzi and Cultrone, 2013, Lawrence, 2006, Cultrone *et al.*, 2005, Arandigoyen *et al.*, 2005), including the amount of mixing water used, is another significant factor, since this will affect them mortar properties such as the pore structure of the hardened mortar (Arandigoyen *et al.*, 2005). According to Arizzi and Cultrone (2013) mortars made with a well-graded calcareous aggregate with rough and angular grains are more carbonated than those made with a less wellgraded siliceous aggregate with polished and round grains, both on the outer part and in the core of the samples. Two main reasons are given: the better packing and cohesion achieved with the first type of aggregate; and the active role of a calcareous aggregate in the transformation of portlandite into calcite because of a

composition similarity and the presence of cavities on the grain surface, which act as nucleation sites for the new-formed calcite (Arizzi and Cultrone, 2013).

In a research in which the authors (Lawrence *et al.*, 2006a) studied the influence of three types of aggregates (silicate sand, crushed oolitic stone and crushed bioclastic stone) in the carbonation, the silicate sand mortar carbonates to a greater and faster extent than the other two mortar mixes (Lawrence *et al.*, 2006a). The carbonation front is at ~12 mm at 90 days (silicate sand), compared with ~8 mm for the other mortars. By 180 days, full carbonation appears to have occurred in the silicate sand mortar, while there is still 5–7.5 mm of material yet to fully carbonate in the other mortars (Lawrence *et al.*, 2006a). The carbonation front in the silicate sand mortar extends over a greater distance than the other two mortars (Lawrence *et al.*, 2006a).

In another study Cultrone *et al.* (2005) state that with the increase of water/lime ratio used in the paste preparation, also the porosity of carbonated lime-pastes shows higher values. An increase in porosity will improve the access of CO₂ to the interior of the mortar, and therefore will impact on the rate of carbonation (Lawrence *et al.*, 2006a). Other ions and inorganic additives such as magnesium (Mg²⁺), silica acid (H₄SiO₄) and sulfates (SO₄²⁻) also may have influence in carbonation process (Pesce, 2014, Park *et al.*, 2008, Tracy *et al.*, 1998a, Tracy *et al.*, 1998b). The characteristics of the lime particles (shape, size and aggregation) also seem to influence the speed of carbonation and the performance of the final product (Cazalla *et al.*, 2000, Ruiz-Agudo and Rodriguez-Navarro, 2010, Arizzi and Cultrone, 2013).

Finally, in terms of environmental conditions, one of the most important parameter affecting the carbonation process is the relative humidity (Houst and Wittmann, 1994, Ferretti and Bažant, 2006a, Papadakis *et al.*, 1991a). Given its importance, the next section is fully dedicated to this phenomenon.

2.5.2 Influence of relative humidity

Different researchers demonstrated the influence of the humidity in the carbonation process (Houst and Wittmann, 1994, Ferretti and Bažant, 2006a, Papadakis *et al.*, 1991a).

At h levels higher than 40%, pores with a radius less than 0.4 nm become blocked (Houst, 1996), and above 90%, all but the larger macropores will be blocked (Papadakis *et al.*, 1991a). Philippi *et al.* (1994) have calculated values for critical radius range from 5 nm at 78.3% h to 100 nm at 99% h (Lawrence, 2005). In another reference the conclusion was that

the carbonation is more rapid at a relative humidity of 50-70% and decreases at higher and lower relative humidity (Walton *et al.*, 1997, Fattuhi, 1988).

According to Lagerblad (2006), a very dry concrete does not carbonate due to the lack of water needed for ions to form and subsequently react and form CaCO_3 . On the other hand, the carbonation is also slow in wet conditions (Lagerblad, 2006). This leads to a humidity value (h) at which the rate of carbonation is maximum (Lagerblad, 2006). This maximum depends on the specific open porosity and specific type of binder. Moreover, it also depends on the geometry of capillary system, which, in practice means that it depends on the water/binder ratio, degree of hydration and type of binder. According to Lagerblad (2006), the maximum speed of carbonation is when h is between 60 and 80% h (inside the concrete). One would expect that a porous concrete will carbonate faster at a higher h than less porous concrete as a narrow capillary more easily becomes blocked by water (Lagerblad, 2006). This was also showed in accelerated experiments by Meland (1985).

Siddiqi (2012) states that the optimal conditions for carbonation occur at a h of 50% (range 40 - 90%). If $h < 40\%$ CO_2 cannot dissolve and if $h > 90\%$ diffusion of carbon dioxide will be inhibited by the water that has filled the pores and hence CO_2 cannot enter the concrete. Moreover, Siddiqi (2012) affirms that the most dangerous range of relative humidity for carbonation is 40% to 80%.

Other references indicate that the highest rates of carbonation in concrete occur when the relative humidity is maintained between 50% and 75% (PCA, 2012, ACI, 1992). Below 25% relative humidity, the degree of carbonation that takes place is considered insignificant. Again, above 75% of relative humidity, the moisture in the pores restricts CO_2 penetration. A similar threshold value (70%) is given by Al-Khaiat and Fattuhi (2002), which states that the carbonate rate will diminish to zero at 100% relative humidity.

For aerial lime the phenomenon is similar to concrete, as high relative humidity would fill pores with water (Lawrence, 2006). This hampers the access of atmospheric CO_2 to uncarbonated $\text{Ca}(\text{OH})_2$ and as cited before, the diffusion of gases in a liquid is slower than in air. Diffusion of gases in a liquid is about 10,000 times slower than in air (Houst, 1996, Lawrence, 2006). It has been shown that 100% of pore surface is available for carbonation between ~40% and ~80% h (Van Balen and Van Gemert, 1994). Below 20% h carbonation cannot occur since there is insufficient pore water present for either $\text{Ca}(\text{OH})_2$ or CO_2 to dissolve (Lawrence, 2006). At h above 90%, less than 50% of pore surface is available for carbonation (Lawrence, 2006). When saturated, a mortar cannot carbonate except via the very much slower liquid diffusion (Arandigoyen *et al.*, 2005, Arandigoyen *et al.*, 2006,

Arandigoyen *et al.*, 2004, Lawrence, 2006). Dheilly *et al.* (2002) studied the influence of storing conditions on the carbonation of powdered Ca(OH)₂. The authors stated that with high h , relatively low levels of carbon dioxide and temperatures ~ 10 °C favored the carbonation process (Dheilly *et al.*, 2002).

As real structures are in general exposed in environment with drying and wetting cycles, this can also affect the carbonation. Cyclic wetting and drying seems to accelerate carbonation in concrete (Lagerblad, 2006). Note also that water is produced by the carbonation reaction and is consumed by the hydration process (Pesce, 2014, Lawrence, 2006, Ferretti and Bažant, 2006a).

2.5.3 Diffusion of CO₂

In this section, general information about the diffusion of carbon dioxide in porous materials is presented. The movement of gases, liquids and ions through mortar or concrete is important because of their interactions with the constituents or the pore water, which can alter the material behavior (Basheer *et al.*, 2001) or modify the mechanical properties (Lanas and Alvarez, 2003, Lanas *et al.*, 2004b). The rate of carbonation depends largely on the diffusivity of carbon dioxide in concrete (Jung *et al.*, 2011) or mortar (Lawrence *et al.*, 2006a, Lawrence, 2006) and the penetration of carbon dioxide is faster when a material is more porous (Houst *et al.*, 1993). Therefore, it is necessary to correctly determine the diffusivity of carbon dioxide in materials to realistically evaluate the carbonation depth (Jung *et al.*, 2011).

The diffusion of gases such as air, oxygen (O₂) or carbon dioxide (CO₂) is primarily controlled by the moisture content (CEB–FIP, 2010). For intermediate moisture contents, the diffusion coefficient in concrete for carbon dioxide or oxygen is in the range of $10^{-7} < D_{CO_2} < 10^{-10} \text{ m}^2 / \text{s}$. According to Model Code (CEB–FIP, 2010) the diffusion coefficient for carbon dioxide D_{CO_2} through carbonated concrete may be estimated as:

$$\log\left(D_{CO_2} / D_{CO_{2,0}}\right) = -0.05 f_{cm} \quad 2.8$$

where: D_{CO_2} is the diffusion coefficient of CO₂ in (m²/s); $D_{CO_{2,0}} = 10^{-6.1}$; and f_{cm} is the mean compressive strength in (MPa) (CEB–FIP, 2010).

The measure of the diffusion coefficient of carbon dioxide in concrete in a natural, or accelerated carbonation experiment is difficult, since the carbon dioxide in concrete can react with some compounds and is consumed as soon as it has diffused inside (Park *et al.*, 2012). Furthermore, the pore structure of the material changes (Arandigoyen *et al.*, 2006, Lawrence *et al.*, 2007, Ngala and Page, 1997).

Papadakis *et al.* (1991b) suggested formulas for the diffusion coefficient of carbon dioxide with the porosity and the relative humidity as variables:

$$D_{co_2} = 1.64 \times 10^{-6} \phi^{1.8} \left(1 - \frac{h}{100}\right)^{2.2} \quad 2.9$$

where: ϕ is the total porosity (%) .

Steffens *et al.* (2002) used for numerical simulation of carbonation, as values for the CO₂ diffusion coefficients, $D_{co_2} = 1.39 \times 10^{-7}$, $D_{co_2} = 3.78 \times 10^{-8}$ and $D_{co_2} = 8.33 \times 10^{-9} m^2 / s$ for curing times of 1, 7 and 28 days, respectively (assuming an higher value for smaller curing time). For Steffens *et al.* (2002) the carbon dioxide dependence of humidity can be expressed as a function of humidity. From experimental tests on OPC pastes, the function is expressed as:

$$f_h = a_1 + \frac{a_2}{1 + (a_3 - h \times a_3)^{a_4}} \quad 2.10$$

and the parameters are identified as: $a_1 = 0.993$; $a_2 = 0.974$; $a_3 = 3.621$ and $a_4 = 5.75$ (Steffens *et al.*, 2002).

In another study, Jung *et al.* (2011) show that the diffusion coefficients of carbon dioxide of carbonated concrete are somewhat lower than those of noncarbonated concrete (Jung *et al.*, 2011) also indicates that the effect of carbonation on the diffusion coefficient is small for concrete with a relatively high w/c . This may be due to the relatively large pore structures for concrete with a high w/c and is more pronounced when the h is low. However, the rate of increase in the diffusion coefficients according to the w/c becomes small when h is high (Jung *et al.*, 2011). This is most likely due to the fact that the variation of pore structures caused by the change of w/c has little effect on the diffusion of carbon dioxide in concrete under high h , because most of the pores are filled with water when the h is high (Jung *et al.*,

2011). The same study indicates that the diffusion coefficient of carbon dioxide decreases with an increase of h for all concrete specimens (Jung *et al.*, 2011).

For lime mortars, the diffusion coefficient has been defined from the study of Van Balen and Van Gemert (1994), as a function of water content (see Figure 2-10).

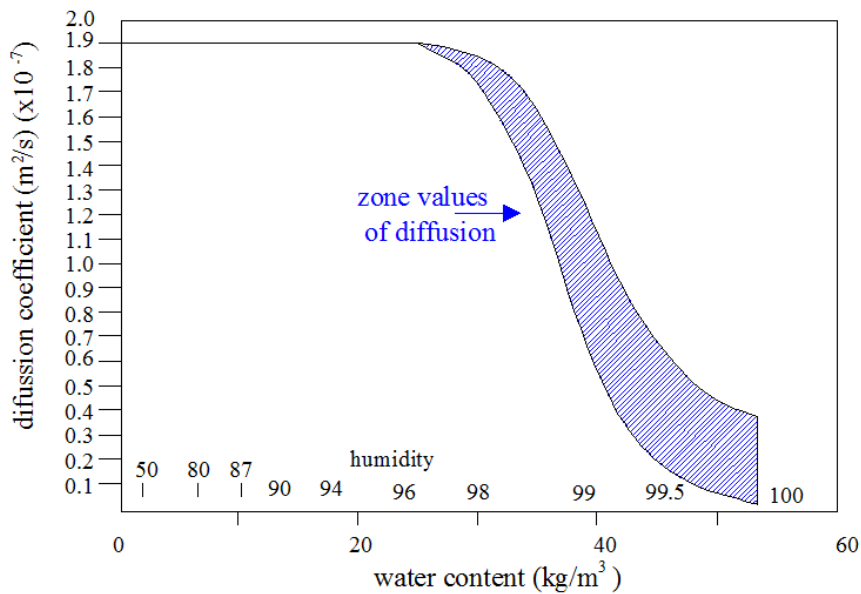


Figure 2-10 – Diffusion coefficient vs water content/humidity (adapted from Van Balen and Van Gemert. (1994))

According to the authors (Van Balen and Van Gemert, 1994), this approach neglects carbon dioxide diffusion, when the water content in the material is between the capillary water content and the critical water content. When the critical water content is reached, capillary water transport to the surface is stopped. Before the critical water content is reached, the large pores can yet be free of water and therefore, theoretically, diffusion of carbon dioxide should be possible.

Experimental results in K.U. Leuven have indicated that the CO₂ diffusion coefficient decreases almost linearly when increasing the water content from a dry mortar to capillary saturation due to the blockage the CO₂ diffusion by water (Cizer *et al.*, 2012). Due to the presence of coarse pores in lime mortars, the influence of water content on CO₂ diffusivity is much less pronounced than in cement mortars composed of sorption pores (Van Gerven *et al.*, 2009). Therefore, CO₂ diffusion in lime mortars can take place at high moisture contents and it is only blocked at a water content above saturation by capillary suction (Van Gerven *et al.*, 2009, Van Balen *et al.*, 1997). This particular property of lime mortars allows

the water vapor transport inside a masonry wall and therefore contributes to the durability of masonry (Van Gerven *et al.*, 2009).

In another reference related to lime material, according to Lawrence (2005) with the h increases, the effective pore radius reduces as a result of the formation of an aqueous film on the walls of the pores. Bentz (1997) affirmed that when the radius of a pore is smaller than the radius computed from the Kelvin-Laplace equation, capillary condensation will occur. Pore sizes below this critical radius are not, therefore, involved in the carbonation process (Johannesson and Utgenannt, 2001, Lawrence, 2006). Porosity can be explained as the relation of open pores, or voids over the total material volume (Li and Ren, 2011, Marshall, 1990).

Saeki *et al.* (1991) studied the change in micro-structure of concrete due to carbonation process. The authors reported (Saeki *et al.*, 1991) that the change in pore volume and pore size distribution due to carbonation depends on water-cement ratio and initial curing period for concrete material. A similar conclusion was obtained by other authors (García-González *et al.*, 2008, Song *et al.*, 2006, Basheer *et al.*, 2001). Pore volume in the carbonated portion is decreased in the case of continuous carbonation test and also denseness of structure induced by carbonation affects the subsequent carbonation process (García-González *et al.*, 2008, Song *et al.*, 2006, Basheer *et al.*, 2001).

According to Ishida and Li (2008) the reduction in the porosity after carbonation can be simplified modeled as a linear function of ratio of remaining quantity of calcium hydroxide and the water-to-cement ratio in the mix, which also coincides with the experimental study presented by Saeki *et al.* (1991):

$$\begin{cases} \phi_c = \alpha\phi \\ \alpha = \alpha_f & (R < \beta) \\ \alpha = 1.25 \times R - 0.25 & (\beta < R \leq 1) \end{cases} \quad 2.11$$

where: ϕ_c is the porosity after the carbonation reaction, and α is the reduction parameter in the porosity and R represent the ratio of quantity of remaining calcium hydroxide to the total quantity of calcium hydroxide generated by hydration (Ishida and Li, 2008).

The parameter α_f represents the porosity reduction ratio after sufficient progress of carbonation. When the degree of carbonation R reaches a value of parameter, the reduction in porosity is assumed to be constant and remains at α_f (Ishida and Li, 2008).

Ishida and Li (2008) affirm that the change in the micro-pore structure due to carbonation depends on the geometric characteristics of original micro-pore structure of hardened cement matrix, and the change in the properties (mass, volume, specific surface area) of hydrates due to carbonation.

$$\begin{cases} \alpha_f = 0.67 \times (w / c) + 0.27 \\ \beta = 0.8 \times \alpha_f + 0.2 \end{cases} \quad 2.12$$

The pore structure and mass transport characteristics of cementitious materials or in mortar may strongly influenced by prior exposure to drying and to carbonation (Ngala and Page, 1997, Lawrence, 2006).

For aerial lime mortar, Lanas and Alvarez (2003) concluded that higher values porosities allow better portlandite (Ca(OH)_2) carbonation and larger amounts of binder increase the total porosity. In another study Lanas *et al.* (2006) concluded that there is a relation between the porosity reduction and a mortar strength increment. Cazalla *et al.* (2002) reports that there a reduction of porosity values with higher degrees of carbonation. Numerically, Saetta and Vitaliani (2004, 2005), and Ferretti and Bažant (2006a) adopted a linear relation between the reaction process and a parameter related to reduction of porosity.

2.5.4 Pore structure changes during the carbonation and the diffusion of CO_2

In aerial lime mortar, there is a complex interaction between water/ CO_2 fluxes and the components present, numerically simulated by Ferretti and Bažant (2006a) and an schematic representation is presented in Figure 2-11. Here, the focus of the compounds of mortar is the Ca(OH)_2 and CaCO_3 , since they are directly involved in the carbonation process.

The humidity diffusion process (water flux) tends to occur, considering that the environment present lower humidity than the mortar, with the consequently drying of the mortar (Oliveira *et al.*, 2015, Azenha, 2009). Together and associated with this phenomenon, there is increase of CO_2 concentration due to the diffusion process, and the conversion of Ca(OH)_2 to CaCO_3 , which also can affect the mortar properties (Lawrence, 2006, Lanas and Alvarez, 2003). The knowledge of the pore size distribution inside the material and how it changes over time is important information, because it influences the rate of transport (CEB–FIP, 1993, Maekawa *et al.*, 2008).

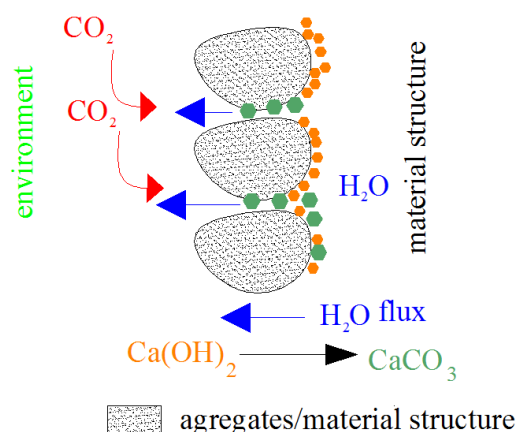


Figure 2-11 – Carbonation process - water and CO₂ fluxes

The size of pores in the cement paste ranges over several orders of magnitude (Gonen and Yazicioglu, 2007). According to their origin and characteristics, they are classified as compaction pores, air pores and capillary pores (which affect durability) and gel pores (CEB–FIP, 1993, CEB–FIP, 2010). Different authors studied the change of specific surface area and pore size distribution due to carbonation in Portland ordinary cement mortar (Johannesson and Utgenannt, 2001, Ngala and Page, 1997). Changes in pore structure caused by carbonation include a significant reduction in total porosity (Houst, 1996), and permeability reductions between 3 and 5 orders of magnitude (Dewaele *et al.*, 1991). These subjects will be discussed with further details in Chapter 3.

The distribution of pore sizes within mortar has a significant effect on its durability and also in the carbonation process (Izaguirre *et al.*, 2010, Lawrence, 2006). Since this distribution is changed by carbonation, measurement of this characteristic provides valuable information on the developing water transport characteristics and potential durability of mortar, as influenced by the ongoing carbonation process (Lawrence, 2006).

As cited, the diffusion of CO₂ through the mortar is controlled by the pore structure (Hall and Hoff, 2004), which is also influenced by the nature and granulometry of filler (Houst *et al.*, 1993). As CaCO₃ crystals form, they can reduce the size of, or even obstruct, the pores and, thereby, reduce the accessibility of CO₂ to the interior of material (Lawrence, 2006, Lawrence, 2005, Lawrence *et al.*, 2006a). This results in a reduction in the average pore radius, shifting the pore size distribution at the expense of macropores and in favor of mesopores (Dewaele *et al.*, 1991). The change in pore size is particularly noticeable in unmodified dispersed hydrated lime mortars, where carbonation can seal the interior from gas percolation (Lawrence, 2006, Lawrence, 2005).

For aerial lime mortar, according to Lawrence (2007), mortar based on silicate sand showed more pores with a very small radius $< 0.01 \mu\text{m}$, but at the silicate sand mortar there were greater amount of bigger voids ($> 10 \mu\text{m}$) (Lawrence *et al.*, 2007). This means a faster carbonation in silicate sand mortar than in calcitic aggregate mortar. The carbonated material an increase of the volume of very small pores ($> 0.03 \mu\text{m}$) has been detected. There is no significant variation in the volume of pores with a radius $> 0.1 \mu\text{m}$, which are not involved in carbonation progress (Lawrence *et al.*, 2007).

As reference, due to lake of specific studies in terms of modeling for aerial lime mortar, the research of Houst and Wittmann (1994) is briefly described. The authors developed a model for the diffusion of CO_2 through hydrated cement paste. The variation of diffusivity as a function of water content and porosity is explained by the authors considering the characteristic microstructure, which has been characterized by water adsorption isotherms and mercury intrusion porosimetry measurements (Lawrence, 2006). A model with two levels in the microstructure is presented by Houst and Wittmann (1994) to describe CO_2 diffusion in a carbonating material. This model identifies three distinct zones for pore sizes distribution. The largest pores allow normal gas diffusion (Houst and Wittmann, 1994). This phenomenon occurs when the mean free path of gas molecules is smaller than the pore diameter. When the pore diameter is smaller than the mean free path of gas molecules, Knudsen diffusion takes place. These two forms of diffusion are illustrated in Figure 2-12 . Normal diffusivity (D_n) is deduced from simple kinetic theory of gas (Houst and Wittmann, 1994);

$$D_n = \frac{1}{3} c_s \lambda \quad 2.13$$

where: c_s is the average molecular speed:

$$c_s = \sqrt{\frac{8RT}{\pi M}} \quad 2.14$$

and λ is the mean free path:

$$\lambda = \frac{RT}{N\pi d^2 P} \quad 2.15$$

where M is molar mass, R is gas constant, T is temperature, N is Avogadro number, d is molecular number, and P is pressure (Houst and Wittmann, 1994).

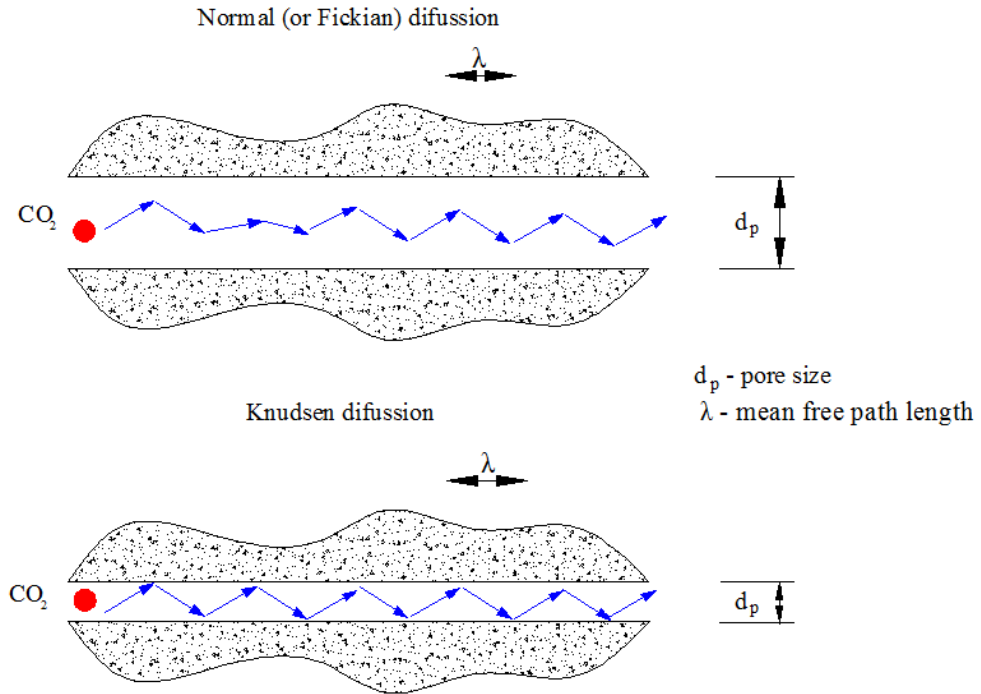


Figure 2-12 – Diffusion processes of CO₂ – Normal and Knudsen diffusion (adapted from Houst and Wittmann (1994))

From Eq. 2.15 it can be deduced that $\lambda_{CO_2} = 0.045\mu\text{m}$ at 296 K and 97000 Pa. For small pores, where the pore diameter is smaller than the mean free path, Knudsen diffusion takes place, with Knudsen diffusivity (D_k) expressed as (Houst and Wittmann, 1994):

$$D_k = \frac{2}{3} c_s r \quad 2.16$$

where r is the radius of capillary in nanometers.

For pores of intermediate size, both Knudsen and normal diffusion occur simultaneously, with diffusivity in the intermediate domain (D_m) (Houst and Wittmann, 1994):

$$D_m = \frac{D_n}{\left(1 + \frac{\lambda}{2r}\right)} \quad 2.17$$

According to Houst and Wittmann (1994) this means that for CO₂ normal diffusion occurs where pore diameters (d_p) are larger than 0.45 μm. Intermediate diffusivity occurs where pore diameters are between 0.045 μm and 0.45 μm, and Knudsen diffusivity occurs when pore diameters are below 0.045 μm (Houst and Wittmann, 1994).

Lanas and Alvarez (2003) investigated the pore structure of lime mortar using mercury intrusion porosimetry (MIP) in order to establish the pore size distribution, showing that carbonation decreases the porosity of lime pastes, but not with the same intensity in all pore size ranges. According to Lanás and Alvarez (2003) the highest range modification is between 0.01 μm and 0.03 μm. This means that diffusion of CO₂ in lime pastes may be modified from normal diffusivity towards Knudsen diffusivity by the carbonation action (Lawrence, 2006). This modification can affect the rate at which CO₂ diffuses through the mortar, and as a result the rate at which it will carbonate (Lawrence, 2006).

During the carbonation, portlandite crystals, Ca(OH)₂, reacts with CO₂ and forms calcite crystals, CaCO₃, as cited before; but calcite crystals have different crystal structure and molar volume, the microstructure of lime and lime-cement pastes changes, such as crystals join to each other creating a net and the material strength increases (Han *et al.*, 2005). Calcium carbonate particles have three crystal morphologies, which can be classified as rhombic calcite, needlelike aragonite and spherical vaterite (Han *et al.*, 2005). Calcite is the most stable phase at ordinary temperature under normal atmospheric conditions, while aragonite and vaterite are metastable polymorphs which readily transform into the stable phase-calcite (Han *et al.*, 2005).

In this phenomenon, kinetic or thermodynamic factors are present (Arandigoyen *et al.*, 2006). If kinetic factors predominate, CaCO₃ will precipitate as aragonite or as vaterite, both of these polymorphs will convert finally into calcite, the more stable polymorph (Han *et al.*, 2005). If thermodynamic factors predominate, CaCO₃ will precipitate as calcite. As it is shown in Table 2-6, the porosity of paste will vary depending on the polymorph formed, although, finally, all the polymorphs will revert to calcite (Han *et al.*, 2005). More information about the CaCO₃ polymorphism can be found in Pesce (2014) and Tucker and Wright (1991).

Although some efforts have been made in the study of ancient mortars, in many aspects the works can still be extended (Bruni *et al.*, 1998, Bianchini *et al.*, 2004, Ingo *et al.*, 2004, Mosquera *et al.*, 2006, Genestar and Pons, 2003). The slow carbonation process is evidenced by Lea (1970), as mortar taken from buildings many hundreds of years old, if undamaged, is found to consist of mainly calcium hydroxide, only the external portions having been

converted to carbonate. Similar conclusions were made by other authors (Adams *et al.*, 1992, Adams *et al.*, 1998). In walls of moderate thickness the final mortar setting can amount to some years, whereas in wall of very large thickness, centuries might be required before final setting occurs (Adams *et al.*, 1992, Adams *et al.*, 1998).

Table 2-6 – Crystal shape (Arandigoyen *et al.*, 2006)

Mineral	Density (g/cm ³)	Molar volume (cm ³)	Crystal shape	Variation of volume (%)
Portlandite	2.23	33.2	Laminar	-
Calcite	2.71	36.93	Prismatic	11.2
Aragonite	2.93	34.16	Fibrous	2.9
Vaterite	2.54	39.4	Spherical	18.7

In ancient mortars, the carbonation process is slow under ordinary circumstances also because the percentage of carbon dioxide in the atmosphere is low (Cultrone *et al.*, 2005).

2.5.5 Measurement techniques

The methods to measure carbonation can be divided in quantitative or qualitative (Villain *et al.*, 2007, Lawrence *et al.*, 2006a). The thermogravimetric analysis, X-Ray diffraction and the thermal differential analysis can measure the content of CaCO₃ (Midgley, 1979, Ramachandran, 1979), therefore they can be classified as quantitative. Other quantitative methods as cited by Lawrence (2005), Lo and Lee (2002), Slegers and Rouxhet (1976), Villain *et al.* (2007). Thermogravimetric analysis (TGA) is the easiest and the most widely used method (Villain *et al.*, 2007, Lawrence *et al.*, 2006a). The measurement of calcium hydroxide and calcium carbonate ensuing from carbonation is possible by TGA (Villain *et al.*, 2007). The colorimetric test (qualitative method) is commonly linked with CO₂ carbonation models, which are based on the diffusion process in the porous material and which imply a steep carbonation front (Villain *et al.*, 2007). Different studies show that the carbonation front is not sharp but gradual (Parrott and Killoh, 1989, Thiery *et al.*, 2004). In this work, two methods (phenolphthalein and thermogravimetric analysis) are described with more detail and are used. It is noted that there is no internationally accepted standard method for the carbonation measurement (Lawrence, 2006). Regarding the size of specimen

under test, the dimensions should be defined by its intended application rather than by any particular norm (Lawrence, 2006, Lawrence, 2005, Lawrence *et al.*, 2006a).

- *Phenolphthalein*

A traditional method of detecting carbonation is the spray in the freshly broken surface of mortar with phenolphthalein (Lawrence, 2006). The chemical formula of phenolphthalein is $C_{20}H_{14}O_4$ (Gonçalves, 2011). The recommendation presented in RILEM (1988), suggest a solution of 1% phenolphthalein in 70% ethyl alcohol for determining the depth of carbonation. Phenolphthalein is an indicator which changes from clear to a deep pink above a *pH* of about 9.3 (see Figure 2-13).

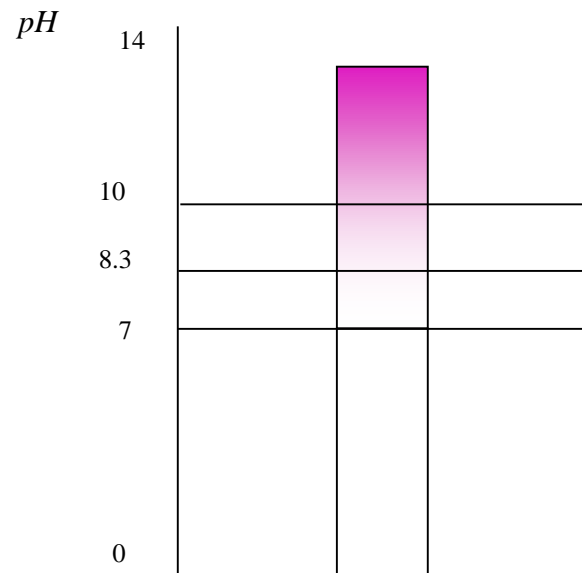


Figure 2-13 – Phenolphthalein indicator - color scale (adapted from Lawrence (2006))

It is the most common method used to detect carbonation in both lime mortars and concrete (Mehta and Monteiro, 2005, RILEM, 1988, Lawrence, 2006, Lawrence, 2005, Lo and Lee, 2002, Fattuhi, 1988, Houst and Wittmann, 2002, Kobayashi *et al.*, 1994, Parrott and Killoh, 1989).

Chemical indicators do not change color sharply at one particular *pH*, but rather over a narrow range (Lawrence, 2006). For phenolphthalein, this range is between 8.3 and 10.0 (see

Figure 2-13) (Richardson, 1988, RILEM, 1988, Mehta and Monteiro, 2005, Lo and Lee, 2002, Lawrence, 2006, Lawrence *et al.*, 2006a).

In order to illustrate some results obtained with the use of phenolphthalein, Table 2-7 shows the data from Lawrence (2006).

Table 2-7 – Carbonation depth (data obtained from Lawrence (2006))

Specimen size (mm)	Material	Age of testing (days)	Carbonation depth (mm)
50 × 50 × 250	mortar based on lime putty; mix 1:3 by volume; 3 types of aggregate	14	2.5 – 3
		28	4.5 – 6.5
		90	9 – 14.5

Verstryngge (2010) studied the carbonation depth with phenolphthalein, in accelerated conditions and using specimens with 40 mm × 40 mm × 160 mm, and an aerial lime mortar (1 volume part of lime on 2.5 volume parts of sand). The conditions in the chamber (box) were kept at a constant temperature of 20 ± 1 °C and a relative humidity of $60 \pm 5\%$. The CO₂ level could not be kept constant, but was monitored by means of a gas analyzer and fluctuated between 2.5 and 9%. The carbonation front progresses from the free end (top of the specimens) inwards and after 4 weeks, a depth of 10 cm is reached, result obtained with phenolphthalein indicator (Verstryngge, 2010). According to the author (Verstryngge, 2010), a small carbonated zone could be observed at the sealed edges of the mortar beams, as they were only covered with paraffin at the age of one month. Other researches also used accelerated carbonation conditions and applied phenolphthalein, to measure the carbonation depth, such as Faria and Martins (2013, 2011) with 5% in carbon dioxide concentration and Pavlík *et al.* (2012) with 5 and 10%.

As previously mentioned the study of carbonation in accelerated conditions (elevated CO₂ concentrations) is still a controversial aspect (Sanjuán *et al.*, 2003, Pacheco Torgal *et al.*, 2012). Other references on the use of phenolphthalein in lime mortar, and further information can be obtained in Cazalla *et al.* (2000) and Rodriguez-Navarro *et al.* (2002).

Finally, other pH indicators (such as thymolphthalein, titan yellow, brilliant orange, etc) have been experimented to detect carbonation in concrete, but with little success (Lawrence, 2006, Parrott, 1990). Further information can be found in Parrott (1990).

- *Thermogravimetry*

Thermogravimetry analysis (TGA) is frequently used for the compositional analysis of materials. This technique measures the weight loss resulting from the thermal decomposition of a material (Earnest, 1988, Adams *et al.*, 1998, Adams *et al.*, 1992, Lawrence, 2006, Lawrence *et al.*, 2006a, Cizer, 2009) and gives results that are intrinsically quantitative. The measured weight losses faithfully reflect the overall reaction taking place (Charsley, 1992; Lawrence, 2006). The requirements for a successful TG analysis include (Larkin, 1988, Lawrence, 2006):

- Good knowledge of analyzed material.
- Awareness that a dependency exists between the components in the mixture.
- Good instrument condition and a pre-analysis purge in order to remove any gases present in the furnace that may react with the sample.
- Component concentrations above 1%.
- Proper selection of test parameters - temperature steps and gradients, atmosphere etc...

The basic technique may be enhanced by using derivative thermogravimetry (dTG) (Warne, 1992). The first derivative of TGA data can be identify the onset and finishing temperatures for individual mass changes (Lawrence, 2006). Literature references indicate that DTA (Differential thermal analysis), along with TGA, X-ray diffraction techniques, electron microscopy and high-temperature microscopy, are important methods for the identification of mortars and for the determination of degree of hydration and carbonation of lime in mortar (Lawrence, 2006). Furthermore, the recarbonation properties of limestones may be studied using controlled atmosphere techniques (Moropoulou *et al.*, 1995).

Each material phase is characterized by its own temperature range of decomposition and by a specific mass loss. According to Villain *et al.* (2007) the lowest temperature of dissociation range is determined by the characteristics of equipment and the heating rate. The maximum temperature of dissociation range is a function of the quantity of the studied phase (Villain *et al.*, 2007).

In literature, different authors adopted distinct experimental setups during the tests, as shown in Table 2-8.

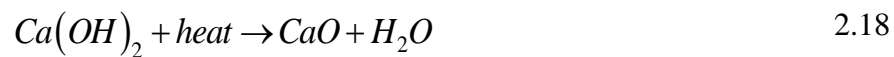
Table 2-8 – TGA experiments in literature (adapted from Lawrence (2006))

Author	Material / Binder	Temperature range (°C)	Temperature increase rate (°C/min)	Atmosphere
Valenti and Cioffi (1985)	cement	20 - 700	10	-
Strydom <i>et al.</i> (1996)	lime	20 - 800	5	Dry N ₂
Dheilly <i>et al.</i> (1998)	lime	20 - 850	0.67	Dry O ₂
Paama <i>et al.</i> (1998)	lime	20 - 900	10	Dry N ₂ /Air
Bakolas <i>et al.</i> (1998)	lime	20 - 1000	10	Dry N ₂
Riccardi <i>et al.</i> (1998)	lime	20 - 1300	10	Dry Air
Ubbriaco and Tasselli (1998)	lime	20 - 950	-	Dry Air
Alvarez <i>et al.</i> (2000)	lime	20 - 1100	10	Dry Air
Balcerowiak (2000)	lime	20 - 950	24	Dry Air
Montoya <i>et al.</i> (2003)	lime	20 - 1050	20	Dry Air
Bruno <i>et al.</i> (2004)	lime	20 - 1000	5 or 10	Dry Air
Ingo <i>et al.</i> (2004)	lime	20 - 1000	20	Dry Air
Moropoulou <i>et al.</i> (2004)	lime	20 - 1000	10	Dry Air
Stepkowska (2005)	cement	20- 1000	1	Dry Air
Maravelaki-Kalaitzaki <i>et al.</i> (2005)	lime	20 - 1000	10	Dry Air
Gualtieri <i>et al.</i> (2006)	lime	20 - 1000	20	Dry N ₂ /Air
Lanas <i>et al.</i> (2005)	lime	20 - 1200	20	Dry Air
Lawrence (2006)	lime	20 - 700	20	Argon
Lawrence <i>et al.</i> (2006a)	lime	20 - 700	20	Argon
Adriano <i>et al.</i> (2009)	lime	20 - 1000	10	Argon
Duran <i>et al.</i> (2010)	lime	20 - 1100	10	Air
Turcry <i>et al.</i> (2014)	cement	20 - 1000	10	Argon

In terms of preparation of samples, these studies are often cited. Villain *et al.* (2007) describe the procedure to prepare the powder samples. First, sawing was carried out under alcohol to cool the blade and to prevent leaching by water. The pieces were selected to avoid the edges and thus skin effects (due to the mold) and by avoiding coarse aggregates, which “dilute” the hydrates and the reaction products, to be measured. The pieces of “concrete mortar” were preserved in airtight bottles, while waiting to carry out the tests.

Ukrainczyk *et al.* (2006) describe that the samples were taken from these representative spots by carefully scraping and drilling concrete in powder. Powder samples were stored in sealed bags to prevent carbonation. Before analyses, powder was additionally grind in corundum crucible. In the present work, a sealing system with the use of plastic bags was adopted, as it will be shown later.

In thermogravimetric analysis each material phase is characterized by its own temperature range of decomposition and by a specific mass loss. For instance, for calcium hydroxide (Eq. 2.18), the evaporation of water (dehydroxylation), and for CaCO_3 , the loss of CO_2 (decarboxylation) (Eq. 2.19) (Atkins, 2010, Atkins and de Paula, 2014, Gameiro *et al.*, 2012, Lawrence, 2006).



Carbonates show distinctive endothermic peaks: at around 840 °C (CaCO_3) and doublets at around 780 and at 860 °C (dolomite), whose position may vary depending on grain size, atmosphere and other concomitant factors (Beck, 1950, Genestar and Pons, 2003, Moropoulou *et al.*, 2005, Vágvölgyi *et al.*, 2008). The temperature range at which dehydroxylation occurs is between 300-550 °C and for the decarboxylation between 650-950 °C. These ranges are based on values in literature (Gameiro *et al.*, 2014, Lawrence, 2006, Lawrence *et al.*, 2006a, Adriano *et al.*, 2009, Lanás *et al.*, 2005), which used similar values. The molecular weights of each composite ($\text{Ca}(\text{OH})_2$, H_2O , CaCO_3 and CO_2) evolved on the two previews cited reactions, are presented in Table 2-9 (Atkins, 2010, Atkins and de Paula, 2014).

The values presented in Table 2-9 are calculated considering the molecular weights of each element involved ($\text{Ca} \approx 40$, $\text{O} \approx 16$, $\text{H} \approx 1$ and $\text{C} \approx 12$) (Atkins, 2010, Atkins and de Paula, 2014).

From the molecular weight (Table 2-9), and based on Eqs. 2.18 and 2.19 is possible to calculate the decomposition weight loss of each compound. The measured weight loss during dehydroxylation is the chemically bound water. The water is given off as a vapor. The measured weight loss can be used to calculate the weight of $\text{Ca}(\text{OH})_2$ originally present.

Each mg of weight loss results from the thermal decomposition of $74/18 = 4.111$ mg of Ca(OH)_2 (Lawrence *et al.*, 2006a, Lawrence, 2006).

Table 2-9 - Molecular weight (Atkins, 2010, Atkins and de Paula, 2014)

Compound	Molar mass (g/mol)
Ca(OH)_2	74
H_2O	18
CaCO_3	100
CO_2	44

For the decarboxylation, the measured weight loss during the process is related to the CO_2 . The CO_2 is given off as a gas. The measured weight loss (due to decarboxylation) can be used to calculate the weight of CaCO_3 originally present. Each mg of weight loss results from the thermal decomposition of $100/44 = 2.272$ mg of CaCO_3 (Gameiro *et al.*, 2012). Beyond, the Ca(OH)_2 and the CaCO_3 , other compounds can be present in mortar, the temperature decomposition range is presented in Table 2-10. The notation adopted in Table 2-10 is typically used for the study of cementitious materials, therefore the formulas of the compounds are expressed in a different format from the typical chemistry rule (see table note).

A typical curve (material mass vs. temperature) for fresh aerial lime mortar, with heating and cooling stages is presented in Figure 2-14. Three main stages are identified (the evaporation of free water, the dehydroxylation and the decarboxylation process). The heat flux curve given by the Differential Scanning Calorimetry (DSC) is useful to understand the nature of reaction (endothermic or exothermic reaction) and the reaction reversibility (during the temperature decrease) (Lawrence *et al.*, 2006a, Lawrence, 2006).

Table 2-10 - Thermal decomposition temperature for TG of hydrated compounds at 20 °C/min (Ubbriaco and Tasselli, 1998, Lawrence, 2006)

Compound Name	Formula ^a	Temperature (°C)
calcium silicate hydrates	CSH	95 - 120
ettringite	C ₄ ASH ₁₂	125 - 135
monosulphate	C ₆ ASH ₃₂	185 - 195
syngenite	K ₂ CaS ₂ H	265 - 275
gypsum (dihydrate)	CSH ₂	160 - 186 (2 peaks)
calcium sulphate hemihydrate	CSH _{1/2}	185
calcium aluminates	CAH ₁₀	110 - 130
	C ₂ AH ₈	175 - 185
	C ₂ AH ₆	280 - 320

^a - S = SO₃; S = Si; A= Al; C = Ca

In Figure 2-14 is presented the range of temperatures for the three main phenomena in this study: free water evaporation, dehydroxylation and decarboxylation.

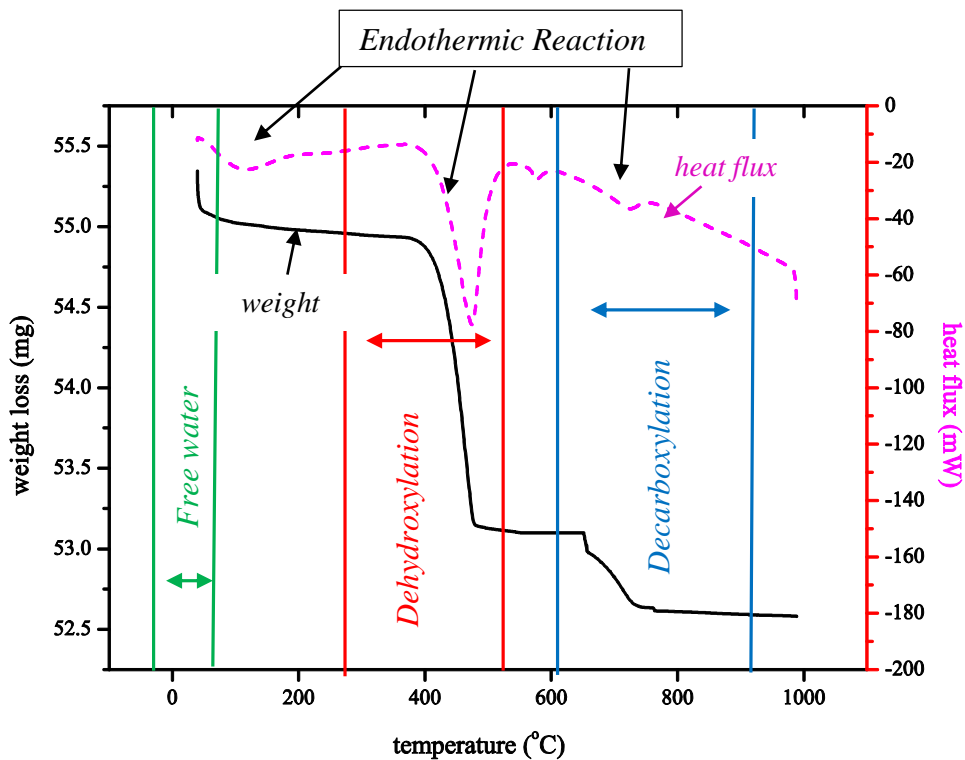


Figure 2-14 – Typical curves from TGA/DSC tests (obtained in one experiment)

For an experimental investigation of aerial lime mortar, determining the carbonation profile (in terms of chemical composition) is an important task, since the compounds present in the

material have significant influence on the mortar behavior. A schematic representation of the profile concentration of the two main compounds ($\text{Ca}(\text{OH})_2$ and CaCO_3) involved in carbonation process in aerial lime mortar, over its own depth can be seen in Figure 2-15. In the most external part of the specimen, where the carbonation occurs faster, the tendency is to present higher amount of CaCO_3 , while in the most internal part, the tendency is to shown a higher presence of $\text{Ca}(\text{OH})_2$ (Cizer *et al.*, n. d, Pesce, 2014).

A transition zone (Sisomphon, 2004, Houst, 1996) can occur, where the carbonation front may not be clearly observed (see Figure 2-15).

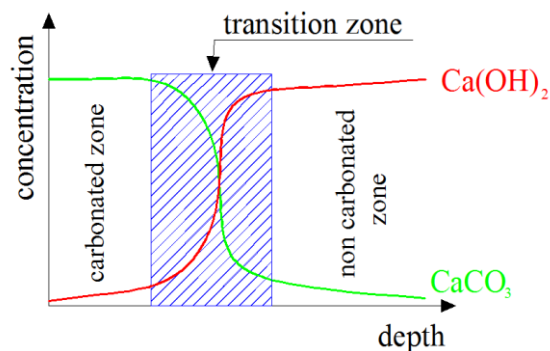


Figure 2-15 – Components profile over material depth

- *The correlation of TGA and phenolphthalein results*

It is important to validate the correlation between the carbonation depth indicated by phenolphthalein spray and chemical results by TGA tests. Gadjia (2001) compared the thermogravimetric results in concrete sampled with the carbonation depth indicated by phenolphthalein spray. The results obtained are indicated in Figure 2-16 and the material slices are collected each 5 mm. The author (Gadjia, 2001) obtained a value around 60% of the carbonated percentage as the indicative of carbonation process by phenolphthalein (the interception of the two curves presented in Figure 2-16).

In another work, by Chang and Chen (2006), carbonation was investigated in an accelerated condition in an environment with high CO_2 concentration (20% CO_2) for 8 and 16 weeks. With thermogravimetric analysis and phenolphthalein techniques, the authors found that the CaCO_3 percentage content equivalent to the carbonation depth indicated by phenolphthalein indicator was significantly smaller (~30%). Therefore, even if the two references are dealing with concrete material, the results are not conclusive.

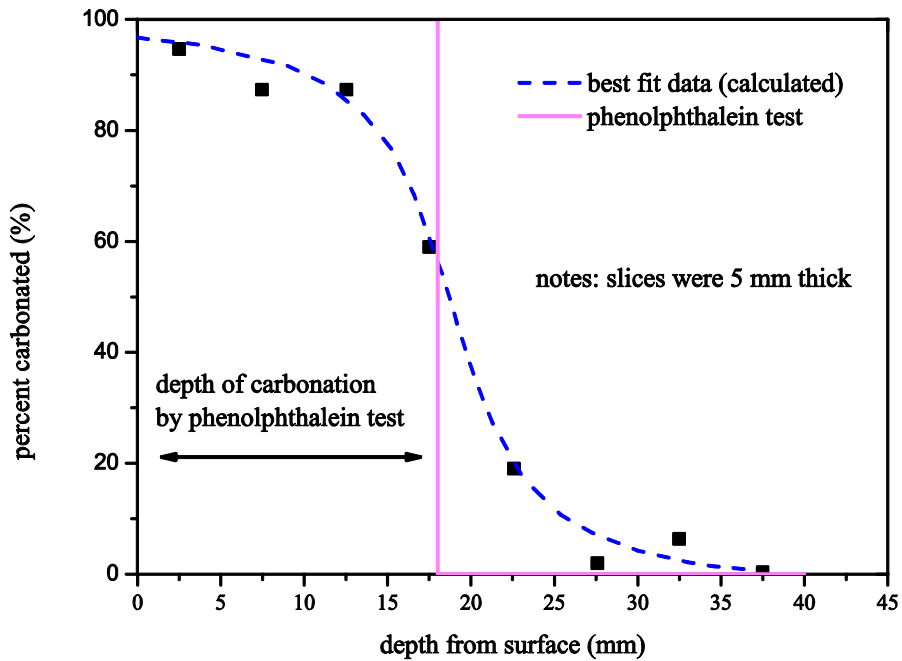


Figure 2-16 – Phenolphthalein vs TGA in concrete (adapted from Gadjja (2001))

For aerial lime mortar, Lawrence (2006) studied the correlation of the carbonation depth by phenolphthalein indicator with TGA profile (see Figure 2-17). The samples were collected each 5 mm at four different ages (14, 28, 90 and 180 days) in an environment with ordinary concentration of CO₂. The author used aerial lime mortar in a proportion (lime:water:sand) (1:1:3), similar to the one adopted in the present work. The carbonation depth obtained by the phenolphthalein spray is indicated by vertical solid lines for 14, 28 and 90 days (see Figure 2-17). The TGA results for different ages are indicated with points connected by dotted lines. The author obtained a value around 60-75% of the carbonated percentage as the indicative of carbonation process by phenolphthalein (the interception of the curves with the vertical lines. Here, the results were obtained for silicate sand, while the other results considering other types of aggregates such as crushed bioclastic stone and crushed oolitic stone may be seen in Lawrence (2006).

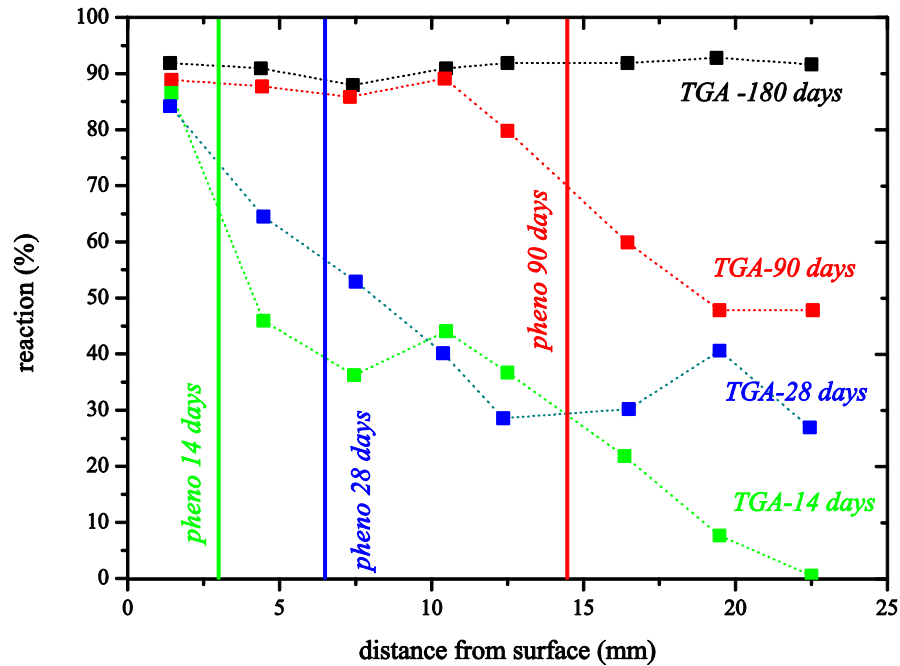


Figure 2-17 – Phenolphthalein vs TGA in aerial lime mortar with silicate sand (adapted from Lawrence (2006))

2.6 Mechanical properties

This section addresses some of the previous studies of mechanical properties (mainly focused in compressive strength and the elasticity modulus) for aerial lime mortar. One important aspect is the curing conditions (Lawrence, 2006, Faria and Martins, 2013), as different curing time and conditions have been used. In Table 2-11 some examples are reported.

In terms of sizes of specimens different geometry have also been adopted, for instance Válek and Matas (2012), Faria and Martins (2013), Margalha *et al.* (2011) and, in some specimens, Baronio *et al.* (1999) adopted the reference of 160 mm × 40 mm × 40 mm cited in EN-1015-11 (CEN, 1999b). Nevertheless, other sizes of specimen were adopted (Lawrence, 2006, Baronio *et al.*, 1999, Teutonico *et al.*, 1993).

In terms of mechanical properties, the focus is usually the compressive strength and the elasticity modulus. Herein, just some general information is shown and more specific data can be found in Chapter 6, in which these two properties are experimentally studied.

Table 2-11 – Curing condition in different references

Author	Curing time and conditions
Teutonico <i>et al.</i> (1993)	demolding after 1 week, then 25 °C, 90% <i>h</i> for 120 days, After this curing period, the blocks were cut to size for the various tests
Baronio <i>et al.</i> (1999)	before demolding: 1 day at 90% <i>h</i> ; then 3 days at 20°C, 75% <i>h</i> in sequence storing: 20 °C, 60% <i>h</i> or external environment
Lanas and Alvarez-Galindo (2003)	demolding after 72 hours, storing in 20 °C, 60% <i>h</i>
Lawrence (2006)	demolding after 5 days, Curing followed BS EN 1015-11:1999 with 7 days at ~90% <i>h</i> , and subsequently at 60% <i>h</i> and 20 °C until testing
Válek and Matas (2010)/Válek and Matas (2012)	20 °C, 65% <i>h</i> ; in 70 days before testing specimens have been subjected to 21 drying-wetting cycles
Faria and Martins (2013)	four types of curing conditions until the age of test, at 20 °C temperature, inside conditioned chambers: 50% <i>h</i> ; 65% <i>h</i> - standard cure; 65% <i>h</i> and 5% carbon dioxide and 95% <i>h</i>

Regarding the study of the compressive strength, an appropriate level of mechanical resistance is required for compatibility, and also required for durability (Lawrence, 2006, Bartos *et al.*, 2000). For instance, in restoration, repair mortar needs to be resistant to stresses inherent in the structure under repair, and to external stresses such as impacts and abrasions (Lawrence, 2006). Such resistance is associated with mechanical strength, making it a fundamental measure of suitability in a repair mortar (Lawrence, 2006, Bartos *et al.*, 2000, Torney *et al.*, 2014). In the context of historical structures, the knowledge of the material strength is also important for the structural integrity (Mahdi, 2015).

Different authors evaluated the compressive strength of lime based mortar (Lanas and Alvarez, 2003, Moropoulou *et al.*, 2005, Henriques *et al.*, 2004). The normative reference for this property is the standard BS EN 1015-11 (CEN, 1999b) for determination of flexural and compressive strength. According to Lawrence (2006), for aerial lime mortar the compressive strength depends on proportions of ingredients and curing conditions. Even if in cement-based materials, the ratio of cement to mixing water has significant influence on the compressive strength of a mortar (Neville, 1995). The effect of the water/lime ratio on the compressive strength of non-hydraulic lime mortars is less well understood (Lawrence *et al.*, 2006a).

One important reference about the study of compressive strength in aerial lime mortar is Lanas and Alvarez (2003). The authors studied mortar with aerial lime, varying aggregate types and binder/aggregates (*b/ag*) ratios ranging from 1:1 to 1:5 by volume. A correlation

between binder amount and mortar strength was observed by the authors, as a binder content increase improves strength within a limit. Binder amounts beyond 2:1 b/ag ratio have shown a strong strength reduction. According to these authors (Lanas and Alvarez, 2003), a large binder content produces an interlocked structure, while the aggregates cause discontinuities in the structure. The porosity increase due to the binder makes carbonation easier, so mortar strength improves. However, in case of binder excess, the increase in voids leads to a strength reduction (Lanas and Alvarez, 2003). The period that the mortar presents the maximum strength has been determined as a function of the binder content: lower b/ag ratio mortars have shown a slight decrease in the strength when the curing time increased.

In another reference, Henriques *et al.* (2004) demonstrated that in lime mortars coarser sands lead to lower porosities, and higher mechanical strengths. Lawrence (2006) demonstrated that air lime mortars made with calcitic aggregates produce materials with high compressive strengths, and the water/lime ratio in air lime mortars has low impact on their compressive strength. The differences in compressive strength between the different aggregate types may well be connected to the way and extent to which the calcite crystals attach themselves to the aggregate particles (Lawrence, 2006, Lanas and Alvarez, 2003). In the same study, (Lawrence, 2006) states that lime putty performs significantly better than dry lime hydrate. Sasse and Snethlage (1997) stated that the elasticity modulus is one of the most important parameters in repair mortars. In building conservation, there is some difficulty in formulating compatible mortars for use in renders and joints, due to requisites of relatively low elasticity modulus and sufficient flexural strength (Velosa and Veiga, 2007). In the context of existing buildings the knowledge of the elasticity modulus and its evolution is important to evaluate the structural behavior specially in terms of deformations (Binda and Saisi, 2002). The results obtained for elasticity modulus seem rather variable (Baronio *et al.*, 1999). One possibility for this fact is associated with the inhomogeneous nature of the mortars (Lawrence, 2006, Baronio *et al.*, 1999). Baronio *et al.* (1999) obtained results with a dynamic modulus being somewhat lower than the static modulus. Another study of such property may be seen in Margalha *et al.* (2011) (modulus of elasticity measured by resonance frequency). Also using resonance frequency, Andrejkovicova *et al.* (2012) studied the evolution of the dynamic modulus of elasticity at 28, 90 and 180 days of curing (lime/sand volumetric ratio of 1:3). The mixture with lime and sand presented 2.38, 2.64 and 3.60 GPa respectively for 28, 90 and 180 days. They also studied the influence of fine and coarse sepiolite (clay mineral) and synthetic zeolite pellets (hydrated crystalline aluminosilicates, they may occur either in nature or be manufactured synthetically) as additives (Andrejkovicova *et al.*, 2012),

but no clear tendency about the influence of the additives for the three ages was observed in terms of dynamic elastic modulus evolution (Andrejkovicova *et al.*, 2012).

In terms of standards, for natural stone, EN 14146 (CEN, 2004) is the test to determine the dynamic modulus of elasticity, and EN 14580 (CEN, 2005b) is the test to determine the static modulus of elasticity. Lawrence (2006) mentions that they may be adopted as reference for the study of such property in mortar.

In this work, phenomena such creep and shrinkage are not detailed, even they were preliminary studied. More details may be found in literature, for instance for creep (Gimbert, 2008, Shrive *et al.*, 1997, Bažant and Baweja, 2000, Tanabe *et al.*, 2008, Sickels Taves, 1995, Anzani *et al.*, 2009, Bažant *et al.*, 1997b, Bažant *et al.*, 1997a, Ferretti and Bažant, 2006b, Anzani *et al.*, 2000, Verstryngge *et al.*, 2011), and for shrinkage (Shimomura and Maekawa, 1997, van Zijl, 2000, Bažant and Baweja, 2000, Sickels Taves, 1995, Bažant, 1988, Brooks and Bakar, 2004, Ferretti and Bažant, 2006b).

For cracking and fracture mechanics aspects, important references are Bažant and Oh (1983), Lotfi and Shing (1994), Luciano and Sacco (1997) and Ferretti and Bažant (2006b), among others.

As shown in this chapter, in literature it is possible to find different references about the studies on aerial lime (Lawrence *et al.*, 2006a, Lawrence *et al.*, 2007, Lawrence, 2006, Lawrence *et al.*, 2006b, Izaguirre *et al.*, 2011, Meneghini, 2014, Arizzi and Cultrone, 2013, Lanas *et al.*, 2004a, Guimarães, 2014, Cizer *et al.*, n. d, Van Gerven *et al.*, 2009, Lanas and Alvarez, 2003, Margalha *et al.*, 2011, Pesce, 2014, Faria and Martins, 2013), but no other reference was found in regards to multi-physics modeling for lime mortar, with exception of the work presented by Ferretti and Bažant (2006a and 2006b).

3 NUMERICAL MODELS FOR MOISTURE AND CARBONATION

3.1 Introduction

This chapter is divided into two main subjects, being the first subject related to the modeling of moisture flux in porous materials with a special focus in the Model Code formulation (CEB–FIP, 1993, CEB–FIP, 2010). The second subject focuses on numerical models to simulate the carbonation process, and special attention is dedicated to the only model used in the literature for simulating the carbonation in aerial lime mortar. This model will also be implemented using the finite difference method.

Moisture transport in porous media plays an important role in a wide variety of processes, such as the degradation of building materials, namely mortar and concrete. Also, the presence of water in building materials can directly influence the material behavior (Martys and Ferraris, 1997). The understanding of the moisture flux in a well-known material such as concrete is important to guide future work in aerial lime mortar, because there are very few studies for this material. In particular, for the simulation of humidity flux, no study could be found in literature for aerial lime mortar.

The properties, performance and durability of cement-based materials such as concrete depend strongly on the moisture content (Xi *et al.*, 1994b, Mehta, 1997, Zhang *et al.*, 2009, Gawin *et al.*, 2003). The moisture content affects the material in different ways, such as the creep behavior, shrinkage, carbonation process, chloride and sulfates ingress, evolution of hydration, freeze-thaw resistance, durability, compressive strength, elastic modulus and others (Oliveira *et al.*, 2015).

The calculation of water transport in unsaturated system was initially developed based on the saturated flow in porous media. This chapter presents selected models from literature, since the drying process in concrete can be simulated in different ways.

Bažant and Najjar (1971) used a numerical formulation based on internal concrete humidity as the driving potential for moisture movements, which included a specific model for the corresponding diffusivity coefficient. This approach has been adopted by Model Code 1990 (CEB–FIP, 1993) and Model Code 2010 (CEB–FIP, 2010), and will also be used in this chapter. In fact, according to FIB Bulletin 70 (FIB, 2013), the parameters proposed by

MC1990/2010 (CEB–FIP, 1993, CEB–FIP, 2010) seem to have been solely derived with basis on diffusion experiments (e.g. the cup-method) and no validation of the Model Code focuses on the humidity profiling of concrete specimens. It is also worth to remark that neither MC90 nor MC2010 (CEB–FIP, 1993, CEB–FIP, 2010) provide any recommendation on how to model the boundary conditions for the humidity field simulation, which nonetheless can have an important influence on the results (Oliveira *et al.*, 2015).

This internal relative humidity will be simulated here within the framework of a single diffusion equation that simulates the process of drying. This equation lumps together the implicit consideration of transport of liquid and gaseous water. The Partial Differential Equation (PDE) that models the humidity (Kim and Lee, 1999, Azenha, 2009, CEB–FIP, 1993, CEB–FIP, 2010, Bažant and Najjar, 1972) is typically solved through the Finite Difference Method (FDM) (Kang *et al.*, 2012, LeVeque, 2007) or the Finite Element Method (FEM) (Di Luzio and Cusatis, 2009b, Di Luzio and Cusatis, 2009a). Herein, focus is given to the humidity and the Model Code approach is highlighted.

Regarding multi-physics modeling, several models have been used to simulate concrete carbonation process, because of its significance to the life of concrete structures. In a simple form, the carbonation process can be modeled with a set of equations in two distinct ways, either called “*decoupled*” or “*coupled*” (Zwillinger, 1998). In “*decoupled*” formulated problems the equations are independent (Molins *et al.*, 2004), while in “*coupled*” problems (Puatatsananon and Saouma, 2005) the different fields interact with each other. Different complexity models have been used to address the carbonation phenomenon (Morandea *et al.*, 2014). Some of the multi-physics models described in literature are summarized and presented next. Nevertheless, the model used by Ferretti and Bažant (2006a, 2006b), which was the first one to be applied in aerial lime mortar, is implemented and detailed.

3.2 *Moisture transport in porous material*

3.2.1 *General remarks about the moisture diffusion process*

The influence of moisture on concrete mechanical aspects and response was studied by different authors (Loukili *et al.*, 1999, Yuan and Wan, 2002, Baroghel-Bouny *et al.*, 1999, Cadoni *et al.*, 2001, Grasley *et al.*, 2006), who studied shrinkage or the developed stresses in the material during the drying process. Also, Bažant and Chern (1985) and Benboudjema

et al. (2005) analyzed the relation between the humidity and the creep behavior. Regarding material durability, the carbon dioxide diffusion and the carbonation processes depend on the humidity (Papadakis *et al.*, 1991a, Ferretti and Bažant, 2006a, Saetta and Vitaliani, 2005, Saetta and Vitaliani, 2004, Saetta *et al.*, 1995), as well as on the chloride ingress process (Oh and Jang, 2007, Saetta *et al.*, 1993b, Lindvall, 2003) and on other multi-physics processes, such as the ingress of sulfates into concrete (Nehdi and Hayek, 2005). Therefore, knowledge of the moisture distribution within concrete or mortar based structures, since construction and throughout service life, can provide a better understanding about their actual performance (Conciatori *et al.*, 2014), and even support measures to prevent damage. Moisture diffusion in concrete has been studied by many authors with different objectives, such as: evaluating the impact of material composition (Bažant and Najjar, 1971, Bažant, 1972, Kang *et al.*, 2012, Persson, 1996, Mjörnell, 1997, Nilsson, 2002), time (Bažant and Najjar, 1971, Bažant, 1972, Kang *et al.*, 2012, Persson, 1996, Mjörnell, 1997, Nilsson, 2002), governing equations or simulation formulations (Zhang *et al.*, 2009, Bažant, 1972, Kim and Lee, 1999, Ishida *et al.*, 2007), choice of driving potential for measurement/simulation (e.g. internal humidity (Kim and Lee, 1999, Oliveira *et al.*, 2015) or actual water content (Janoo *et al.*, 1999, Klysz and Balayssac, 2007), and other aspects (Nilsson, 2002, Roels, 2000, Zhang *et al.*, 2014).

The drying process in concrete is a complex mechanism, as different aspects are coupled and involved on the transport of water in porous materials. As water is present in the porous matrix under the form of gas and liquid, several simulation approaches have explicitly considered both states of water in their modeling assumptions and governing equations (Gawin *et al.*, 1996, Whitaker, 1977). In spite of such complexity, it has already been shown that the simulation of concrete drying can be simplified and reduced to a single diffusion equation, based on the assumption that the drying of weakly permeable materials is mainly achieved by the transport of moisture in its liquid form (Mainguy *et al.*, 2001). In another study, Baroghel-Bouny *et al.* (1999) define internal relative humidity of concrete as the relative humidity (h) of the gaseous phase in equilibrium with the interstitial liquid phase in the pore network of the material. This chapter presents a review of the literature focusing on moisture, humidity, relevant concepts and possible formulations. As mentioned above, the present chapter addresses studies in concrete, a well-known material that will serve as reference.

3.2.2 Drying process

Evaporation of water is usually understood as evaporation of free water surface but, for porous media such as concrete or mortar, further considerations are necessary.

Cementitious materials are known to have a wide range of diameters in their pore structure, spanning from radiuses as small as 10^{-10} m (gel pores), to radiuses up to 10^{-2} m (air voids/capillary pores) (Jennings *et al.*, 2008). This complex structure of pores, and associated connectivity network, are randomly distributed (Zhang, 2014) (Table 3-1).

Table 3-1 – Pore size distribution in cementitious materials (adapted from Zhang (2014))

Types of pores	Description	Size	Water	Properties
Capillary pores	Large	10 μ m - 50 nm	Evaporable bulk water	Permeability, strength
	Medium	50 - 10 nm	Evaporable moderate menisci	Permeability, strength (high h)
Gel pores	Small	10 - 2.5 nm	Evaporable strong menisci	Shrinkage (up to h of 50%)
	Micro	2.5 - 0.5 nm	Non-evaporable no-menisci, inter-molecular interactions	Shrinkage, creep (h between 33 - 11%)
Interlayer spaces	Structural	< 0.5 nm	Non-evaporable ionic / covalent bond	Shrinkage, creep (h < 11%)

According to Azenha (2009), due to the existence of pores with radius smaller than 1μ m, significant lowering of vapor pressure within the pores can occur according to the Kelvin equation. This equation describes the change in vapor pressure due to a curved liquid/vapor interface.

Pores smaller than 1μ m exhibit energetic retention of moisture, and the porous media where this pore range exists are therefore called hygroscopic (Scheffler and Plagge, 2011). Along drying of initially saturated porous media four main stages can be distinguished, as depicted in (Keey, 1972). Firstly (Stage I), moisture flows as liquid water under hydraulic gradients. In Stage II, because of drying, some air pockets appear, and water withdraws to the waists of the pores, migrating either by creeping along the capillary walls or by successive evaporation and condensation between liquid bridges (Smith, 1994, Azenha, 2009). On further drying (Stage III), the liquid bridges evaporate entirely, leaving only adsorbed moisture behind. In the final Stage IV, moisture just flows as vapor along the dry pores. These stages are schematic illustrated in Figure 3-1.

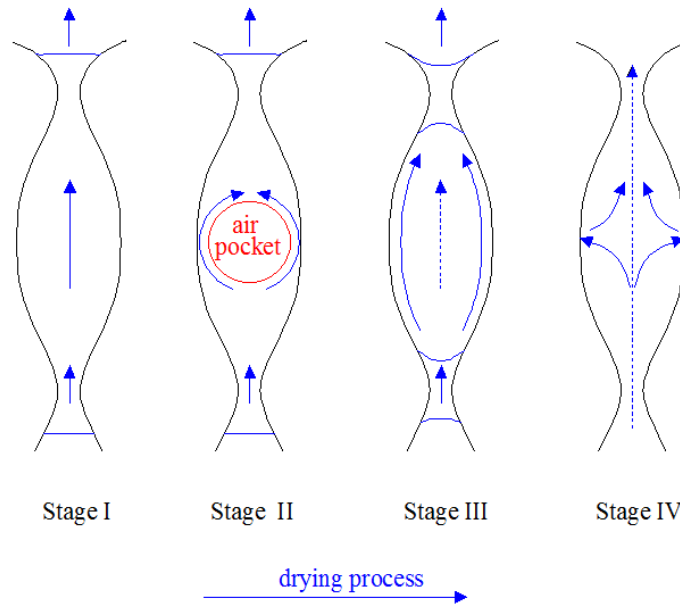


Figure 3-1 – Drying process in porous material (adapted from Keey (1972))

In terms of global drying of cementitious solid, distinct behaviors may be expectable, according to the moisture condition of the pore structure. In general terms, three main phases may be distinguished on the global drying of cementitious solids, and accordingly the attention is drawn to Figure 3-2, where a schematic plot of the rate evolution of weight loss in an initially saturated porous solid is presented (Azenha, 2009).

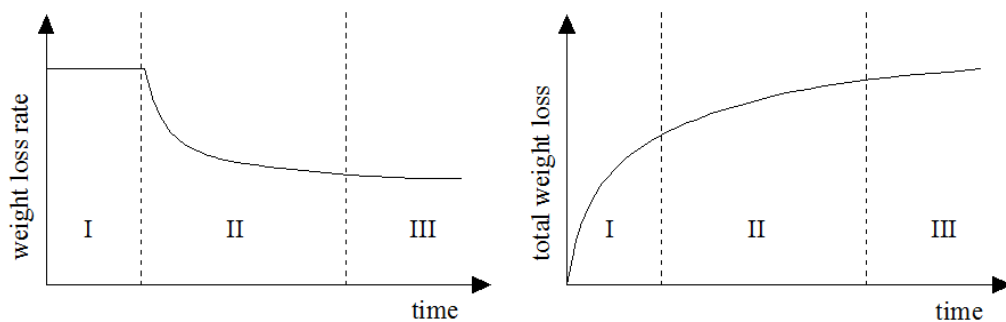


Figure 3-2 – Weight loss over time (adapted from Azenha (2009) and Pel *et al.* (2002b))

At an initial phase *I*, superficial moisture is present, and therefore the drying rate is controlled by factors related to the surrounding environment (radiation, wind, air temperature and humidity, etc.), rather than to the moisture profile inside the solid (Azenha, 2009). The drying rate is constant, occurring in a similar way to the drying of a free water surface.

Therefore, it may be stated that during this initial phase the moisture transport in the material is faster than the mass transfer to the atmosphere by the air flow (Pel *et al.*, 2002b).

As drying proceeds (phase *II*), the water supply to the surface of the solid by capillary forces becomes insufficient to replace the liquid being evaporated. The water film that initially existed on the surface starts to be disrupted at some points (Azenha, 2009). Consequently, the global drying rate decreases during this stage.

Finally, on phase *III*, a residual slow drying stage starts, which may persist as a near steady state condition for long periods of time. This stage apparently occurs when the cementitious surface becomes so desiccated that further conduction of liquid water to the surface is limited to the few small sized pores that remain saturated (or partially saturated) in equilibrium with the surrounding environment (Azenha, 2009). The water transmission through the desiccated layer occurs primarily by the slow process of vapor diffusion (Hillel, 1980). This stage is called diffusion controlled because the rate of evaporation from the solid is completely governed by the diffusion characteristics of the solid (Han and Zhou, 2013). In this situation, the third condition for evaporation mentioned before has become the key factor for the rate of moisture loss. According to Selih *et al.* (1996), this stage of drying starts when the average moisture content decreases below 70 - 80% of total saturation.

Considering the scenario just described, in freshly cast concrete surfaces exposed directly to the environment, the transition from phase *I* to the subsequent phases of drying has been identified by Al-Fadhala and Hover (2001). These authors proposed an empirical equation to predict the decrease of the rate of moisture loss from a cementitious surface when compared to the rate of moisture loss from a water pan, as:

$$\frac{E_c}{E_s} = e^{-\left(\frac{t}{a}\right)^{1.5}} \quad 3.1$$

where: E_c is the moisture emissivity coefficient for the concrete/mortar, E_s is the moisture emissivity coefficient for the water pan, t is the time after casting and a is a time constant that depends on the mixture ($a = 3.75$ for concrete; $a = 6.16$ for mortar) (Al-Fadhala and Hover, 2001).

This equation, presented by Al-Fadhala and Hover (2001) is not for universal application, or for any composition of concrete/mortar, as the evolution of the rate of moisture loss is dependent on many factors, such as: the water vapor concentration in the atmosphere, the

wind speed, the water/cement (w/c) ratio of the concrete/mortar, the geometry of the specimen under consideration, the temperature field created by the exothermic hydration reactions in cementitious materials, the age at which the surface is exposed to the environment and the hydration extent (Azenha, 2009).

3.2.3 Numerical simulation of the moisture field

This section presents the general aspects regarding numerical simulation of moisture fields in concrete, focusing namely on the driving potential (absolute water content of average pore humidity), governing equations, diffusion properties and boundary condition consideration. For this purpose, a prismatic Representative Elementary Volume (REV) with dimensions $2dx$, $2dy$ and $2dz$ (see Figure 3-3), with its sides parallel to the coordinate axes, is considered.

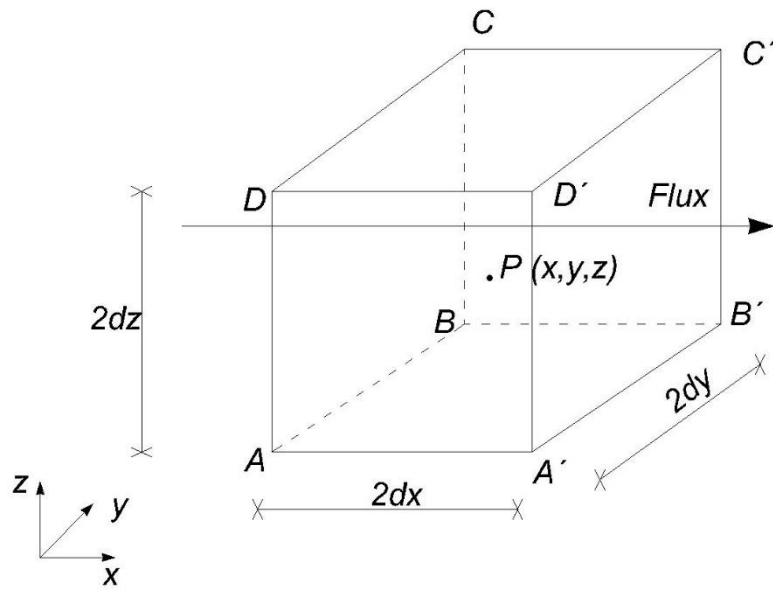


Figure 3-3 – Water movement within the REV (adapted from Azenha (2009))

The center of the REV is $P(x,y,z)$, where the concentration of evaporable water is W_e . The water flux along axis x and through face $ABCD$ can be expressed as:

$$Q_1 = 4dydz \left(J_x - \frac{\partial J_x}{\partial x} dx \right) \quad 3.2$$

where: Q_1 is the water flux along axis x through face $ABCD$ and J_x is the diffusion flux in direction x .

Based on a similar reasoning, the flux through face $A'B'C'D'$ reads:

$$Q_2 = 4dydz \left(J_x + \frac{\partial J_z}{\partial x} dx \right) \quad 3.3$$

where: Q_2 is the water flux through face $A'B'C'D'$.

By using Eqs. (3.2) and (3.3), the contribution of these two faces for the increase of the diffusing substance in the REV may be obtained as:

$$Q_z = -8dxdydz \left(\frac{\partial J_z}{\partial x} dx \right) \quad 3.4$$

where: Q_x is the water flux along axis x .

The contributions of the other four faces of REV can be obtained analogously as:

$$Q_y = -8dxdydz \left(\frac{\partial J_y}{\partial x} dx \right) \quad 3.5$$

$$Q_z = -8dxdydz \left(\frac{\partial J_z}{\partial x} dx \right) \quad 3.6$$

where: Q_y is the water flux along axis y and Q_z is the water flux along axis z , J_y is the diffusion flux in direction y and J_z is the diffusion flux in direction z .

Concrete and mortar are reacting porous media, whose total water concentration W corresponds to the sum of W_e and the non-evaporable water concentration W_n . Therefore, the global rate of increase of water in the REV may also be expressed as a function of the variation in the total water concentration over time, as:

$$Q = -8dxdydz \left(\frac{\partial (W_e + W_n)}{\partial t} \right) \quad 3.7$$

where: W_n is the non-evaporable water and W_e is the evaporable water.

3.2.4 General considerations for thermodynamic model for moisture transport and equilibrium

This section summarizes the model presented by Maekawa *et al.* (1999) and Ishida *et al.* (2007). The authors, in order to model the moisture transport, formulated the water flux of both liquid and vapor, driven by pore pressure and vapor density. In addition, moisture state in the system can be obtained by combining thermodynamic theory and computed micro-pore structure (Maekawa *et al.*, 1999, Ishida *et al.*, 2007). The law of mass conservation governing the moisture balance in a system is expressed by:

$$\frac{\partial \theta_w}{\partial t} + \text{div}(J(\theta_w, T, \nabla \theta_w, \nabla T)) + Q = 0 \quad 3.8$$

where: θ_w : is the mass of moisture in a unit volume of concrete (kg/m^3), J is the moisture flux ($\text{kg}/\text{m}^2 \times \text{s}$), T is the temperature (K), and Q is the sink term corresponding to water consumption due to hydration ($\text{kg}/\text{m}^3 \times \text{s}$).

These authors (Maekawa *et al.*, 1999, Ishida *et al.*, 2007) also develop the equilibrium between liquid and vapor phases of water under arbitrary temperatures. The potential term for the moisture in a porous material can be expressed as:

$$\frac{\partial \theta_w}{\partial t} = \frac{\partial (\rho_l \phi S)}{\partial t} \quad 3.9$$

where: ρ_l is the density of liquid water (kg/m^3), ϕ is the porosity, and S is the degree of saturation of porosity.

In order to generalize the modeling of moisture flux with respect to temperature, the flow driven by both the pore pressure gradient and the temperature gradient is considered. In this case, the moisture flux J ($\text{kg}/\text{m}^2 \times \text{s}$) for both vapor and liquid water can generally be expressed as:

$$J = -(D_p \nabla p_l + D_t \nabla t) \quad 3.10$$

where: D_p is the moisture conductivity ($\text{kg/Pa}\times\text{m}\times\text{s}$) with respect to the pore pressure gradient, and D_t is the moisture conductivity ($\text{kg/K}\times\text{m}\times\text{s}$) with respect to the temperature gradient.

The isotherm curve, and other considerations about the model, can be obtained in Maekawa *et al.* (1999) and Ishida *et al.* (2007).

3.2.5 Thermo-hygro-mechanical model

This section presents general information about a thermo-hygro-mechanical model proposed to simulate the moisture field (Gawin *et al.*, 2002b, Gawin *et al.*, 2003, Gawin *et al.*, 2006, Gawin *et al.*, 2002a). According to these authors, phase transitions and chemical reactions are of importance when the performance of massive concrete structures at early stages of maturing is analyzed (Gawin *et al.*, 2002b, Gawin *et al.*, 2003, Gawin *et al.*, 2006, Gawin *et al.*, 2002a). With a traditionally phenomenological approach (Bažant and Najjar, 1972), it seems rather difficult to take into account important changes of material properties, e.g. porosity, density, permeability or compressive strength during concrete hardening. In a phenomenological description, the effect of phase transitions and chemical reactions on material performance is lumped in the model parameters. The material aging is described in terms of concrete maturity or equivalent time, if considered at all, which causes theoretical problems in nonlinear modeling. On the contrary, when a mechanistic approach is applied, it is possible to consider all these effects explicitly (Gawin *et al.*, 2002b, Gawin *et al.*, 2003, Gawin *et al.*, 2006, Gawin *et al.*, 2002a), because they appear directly in the model equations. Moreover, it is possible to take into account full coupling and interactions between various phenomena and material properties (Gawin *et al.*, 2006). The solid skeleton voids are filled partly by liquid water and partly by a gas phase. The liquid phase consists of bound water, which is present in the whole range of moisture content, and capillary water, which appears when the degree of water saturation exceeds the upper limit of the hygroscopic region.

The general equation reads (Gawin *et al.*, 2002b, Gawin *et al.*, 2003, Gawin *et al.*, 2006, Gawin *et al.*, 2002a):

$$\begin{aligned}
& \frac{(1-\phi)}{\rho^s} \frac{\partial \rho^s}{\partial t} + \text{div} v^s + \frac{\phi}{\rho^s} \frac{\partial \rho^w}{\partial t} + \frac{\phi}{S^s} \frac{\partial S_w}{\partial t} + \frac{1}{S_w \rho^w} \text{div} (\phi S_w \rho^w v^w) \\
& = \frac{\dot{m}_{hydr} - \dot{m}_{vap}}{S_w \rho^w} - \frac{\dot{m}_{hydr}}{\rho^s}
\end{aligned} \tag{3.11}$$

where: t denotes time (s), \dot{m}_{hydr} means mass source of skeleton and corresponding sink of liquid water mass (g), ρ is the density (g/m³), v is the velocity (m/s), S_w is degree of saturation of the pores with liquid water (%), \dot{m}_{vap} is the vapor mass source caused by the liquid water evaporation or desorption (for low values of the relative humidity inside the material pores) (g), ϕ is the total porosity, and the symbols s and w , denote solid skeleton and the liquid water in general.

The formulation presented in this section considers complex phenomena and the different material phases are included in Eq. 3.11. Therefore, obtaining some of the parameters from experiments can be considerate a difficult task.

Other models to simulate the water/humidity flux in cementitious materials have been developed but, for the sake of brevity, are not presented herein. More information on this can be found in Di Luzio and Cusatis (2009b, 2009a), Bary and Sellier (2004) and Ulm and Coussy (1995).

3.2.6 General considerations and governing equations in terms of humidity

Water in concrete or mortar (W) is usually classified in two main categories (Taylor, 1977, Powers and Brownyard, 1948): evaporable water (W_e) and non-evaporable water (W_n). Evaporable water corresponds to the parcel of the total water that is available for transport and may ultimately evaporate to the outer environment. Evaporable water comprises the interlayer water between the layers of reacted material, the adsorbed water at the pore surfaces and the capillary condensed water in the pores. The rest of the water in the cementitious material, which is either chemically combined or with strong physical bonds to the material, is called non-evaporable water (Neville, 1995, Granger, 1996). The total water (W) corresponds to the sum of W_e and W_n . It is however known that during early ages, cement hydration causes transformation of significant parts of W_e into W_n . Mass balance equations for moisture content in concrete since early ages should therefore account for this phenomenon (Azenha, 2009, Taylor, 1977), as:

$$\dot{W}_e = \text{div}(D \text{grad}(W_e)) - \dot{W}_n \quad 3.12$$

where: D is the diffusion coefficient (m^2/s) and the superscript sign ‘.’ stands for the first derivative in time.

Other formulations based on water content (in addition to the modeling cited above), with specific multi-phase models that consider liquid and vapor water, as well as convection transport within the porous medium, are available (Jennings *et al.*, 2008, Granger *et al.*, 1997, Pel *et al.*, 2002a).

Alternatively to the water concentration modeling, some authors propose formulations based on internal relative humidity h as the driving potential. Internal humidity of the material can be defined as the relative humidity of the gaseous phase in equilibrium with the interstitial liquid phase in the pore network of the material (Baroghel-Bouny *et al.*, 1999, Azenha, 2009). According to Xi *et al.* (1994a) and Roncero (2000), boundary conditions are easier to express in terms of h than in terms of W . Furthermore, internal profiling of moisture fields through non-destructive and quantitative methods is more feasible through h than W (Kang *et al.*, 2012, Kim and Lee, 1999, Baroghel–Bouny, 1996, Zhang *et al.*, 2012, Xi *et al.*, 1994b). This is an important aspect when validation of simulation models is envisaged.

Authors that model moisture fields for shrinkage prediction also defend the advantages of considering internal h due to the simplicity of the relationship between h and local shrinkage strains (Azenha, 2009). For usual w/c ratios the drop in h due to chemical hydration of cement is relatively small (less than 3%), and thus it can be neglected even if hydration reactions have not ceased. This is not the case when W is used as a potential, as W_n and W_e vary significantly during hydration.

It is possible to plot the relationship between internal h and W (expressed in mass) for a specific concrete at constant temperature. This relationship is known as moisture isotherm (adsorption/desorption) (Baroghel–Bouny, 1996), and is qualitatively depicted in Figure 3-4. It can be seen that the adsorption and desorption curves are different, highlighting the hysteretic behavior of concrete in regard to water retention (Azenha, 2009, ACI, 2006). This hysteresis is usually explained with the so-called ink-bottle effect (Brunauer, 2007, Bazant and Bazant, 2012).

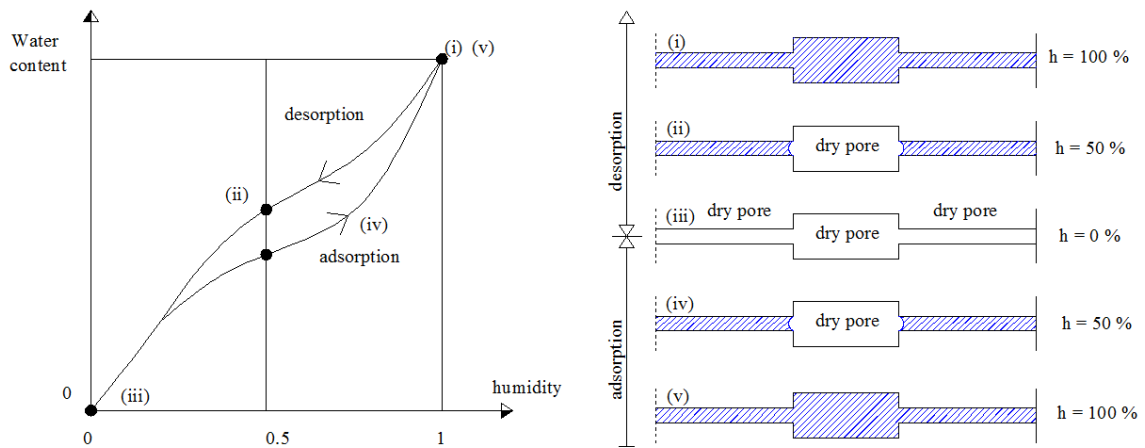


Figure 3-4 – Typical shape of a moisture sorption isotherm for concrete (adapted from Azenha (2009)).

Bearing in mind that the slope of the moisture isotherm (moisture capacity) can be expressed by $\partial W/\partial h$, that the self-desiccation can be expressed by $\partial h_s/\partial t$, and that humidity diffusion can be expressed by the term D_h , Eq. 3.12 may be transformed into a format based on internal relative humidity, so that it reads:

$$\frac{\partial h}{\partial t} = \left(\frac{\partial W}{\partial h} \right)^{-1} \text{div} (D_h \text{grad} (h)) + \frac{\partial h_s}{\partial t} \quad 3.13$$

The transformation of Eq. 3.12 into Eq. 3.13 implies the factor $(\partial W/\partial h)^{-1}$ at the right-hand side of the equation. This factor is the reciprocal of the slope of the moisture isotherm $W = f(h)$. Some authors defend that moisture capacity of cementitious materials at usual environmental relative humidity ($h > 50\%$) is fairly constant (Roncero, 2000), thus motivating a further simplification on Eq. 3.13, by lumping terms $(\partial W/\partial h)^{-1}$ and D_h into a single term called D_h^* . This simplification is even more reasonable if solely desorption processes are envisaged (frequently valid in sheltered concrete subjected to drying). It is however remarked that other authors such as Baroghel-Bouny (2007) reported quite distinctive slopes of $(\partial W/\partial h)^{-1}$ at high humidity ranges, thus limiting the validity of the above-mentioned simplification. In coherence with the varying-slope assumption for the moisture isotherm, Xi *et al.* (1994a) proposed a mathematical model to predict experimental adsorption isotherms for cement pastes. Nonetheless, no general validated model was found in the literature in regard to the prediction of moisture isotherms in concrete (Azenha, 2009).

Therefore, moisture isotherms in concrete are usually obtained experimentally (Hansen, 1986, Anderberg and Wadsö, 2008).

The simplification of considering a constant slope for the moisture isotherm (allowing the use of a single term D_h^*) is adopted in this work, given the lack of a general model of the moisture isotherm for concrete and the inherent simplicity of application of such approach, already adopted in MC1990/2010. The total reduction of humidity (Δh_{total}) in concrete occurs due to two factors, namely, the humidity diffusion process (Δh_d) and the self-desiccation (Δh_s) (see Figure 3-5).

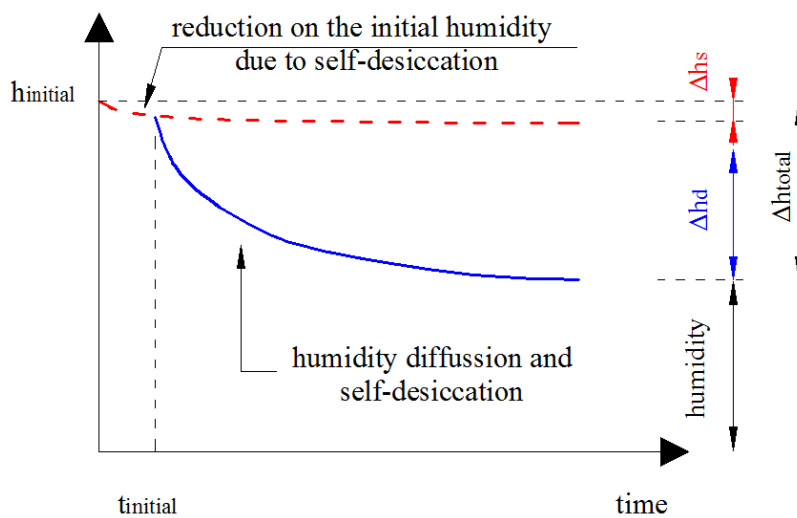


Figure 3-5 – Variation of relative humidity in concrete since early ages

The MC1990/2010 makes some additional considerations about the term $(\partial h_s / \partial h)$ of Eq. 3.13, as it can be considered negligible outside the scope of the early ages, during which most of the hydration reactions occur. This implies that $(\partial h_s / \partial h)$ can be assumed negligible in the study of hardened concrete, if the effect is taken into account through the initial conditions of the problem, e.g. initial humidity of ~ 95% at 28 days to consider internal reductions due to self-desiccation.

As a result of the reasoning above, Eq. 3.13 can be transformed into Eq. 3.14 below, which coincides with the formulation proposed by MC90/MC2010 (Eq. 3.14) (Bažant and Najjar, 1972, Kim and Lee, 1998, CEB–FIP, 2010, CEB–FIP, 1993).

$$\frac{\partial h}{\partial t} = \text{div } D_h^* (\text{grad}(h)) \quad 3.14$$

When a diffusion equation (like Eq. 3.14) is adopted, different phenomena are put together (Mason and Malinauskas, 1983). A schematic representation of the mechanisms are presented in Figure 3-6.

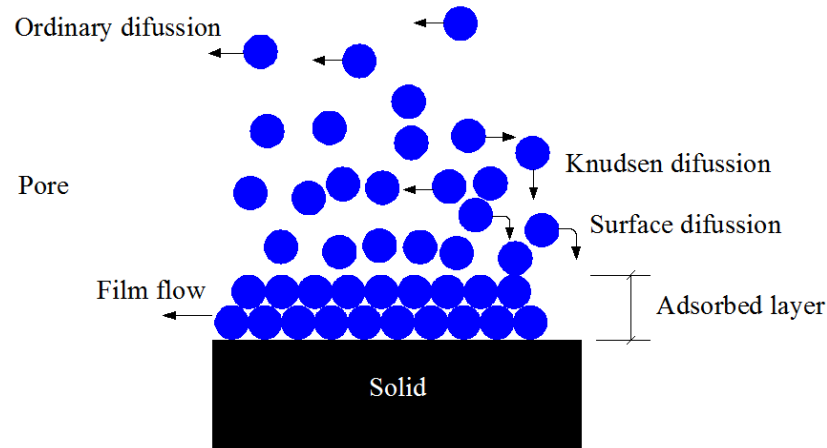


Figure 3-6 – Representation of different mechanisms involved in drying process (adapted from Mason and Malinauskas (1983))

The ordinary diffusion is commonly found in both conditions, low and high h , and is caused by the concentration gradient. The Knudsen diffusion happens when the pore size is the same as or smaller than the mean free path of water molecules (Reinecke and Sleep, 2002). Surface diffusion takes place when the water molecules are adsorbed by pore walls (which is the case if h is low) (Wedler and Charola, 2008).

Capillary transport is the movement of liquid under the gradient of capillary pressure in porous media, which is the result of interactions between liquid-water and pore walls. In coherence with Mainguy *et al.* (2001) the complex set of equations can be reduced to a diffusion-like equation. More information about the different phenomena involved in moisture transport in porous media can be found in Zhang (2014).

- *Diffusion coefficient*

When considering h as the driving potential for the moisture simulations, the diffusion coefficient has been defined as a nonlinear function of the local relative humidity or of the moisture content by authors such as (Bažant and Najjar, 1971, Mjörnell, 1997, Mensi *et al.*, 1998, Martinola and Sadouki, 1998, Sadouki and van Mier, 1997, Christensen, 1979, Suwito

et al., 2006). The most widespread formulation for moisture diffusivity in concrete, using h as the driving potential, was proposed by Bažant and Najjar (1971) and was included in MC90 and MC2010. For isothermal conditions the diffusion coefficient can be expressed as a function of the pore relative humidity $0 < h < 1$ (Bažant and Najjar, 1971, CEB–FIP, 2010, CEB–FIP, 1993), as:

$$D_h = D_1 \left[\alpha + \frac{1 - \alpha}{1 + \left[\frac{(1-h)}{(1-h_c)} \right]^n} \right] \quad 3.15$$

where: D_1 is the maximum D_h for $h = 1$ (m^2/s); D_0 is the minimum D_h for $h = 0$ (m^2/s), $\alpha = D_0/D_1 = 0.05$, h_c is the relative pore humidity at $D_h(h) = 0.5 \times D_1$ ($h_c = 0.80$) and n is an exponent ($n = 15$).

According to MC90 and MC2010, D_1 is defined as a function of the mean compressive strength of concrete f_{cm} expressed in MPa as:

$$D_1 = \frac{D_{1,0}}{f_{cm} - 8} \quad D_{1,0} = 1 \times 10^{-8} \left[\text{m}^2 / \text{s} \right] \quad \text{or} \quad D_{1,0} = 864 \left[\text{mm}^2 / \text{day} \right] \quad 3.16$$

These parameter values were also used by Kim and Lee (1999) for their simulations. But there are other approaches to calculate the humidity diffusivity coefficient and Xi *et al.* (1994b) proposed a different formulation:

$$D_h = \alpha_h + \beta_h \left[1 - 2^{-10\gamma_h(h-1)} \right] \quad 3.17$$

where: α_h , β_h and γ_h , are the coefficients to be calibrated with experimental data.

In Kim and Lee (1999), there are some proposed formulation for these three parameters as functions of w/c .

An approach based on capillary porosity of concrete P_{cap} is put forward by Mjörnell (1997), as:

$$D_h(h) = D^{60\%} + (D^{100\%} - D^{60\%}) \times \left(\frac{h - 0.6}{0.4} \right)^k \quad 3.18$$

$$D^{60\%} = a + bP_{cap} \quad 3.19$$

$$D^{100\%} = c + dP_{cap}^2 \quad 3.20$$

$$P_{cap} = \frac{(w/c) - 0.39\alpha_c}{(w/c) + 0.32} \quad 3.21$$

where: a , b , c , d and k are fitting parameters, and α_c is the degree of hydration.

The dependence of the diffusion coefficient in regard to the moisture potential has also been made by Mensi *et al.* (1998) (using W as the driving potential), and Martinola and Sadouki (1998) (using h as the driving potential) with recourse to exponential functions. The equation of the latter approach is given by:

$$D_h(h) = ae^{bh} \quad 3.22$$

where: a and b are model parameters.

A comparative results of the four presented models is shown in Figure 3-7 (for each model the adopted values are also presented) The parameter values of different models were adapted to be in coherence with the values obtained from the Model Code formulation and, therefore, the results presented in Figure 3-7 are just indicative of the tendencies. For practical purposes, the values should be obtained and fitted experimentally.

Another model based on the approach for composite materials developed by Christensen (1979) was devised, accounting for the presence of aggregates and reading:

$$D_h = D_{hcp} \left(1 + \frac{g_i}{[1 - g_i]/3 + 1 / [(D_{hagg} / D_{hcp}) - 1]} \right) \quad 3.23$$

where: D_{hcp} is the cement paste diffusivity, D_{hagg} is the aggregates diffusivity and g_i is the aggregate volume fraction. However, it is stated by Suwito *et al.* (2006) that the D_{hagg} term in concrete is very small, and can therefore be neglected.

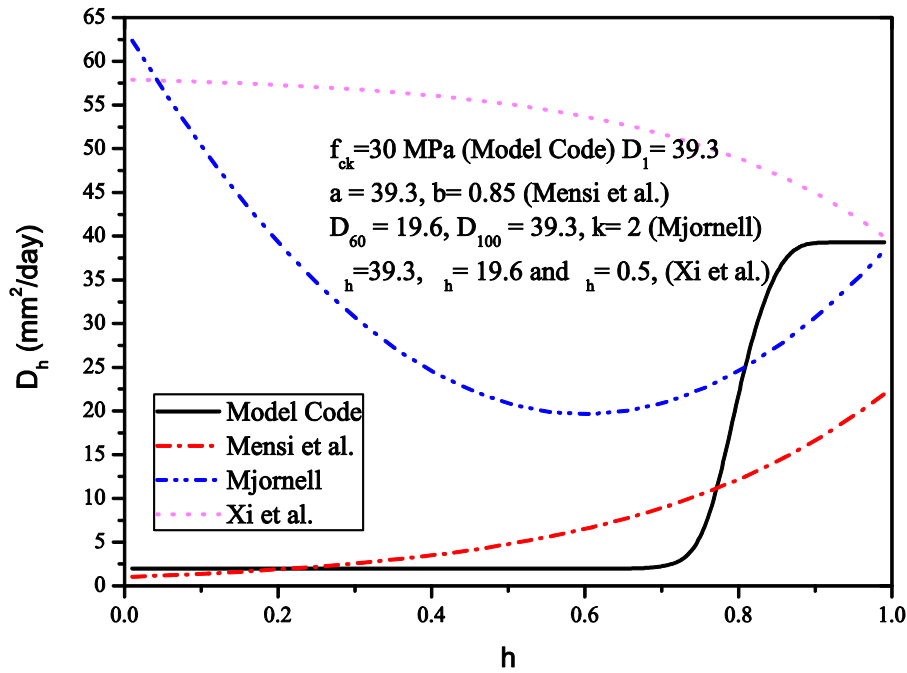


Figure 3-7 – Comparative of diffusivity models

- *Boundary conditions*

With regard to the boundary conditions to apply for the humidity field modelled according to Eq. 3.14, two standard strategies can be used. The first strategy corresponds to imposing the value of the environmental humidity to the concrete surface (Dirichlet boundary condition) (Ferretti and Bažant, 2006a, Zill, 2012, Crank, 1979). The alternative strategy corresponds to the application of Neumann’s boundary condition, through the use of a proportionality factor ($f_{boundary}$) between the exposed surface flux, and the humidity difference between the environment (h_{en}) and the concrete surface (h_{surf}) (Azenha, 2009, Shimomura and Maekawa, 1997):

$$D_h \left(\frac{\partial h}{\partial x} \right)_s = f_{boundary} (h_{en} - h_{surf}) \quad 3.24$$

where x is the coordinate in the direction perpendicular to the boundary surface.

Alternatively to the above-cited approaches, Bažant and Najjar (1972) dealt with the boundary condition issue by assuming an additional thickness to the specimen (i.e., the equivalent surface thickness). Through a comparison between analytical and experimental results, they recommended an equivalent surface thickness of 0.75 mm (Bažant and Najjar,

1972, Kim and Lee, 1999), at the end of which a Dirichlet condition would be applied. Nonetheless, no further research works were found to adopt this modeling strategy for the boundary conditions.

The MC90 and MC2010 do not provide recommendations for modeling the boundary condition for humidity diffusion. Research works that use the governing Eq. 3.14 have either used Dirichlet (Ferretti and Bažant, 2006a) or Neumann conditions (Kim and Lee, 1999, Oliveira *et al.*, 2015).

If an analogy is made to thermal field simulations, it is easily acknowledged that Dirichlet and Neumann conditions should be used in quite distinct situations (LeVeque, 2007, Zill, 2012). In fact, the imposition of a given temperature in the boundary of a solid is rare, whereas boundaries that correspond to direct contact with the surrounding environment lead to the consideration of Neumann boundary conditions (Shimomura and Maekawa, 1997). The temperature in the surface of a solid in contact with the atmosphere is systematically distinct from that of the boundary surface. The surface boundary coefficient for thermal models is furthermore dependent on the wind speed in the vicinity of the surface, which can increase the intensity of thermal exchanges. It has also been demonstrated that the surface humidity is distinct from the environmental one (Nilsson, 2002) and that the moisture exchange intensity can be dependent on wind speed at very early ages, when a wet film is still present on the cementitious material (Azenha *et al.*, 2007a, Azenha *et al.*, 2007b).

In coherence with this acknowledged relevance of using Neumann boundary conditions for the simulation of moisture fields, both Sakata (1983) and Akita *et al.* (1997) have obtained experimental correlations between the boundary coefficient and the w/c ratio.

Theoretical approaches to the moisture diffusion problem are presented by Shimomura and Maekawa (1997), Yiotis *et al.* (2007), and Zhi *et al.* (2010). These authors also acknowledge the importance of considering Neumann boundary conditions, namely through the adoption of a surface factor related to porosity.

In a pioneer study, Sakata (1983) correlated the boundary coefficient with the w/c ratio with a linear correlation, as:

$$f_{boundary} = 5.2 \times w/c - 2.055 \rightarrow in [cm/day] \quad 3.25$$

where: w/c is the water cement ratio.

The results presented by Sakata (1983), for concretes with a range of w/c from 0.42 to 0.56, were analyzed and have significant dispersion of values. In another study Akita *et al.* (1997) measured the mass decrease of six concrete mixes with w/c ratios ranging from 0.3 to 1.0, and the authors proposed the following definition for the surface factor/boundary coefficient:

$$f_{boundary} = \frac{0.5}{w/c + 0.1} + 2.5 \rightarrow in [cm / day] \quad 3.26$$

However, findings were contradictory: Sakata (1983) claims that an increase in w/c leads to an increase of the boundary coefficient, whereas Akita *et al.* (1997) observed an opposite trend. In another approach Yiotis *et al.* (2007) modelled the boundary condition, coupling the external and internal mass transfer during drying of a porous medium. Taking into account the above reasoning, the approach adopted in this work focuses on the adoption of Neumann boundary conditions for surfaces in contact with the environment.

3.2.7 Integrated discussion of the moisture modeling

Different models with diverse complexity have been presented to simulate the moisture flux in porous materials. Even with the implicit simplifications, the Model Code formulation has been chosen here. It is a relatively simple model capable of simulating the humidity diffusion process in cementitious materials, and it has been tested by different authors (Azenha, 2009, Kim and Lee, 1999, Bažant and Najjar, 1971).

Aerial lime mortar, as already stated, is material with a complex behavior and several unknown parameters. The adoption of a model with less complexity can help an easier preliminary understanding of humidity flux. For practical applications, this formulation (Model Code) also presents advantages (Oliveira *et al.*, 2015).

Other models, such as the proposed by Gawin *et al.* (1996) or Maekawa (1999), are more complex and consider explicitly additional effects, but some variables or phenomena (for instance the transition of liquid to vapor water) are difficult to measure experimentally. In opposition with this complexity, recently Oliveira *et al.* (2015) demonstrated the applicability of Model Code formulation for nine different concrete compositions, more information will be presented in Chapter 4.

3.3 *Multi-physics models for simulation of carbonation*

3.3.1 *General remarks*

In concrete or cement mortar, carbonation leads to a progressive decalcification of the hydrated cement paste. This decalcification occurs when the calcium concentration decreases in the pore water because of the calcium consumption induced by the carbonation reaction (Bary and Sellier, 2004).

The pore interstitial solution constitutes a very alkaline environment (pH close to 13.5), in which the rebars are passive (Villain *et al.*, 2007). When carbon dioxide (CO₂) from the atmosphere penetrates into the concrete pores, it dissolves in the interstitial solution and thereby modifies the chemical balances between the solution and the hydrates. This leads to the precipitation of calcium carbonates (CaCO₃) in ordinary Portland cementitious materials, as well as the densification of the microstructure and the decrease of the pH the interstitial solution (Villain *et al.*, 2007). Therefore, the reinforcement is not protected anymore. Carbonation thus leads to the degradation of the reinforced concrete structures (Villain *et al.*, 2007, Bary and Sellier, 2004, Burkan Isgor and Razaqpur, 2004, Chang and Chen, 2006, Cultrone *et al.*, 2005, Ewertson and Petersson, 1993, Glasser *et al.*, 2008).

The carbonation phenomenon in cementitious materials is a very relevant subject and it has been studied by different authors. On the contrary, for aerial lime mortar, there is only one numerical work regarding the theme (Ferretti and Bažant, 2006a, Ferretti and Bažant, 2006b). For carbonation, the behavior of both material (cement based materials and aerial lime mortars) can be considered similar in several aspects. Therefore, this section presents the description of numerical models used by different authors to simulate the carbonation process using multi-physics equations mostly developed for concrete.

3.3.2 *Simple diffusion equations*

The multi-physics models from literature presented next are based on the CO₂ modeling using a simple diffusion equation. Isgor and Razaqpur (2004) presented a general diffusion model implemented in FEM (Finite Element Method) for thermo-carbo-hygro simulations, decoupled with mechanical aspects. Steffens *et al.* (2002) adopted a diffusion model to simulate the carbonation process in concrete. The model proposed by Steffens *et al.* (2002)

combines results of extensive studies by Bunte and Rostasy (1994) on diffusion of CO₂ in different types of concrete and the modeling of the reaction kinetics of carbonation by Saetta *et al.* (1993b) with a coupled temperature and moisture model for concrete. The CO₂ penetrates into the concrete mainly gaseous by diffusion through air-filled pores. The diffusion through water-filled pores and the convection within water that moves in the pores may be neglected (Steffens *et al.*, 2002).

A similar mathematical model of carbonation is presented by Meier *et al.* (2007) considering the kinetics of the carbonation reaction described by a power-law with a humidity-dependent multiplier (Saetta *et al.*, 1995, Steffens *et al.*, 2002).

Peter *et al.* (2008), include the hydration reactions in the simplified model presented by Mier *et al.* (2007), which neglects carbonation of the C-S-H phases and of the unhydrated components C₂S (dicalcium silicate - 2CaO • SiO₂) and C₃S (tricalcium silicate - 3CaO • SiO₂). According to the authors, the numerical simulations show that the latter two constituents only have a small influence on the total outcome in the late stage of hydration considered. This effect occurs even if we assume that all of C₂S are completely accessible to their carbonation reactions. Therefore, it seems reasonable to neglect them in carbonation prediction models (Peter *et al.*, 2008). Another reference that uses a diffusion model to simulate the carbonation process in concrete is Talukdar *et al.* (2012).

The model presented by Saetta (1992), Saetta and Vitaliani (2004) and Ferretti and Bažant (2006a) is detailed next, given its relevance for the present work.

- *Model of Ferretti and Bažant (2006)*

This model is a multi-physics coupled model (there are dependencies between the fields) involving four main fields, moisture, heat, pollutant flow (CO₂) and reaction. The numerical model for deterioration was developed, considering the characterization of the concrete and the environmental conditions. The model is based on studies by Saetta (1992) and Saetta *et al.* (1995), and improved with new features as it considers the combination of moisture, heat and pollutant (CO₂) flows through concrete, including chemical reactions between cementitious components and the aggressive species (Saetta and Vitaliani, 2004)

The equations used to model the phenomena are presented below. For moisture, Ferretti and Bažant (2006a) rewrote the equations Saetta and Vitaliani (2004), disregarding the temperature field and coupling the phenomena as Saetta and Vitaliani (2004).

The humidity field (Saetta *et al.*, 1993a, Saetta and Vitaliani, 2005, Saetta *et al.*, 1995, Ferretti and Bažant, 2006a) is governed by:

$$\frac{\partial h}{\partial t} = \nabla(C_w \nabla h) + \alpha_2 \frac{\partial R}{\partial t} \quad 3.27$$

where: h is humidity (%), α_2 is the parameter related to the water generation during the carbonation process (more details are presented next), C_w is the diffusion of water (mm^2/day) and R is the degree of chemical reaction (%).

The coefficient α_2 is related to the maximum content of calcium carbonate $[\text{CaCO}_3]_{\max} = P_{\max}$ (the term P symbolizes the formation of a precipitate – CaCO_3), which depends mainly on the material composition and on the angular coefficient of the sorption-desorption isotherm k , dependent basically on temperature, according to Saetta and Vitaliani (2004):

$$\alpha_2 = \frac{PM(H_2O)}{PM(\text{CaCO}_3)} kP_{\max} = 0.18kP_{\max} \quad 3.28$$

where: PM represents the molecular weight of the given molecule.

Such equation derives from the kinetic of the carbonation reaction. For every CaCO_3 molecule produced by the reaction, a H_2O molecule is also produced, in terms of molecular mass, as given by (Saetta and Vitaliani, 2004):

$$M_{H_2O} = M_{CaCO_3} \frac{PM(H_2O)}{PM(\text{CaCO}_3)} \quad 3.29$$

where: M represents the molecular mass of the molecule indicated in subscript.

As a consequence, in terms of mass per unit volume, Eq. 3.29 becomes:

$$\frac{M_{H_2O}}{V_{cls}} = \frac{M_{CaCO_3}}{V_{cls}} \frac{PM(H_2O)}{PM(\text{CaCO}_3)} \quad 3.30$$

where: V_{cls} is the considered volume's element, therefore (Saetta and Vitaliani, 2004):

$$dw = dP^* \frac{PM(H_2O)}{PM(CaCO_3)} \quad 3.31$$

where: dw represents the water content variation per unit volume and unit time, while dP^* is the variation of the calcium carbonate concentration (such variables are both expressed in kg/m^3) (Saetta and Vitaliani, 2004).

By using the well-known expression of the sorption-desorption isotherms, i.e., $k_h dw = dh$, and expressing the calcium carbonate content as $dR = dP^*/P_{max}$, it is possible to write (Saetta and Vitaliani, 2004):

$$\frac{\partial h}{\partial t} = \frac{PM(H_2O)}{PM(CaCO_3)} k P_{max} \frac{\partial R}{\partial t} \quad 3.32$$

which compared with Eq. 3.32, with $PM(H_2O) = 18.015$ and $PM(CaCO_3) = 100.088$ (Atkins, 2010), gives Eq. 3.28.

Assuming, for instance, that $P_{max} = 0.0096 \text{ kg/m}^3$ and $k_h = 1 \text{ m}^3/\text{kg}$, then $\alpha_2 = 0.0017$. The analytical determination of the coefficient α_2 proves somewhat uncertain because it is difficult to unequivocally assign the coefficients k_h and P_{max} . These parameters may take on different values as the carbonation process progress (Saetta and Vitaliani, 2004).

The carbon dioxide diffusion field is governed by (Saetta *et al.*, 1993a, Saetta and Vitaliani, 2005, Saetta *et al.*, 1995, Ferretti and Bažant, 2006a):

$$\frac{\partial c}{\partial t} = \nabla(D_c \nabla c) - \alpha_3 \frac{\partial R}{\partial t} \quad 3.33$$

where: α_3 is the parameter related to gas consumption during the carbonation process, D_c represents the diffusion of the aggressive gas (CO_2 for instance) and c is the gas concentration (%).

Eq. 3.33 is based on the second Fick's law (Saetta *et al.*, 1993a, Saetta *et al.*, 1995, Saetta, 1992). Detailed information on Fick's laws principles can be found in Shackelford (2009). The parameter α_3 also depends on the chemical reaction of carbonation, and based on a considerations on the chemistry of this reaction, the following relation can be drawn (Saetta and Vitaliani, 2004):

$$\alpha_3 = \frac{PM(CO_2) P_{max} c_{env}}{PM(CaCO_3) g_{max} \beta_v} \quad 3.34$$

where: c_{env} is the external volumetric fraction of CO_2 (%), g_{max} represents the maximum concentration of CO_2 in concrete, expressed in g/m^3 , and β_v is the percentage of air inside the material (%).

Assuming that $P_{max} = 9.61 \text{ g/m}^3$, $g_{max} = 3.60 \text{ g/m}^3$ and $\beta_v = 0.001$ (i.e., that the percentage of air inside the concrete/mortar is 0.1% or 1000 cm^3 of air/ m^3 of material), and $c_{env} = 0.035\%$, then $\alpha_3 = 0.40$ (valued adopted by Ferretti and Bažant (2006a)). The measurement of α_3 is difficult because it depends on the porosity and internal humidity, which vary in time, and on the parameters c_{max} and P_{max} , whose values must be estimated on the basis of the type of material.

The reaction field is governed by (Saetta *et al.*, 1993a, Saetta and Vitaliani, 2005, Saetta *et al.*, 1995, Ferretti and Bažant, 2006a):

$$\frac{\partial R}{\partial t} = \alpha_4 \times F_1^R(h) \times F_2^R(c) \times F_3^R(R) \times F_4^R(T) \quad 3.35$$

where: T is the temperature (K).

Eq. 3.35 was originally proposed by Saetta (1992) and carbonation (the degree of reaction) is defined as (Saetta *et al.*, 1993a, Saetta and Vitaliani, 2005):

$$R = \frac{[CaCO_3]}{[CaCO_3]_{max}} \quad 3.36$$

where: $[CaCO_3]_{max}$ is the maximum mass concentration of calcium carbonate (kg/m^3), and $[CaCO_3]$ is the actual mass concentration of $CaCO_3$ (kg/m^3).

The functions F_1 to F_4 , are defined next (Saetta *et al.*, 1993a, Saetta and Vitaliani, 2005, Saetta *et al.*, 1995, Ferretti and Bažant, 2006a). Function F_1 describes the influence of the presence of water, by correlating the humidity and the reaction, given by:

$$F_1^R(h) = \begin{cases} h=1 \rightarrow 0 \\ 0.5 \leq h < 1 \rightarrow 2.5 \times (h-0.5) \\ h < 0.5 \rightarrow 0 \end{cases} \quad 3.37$$

This function was initially adopted by Saetta (1992), and was based on experimental data presented by Houst and Wittman (1986). It has been used by different authors (Peter *et al.*, 2008, Ferretti and Bažant, 2006a, Saetta and Vitaliani, 2004, Saetta *et al.*, 1993a, Saetta *et al.*, 1995).

Function F_2 describes the influence of aggressive species and reads:

$$F_2^R(c) = \frac{c}{c_{max}} \quad 3.38$$

where: c is the carbon dioxide concentration (% or ppm), and c_{max} is the maximum CO₂ concentration (% or ppm).

Function F_3 describes the degree of chemical reaction and reads:

$$F_3^R(R) = 1 - R \quad 3.39$$

The values of α_1 , α_2 , α_3 and α_4 vary according to the characteristics of the concrete or mortar and reagents (Saetta *et al.*, 1993a, Saetta and Vitaliani, 2005).

The effective diffusivities can be calculated as (Ferretti and Bažant, 2006a):

$$C_w = C_{w,rif} \times f_1^*(h) \times f_2(T) \times f_3(t_e) \times f_4(R) \quad 3.40$$

$$Dc = Dc_{rif} \times f_1(h) \times f_2(T) \times f_3(t_e) \times f_4(R) \quad 3.41$$

where: $C_{w,rif}$ and Dc_{rif} are the diffusivities in standard conditions for water and CO₂ respectively (mm²/day).

The function $f_1^*(h)$ is defined in Saetta *et al.* (1998):

$$f_1^*(h) = \alpha + \frac{1 - \alpha}{1 + \left(\frac{1-h}{1-h_c}\right)^n} \quad 3.42$$

where: α , h_c and n were already defined in Eq. 3.15 ($\alpha = 0.05$, $h_c = 0.75$ and $n = 6$) (Ferretti and Bažant, 2006a).

For gas diffusion phenomena (for instance CO₂), the following expressions are given (Ferretti and Bažant, 2006a):

$$f_1(h) = (1-h)^{2.5} \quad 3.43$$

$$f_2(T) = \exp\left[\frac{E_a}{R}\left(\frac{1}{T_0} - \frac{1}{T}\right)\right] \quad 3.44$$

where: T_0 is the reference temperature (296 K), E_a is the activation energy (kJ/mol), R is the universal gas constant (J/mol×K), and T is temperature.

Function $f_3(t_e)$ is related to the concept of equivalent age, and reads:

$$f_3(t_e) = \chi + (1 - \chi) \left(\frac{28}{t_e}\right)^{0.5} \quad 3.45$$

where: t_e is the equivalent age (days).

More information about the concept of equivalent age can be obtained in Bažant (1988), Granger (1996) and Azenha (2009). The equivalent age can be calculated as (Ferretti and Bažant, 2006a, Bažant, 1988):

$$t_e = \int_0^t \left[1 + (5-5h)^4\right]^{-1} dt \quad 3.46$$

For this last equation, a different value has to be used for the parameter χ , given by:

$$\chi = \frac{D_{\infty}}{D_{28}} \quad 3.47$$

where: D_{∞} is the aggressive species diffusion coefficient at time = infinity (mm^2/day) and D_{28} is the aggressive species diffusion coefficient at 28 days (mm^2/day) (Ferretti and Bažant (2006a), give $\chi = 0.8$).

The parameter χ represents the ratio of the diffusivity at time infinity) (D_{∞}) to the diffusivity at 28 days (D_{28}). Depending on the particular diffusion process the chemical reaction produces a precipitate, like the calcium carbonate in the carbonation process. The diffusion process is retarded with the decreasing of the porosity and the function $f_4(R)$ can be given as (Buenfeld and Hassanein, 1998):

$$f_4(R) = 1 - \zeta R \quad 3.48$$

where: the parameter ζ varies between 0 and 1, and measures the slowing of diffusion phenomenon due to reduction of the porosity (Saetta *et al.*, 1995, Saetta, 1992, Saetta and Vitaliani, 2005). Ferretti and Bažant (2006a) adopted $\zeta = 0.3$, meaning that a reduction of 30% for the diffusivity value occurs with the total reaction.

Function F_4^R describes the influence of the temperature on the evolution of the chemical reaction and is defined by (Steffens *et al.*, 2002, Ferretti and Bažant, 2006a):

$$F_4^R(T) = A \times e^{-\frac{E_a}{RT}} \quad 3.49$$

where: A is the impact number (the number of collisions of reactive particles per second) (Steffens *et al.*, 2002) and E_a is the activation energy (kJ/mol).

3.3.3 Model of ion transport in porous media - Poisson-Nernst-Planck model

This section presents some basics information about the Poisson-Nernst-Planck model to represent the ion transport in the carbonation process. It is known that the transport of different ions in an ideal electrolyte can be described by the equations of mass balance (Nemst-Planck), ionic flux (Kontturi *et al.*, 2008), current conservation and electroneutrality.

In an one-dimension medium, it can be written as follows (Bard and Faulkner, 1980, Kubo, 2007):

$$\frac{\partial C_i}{\partial t} = -\nabla J_i \quad 3.50$$

where: C_i is the concentration of species i (mol/m³) and J_i is the flux of species i (mol/m²/s) (Bard and Faulkner, 1980, Kubo, 2007).

The convection is assumed to be negligible in this model, the total flux can be expressed by (Bard and Faulkner, 1980, Kubo, 2007):

$$J_i = -D_i \nabla c_i - z_i D_i \left(\frac{F}{RT} \nabla \phi_v \right) c_i \quad 3.51$$

$$i = F \sum_{i=1}^n z_i J_i \quad 3.52$$

where: z_i is the charge number of the ionic species i ; F is the Faraday constant (9.648×10^4 °C/mol), R is the gas constant (8.3143 J/mol×K); ϕ_v is the potential (V); and i is the current density applied to the pore solution (A/m²) (Bard and Faulkner, 1980, Kubo, 2007).

$$\sum_{i=1}^n z_i C_i = 0 \quad 3.53$$

$$\frac{\partial C_i}{\partial t} = \nabla \left[D_i \nabla C_i - z_i D_i \left(\frac{i}{F} + \frac{\sum_{i=1}^n z_i \nabla D_i}{\sum_{i=1}^n z_i^2 \nabla D_i} \right) \right] \quad 3.54$$

Since there is no material current divergence, the current density satisfies (Bard and Faulkner, 1980, Kubo, 2007):

$$\nabla i = 0 \quad 3.55$$

For porous media, such as concrete, mortar or a hydrated cement paste, the porosity and tortuosity need to be taken into account, leading to (Bard and Faulkner, 1980, Kubo, 2007):

$$\tau^2 \frac{\partial C_i}{\partial t} = \nabla \left[D_i \nabla C_i - z_i D_i \left(\frac{\tau i}{\varepsilon^3 F} + \sum_{i=1}^n z_i \nabla D_i \right) \right] \quad 3.56$$

where: τ is the tortuosity of pore structure and ε is the volume fraction of porosity.

The potential gradient (ϕ_v) in the pore solution can be defined by (Poisson equation) (Bard and Faulkner, 1980, Kubo, 2007):

$$\nabla \phi_v = - \frac{RT}{F} \frac{\frac{i}{F} + \sum_{i=1}^n z_i \nabla C_i}{\sum_{i=1}^n z_i^2 D_i C_i} \quad 3.57$$

More information about the applicability of Poisson-Nernst-Planck equation in concrete simulations can be found in (Samson and Marchand, 1999, Kubo, 2007, Truc *et al.*, 2000a, Truc *et al.*, 2000b, Kubo *et al.*, 2007, Lu, 1997).

3.3.4 Phase equilibrium model

An example of applicability of the phase equilibrium model is the software PHREEQC (adopted in Section 2.5) (Parkhurst, 1995). For this model, the compositions of the gas, liquid and solid phases are determined by solving simultaneously the mass conservation law of master species, the law of charge balance and the mass-action equations, describing the constitutive behavior of aqueous and gaseous species and hydrates. The mass-action equations can be written as (Hosokawa *et al.*, 2011b, Hosokawa *et al.*, 2011a, Yeh and Tripathi, 1991):

$$K_p = \prod_i^n (\gamma_i C_i)^{n_{i,p}} \quad 3.58$$

where: K_p is the thermodynamic equilibrium constant of hydrate p , γ_i is the activity coefficient of ion species i (it relates the concentration of an ion to its activity in a given solution) (g/mol), $n_{i,p}$ is the stoichiometric coefficient of the aqueous species i in hydrate p , and C is the specimen concentration (mol/g).

The Henry's law constant defines the partial pressure of the gas component. In general, the partial pressure of a gas component is described as (Hosokawa *et al.*, 2011b, Hosokawa *et al.*, 2011a, Yeh and Tripathi, 1991):

$$P_g = K_H^{-1} \prod_i^n (\gamma_i C_i)^{n_{i,g}} \quad 3.59$$

where: P_g is the partial pressure of gas component g (atm) calculated using activities in the aqueous phase, K_H is the Henry's law constant for the gas component (it depends on the solute, the solvent and the temperature) (L×atm/mol), γ_i is the activity coefficient of ion i (g/mol), and $n_{i,g}$ is the stoichiometric coefficient of the aqueous species i in the dissolution equation (Hosokawa *et al.*, 2011b, Hosokawa *et al.*, 2011a, Yeh and Tripathi, 1991).

A thermodynamic development of this model has been performed based on bulk and surface mass action laws. The approach stresses the relevance of the equilibrium description of the C-S-H (calcium silicate hydrate) compared to traditional standard bulk solubility concepts. Hosokawa *et al.* (2011) developed a model that reproduces the changes in phase composition of the hardened cement paste with the combined process of chloride attack and carbonation process. The model combines a mass transfer model with a thermodynamic phase equilibrium model. The mass transfer model calculates the transfer of aqueous species in the pore solution and CO₂ in the gas phase in the concrete pores (Hosokawa *et al.*, 2011b, Hosokawa *et al.*, 2011a).

The model (Hosokawa *et al.*, 2011b, Hosokawa *et al.*, 2011a) coupled the chemical module (phase equilibrium) with the mass transfer, using the Poisson-Nernst-Planck equation to describe the mass conservation and flow conditions. The model assumes that the cement hydrates are assumed to give away and receive certain amounts of aqueous species according to chemical reactions such as dissolution, precipitation and surface adsorption. This behavior of the hydrates is governed by the adopted phase equilibrium model. The moisture migration

relevant to the mass transport is ignored in the model (Hosokawa *et al.*, 2011b, Hosokawa *et al.*, 2011a, Johannesson *et al.*, 2009).

3.3.5 Mass transport coupled model

A carbonation model based on thermo-hygro physics is presented by Ishida and Li (2008) Ishida and Maekawa (2001) Ishida *et al.* (2004). This models is an extension of hygro model presented in Section 3.2.4. According to the authors, a reaction of C-S-H gel was newly added to the previews existing model (Maekawa *et al.*, 1999) and the calcium hydroxide reaction. The model coupled with moisture equilibrium/transport gives reasonable predictions for carbonation progresses under low and high CO₂ concentrations. Temperature dependent parameters were also adopted in the system (Ishida and Li, 2008).

The law of mass conservation for carbon dioxide, which is the governing equation to be solved in numerical analysis of the carbonation phenomenon, can be expressed as (Ishida and Li, 2008):

$$\frac{\partial}{\partial t} \left\{ \varphi \left[(1-S) \times \rho_g + S \rho_d \right] \right\} + \text{div} J_{co_2} - Q_{co_2} = 0 \quad 3.60$$

where: φ is the porosity; S is the degree of saturation of pores, which is estimated by coupled moisture transport and equilibrium model (Ishida *et al.*, 2007); ρ_g is the concentration of gaseous carbon dioxide (kg/m³); ρ_d is the concentration of dissolved carbon dioxide in pore water (kg/m³); J_{CO_2} is the total flux of dissolved and gaseous carbon dioxide (kg/m²×s); and Q_{CO_2} is the sink term (kg/m³×s), which corresponds to the quantity of carbon dioxide consumed by the carbonation reaction in the micro-pore structure development model (Nakarai *et al.*, 2006, Ishida and Li, 2008, Maekawa *et al.*, 1999).

Ishida and Li (2008) classified the pores in the cement paste into three types: interlayer, gel pores, and capillary pores. Capillary pores are free spaces for the precipitation of hydrates, whereas gel pores are located inside the C-S-H gel grain and in the inter-particle space between the hydrate products. Interlayer pores comprise the volume of water residing between the layer structures of C-S-H.

The porosity formulation adopted by Ishida and Li (2008) was already presented in Section 2.5.3. Song *et al.* (2006) presented an analytical technique for carbonation prediction in early-aged cracked concrete, considering both CO₂ diffusion of pore water in sound concrete and

in cracked concrete. Characteristics of diffusivity on the carbonation in early-aged concrete were studied through finite element analysis implemented with the multi-component hydration heat model and micro-pore structure formation model (Song *et al.*, 2006). The model considers the reaction with dissolved CO_2 , $\text{Ca}(\text{OH})_2$, and CaCO_3 based on the characteristics of early-aged concrete obtained by the so-called multi-component hydration model and micro-pore structure formation model (Ishida and Maekawa, 2001, Maekawa *et al.*, 2003). These authors adopted an equivalent diffusivity of CO_2 in cracked concrete, in order to obtain the carbonation behavior in cracked concrete. The results for carbonation prediction using FEM analysis are verified with experimental results for concrete manufactured with different water-cement ratios and crack widths.

3.3.6 *Other multi-physics carbonation models*

Other models were used to model concrete carbonation. The model proposed by Bary and Sellier (2004) is based on macroscopic mass balance equations for the water, the carbon dioxide contained in the gaseous phase and the calcium contained in the pore solution, which are supposed to completely define the problem of atmospheric carbonation in concrete. These equations govern the diffusion and permeation processes of the three variables: saturation degree, carbon dioxide partial pressure and calcium concentration in pore solution (Bary and Sellier, 2004).

The coupling of carbonation and chloride diffusion has been also investigated. A heat, relative pore humidity, chloride, and carbonation fields model was implemented in a two-dimensional coupled nonlinear finite-difference code (Puatatsananon and Saouma, 2005). Coupling between carbonation and chloride diffusion is explored in the context of both homogeneous and heterogeneous concrete models (Puatatsananon and Saouma, 2005).

3.3.7 *Discussion*

Carbonation of aerial lime mortar is a complex phenomenon and is not stabilized in literature. The first model used to simulate aerial lime mortar carbonation was presented by Ferretti and Bažant (2006a). Other multi-physics models (as the models presented herein, with exception to the ones presented in Sections 2.5) have additional complexity, for instance the simulation of the CO_2 diffusion process. The measurement of the parameters used in such models is a very complex task. For instance, the Poisson-Nernst-Planck model requires

measuring the ionic activity of each involved ion, which is not trivial. Even with the adoption of a chemical model (for instance the phase equilibrium model) several implicit considerations should be taken into account, what makes difficult their practical use. Another example is the model presented by Ishida and Li (2008), which requires the measurement of the concentration of dissolved carbon dioxide in pore water.

Therefore, considering the complexity involved and the requirements of information about the material, the model presented by Ferretti and Bažant (2006a) has been adopted in the present work.

4 NUMERICAL IMPLEMENTATION

4.1 Introduction

This chapter presents the description of the numerical implementation using the Finite Difference Method (FDM) to solve the humidity diffusion equation (decoupled of other fields). After this initial implementation, the multi-physics coupled equations for carbonation were also implemented through the FDM. The two implementations were done considering two relatively simple models, because of the reasons described in previous chapter (Chapter 3). For the humidity field, the chosen model was the Model Code approach (CEB–FIP, 1993, CEB–FIP, 2010). For the multi-physics model (hygro-carbo), the formulation presented by Ferretti and Bažant (2006a) was adopted. The models were implemented in 1D/axisymmetric conditions and 2D. The Newton-Raphson method was adopted to solve the nonlinear systems of equations.

Firstly, some parametric analyses are presented for the humidity field, and then the developed code is applied to simulate the diffusion process of concrete specimens in 1D/axisymmetric conditions. For the multi-physics code, the results for 1D conditions were validated with the results obtained by Ferretti and Bažant (2006a). The subsequent results from the implementation in 2D were simply verified. Subsequently, sensitivity analyses were carried out and the main results found are presented.

4.1.1 Implementation of humidity field in 1D

This section presents a brief description of the numerical implementation using the Finite Difference Method (FDM) in 1D to solve the humidity diffusion equation. The simplicity of this implementation for 1D problems makes it suitable for design purposes through spreadsheets. Details about the mathematical background of the FDM can be found in Incropera *et al.* (2007) and Özisik (2002).

The mathematical equations were developed for an infinite slab, symmetrical in regard to its middle plane. The corresponding discrete model had a finite number of nodes, starting from node 1 in the vicinity of the boundary, progressively numbered until the extremity node, at the symmetry plane. The notation adopted herein considers that “ i ” represented the i^{th} node,

and “ n ” the n^{th} time step. Therefore, the humidity at node i and time step n was denoted by the following set of superscript and subscript: h_n^i .

The time and space discretization for the FDM can be assumed for small intervals of time ($dt = \Delta t$) and length ($dx = \Delta x$). The implementation considers the field equation shown in Eq. 3.14, which can be adapted through the application of the chain rule and transformed as in Stewart (2007), yielding:

$$\frac{\Delta h}{\Delta t} = \nabla D_h \nabla h + D_h \nabla^2 h \quad 4.1$$

In 1D FDM case, the nabla (∇) and the Laplace operators (∇^2) applied to h read:

$$\nabla h = \frac{\partial h}{\partial x} = \frac{h_{n+1}^{i+1} - h_{n+1}^i}{\Delta x} \quad 4.2$$

$$\nabla^2 h = \frac{h_{n+1}^{i+1} - 2h_{n+1}^i + h_{n+1}^{i-1}}{(\Delta x)^2} \quad 4.3$$

Accordingly, the operator ($\partial h / \partial t$) could be expressed by:

$$\frac{\partial h}{\partial t} = \frac{h_{n+1}^i - h_n^i}{\Delta t} \quad 4.4$$

The introduction of Eqs. 4.2 to 4.4 into Eq. 4.1 resulted in:

$$\frac{h_{n+1}^i - h_n^i}{\Delta t} = \nabla D_{h,n+1}^i \frac{h_{n+1}^{i+1} - h_{n+1}^i}{\Delta x} + D_{h,n+1}^i \frac{h_{n+1}^{i+1} - 2h_{n+1}^i + h_{n+1}^{i-1}}{(\Delta x)^2} \quad 4.5$$

Assuming that the distance between consecutive nodes is small, it was plausible to infer that small spatial variation of D_h would occur between consecutive nodes. In view of such reasoning, the term $\nabla D_h \left((h_n^{i+1} - h_n^i) / \Delta x \right)$ in Eq. 4.5 could be considered negligible and thus disregarded. This term represents a second order derivate and its value in the simulations

presented herein was about 10^{-6} times smaller than the other terms of the equation. Therefore, Eq. 4.5 becomes:

$$\frac{h_{n+1}^i - h_n^i}{\Delta t} = D_{h,n+1}^i \frac{h_{n+1}^{i+1} - 2h_{n+1}^i + h_{n+1}^{i-1}}{(\Delta x)^2} \quad 4.6$$

This equation may be rewritten as:

$$h_{n+1}^i = h_n^i + \Delta t D_{h,n+1}^i \frac{h_{n+1}^{i+1} - 2h_{n+1}^i + h_{n+1}^{i-1}}{(\Delta x)^2} \quad 4.7$$

In FDM, the final equation for inner nodes (nodes not located on the boundary or the symmetry plane) can be re-written in a more compact format as:

$$h_{n+1}^i (1 + 2r^i) - r_{n+1}^i \times h_{n+1}^{i+1} - r_{n+1}^i \times h_{n+1}^{i-1} = h_n^i \quad 4.8$$

$$r_{n+1}^i = \frac{\Delta t \times D_{h,n+1}^i}{(\Delta x)^2} \quad 4.9$$

Accordingly, the boundary flux at the extremity node can be expressed by:

$$D_h^i \frac{h_{n+1}^{i+1} - h_{n+1}^{i-1}}{2\Delta x} = f_{boundary} (h_{en} - h_{surf}) \quad 4.10$$

("i-1" is a fictitious node created to solve the equation, and h_{n+1}^{i-1} a fictitious humidity).

Solving the Eq.4.10 in terms of h_{n+1}^{i-1} and replacing in Eq. 4.8:

$$h_n^i = -2r^i h_{n+1}^{i+1} + (1 + 2r^i \beta) h_{n+1}^i - 2r^i \gamma \quad 4.11$$

$$\beta = 1 + \frac{f_{boundary} \times \Delta x}{D_{h,n+1}^i} \quad 4.12$$

$$\gamma = \frac{\Delta x \times h_{en} \times f_{boundary}}{D_{h, n+1}^i} \quad 4.13$$

The parameters h_{en} and $f_{boundary}$ are related to the node on the contact with the environment, for sake of simplicity the superscripts and subscripts have been dropped.

The node that pertains to the symmetry plane has null flux, and its corresponding equation can be written as:

$$h_{n+1}^i (1 + 2r_{n+1}^i) - 2r_{n+1}^i \times h_{n+1}^{i-1} = h_n^i \quad 4.14$$

By assembling Eqs. 4.11 and 4.14 for the extremity nodes (boundary and symmetry) and Eq. 4.8 for the set of internal nodes (see Figure 4-1), it is possible to express the set of equations in matrix form, as shown in Eq. 4.15 (for simplicity of representation this set of equations pertains to a set of 6 nodes). Note that γ, β and r have been defined above and the superscripts and subscripts have been dropped for conciseness.

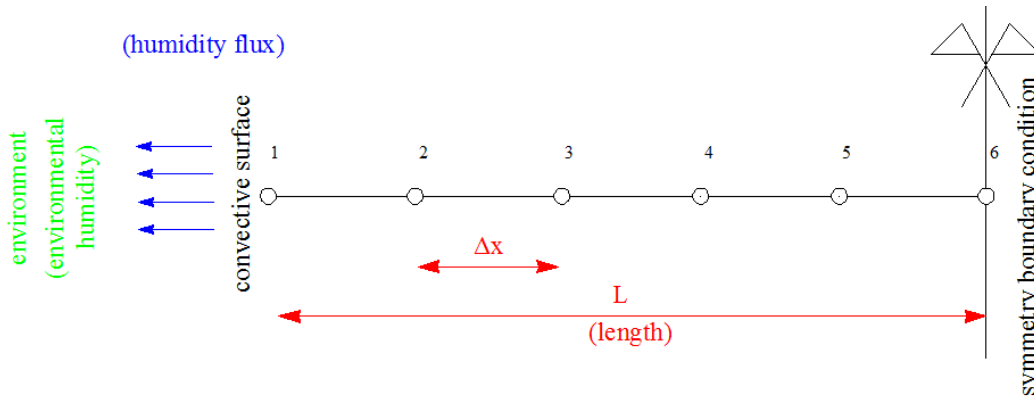


Figure 4-1 - 1D grid in FDM

$$\begin{bmatrix} 1+2r\beta & -2r & 0 & 0 & 0 & 0 \\ -r & 1+2r & -r & 0 & 0 & 0 \\ 0 & -r & 1+2r & -r & 0 & 0 \\ 0 & 0 & -r & 1+2r & -r & 0 \\ 0 & 0 & 0 & -r & 1+2r & -r \\ 0 & 0 & 0 & 0 & -2r & 1+2r \end{bmatrix} \times \begin{bmatrix} h_{n+1}^1 \\ h_{n+1}^2 \\ h_{n+1}^3 \\ h_{n+1}^4 \\ h_{n+1}^5 \\ h_{n+1}^6 \end{bmatrix} = \begin{bmatrix} h_n^1 + 2r\gamma \\ h_n^2 \\ h_n^3 \\ h_n^4 \\ h_n^5 \\ h_n^6 \end{bmatrix} \quad 4.15$$

The humidity in each step is calculated in an incremental/iterative process. The h value obtained on time step “ n ” is adopted as the first trial value for step “ $n+1$ ”, particularly in regard to the estimation of D_h (implicit backward-Euler formulation) (Holmes, 2007). This is a typical nonlinear process, because of the dependence of D_h on h . The Newton-Raphson method is used to solve the nonlinear system of equations (Kelley, 1987).

For each iteration a residuals vector $\left(\begin{matrix} \hat{\psi}_{n+1}^i \end{matrix} \right)$ is calculated as:

$$\hat{\psi}_{n+1} = \left[\hat{h}_{n+1} \right]^{j+1} - \left[\hat{h}_{n+1} \right]^j \quad 4.16$$

where: the symbol $(\hat{\cdot})$ denotes the vector and the superscript $(^j)$ denotes the iteration.

The residual vector is calculated with the difference of humidity values in two consecutive iterations. The convergence criterion was based on the comparison between the norm of the residuals vector with the maximum tolerance, which was assumed equal to 0.0001. More information about the calculation of the residual vector and the overall procedure can be found in Azenha (2009). The Newton-Raphson process is explained with more details in Section 4.4.

4.1.2 Numerical implementation in axisymmetric conditions

All the previous considerations for 1D were herein adopted as the implementation in axisymmetric conditions is similar to 1D. Therefore, this section presents just the distinct aspects about the grid discretizations all the other points are similar to 1D implementation. For axisymmetric conditions the representation of the grid is shown in Figure 4-2. Discretizations in two different directions are herein adopted, the angular ($\Delta\theta$) and the radial (Δp). In radial direction each node has a distance Δp from the neighbor one. Assuming three lines of node positioned for angular discretization in $\theta-1$, θ , and $\theta+1$.

The node $p^{i,\theta}$ denotes the node in position r^i , and line θ . This node has a distance p_0 from the center, and it is surrounded by nodes $p^{i,\theta+1}$, $p^{i,\theta-1}$, $p^{i+1,\theta}$ and $p^{i-1,\theta}$ (Figure 4-2).

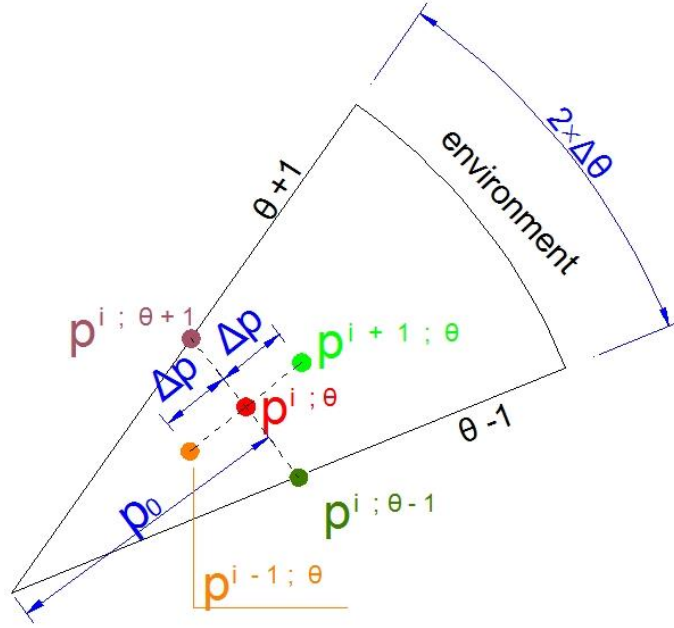


Figure 4-2 - Axisymmetric condition for FDM (adapted from Croft and Lilley (1977))

Therefore the general equation for the nabla (∇) and Laplace (∇^2) operators for humidity field in axisymmetric conditions can be written as (Croft and Lilley, 1977):

$$\frac{\partial h}{\partial p} + \frac{1}{p} \frac{\partial h}{\partial \theta} \quad 4.17$$

$$\nabla^2 h(p, \theta) = \frac{\partial^2 h}{\partial p^2} + \frac{1}{p} \frac{\partial h}{\partial p} + \frac{1}{p^2} \frac{\partial^2 h}{\partial \theta^2} \quad 4.18$$

Assuming that the distance between consecutive nodes is small, it is plausible to infer that small spatial variation of D_h will occur between consecutive nodes. In view of such reasoning, the term $\nabla D_h \left(\frac{\partial h}{\partial p} + \frac{1}{p} \frac{\partial h}{\partial \theta} \right)$ in Eq. 4.18 can be considered negligible and thus disregarded. Therefore, replacing the definition of nabla presented, one obtains:

$$\frac{h_{n+1}^{i,\theta} - h_n^{i,\theta}}{\Delta t} = D_h^{i;\theta} \left(\frac{h_{n+1}^{i-1;\theta} - 2h_{n+1}^{i;\theta} + h_{n+1}^{i+1;\theta}}{(\Delta p)^2} + \frac{h_{n+1}^{i-1;\theta} - h_{n+1}^{i+1;\theta}}{2p_0 \Delta p} + \frac{h_{n+1}^{i;\theta+1} - 2h_{n+1}^{i;\theta} + h_{n+1}^{i;\theta-1}}{(p_0)^2 (\Delta \theta)^2} \right) \quad 4.19$$

Adopting no variation on the angular variation ($\Delta\theta$) due to the axisymmetric condition (Eq. 4.20), Eq. 4.21 is obtained as (Özisik, 1993):

$$h_{n+1}^{i;\theta+1} = h_{n+1}^{i;\theta} = h_{n+1}^{i;\theta-1} \quad 4.20$$

$$\begin{aligned} \frac{h_{n+1}^{i;\theta} - h_n^{i;\theta}}{\Delta t} = & h_{n+1}^{i;\theta} \times \left(1 + \frac{2 \times D_h^{i;\theta}}{(\Delta p)^2} \right) + h_{n+1}^{i-1;\theta} \times (-D_h^{i;\theta}) \times \left(\frac{1}{(\Delta p)^2} + \frac{1}{2 p_0 \Delta p} \right) \\ & + h_{n+1}^{i+1;\theta} \times (-D_h^{i;\theta}) \times \left(\frac{1}{(\Delta p)^2} - \frac{1}{2 p_0 \Delta p} \right) \end{aligned} \quad 4.21$$

For the boundary, the assumption once more of the Neumann's boundary condition provides (Özisik, 1993):

$$D_h^{i;\theta} \frac{\partial h}{\partial p} = f_{boundary} (h_{n+1}^{i;\theta} - h_{env}) \quad 4.22$$

Adopting a fictitious node for “ $i+1$ ” and a fictitious humidity $h_{n+1}^{i+1;\theta}$ as done in 1D implementation, Eq. 4.22 can be re-written as:

$$h_{n+1}^{i+1;\theta} = h_{n+1}^{i-1;\theta} + \frac{2\Delta p \times f_{boundary} \times (h_{env} - h_{n+1}^{i;\theta})}{D_h^{i;\theta}} \quad 4.23$$

Solving in terms $h_{n+1}^{i+1;\theta}$ of and replacing in Eq. 4.21, the final equation for the boundary can be expressed as:

$$\begin{aligned} h_n^{i;\theta} = & -h_{env} \times (-2\Delta p) \times (-\Delta t) \times f_{boundary} \times \left(\frac{1}{(\Delta r)^2} + \frac{1}{2 p_0 \Delta r} \right) \\ & + h_{n+1}^{i-1;\theta} \times \left(2 \times (-D_h^{i;\theta} \Delta t) \times \left(\frac{1}{(\Delta p)^2} \right) \right) \end{aligned} \quad 4.24$$

The axisymmetric implementation was verified with a simple example with the TNO-DIANA[®] (TNO-DIANA-BV, 2010).

More details about the FDM implementation for 1D and axisymmetric conditions can be found in LeVeque (2007), Azenha (2004), Thomas (1995) and Özisik (1993).

4.1.3 Humidity implementation in 2D

This section presents the general aspects regarding the numerical simulation of humidity field for 2D condition in FDM assuming the same considerations as for the 1D conditions.

For 2D condition the representation of the grid is shown in Figure 4-3. Two generic axis are defined x (horizontal direction) and y (vertical direction). The discretizations in the two different directions are (Δx) in axis x and (Δy) in axis y axes.

The generic node $v^{i,j}$ denotes the node in position i (x direction), and j (y direction). This node is surrounded by nodes $v^{i,j+1}$, $v^{i,j-1}$, $v^{i+1,j}$ and $v^{i-1,j}$ (see Figure 4-3).

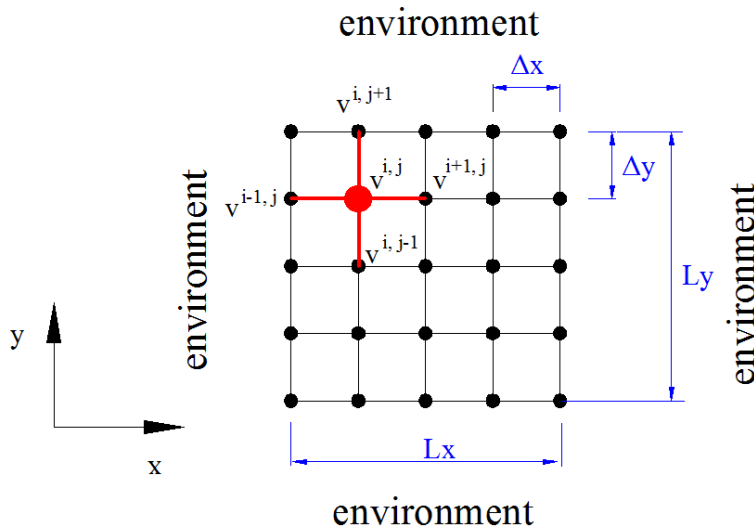


Figure 4-3 - 2D grid for FDM

For 2D analysis the operator nabla (∇) can be expressed as (Croft and Lilley, 1977):

$$\nabla h = \frac{\partial h}{\partial x} + \frac{\partial h}{\partial y} = \frac{h_{n+1}^{i,j} - h_{n+1}^{i-1,j}}{\Delta x} + \frac{h_{n+1}^{i,j} - h_{n+1}^{i,j-1}}{\Delta y} \quad 4.25$$

In 2D condition, for node $v^{i,j}$, the Laplace or nabla squared (∇^2) operator reads (Croft and Lilley, 1977):

$$\nabla^2 h = \frac{h_{n+1}^{i+1,j} - 2h_{n+1}^{i,j} + h_{n+1}^{i-1,j}}{(\Delta x)^2} + \frac{h_{n+1}^{i,j+1} - 2h_{n+1}^{i,j} + h_{n+1}^{i,j-1}}{(\Delta y)^2} \quad 4.26$$

The operator nabla for node $v^{i,j}$, D_h can be expressed as:

$$\nabla D_h = \frac{\partial D_h}{\partial x} + \frac{\partial D_h}{\partial y} = \frac{D_{h,n+1}^{i,j} - D_{h,n+1}^{i-1,j}}{\Delta x} + \frac{D_{h,n+1}^{i,j} - D_{h,n+1}^{i,j-1}}{\Delta y} \quad 4.27$$

Replacing the definitions presented in Eqs. 4.25, 4.26 and 4.27 in Eq. 4.1, results in:

$$\begin{aligned} \frac{\Delta h}{\Delta t} = & \left(\frac{D_{h,n+1}^{i,j} - D_{h,n+1}^{i-1,j}}{\Delta x} + \frac{D_{h,n+1}^{i,j} - D_{h,n+1}^{i,j-1}}{\Delta y} \right) \left(\frac{h_{n+1}^{i,j} - h_{n+1}^{i-1,j}}{\Delta x} + \frac{h_{n+1}^{i,j} - h_{n+1}^{i,j-1}}{\Delta y} \right) + \\ & D_{h,n+1}^{i,j} \left(\frac{h_{n+1}^{i+1,j} - 2h_{n+1}^{i,j} + h_{n+1}^{i-1,j}}{(\Delta x)^2} + \frac{h_{n+1}^{i,j+1} - 2h_{n+1}^{i,j} + h_{n+1}^{i,j-1}}{(\Delta y)^2} \right) \end{aligned} \quad 4.28$$

The terms of second order can be once more neglected, to obtain:

$$\frac{h_{n+1}^{i,j} - h_n^{i,j}}{\Delta t} = D_{h,n+1}^{i,j} \left(\frac{h_{n+1}^{i+1,j} - 2h_{n+1}^{i,j} + h_{n+1}^{i-1,j}}{(\Delta x)^2} + \frac{h_{n+1}^{i,j+1} - 2h_{n+1}^{i,j} + h_{n+1}^{i,j-1}}{(\Delta y)^2} \right) \quad 4.29$$

$$h_{n+1}^{i,j} - h_n^{i,j} = \Delta t \times D_{h,n+1}^{i,j} \left(\frac{h_{n+1}^{i+1,j} - 2h_{n+1}^{i,j} + h_{n+1}^{i-1,j}}{(\Delta x)^2} + \frac{h_{n+1}^{i,j+1} - 2h_{n+1}^{i,j} + h_{n+1}^{i,j-1}}{(\Delta y)^2} \right) \quad 4.30$$

More information about the implementation in 2D conditions may be seen in literature (Croft and Lilley, 1977, Özisik, 1993).

For 3D conditions the same principles could be applied, with the extension of the previously given equations.

4.2 Sensitivity analyses

4.2.1 General considerations

This section aims to analyze the influence of the main parameters involved in the calculation of moisture fields according to Eqs. 3.14, 3.15 and 3.24. The relevant parameters are the boundary transfer coefficient $f_{boundary}$ and the diffusion coefficient D_h , which depends on several other parameters itself. As a starting point, for calculation of D_h parameter, the proposal of MC2010 for a Normal Strength Concrete ($f_{cm} = 30$ MPa) was considered. Therefore, the following initial parameters for calculation of D_h were adopted: $\alpha = 0.05$, $h_c = 0.80$, $D_I = 39.3$ mm²/day and $n = 15$ (CEB–FIP, 2010, CEB–FIP, 1993). In regard to the boundary transfer coefficient, the initial value for the sensitivity studies was $f_{boundary} = 3.0 \times 10^{-4}$ m/day or equivalently 3.0×10^{-1} mm/day, which is in the same order of magnitude of the corresponding coefficient used by Kim and Lee (1999), $f_{boundary} = 5.02 \times 10^{-4}$ m/day.

The selected example for the sensitivity analysis consisted in an infinite concrete slab with 60 cm thickness, symmetric in regard to its middle plane and in contact with the same environment at both surfaces. Concrete was considered as hardened and initially fully saturated ($h = 100\%$), in correspondence to many practical situations of exposure for curing. The surrounding environment was considered to have a constant temperature of $T = 20$ °C and constant environmental humidity $h_{environment} = 50\%$. Self-desiccation of concrete at early ages was disregarded.

Even though the sensitivity analyses focused in a set of 5 simulation parameters (α , h_c , n , D_I and $f_{boundary}$), the obtained results had shown that D_I and $f_{boundary}$ were the most influential parameters on humidity fields. Therefore, for the sake of brevity, the presentation of sensitivity analyses will be limited to these two parameters. In all analyses, constant time step and constant spatial discretization were applied as $\Delta t = 1$ day and $\Delta x = 1$ cm, respectively. It is noted that similar studies were made involving slabs with distinct thicknesses (20 and 100 cm) and concretes with distinct compressive strengths (15 and 50 MPa). The conclusions of such parametric analyses were similar to the ones presented next.

4.2.2 Sensitivity analyses regarding $f_{boundary}$

The influence of the $f_{boundary}$ on the humidity diffusion process was studied by increasing or decreasing it using a factor of ten, in regard to the reference values. Further to these scenarios, two additional simulations were made: one considering Dirichlet boundary conditions (i.e. prescribed humidity at the boundary), and another considering the approach of a fictitious additional length of 0.75 mm, as proposed by Bažant and Najjar (1972).

The results of simulation for the depth of 20 cm from the surface are depicted in Figure 4-4, whereas the humidity profiles for the ages of 500 days and 50 years are shown in Figure 4-5.

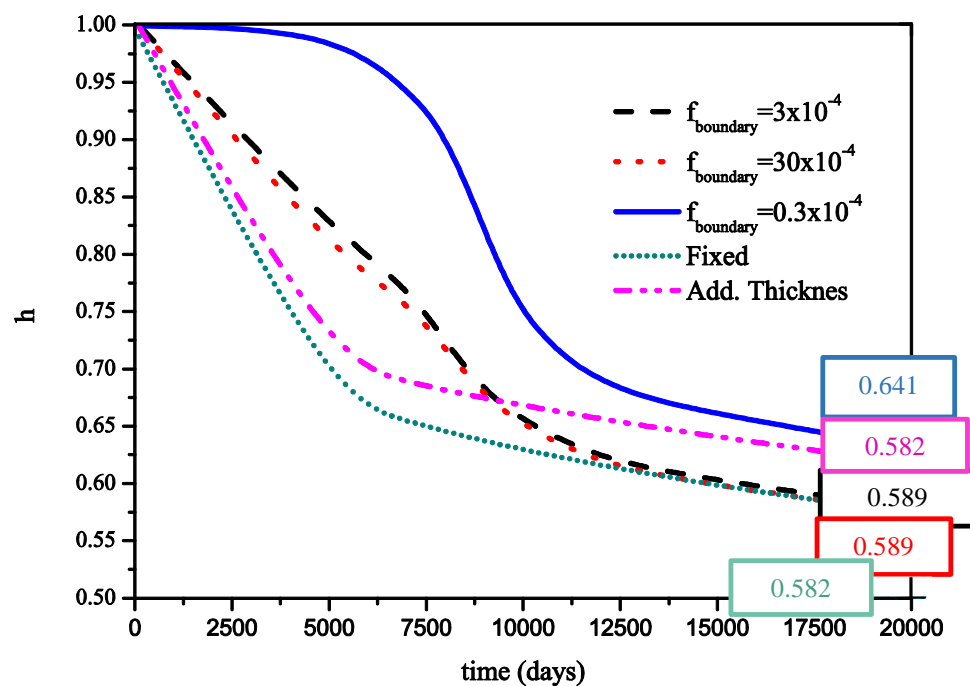


Figure 4-4 -Parametric analyses of the effect of $f_{boundary}$ (m/day) (box value is the value for 50 years) on the humidity computed at 20 cm depth

Based on the observation of Figure 4-4 and Figure 4-5, it is relevant to mention that, when the value of the $f_{boundary}$ was the highest ($f_{boundary} = 30 \times 10^{-4}$ m/day), the drying behavior approaches the one that was obtained with Dirichlet conditions (fixed surface humidity). However, the decrease in $f_{boundary}$ by a factor of 10 and 100 in regard to the maximum value led to significantly different results. This showed that the boundary coefficient could be quite relevant in humidity simulation

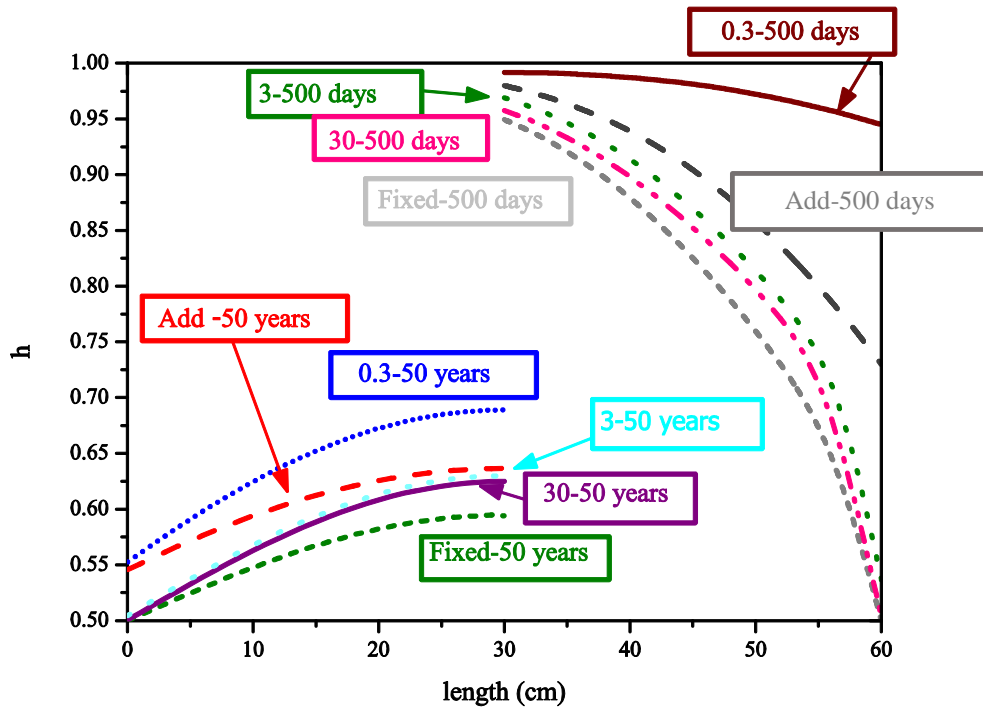


Figure 4-5 -Humidity profiles at the ages of 500 days and 50 years: parametric study regarding the boundary conditions (box caption with $f_{boundary} (10^{-4})$ (m/day) - age). Given the symmetry only half of the profile is given for each age

It is also worth to note that the fictitious additional thickness proposed by Bažant and Najjar (1972) allowed obtaining a behavior that differed from the Dirichlet boundary condition, and resembled an intermediate behavior between that of $f_{boundary} = 3 \times 10^{-4}$ m/day and $f_{boundary} = 0.3 \times 10^{-4}$ m/day.

4.2.3 Sensitivity analyses regarding D_I

In order to evaluate the impact of the D_I factor in the simulation results, a similar strategy was adopted, centered on the reference value recommended by MC2010 for the applicable concrete strength, with $D_I = 39.3$ mm²/day and considering two alternative values of D_I : one of them 10 times higher and another 10 times lower than the reference value. The computed humidity at 20 cm depth along time is shown in Figure 4-6, whereas Figure 4-7 shows the humidity profiles at the ages of 500 days and 50 years.

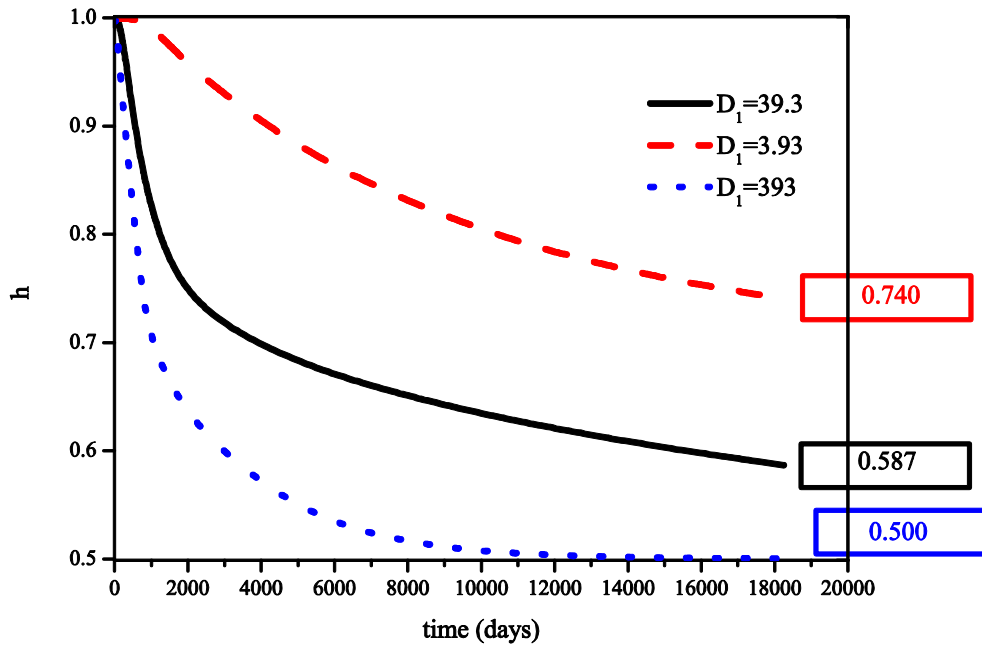


Figure 4-6 - Parametric analyses of the effect of D_1 (box value is the value for 50 years) on the humidity computed at 20cm depth ($[D_1]=\text{mm}^2/\text{day}$)

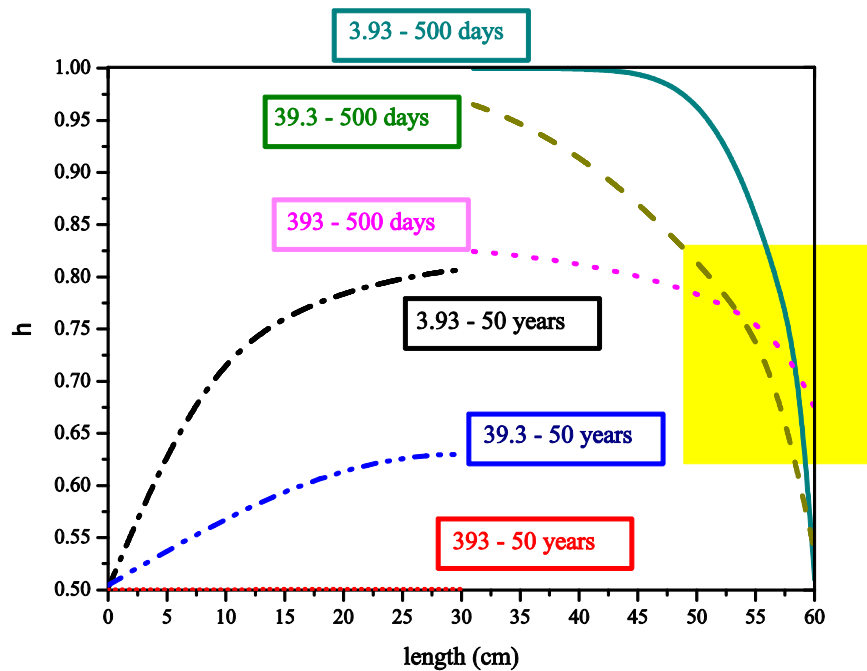


Figure 4-7 – Humidity profiles at the ages of 500 days and 50 years: parametric study regarding the maximum diffusivity (Box caption with $[D_1 \text{ mm}^2/\text{day}]$ - age). Given the symmetry only half of the profile is presented for each age

The observation of Figure 4-6, and Figure 4-7 for the age of 50 years, confirmed the expectable tendency of faster drying when higher D_1 coefficients were considered. As a matter of fact, the analysis that considers $D_1 = 393 \text{ mm}^2/\text{day}$ led to a full humidity

equilibrium with the outer environment ($h = 50\%$) at the end of the period of analysis. The effect of D_I was in fact very relevant as a decrease of D_I from the reference value to $3.93 \text{ mm}^2/\text{day}$ caused the humidity calculated at 50 years age in the symmetry to be increased by almost 20%.

There is an interesting aspect to remark regarding the results at 500 days age plotted in Figure 4-7: the humidity computed within the first $\sim 5 \text{ cm}$ near the surface was higher when $D_I = 393 \text{ mm}^2/\text{day}$ than when $D_I = 39.3 \text{ mm}^2/\text{day}$ (highlighted region in Figure 4-7). Even though this would seem surprising at first sight, it is easily explained by the significant flow of humidity that is migrating towards the surface in the case of $D_I = 393 \text{ mm}^2/\text{day}$. Therefore, even though the humidity diffusion coefficient is very high and would theoretically lead to lower surface humidity when compared to the other cases, it ended up leading to higher humidity due to the intense transport occurring from the inner regions.

4.3 Applications in concrete - Simulation of 1D specimens

This section describes the numerical simulations of humidity fields carried out for three sets of experiments with concrete specimens, in which moisture profiling with embedded humidity sensors was performed. The basic intent is to test the performance of direct application of MC2010 for diffusivity, while trying to assess the boundary condition coefficient based on Neumann's formulation. It is noted that all case studies presented were considered with the values of α , h_c and n recommended by MC2010.

The first set of experiments, conducted by Kim and Lee (1999), considered three different concrete compositions using $10 \text{ cm} \times 10 \text{ cm} \times 20 \text{ cm}$ specimens. After an initial period in which the specimens were kept inside their mold, they were submerged in water from the age of 1 day until the age of 28 days. At 28 days, the specimens were removed from water, their surfaces were sealed according to the scheme in Figure 4-8, and placed in a climatic chamber with $T = 20 \pm 1 \text{ }^\circ\text{C}$ and $h_{env} = 50 \pm 2\%$. As evaporation could only take place through a $10 \text{ cm} \times 10 \text{ cm}$ surface, these specimens endured an one-dimensional moisture flow, similar to that of an infinite slab of 40 cm thickness exposed in both surfaces (all sealed surfaces act as symmetry planes in terms of moisture flow). Humidity sensors were placed at three distinct depths measured perpendicularly to the evaporating surface: 3 cm , 7 cm and 12 cm .

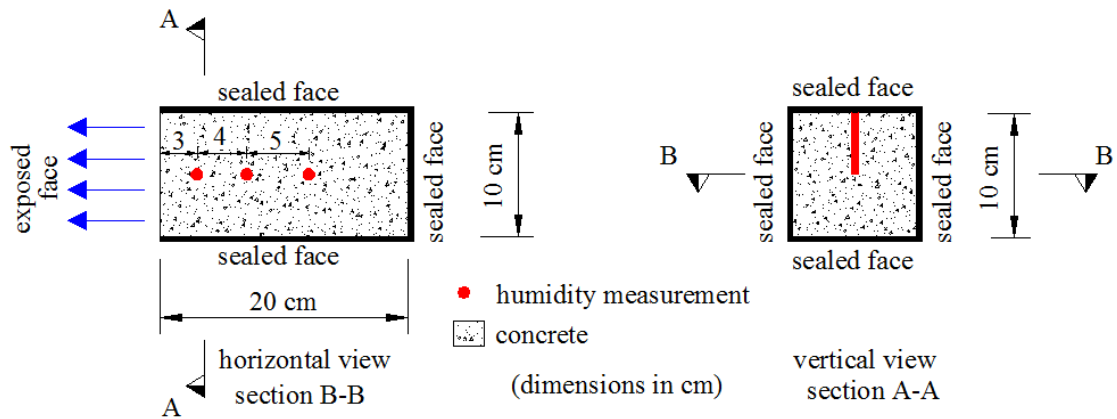


Figure 4-8 – Geometry and size of test (adapted from Kim and Lee (1999))

The cement used in the experiments was ordinary Portland cement (ASTM Type I), with river sand as fine aggregate and crushed granite gravel passing the 19 mm sieve as coarse aggregate. Detailed mix proportions of the three studied concrete specimens (*H*, *M* and *L*), as well as their corresponding compressive strengths are given in Table 4-1.

Table 4-1 – Concrete compositions by Kim and Lee (1999)

Specimen	w/c	Water (w)	Cement (c)	Sand (S)	Gravel (G)	S.P ^a	f'_c (MPa)
<i>H^b</i>	0.28	151	541	647	1055	2.0	76
<i>M^b</i>	0.40	169	423	736	1016	0.5	53
<i>L^b</i>	0.68	210	310	782	955	-	22

^a. Superplastizer.

^b. *H*, *M*, and *L* denote high, medium, and low-strength concrete, respectively.

Simultaneously to the mentioned experiments, Kim and Lee (1999) performed measurements on sealed specimens as to infer the humidity decrease associated to self-desiccation. At the age of 28 days, the recorded value was stabilized at approximately 95% for mixes *H* and *M*, whereas the value for mix *L* was ~99%. These values were used as starting conditions for the humidity of concrete in the simulations herein.

An initial simulation attempt was made by strictly following the MC2010 recommendations for diffusivity and enforcing Dirichlet boundary conditions (i.e. prescribed humidity on the

evaporating surface). Figure 4-9 shows the comparison between such numerical simulation and experimental results for the mix *M*. The results show a relatively reasonable coherence for the depths of 3 cm and 7 cm, but the humidity values at 12 cm depth are being clearly overestimated at all ages.

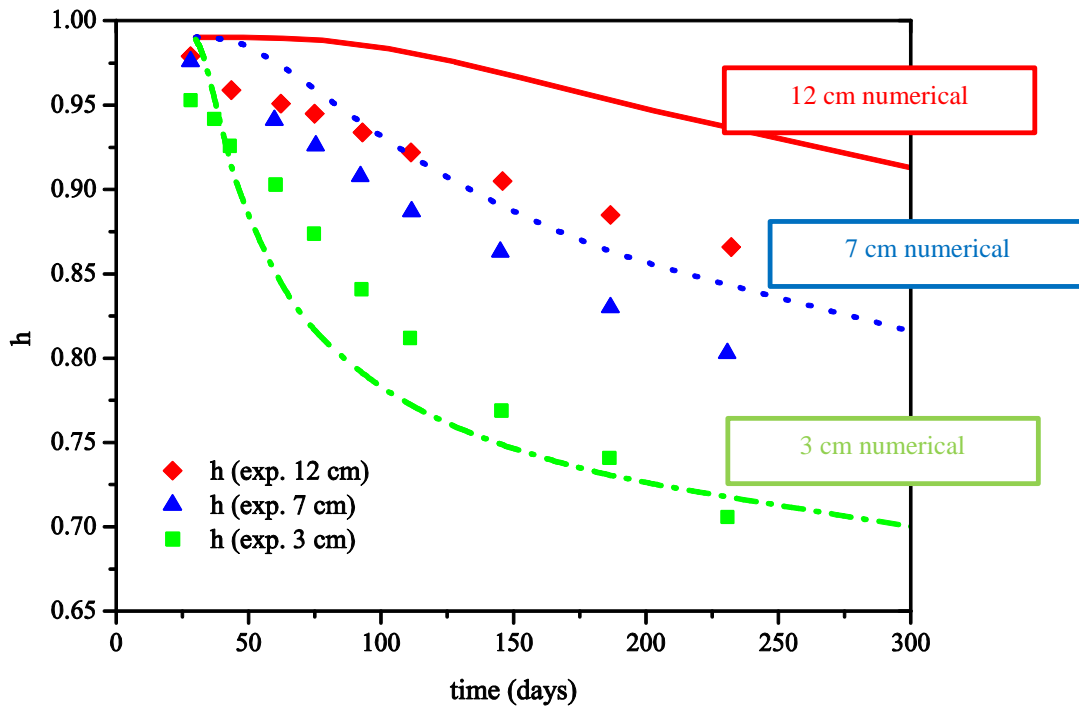


Figure 4-9 – Specimen *M* - Experimental humidity data from Kim and Lee (1999) and numerical simulation ($D_I = 16.1 \text{ mm}^2/\text{day}$ - Fixed boundary condition) (no self-desiccation was considered)

Due to the inability of MC2010 together with prescribed boundary conditions in satisfying the experimental results, a strategy of evaluating the fitness of considering Neumann boundary conditions was carried out. The results of solely adjusting the boundary coefficient did not provide significant improvements in the agreement with the experimental results. Therefore, a combined strategy of searching for the adequate $f_{boundary}$, together with slight adjustments of the D_I parameter (originally considered as $16.1 \text{ mm}^2/\text{day}$) was pursued. As a result, the results of the best combination of $f_{boundary}$ and D_I values are shown in Figure 4-10. It can be noticed that a change of D_I from $16.1 \text{ mm}^2/\text{day}$ to $32 \text{ mm}^2/\text{day}$ and the introduction of $f_{boundary} = 3.2 \times 10^{-4} \text{ m/day}$ provided simulation results that approximated the experimental results quite satisfactorily, with particularly relevant improvement at the depth of 12 cm.

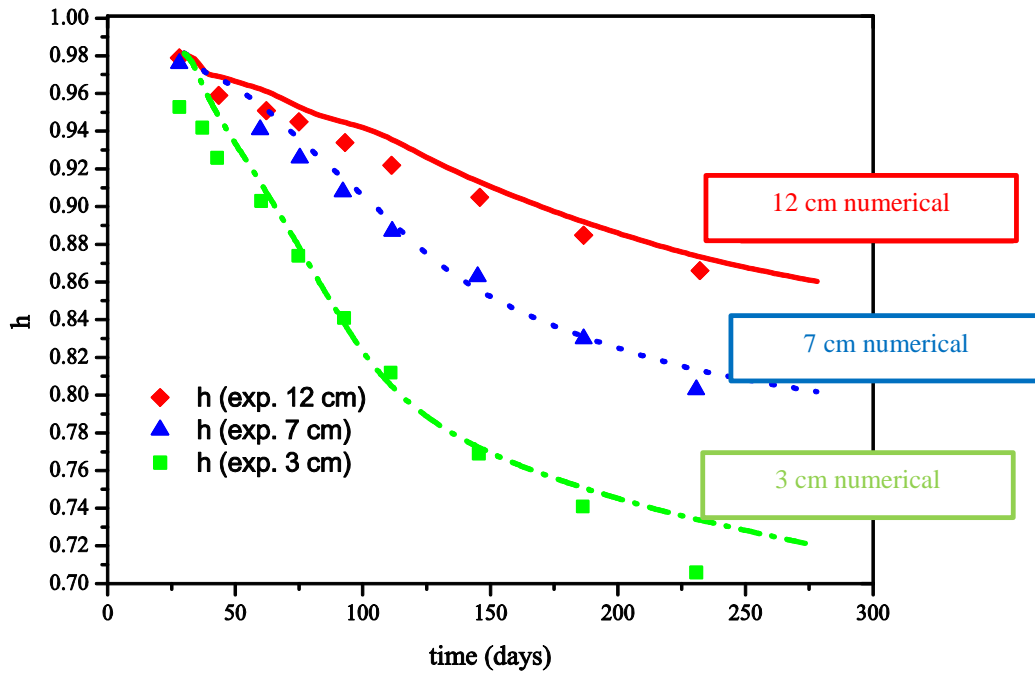


Figure 4-10 – Specimen *M* - Experimental humidity data (Kim and Lee, 1999) and numerical simulation - ($D_I = 32 \text{ mm}^2/\text{day}$ / $f_{\text{boundary}} = 3.2 \times 10^{-4} \text{ m/day}$)

Complementarily to the informed guess strategy mentioned above, it is remarked that all fitting processes mentioned in this work were further performed for a wide range of values for both D_I and f_{boundary} parameters, as to evaluate the uniqueness of the initially obtained solution. In fact, D_I was studied in the range $0.1 \text{ mm}^2/\text{day}$ to $200 \text{ mm}^2/\text{day}$ with increments of $0.5 \text{ mm}^2/\text{day}$. Simultaneously, f_{boundary} was varied in the range $0.1 \times 10^{-4} \text{ m/day}$ to $100 \times 10^{-4} \text{ m/day}$. These ranges took into consideration the recommendations of MC90/2010 and work of Kim and Lee (1999).

For all the subsequent simulations (specimens *H* and *L*), the proposed value for D_I given by the equation presented on the MC2010 and imposed boundary conditions, were tested and the results are similar, showing the same tendency to the one showed on the Figure 4-9. For the concrete specimen *L*, after observing that the combined use of MC2010 parameters with a prescribed boundary conditions did not lead to acceptable agreement with the experiments, the same procedure was adopted. The inverse fitting process had a starting point in the D_I value proposed by MC2010 for this concrete ($D_I = 39.3 \text{ mm}^2/\text{day}$) and the f_{boundary} obtained for concrete specimen *M* ($f_{\text{boundary}} = 3.2 \times 10^{-4} \text{ m/day}$). The best-fit set of parameters did not significantly deviate from the initial values, with $D_I = 52 \text{ mm}^2/\text{day}$ and $f_{\text{boundary}} = 4.8 \times 10^{-4} \text{ m/day}$. The corresponding results are shown in Figure 4-11, where a fairly good agreement with the measured values can be observed. A similar overall strategy was applied for

specimen H, in which again the direct application of MC2010 with Dirichlet boundary conditions did not yield good coherence with the experimental measurements. The starting point for the trial and error procedure involved $D_I = 11.4 \text{ mm}^2/\text{day}$ (as proposed by MC2010) and $f_{\text{boundary}} = 3 \times 10^{-4} \text{ m/day}$ (value used in specimen M). The best-fit also involved a slight increase in D_I to $20 \text{ mm}^2/\text{day}$, as it also had occurred in the cases of specimens M and L. The f_{boundary} value was decreased from 4.8×10^{-4} to $2.0 \times 10^{-4} \text{ m/day}$.

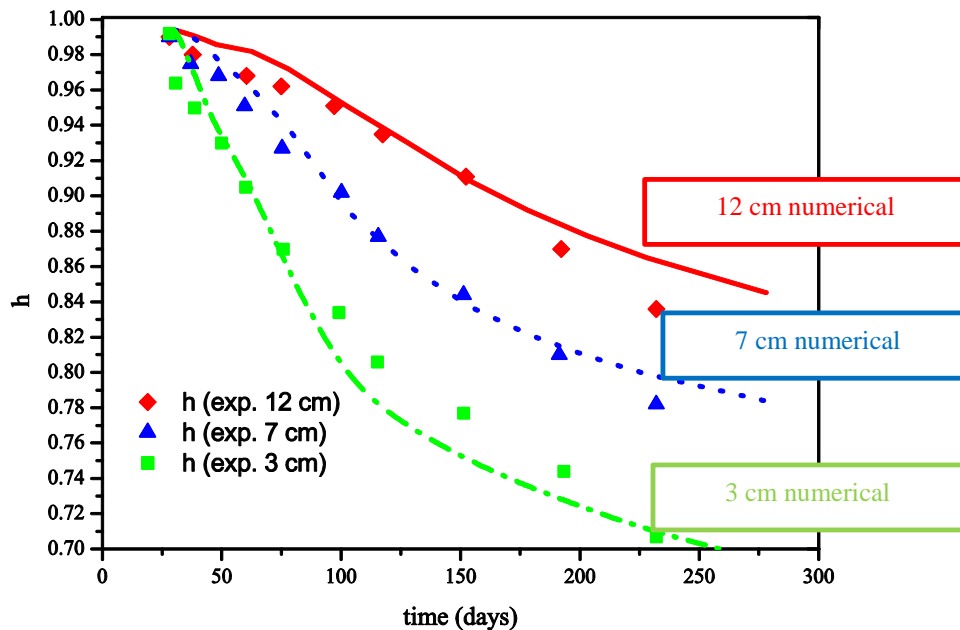


Figure 4-11 – Specimen L - Experimental humidity data from Kim and Lee (1999) and numerical simulation ($D_I = 52 \text{ mm}^2/\text{day}$ / $f_{\text{boundary}} = 4.8 \times 10^{-4} \text{ m/day}$) - $w/c = 0.68$ - Experiments start after 28 days

This process resulted in best fit scenarios for the studied depths of measurement that matched those that had been predicted by the “informed guess” strategy, thus confirming the uniqueness of the obtained solution, Such uniqueness can be further assessed by observation of the R^2 values of each calculated pair of D_I , f_{boundary} , ($w/c = 0.28$) which is graphically represented in Figure 4-13.

The peak of R^2 that surpasses 0.99 is indeed confined to a very limited region of the diagram. The results of this best-fit combination of parameters are shown in Figure 4-12.

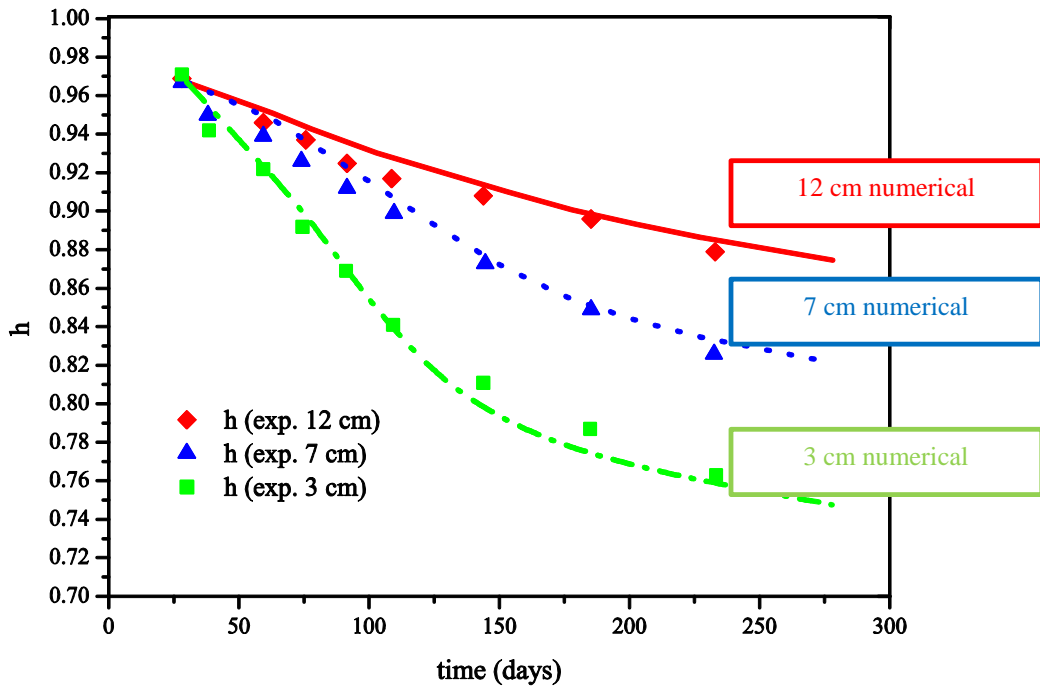


Figure 4-12 – Specimen *H* - Experimental humidity data (Kim and Lee, 1999) and numerical simulation ($D_I=20 \text{ mm}^2/\text{day} / f_{boundary}= 2 \times 10^{-4} \text{ m/day}$) - $w/c = 0.28$ - Experiments start after 28 days

Two final remarks are given in regard to the fitting strategy/results for the three concretes. Firstly, all models needed to use slightly higher values of D_I in comparison to those proposed by MC2010. Secondly, the best fit for $f_{boundary}$ seems to follow a tendency of higher values of $f_{boundary}$ for concretes of lower compressive strength. This could be an indication that $f_{boundary}$ might be proportional to the surface porosity (which is closely related to compressive strength).

The second set of experiments, conducted by Persson (1996), consisted in casting circular slabs of 1 m diameter and 0.1 m thickness, with five different concretes, schematically shown in Figure 4-14. The uniqueness of the $D_I / f_{boundary}$ pairs obtained was confirmed for all cases through extensive simulations of possible combinations of both parameters within wide variation spectra. It is interesting to observe that the post-fitting results provided similar or slightly higher values of D_I , when compared to the initial estimates of MC2010.

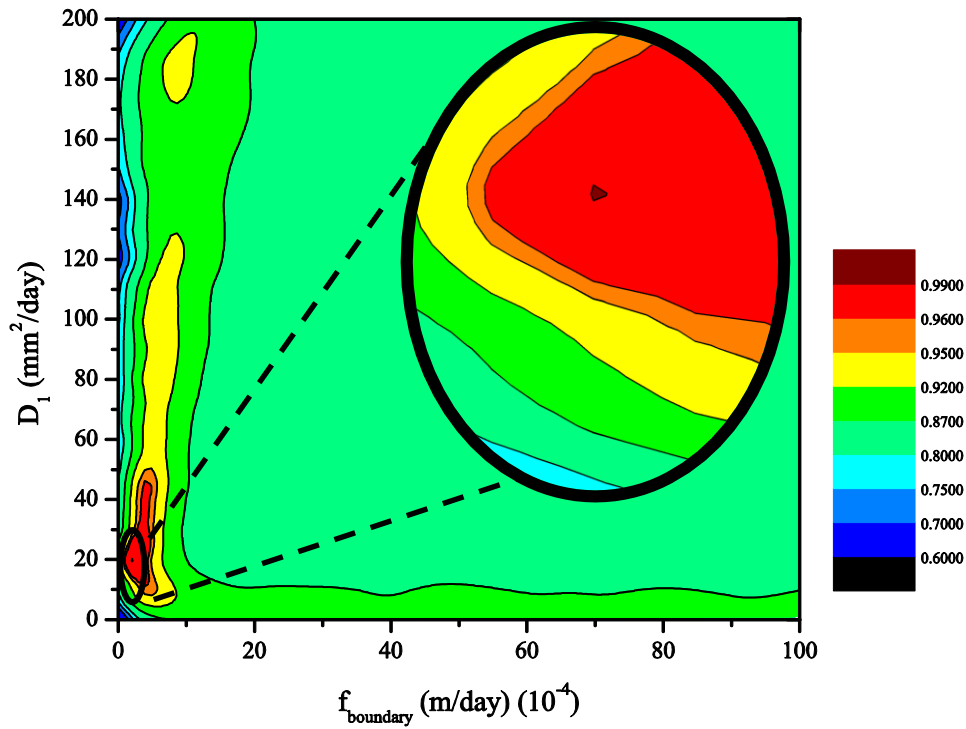


Figure 4-13 – R^2 coefficient simulation of concrete H ($w/c = 0.28$) and D_1 and $f_{boundary}$

The concrete mixes had average compressive strengths of $f_{cm, Mix1} = 80$ MPa, $f_{cm, Mix2} = 37$ MPa, $f_{cm, Mix3} = 57$ MPa, $f_{cm, Mix4} = 67$ MPa and $f_{cm, Mix5} = 91$ MPa. The numerical simulation of these experiments required the use of the axisymmetric formulation. The humidity decreases in the sealed specimens are presented as [day, humidity], for *Mix 1* [28, 0.92; 90, 0.88; 446, 0.86], *Mix 2* [28, 0.96; 90, 0.96; 440, 0.96], *Mix 3* [28, 0.97; 90, 0.95; 446, 0.88], *Mix 4* [28, 0.95; 90, 0.88; 446, 0.83] and *Mix 5* [28, 0.88; 90, 0.81; 446, 0.76].

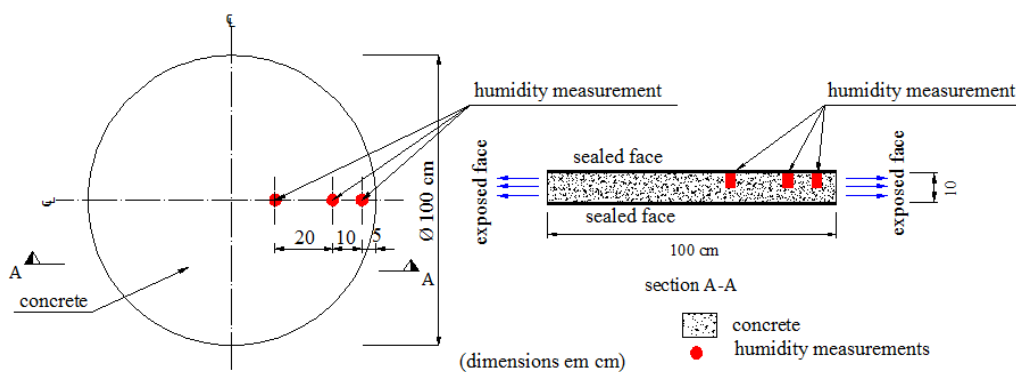


Figure 4-14 – Schematic representation of the geometry and size of test specimens (adapted from Persson (1996))

Again, the direct application of the parameters of MC2010 for D_I ($D_{I,Mix1} = 12.2$; $D_{I,Mix2} = 29.8 \text{ mm}^2/\text{day}$; $D_{I,Mix3} = 17.6 \text{ mm}^2/\text{day}$; $D_{I,Mix4} = 14.6 \text{ mm}^2/\text{day}$; and $D_{I,Mix5} = 10.4 \text{ mm}^2/\text{day}$) and assumption of Dirichlet boundary conditions, led to inadequate agreement between numerical results and monitored h . In pursuit for better agreement, D_I was kept a very similar value to the initial value: $D_{I,mix1} = 12.0 \text{ mm}^2/\text{day}$; $D_{I,mix2} = 30 \text{ mm}^2/\text{day}$, $D_{I,mix3} = 8 \text{ mm}^2/\text{day}$, $D_{I,mix4} = 13 \text{ mm}^2/\text{day}$, $D_{I,mix5} = 8 \text{ mm}^2/\text{day}$, while the fitted values of $f_{boundary}$ for Mix 1, 2, 3, 4 and 5 were respectively $1.4 \times 10^{-4} \text{ m/day}$, $3.0 \times 10^{-4} \text{ m/day}$, $1.0 \times 10^{-4} \text{ m/day}$, $1.5 \times 10^{-4} \text{ m/day}$ and $0.8 \times 10^{-4} \text{ m/day}$, which are similar to the values reported for similar strength classes in the previous example. The comparative study between experimental data and numerical results, and more extensive information can be found in Oliveira *et al.* (2015).

Finally, the third author considered, Kang *et al.* (2012), performed experiments on prismatic concrete specimens with dimensions $100 \text{ mm} \times 100 \text{ mm} \times 300 \text{ mm}$. These specimens were kept under sealed conditions until 1 day age, and at such age, the surfaces of $100 \text{ mm} \times 100 \text{ mm}$ were exposed to drying as shown in Figure 4-15. The numerical simulation and the comparison between experimental data can again be found in Oliveira *et al.* (2015), and confirm that the above statements remain valid.

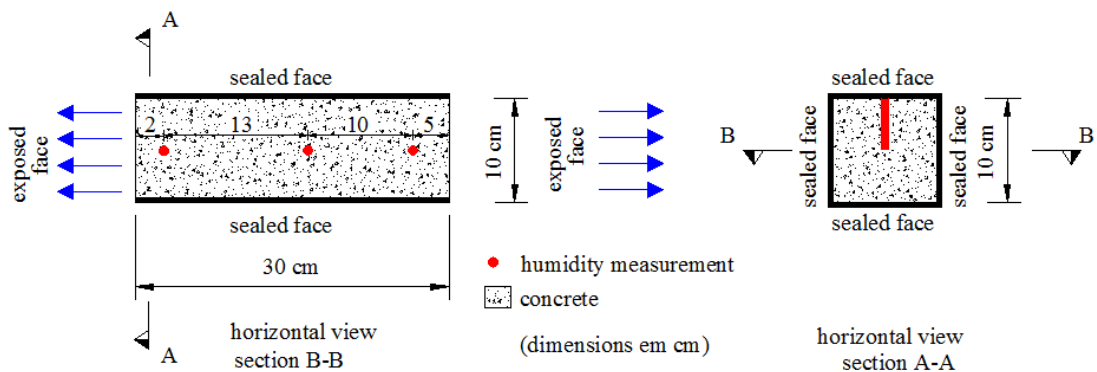


Figure 4-15 – Geometry and size of test specimens (adapted from Kang *et al.* (2012))

As a conclusion, the code using FDM (1D and axisymmetric) (LeVeque, 2007) was used to perform sensitivity analyses and to reproduce the behavior of multiple experiments using distinct concrete compositions (Kang *et al.*, 2012, Persson, 1997, Kim and Lee, 1999). The integrated analysis of results allows supporting the recommendations about the diffusivity and boundary transfer coefficients, given above.

4.4 Multi-physics model implementation

The coupling of thermal field with the other fields was eliminated by Ferretti and Bažant (2006a), as presented in Chapter 3. Therefore the decoupled thermal field was also implemented in FDM for 1D condition (Azenha, 2004). Because of the similarity with humidity field, the implementation will be omitted and as all simulations of the present work assume constant temperature, for the sake of brevity, no further details will be herein presented. Some tests and simulations were also done using the thermal model, for the sake of brevity they are not presented. More information can be found in Azenha (2009) and Incropera *et al.* (2007).

Due to the similarity of fields between carbon dioxide field and the simple humidity field presented before, the implementation of the former will also be omitted herein. Therefore, the only field detailed next is the reaction (R).

The model has been implemented in 1D, axisymmetric and 2D conditions. For brevity and due to the similarity with the 1D implementation, the 2D and axisymmetric implementations are not presented herein. The used notation for reaction field R is the same as previous used in humidity field, where “ i ” represents the node, and “ n ” the time step, as:

$$R_{n-step}^{i-node} \quad 4.31$$

For small values of time step and of length between the nodes, it is possible to assume $dx = \Delta x$ and $dt = \Delta t$. Eq. 3.35 represents the equation used to simulate the reaction field. Replacing in Eq. 3.35 the definition of $F_2(c)$, provides:

$$\frac{\partial R}{\partial t} = \alpha_1 \times F_1^R(h) \times \frac{c}{c_{max}} \times F_3(R) \times F_4(T) \quad 4.32$$

Reaction over time in FDM can be expressed as:

$$\frac{\partial R}{\partial t} = \frac{R_{n+1}^i - R_n^i}{\Delta t} \quad 4.33$$

Replacing Eq.4.33 in Eq.4.32, it is possible to obtain:

$$R_{n+1}^i = R_n^i + \Delta t \times (\alpha_1 \times F_4^R(T) \times F_1^R(h) \times \frac{c_{n+1}^i}{c_{\max}} \times (1 - R_{n+1}^i)) \quad 4.34$$

This equation can be recast as:

$$\left(1 + \Delta t \times \left(\alpha_1 \times F_4(T) \times F_1(h) \times \frac{c_{n+1}^i}{c_{\max}} \right) \right) \times R_{n+1}^i = R_n^i + \Delta t \left(\alpha_1 F_4(T) \times F_1(h) \times \frac{c_{n+1}^i}{c_{\max}} \right) \quad 4.35$$

Reorganizing the equation, the expression for inner nodes (not in symmetry or in boundary) for the reaction field reads:

$$\left(1 + \Delta t \times \left(\alpha_1 \times F_4^R(T) \times F_1^R(h) \times \frac{c_{n+1}^i}{c_{\max}} \right) \right) \times R_{n+1}^i + \Delta t \left(\alpha_1 F_4^R(T) \times F_1^R(h) \times \frac{c_{n+1}^i}{c_{\max}} \right) = R_n^i \quad 4.36$$

The definition of $F_4^R(T)$ will not be used herein, because the temperature is assumed constant.

For coupled humidity field, considering the development done in Section 4.1.1 (decoupled humidity field) and the humidity coupled equation with reaction field (Eq. 3.27) (term $\alpha_2(\partial R/\partial t)$), the final equation for humidity field for inner nodes (except in the boundary and symmetry) is given by:

$$h_{n+1}^i \times \left(\left(1 + 2 \times \Delta t \times \frac{C_{w,n+1}^i}{(\Delta x)^2} \right) - \Delta t \times \left(C_{w,n+1}^i \times \frac{h_{n+1}^{i+1} + h_{n+1}^{i-1}}{(\Delta x)^2} \right) \right) - \alpha_2 \times R_{n+1}^i = h_n^i - \alpha_2 \times R_n^i \quad 4.37$$

As already cited in Chapter 3 the effective humidity and CO₂ diffusivity depends on the other fields (R , h and c) and C_w , from Eq. 4.37 is needed to solve numerically the problem. Here, this development is omitted for the sake of brevity.

Considering the equation for carbon dioxide (Eq. 3.33), with the coupling term related to reaction field (term $\alpha_3(\partial R/\partial t)$), the following expression is obtained in case of the inner nodes (except in the boundary and symmetry):

$$c_{n+1}^i \times \left(\left(1 + 2 \times \Delta t \times \frac{Dc_{n+1}^i}{(\Delta x)^2} \right) - \Delta t \times \left(Dc_{n+1}^i \times \left(\frac{c_{n+1}^{i-1} + c_{n+1}^{i+1}}{(\Delta x)^2} \right) \right) \right) + \alpha_3 R_{n+1}^i = c_n^i + \alpha_3 R_n^i \quad 4.38$$

For the boundary and symmetric nodes, Eqs.4.37 and 4.38 can be easily adapted as done for the decoupled humidity field in Section 4.1.1 using Neumann boundary condition, or an imposed/fixed value in Dirichlet formulation. The terms in time “n+1” are in the left side of the equations, while the terms in time “n” is in right side. The schematic representation of the solution of the coupled system of equations is shown in Figure 4-16.

The symbol (^) denotes a matrix or a vector, while the superscript/subscript denotes the iteration/step. \hat{H}_n , \hat{R}_n and \hat{c}_n represent respectively the humidity, reaction and carbon dioxide vectors for each field in time “n”. \hat{RHc} is a vector with all the fields (reaction, humidity and carbon dioxide). Generically the matrix in right side matrix is denominated \hat{F}_n^i , the vector with all the fields in time “n+1” as \hat{RHc}_{n+1}^i and the residual vector of iterations as $\hat{\psi}$. Three different tolerance values ($toler_{humidity}$, $toler_{reaction}$ and $toler_{carbon_dioxide}$) were adopted because the order of magnitude of each field was different.

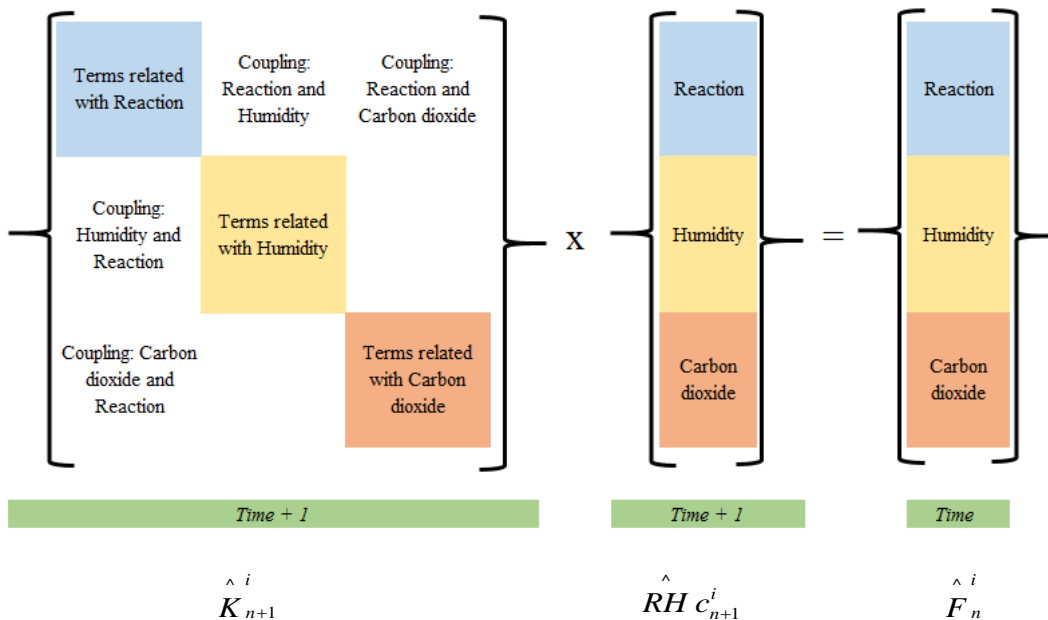


Figure 4-16 – System of nonlinear equations

The numerical model used the implicit backward Euler formulation in FDM, while the nonlinear process is solved by Newton-Raphson algorithm. The generic solution for the implemented algorithm is presented in Figure 4-17.

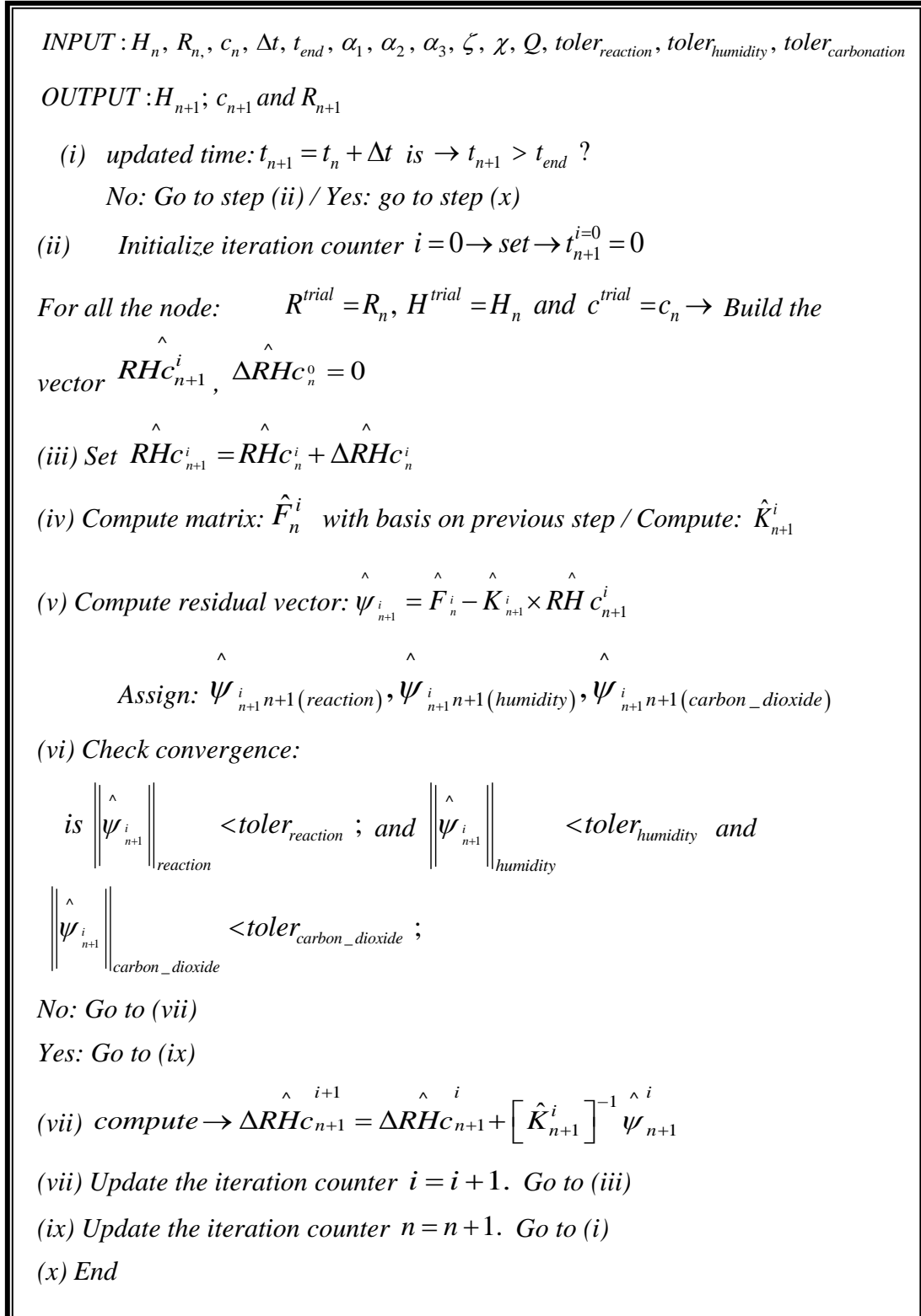


Figure 4-17 – Schematic representation of numerical solution (adapted from Azenha (2009))

To solve the problem, Ferretti and Bažant (2006a) state that the system of nonlinear ordinary differential equations is diffusion-dominated and involves components that decay at widely different rates. For this reason, the authors conclude that the system can be stiff and the classical explicit numerical methods of integration in time can lead to inaccurate results if the time steps are not small enough. For this reason, they adopted a time integration scheme based on a backward difference formula of order two (Shampine, 1994). Here, a simple backward formulation is adopted together with relatively small time steps ($\Delta t \leq 10$ days), except in some parametrical analyses, where $\Delta t = 20$ and 50 days were also tested. The number of iteration increases considerably with the increase of the time step.

It is worth to mention that, for some combinations of values, mesh discretization and time step, the software presented convergence problem. These difficulties occurred especially in case of small nodal spacing and fast diffusion processes. For these cases, the time step was than reduced, and another analysis was started.

In the present work, for the tolerances, values such as: $toler_{humidity} = toler_{reaction} = 10^{-4}$, and $toler_{carbon\ dioxide} = 10^{-5}$ were adopted.

4.4.1 Program verification and preliminary analyses

In order to validate the implemented model, the 1D results presented by Ferretti and Bažant (2006a) were simulated. These authors studied the failure of Pavia Tower in Italy (see Section 2.2.5, which in 1989 and eight centuries after its construction collapsed suddenly, with imperceptible warning signals (more details about the assumptions will be given below, together with the validation of the results obtained with the present implementation).

According to Ferretti and Bažant (2006a) in Pavia, environmental humidity is high and almost constant throughout the year. Fitting the available data the authors proposed the environmental equation for the relative humidity as:

$$h(t) = 80\% + 7\% \cos(2\pi t) \quad 4.39$$

with time t in years.

The concentration of CO_2 in the air c_{env} is about 0.035%, and it was assumed constant, while the initial reaction for the boundary was assumed equal to one (Ferretti and Bažant, 2006a).

Then, for the nodes in contact with the environment, the boundary conditions were (Ferretti and Bažant, 2006a):

$$\begin{aligned} R(0,t) = R(\text{boundary},t) = 1, \quad h(0,t) = h(\text{boundary},t) = h(t), \\ c(0,t) = c(\text{boundary},t) = 0.035\% \end{aligned} \quad 4.40$$

This corresponds to complete carbonation of the surface. The initial conditions for the inner part are given by:

$$t = t_0 \rightarrow h(x,t_0) = 1.0, \quad R(x,t_0) = 0, \quad c(x,t_0) = 0. \quad 4.41$$

The massive wall was assumed to be at constant uniform temperature, equal to the annual average of $T = 284 \text{ K}$ ($11 \text{ }^\circ\text{C}$) in Pavia. The temperature variations produced by exothermic reactions during setting, hardening and ageing were disregarded.

All the adopted parameters values were based on the work presented by Ferretti and Bažant (2006a).

The effective diffusivity in the external leaf is obtained by reducing the diffusivity of lime concrete in proportion to the cross section area fraction of the joints, which is about 1/4 (see Figure 4-18). The adopted parameter used by Ferretti and Bažant (2006a) are summarized in Table 4-2.

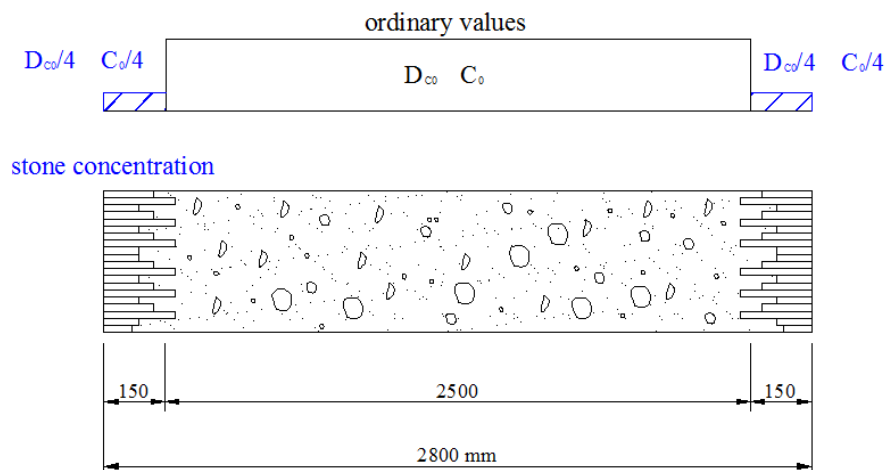


Figure 4-18 – Pavia tower - Cross section of a wall (adapted of Ferretti and Bažant (2006a) and Anzani *et al.* (2009))

Different configurations of time steps and nodal distance between the finite difference nodes were tested to validate the independence of the analysis from time and spacing discretization.

Table 4-2 –Adopted parameters (Ferretti and Bažant, 2006a)

Parameter	Value	Description
$C_{w, rif}$	10 mm ² /day	Humidity Field – Initial Diffusivity
h_c	0.75	Humidity Field – Diffusion coefficient
n	6	Humidity Field – Diffusion coefficient
α_0	0.05	Humidity Field – Diffusion coefficient
α_3	0.4	Coupling constant reaction – CO ₂ fields
α_2	0.0017	Coupling constant reaction – humidity field
$D_{c, rif}$	2400 mm ² / day.	CO ₂ field – Initial Diffusivity
Q_w/R	2700 K	Activation Energy / Gas constant
$\alpha_1 f_4^*(T)$	0.019 day ⁻¹	Reaction field constant
χ	0.8	Humidity field parameter
T_0	296 K	Reference temperature
ζ	0.3	Diffusivity reduction due to carbonation process

An example of low dependence of the time step is present in Figure 4-19, Figure 4-20 and Figure 4-21 ($\Delta x = 1.25$ cm) and $\Delta t = 2.5, 4, 5, 10$ and 50 days (the sake of simplicity, the time steps were denominated by “ dt ” on the following figures).

Even if the final results tended to not have a significant dependence of the time step values, the convergence had a large dependence on the temporal discretization. The number of iterations increased with the for longer time steps.

For the three studied fields the results demonstrate that the model presents low dependence of temporal discretization, for the tested range of values.

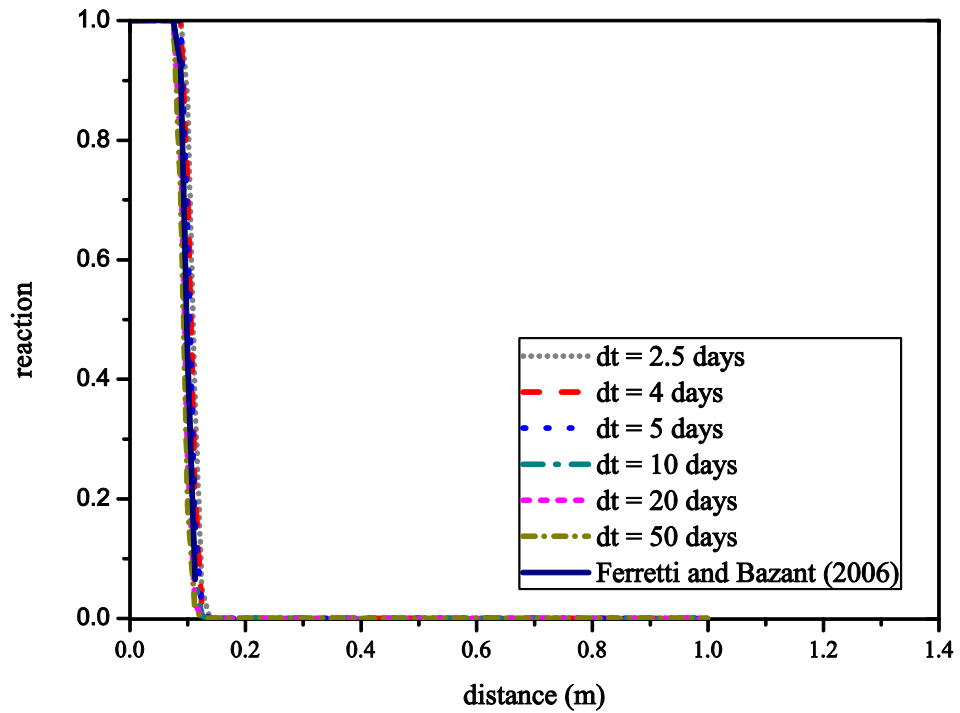


Figure 4-19 – Comparative results for reaction field/carbonation degree for 50 years (different time steps, $\Delta x = 1.25$ cm) - Given the symmetry only half of the profile is presented

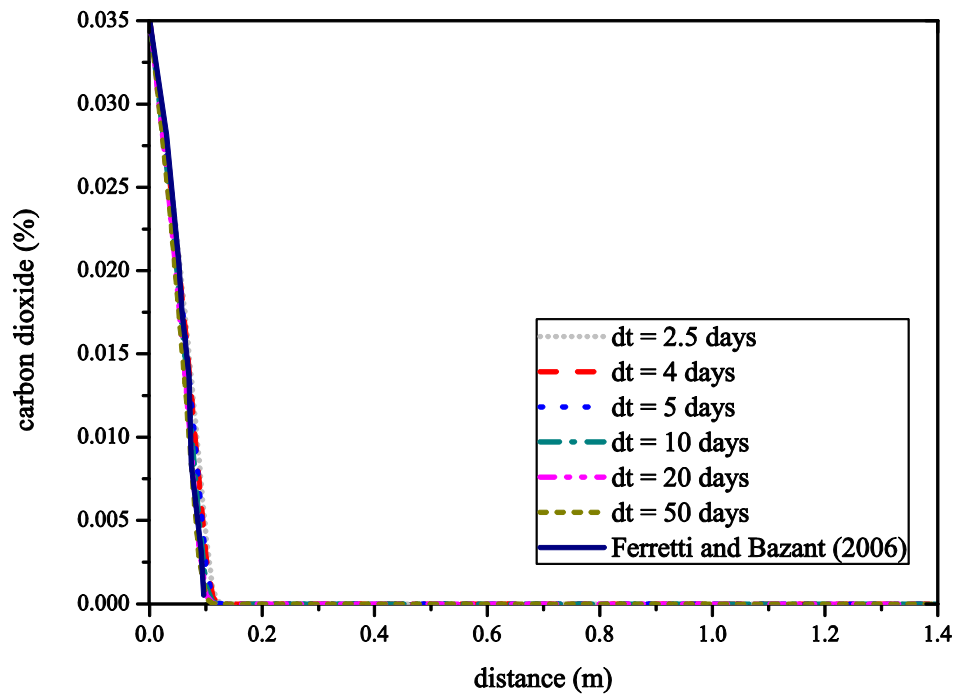


Figure 4-20 – Comparative results for carbon dioxide field for 50 years (different time steps, $\Delta x = 1.25$ cm) - Given the symmetry only half of the profile is presented

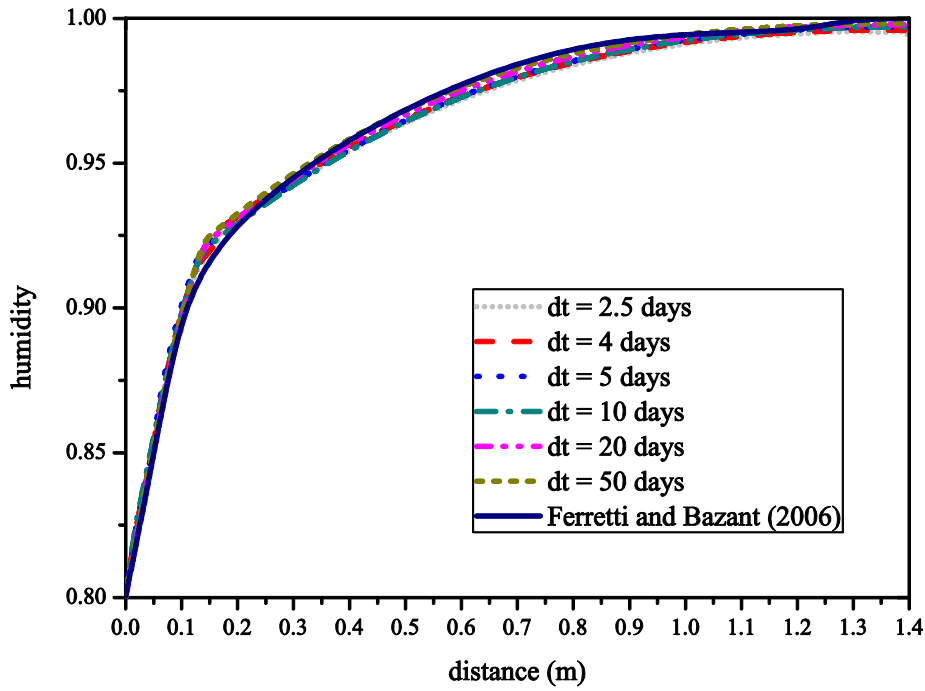


Figure 4-21 – Comparative results for humidity field for 50 years (different time steps, $\Delta x = 1.25$ cm) - Given the symmetry only half of the profile is presented

For 200 years the influence of the spatial discretization was analysed (Δx). Four different values were studied (1.25, 2.5, 5 and 7.5 cm), as Figure 4-22 presents.

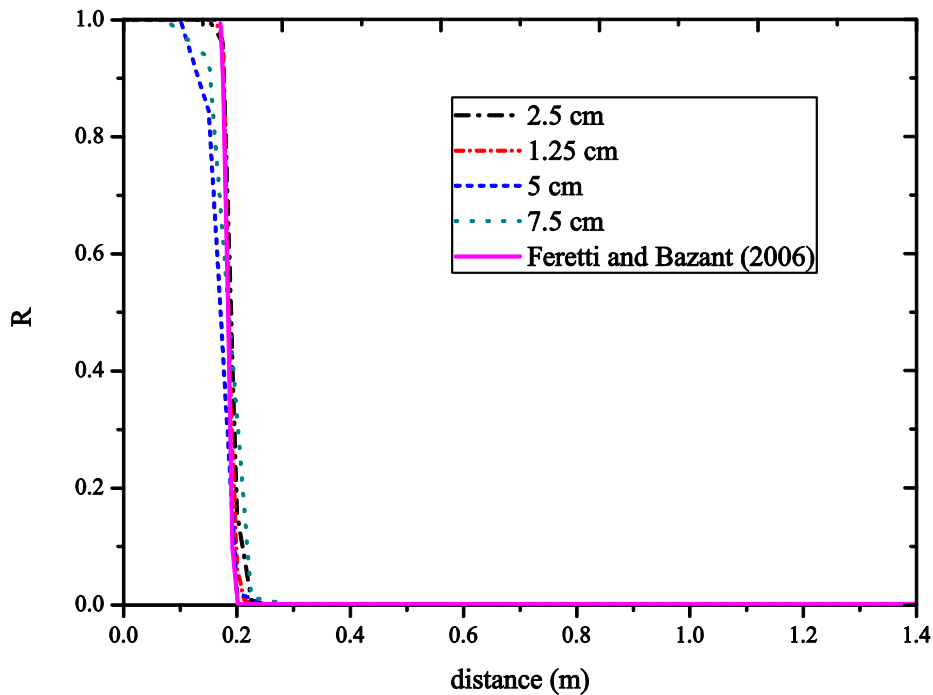


Figure 4-22 – Comparative results for carbon for reaction field/carbonation degree, after 200 years (four different spatial discretization, $\Delta t = 10$ days) - Given the symmetry only half of the profile is presented

For the simulations of 200 years, constant time discretization was adopted ($\Delta t = 10$ days). The results for humidity and CO_2 were also coherent with the values of Ferretti and Bazant (2006a) presenting small discrepancies ($\sim 3\%$), for the sake of brevity these results are not shown.

As Figure 4-22 shows, the results presented small discrepancies, around the distance of ~ 15 cm (horizontal axis). For the presented range of values, the results showed the tendency of small influence on the results.

For 400 and 800 years for reaction field (R) the comparatives are respectively presented in Figure 4-23 and Figure 4-24 (for the sake of simplicity, the time steps were denominated by “ dt ” on the following figures). For the simulations of 400 and 800 years, constant time and spatial discretization were adopted ($\Delta t = 10$ days and $\Delta x = 1.25$ cm).

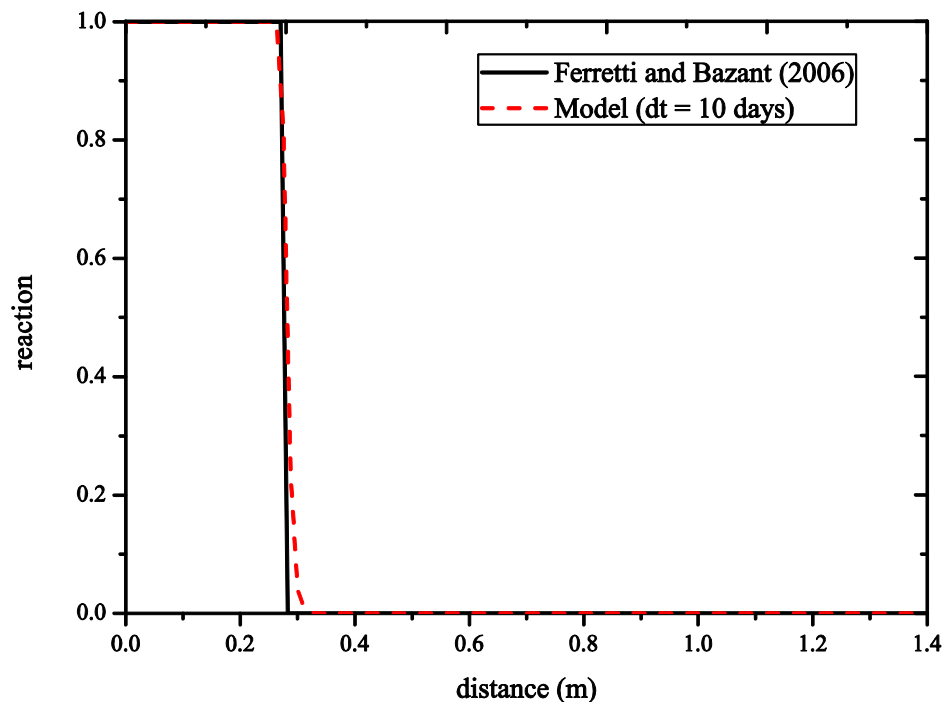


Figure 4-23 – Comparative results for reaction field for 400 years ($\Delta t = 10$ days and $\Delta x = 1.25$ cm) - Given the symmetry only half of the profile is presented

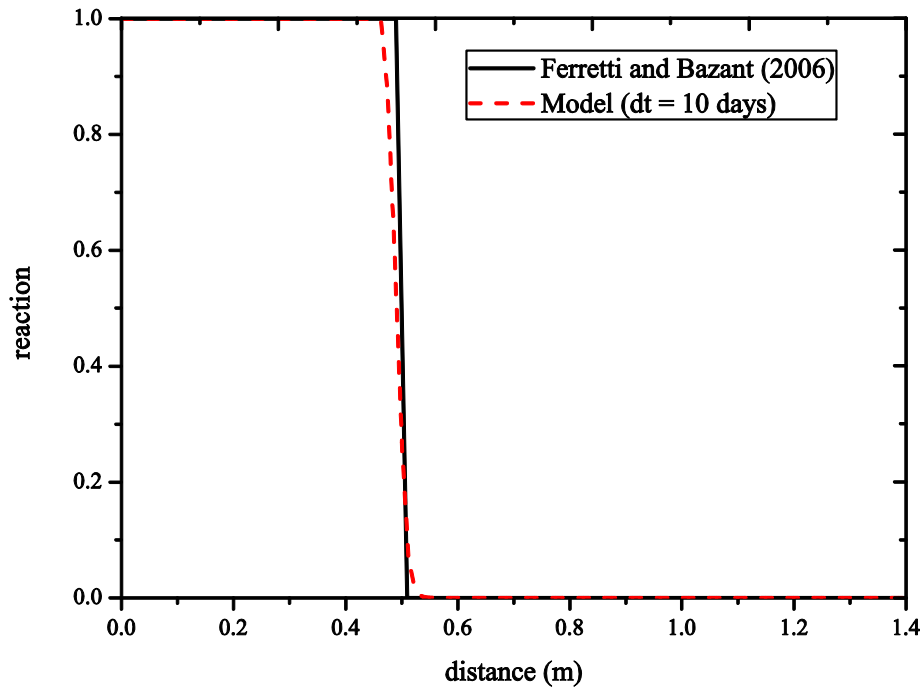


Figure 4-24 – Comparative results for reaction field for 800 years ($\Delta t = 10$ days and $\Delta x = 1.25$ cm) - Given the symmetry only half of the profile is presented

In general terms the implemented model could reproduce the results presented by Ferretti and Bažant (2006a). The results for humidity and CO₂ fields were in agreement with the data obtained by Ferretti and Bažant (2006a), presenting small discrepancies (~3%). For the sake of brevity these results are not shown.

- *Sensitivity analyses*

Several sensitivity analyses were done changing the input model parameters. For these, a 1D wall with two meters (2 m) length, in contact with the environment in the two boundaries was simulated. The obtained results are presents for one meter, because of the symmetry condition (at 1 meter). For the numerical simulations, the distance “zero” (the first node) represented the node in contact with the environment, and the node located at distance one meter (1 m) was the symmetric one.

In order to illustrate the obtained results, the analyses for 50 years are shown. The parametric analyses regarding the CO₂ initial diffusivity ($D_{c,rif}$) was studied and all the parameters were based on the Ferretti and Bažant (2006a) (see Table 4-2).

The parametric results for CO₂ initial diffusivity are shown, because the large influence of this parameter on the final carbonation results. A range from one hundred times higher and smaller the value adopted from Ferretti and Bažant (2006a) was considered ($D_{c,rif} = 2400$ mm²/day, this is cited as the next figures as “*typical value*”). Time and nodal discretization were adopted with constant values ($\Delta t = 1$ day and $\Delta x = 1.25$ cm). For the initial conditions, the considerations adopted above were maintained (Eqs. 4.40 and 4.41). Figure 4-25 shows the results for CO₂ concentration and Figure 4-26 shows the results for the reaction field.

The carbonation profile was significantly affected by the initial diffusivity of CO₂. This effect was expected, because there is a direct correlation between the fields. After 50 years, the wall presented distinct reaction profiles, according to the used parameter. For instance, the carbonation front was located on the first 5 cm of the wall, if the diffusivity $D_{c,rif} = 24$ mm²/day (the smallest value); while the wall presented around 80 cm with $R = 1$, for $D_{c,rif} = 240000$ mm²/day. These cases with extreme values illustrated, how important is the parameters’ selection for the numerical model.

Figure 4-27 shows the results for the humidity field. The influence of the studied parameter ($D_{c,rif}$) was on the carbon dioxide and reaction fields. In opposition, the parameter did not affect significantly the humidity field. The tendency for 50 years was also observed for different ages (for the sake of brevity, other results are omitted here).

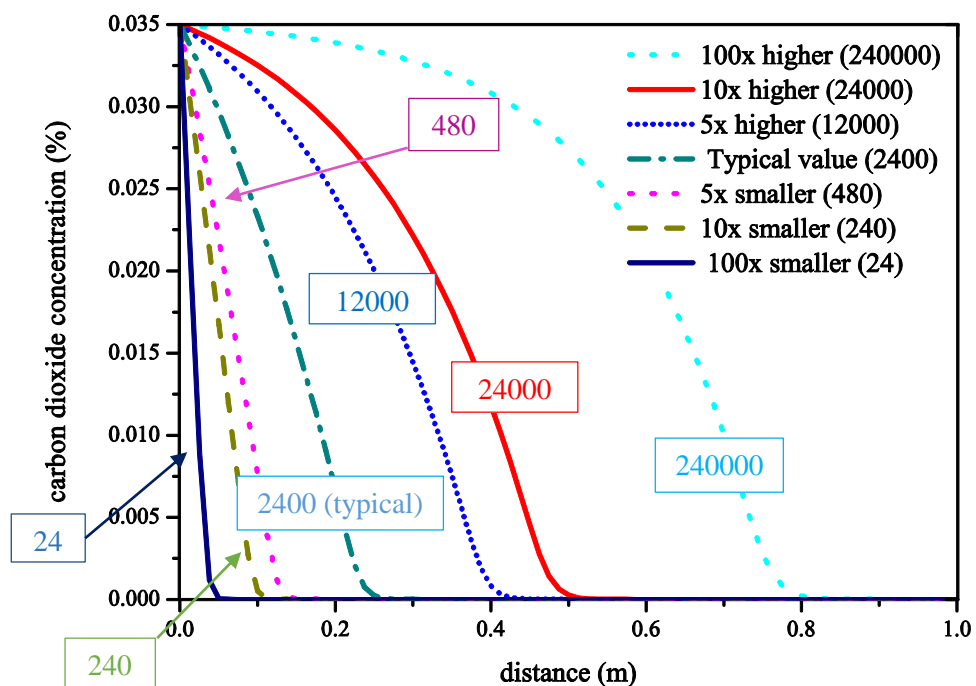


Figure 4-25 – Parametric analyses, results for carbon dioxide field - Initial CO₂ diffusivity (values in mm²/day) - 50 years - Given the symmetry only half of the profile is presented

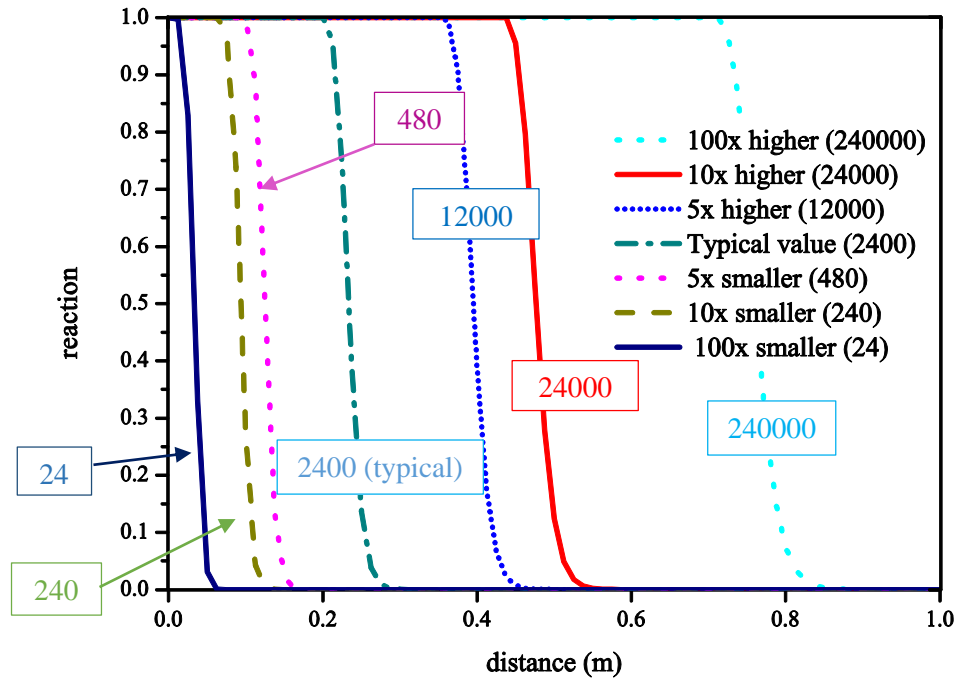


Figure 4-26 – Parametric analyses, results for reaction field - Initial CO₂ diffusivity (values in mm²/day) - 50 years - Given the symmetry only half of the profile is presented

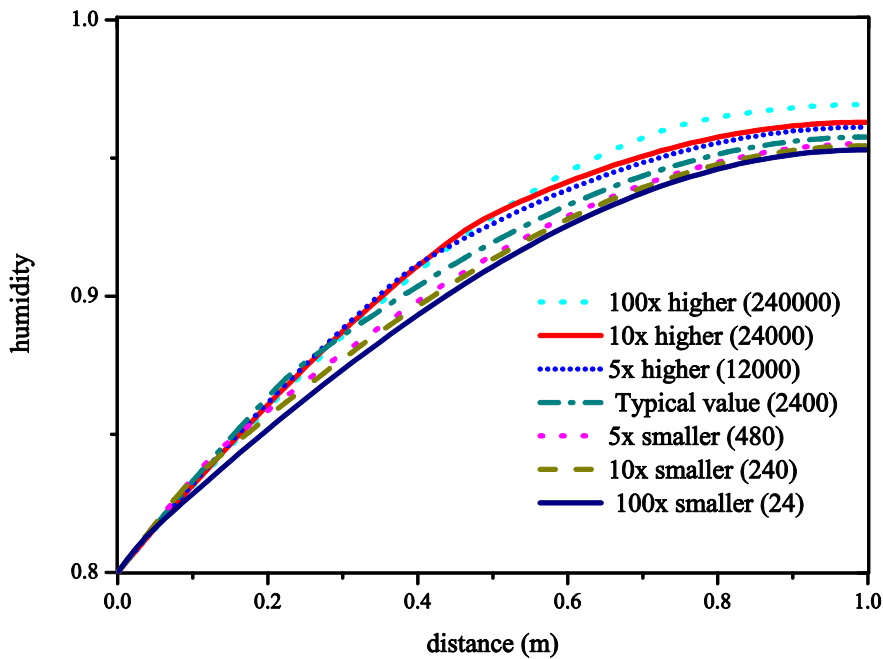


Figure 4-27 – Parametric analyses, results for humidity field - Initial CO₂ diffusivity (values in mm²/day) - 50 years - Given the symmetry only half of the profile is presented

The same range of values for the initial carbon dioxide diffusivity ($D_{c,rif}$) was adopted, and in order to illustrate the behavior for longer ages. A node located at 40 cm from the boundary in contact with the environment was selected. The results for reaction field, for this node, in analyses over 500 years (~182500 days) are shown in Figure 4-28. For horizontal axis, the

upper scale in Figure 4-28 is indicated in “years” and the bottom is indicated in “days” to facilitate the understanding.

The results presented in Figure 4-28, indicated the significant dependence of the reaction profile for this depth, according with the value for the initial the CO₂ diffusivity. The same dependence happened for the others depths (for the sake of brevity they are not shown).

Specifically for the results in Figure 4-28, when the highest value for the carbon dioxide diffusivity was adopted, $D_{c,rif} = 240000 \text{ mm}^2/\text{day}$ or equivalently one hundred time higher than the value cited by Ferretti and Bažant (2006a), after around 30 years (~1095 days), the reaction was completely ($R = 1$). In opposition, for the $D_{c,rif} = 2400 \text{ mm}^2/\text{day}$ or equivalently the value cited by Ferretti and Bažant (2006a), the reaction reached values close to one ($R \approx 1$) after around 400 years (~146000 days).

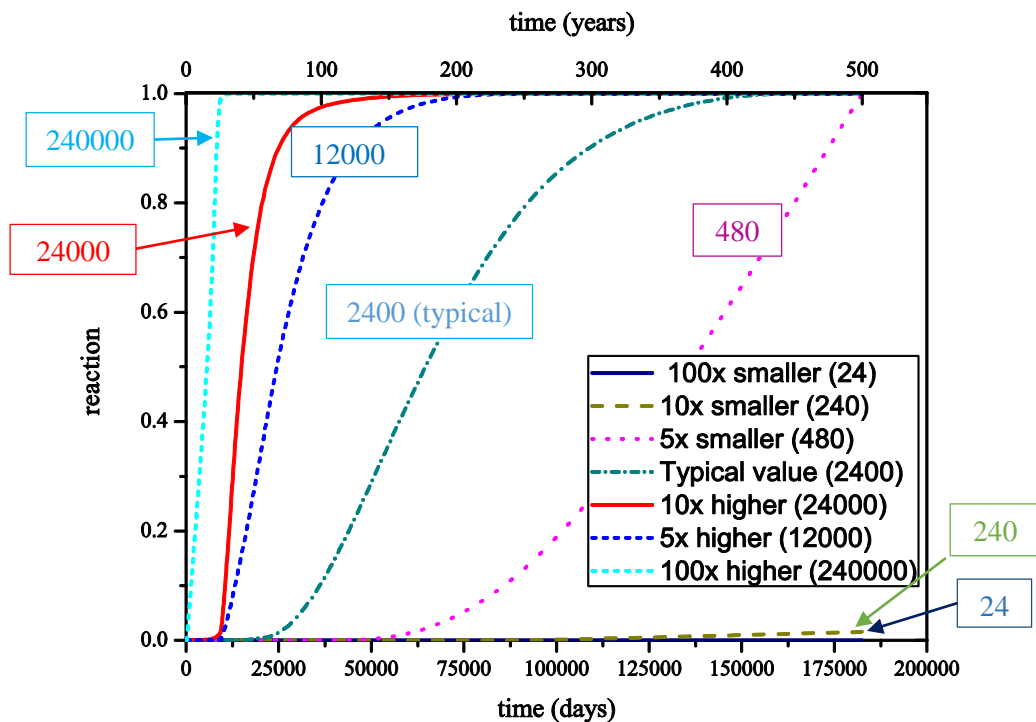


Figure 4-28 – Parametric analyses, results over time for reaction field – Initial CO₂ diffusivity (values in mm²/day) (0 to 500 years)

For the two lower values $D_{c,rif} = 24 \text{ mm}^2/\text{day}$ and $D_{c,rif} = 240 \text{ mm}^2/\text{day}$ (respectively one hundred times and ten times smaller than the value cited by Ferretti and Bažant (2006a), after 500 years, almost no reaction happened for this node.

Once more, these results illustrated the significant relevance of the parameters values, for the final results.

For large structures, according with the adopted numerical modeling (Ferretti and Bažant, 2006a), the inner part of the material supplies humidity for the external one, therefore it maintains elevated values of humidity for longer ages. For structures with smaller dimension, the humidity diffusion happens faster, because of the smaller contribution of those parts.

As presented in Eq. 3.43, the model adopted assumes that elevated humidity values (~ 1) blocks the ingress of CO_2 , and consequently, there is a reduction on the carbonation rate, because these two fields are directly connected. Therefore, for larger structures, the carbonation process tends to happen slower than for smaller ones. This effect is initially presented in Ferretti and Bažant (2006a).

In order to exemplify the concept, three wall were simulated adopting different thicknesses, they presented: 4.0 m, 2.0 and 1.0 m, with symmetry in the middle of their lengths, respectively at 2.0 m, 1.0 and 0.5. In the extremities, two boundaries in contact with the environment were adopted. The same considerations and parameters presented in Table 4-2 were assumed, also constant time and spatial discretization ($\Delta t = 10$ days and $\Delta x = 1.25$ cm). The values for the thicknesses were based in literature, for instance the wall of the Pavia Tower (Binda *et al.*, 1992, Binda *et al.*, 2001, Pavía and Treacy, 2006).

Because of the symmetry, the results are presented for just half of the thicknesses. For the sake of brevity, the results for each field, for the three section are presented in the same figures. The values are shown for analyses at 200 years, similar conclusions were found also for different ages of study. Figure 4-29 presents the results for reaction field, for the three scenarios.

For the reaction field, the wall with 1 meter presented complete carbonation after 200 years, and for the other two examples, the results were ~ 55 cm for wall with thickness of two meters, and ~ 50 cm for the one with four meters.

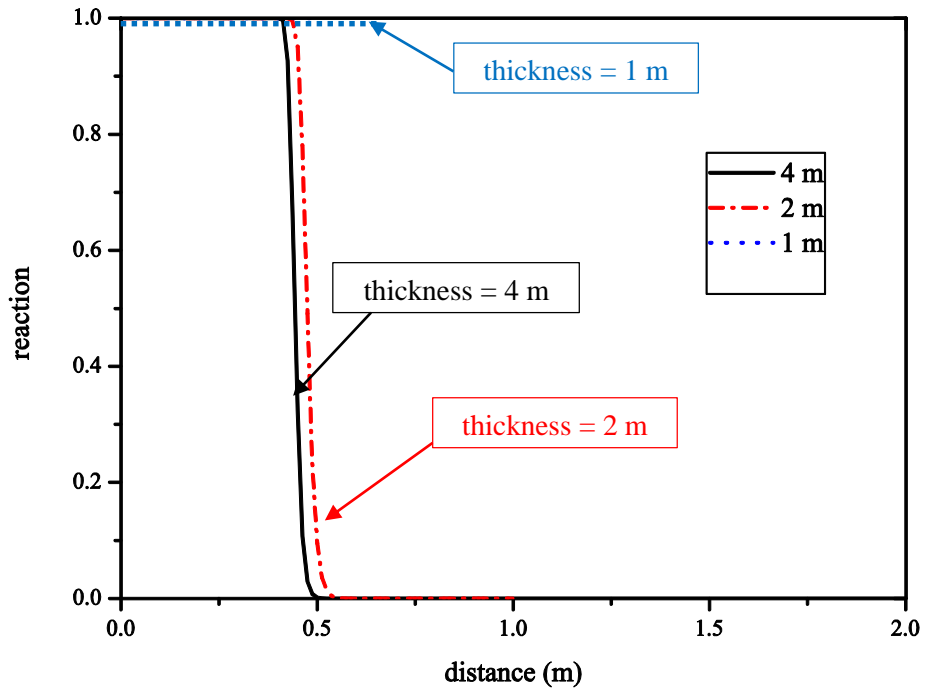


Figure 4-29 – Comparative results for reaction - 200 years, three different wall thicknesses ($\Delta t = 10$ days and $\Delta x = 1.25$ cm) - Given the symmetry only half of the profiles is presented

The results for carbon dioxide field is presented in Figure 4-30.

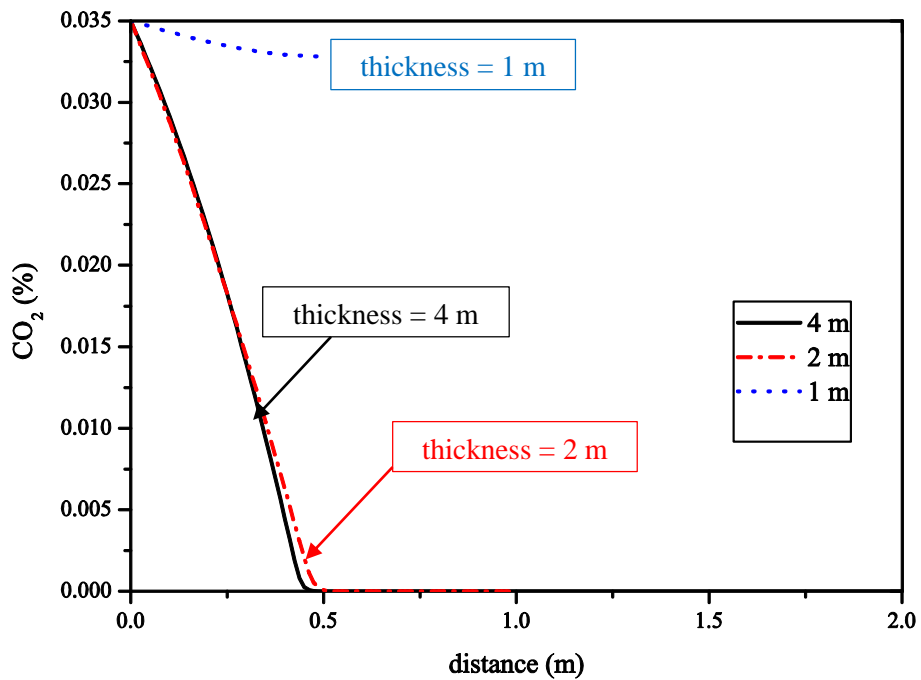


Figure 4-30 – Comparative results for CO₂ - 200 years, three different wall thicknesses ($\Delta t = 10$ days and $\Delta x = 1.25$ cm) - Given the symmetry only half of the profiles is presented

For the CO₂ field, the wall with one (1) meter thickness presented a value similar to the maximum for all the extension after 200 years, while for the other thicknesses the presence of CO₂ was ~50 cm. Figure 4-31 presents the results for humidity field.

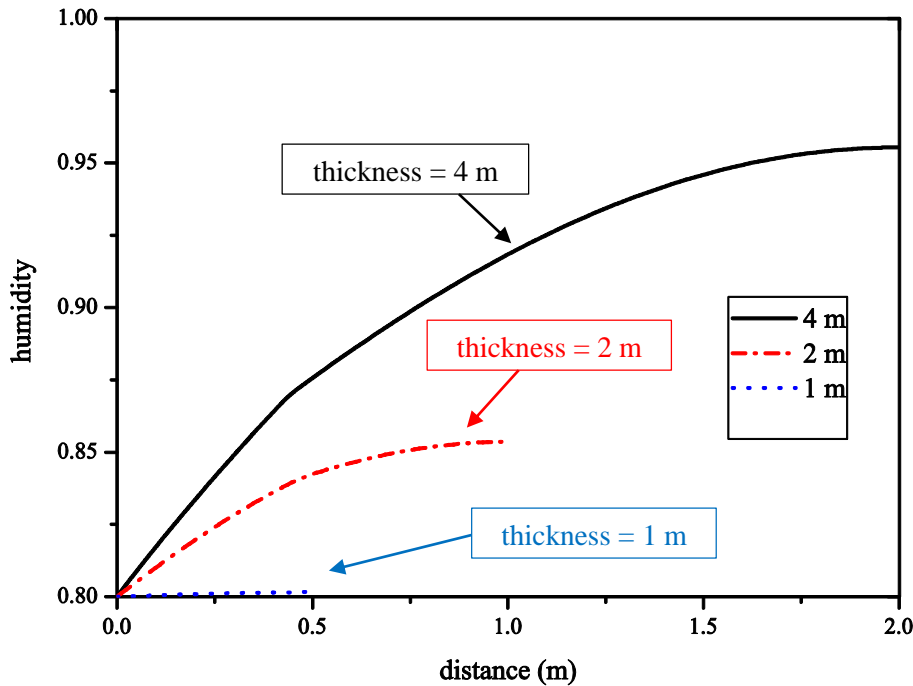


Figure 4-31 – Comparative results for humidity - 200 years, three different wall thicknesses ($\Delta t = 10$ days and $\Delta x = 1.25$ cm)

For this field, the smallest wall presented humidity values in equilibrium with the environment (~0.8), while for the two meters thickness wall the maximum humidity was ~0.85 and for the four meters one, it was ~95%.

The effect will be experimentally study in next chapters with tests in small specimens.

- *2D modeling*

The 2D model was tested with simple verifications, considering the geometry, the symmetry and the 1D modeling, for the sake of brevity, these results are not be presented. In order to simply exemplify the results obtained by the program implemented in 2D, a section with 30 cm × 30 cm was simulated. This geometry, for instance it could represent a cross section of a column. For the model, a quadrangular discretization with 25 nodes in each direction were adopted, with $\Delta x = \Delta y = 1.25$ cm (see Figure 4-32).

For the 2D example the same conditions, and values for parameters presented in Table 4-2, were assumed, except for the humidity boundary conditions. For this field, a boundary

coefficient was adopted in all the four sides of the quadrangular section ($f_{boundary} = 1 \times 10^{-4}$ m/day or equivalently $f_{boundary} = 1 \times 10^{-1}$ mm/day), this value was based on the range of data presented by Oliveira *et al.* (2015) for a low humidity diffusivity.

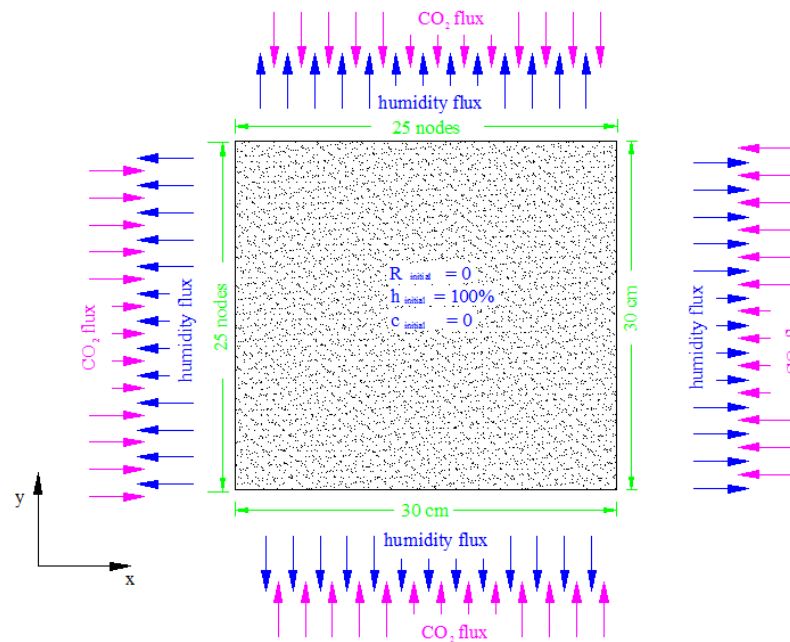


Figure 4-32 – Quadrangular section adopted for 2D study

The numerical results for 30 days are summarized for reaction, humidity and carbon dioxide fields respectively in Figure 4-33 to Figure 4-35.

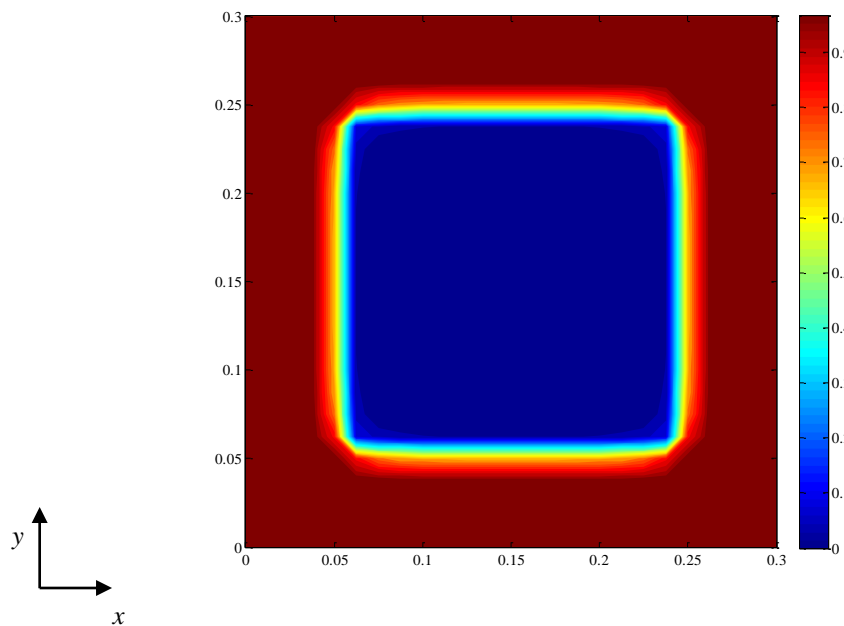


Figure 4-33 – Reaction field - 2D model - 30 days

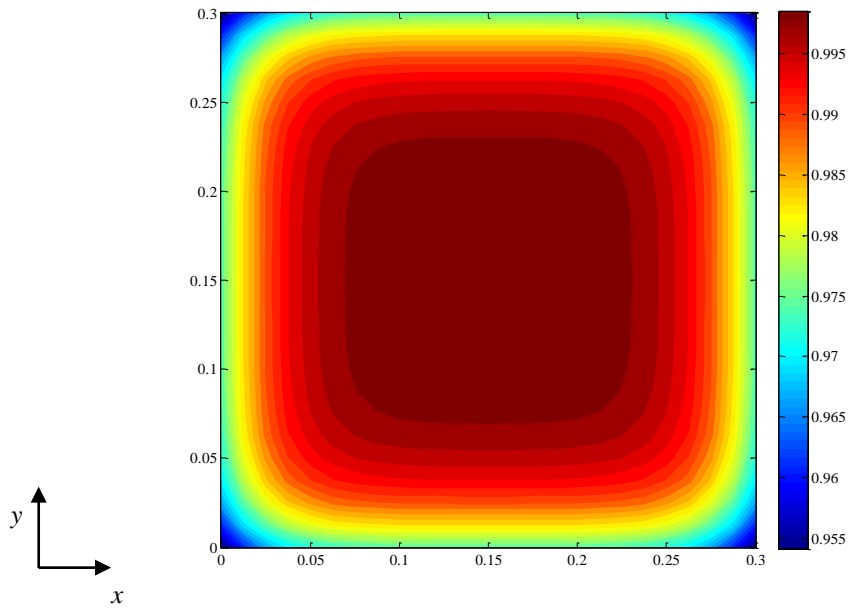


Figure 4-34 – Humidity field - 2D model - 30 days

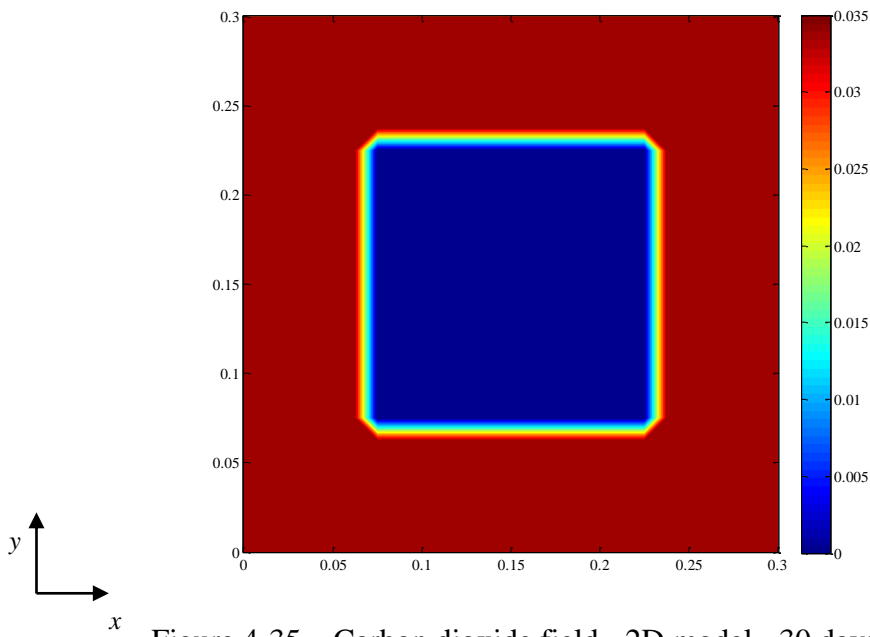


Figure 4-35 – Carbon dioxide field - 2D model - 30 days

For the geometry and the boundaries conditions adopted, the symmetrical character of the results might be observed.

The initial CO₂ diffusivity adopted by Ferretti and Bažant (2006a) and replicated here was around 240 times higher than the value for the initial diffusivity for humidity, this fact justifies, the faster CO₂ ingress, than the humidity diffusion. The results presented in Figure

4-33 to Figure 4-35 showed a fast increase of the CO₂ concentration, and consequently the reaction on the regions close to the boundaries.

Analyzing the node in the center of the section ($x = y = 15$ cm), the profile for the reaction field over time is presented in Figure 4-36.

The maximum value of R for all the section was reached around the day 70. Similar values were obtained for carbon dioxide field, while for humidity results, the internal values for this field were in equilibrium with the environment around 2000 days, because of the pair of $f_{boundary}$ and the maximum diffusivity adopted for the humidity flux. The pair of parameter provided a slow diffusion process.

Other examples with different geometries and boundary conditions were simulated, using the implemented software, for the sake of brevity the results are not presented.

Because of the strong nonlinearity, the complexity of the fields' interactions, and the large number of matrices involved during the processing, the 2D code demanded long time to process an analysis, for practical use more development is still required. Another possibility is the adoption of a specific commercial software to solve the system of equations.

Still, in the present work, the 1D and the axisymmetric implementations was adopted to simulate the experiments in Chapter 7.

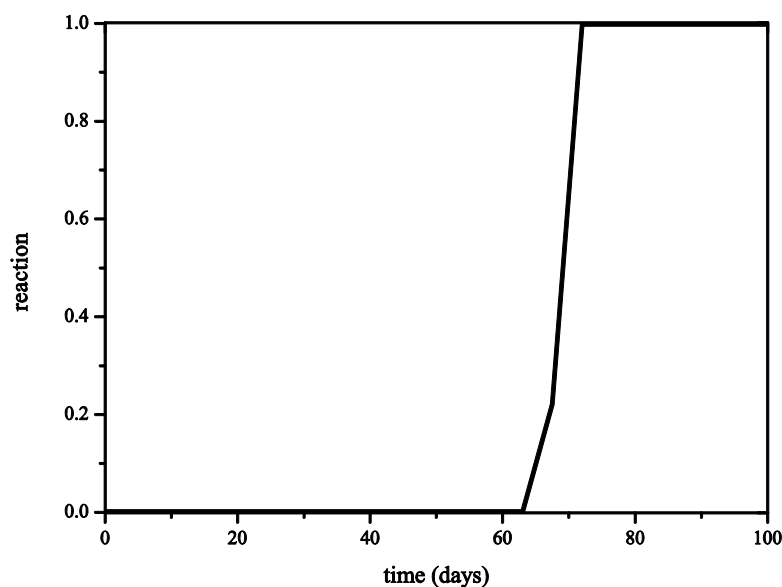


Figure 4-36 – Profile of reaction field over time - 2D model

5 EXPERIMENTAL PROGRAM FOR HUMIDITY FLUX STUDY

5.1 Introduction

The scarce literature about the study of mortars based on aerial lime (Lanas and Alvarez, 2003, Cultrone *et al.*, 2005), does not explain diverse questions especially in terms of experiments and parameters to support multi-physics modeling. Therefore, in synergy with the multi-physical study of aerial lime mortar, a pilot experimental campaign is proposed and carried out in the present chapter.

This chapter aims to report the raw material characterization, the processes of mixing, general information about the preparation of specimens and the main results from a set of experimental studies.

Initially, the raw materials (lime and different sands) were characterized with thermogravimetric analyses (TGA) and X-Ray fluorescence (XRF). The first task regarding the specimen preparation was to obtain a suitable mixture. In fact, the observed shrinkage cracking problems in aerial lime mortar led to the necessity of some mixing tuning. The chosen mixture for the present study was in agreement with the compositions cited in literature for ancient construction, as well as recent scientific works on this material (see Section 2.4.3). With the selected mortar mixture, the experiments for monitoring the humidity profiles in aerial lime mortar specimens over time were started.

As presented in Chapters 3 and 4, different authors already measured the humidity diffusion process in concrete (Kim and Lee, 1999, Kang *et al.*, 2012, Persson, 1996, Persson, 1997). However, no literature reference could be found in what concerns humidity profiling in aerial lime mortars.

The decrease of humidity in cement based or lime based mixtures happens because of two phenomena: the self-desiccation (for the sake of the simplicity the use of this term was introduced from the study of cementitious based materials) and diffusion process. These two phenomena were experimentally investigated. The schematic representation of the experiments is shown in Table 5-1, together with the respective sections within this thesis. A prismatic specimen with the objective to simulate the 1D flux was initially studied (

Figure 5-1 a). To investigate the internal relative humidity evolution under sealed conditions, companion specimens in sealed conditions, isolated from environmental contact, were also studied.

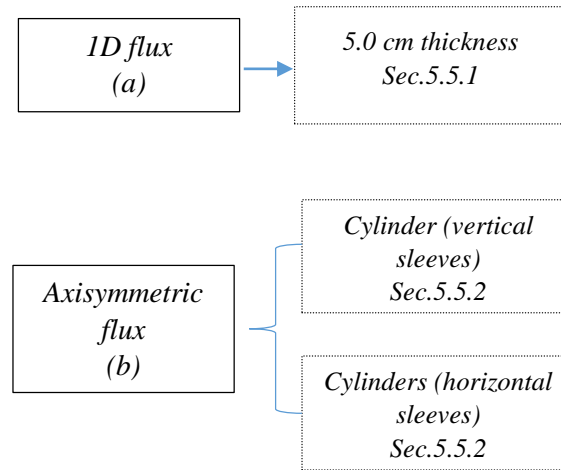


Figure 5-1 – Outline of humidity experiments

In an integrated work, coupling the humidity field, the carbonation field, and the evolution of the elastic modulus experimentally, cylindrical specimens were monitored, with diameter of 6 cm and height of 12 cm. For the humidity profile, two sleeves were cast inside the specimen at different depths (see Table 5-1 b). With the same geometry, a sealed specimen was also studied.

5.2 Characterization of raw materials

5.2.1 General aspects

This section describes the characterization of the raw materials (lime and sands) used for the preparation of the aerial lime mortar. Again, as stated, two techniques were applied: thermogravimetric analyses (TGA) and X-Ray fluorescence spectroscopy (XRF).

The principles of thermogravimetric analyses have been explained in Section 2.5.5. For these tests, the apparatus used was a TGA 2960 SDT V3.0F, manufactured by TA Instruments (TecMinho, 2014, TA, 1997) - Figure 5-2 (a). The equipment can perform simultaneous DSC and TGA testing by measuring both the heat flows (DSC) and weight changes of the sample (Kim, 2006, TecMinho, 2014). Figure 5-2 (b) depicts the crucible used for the TGA tests.

Inside of this recipient, the collected sample was inserted and the set (recipient + sample) was positioned inside the TGA equipment.

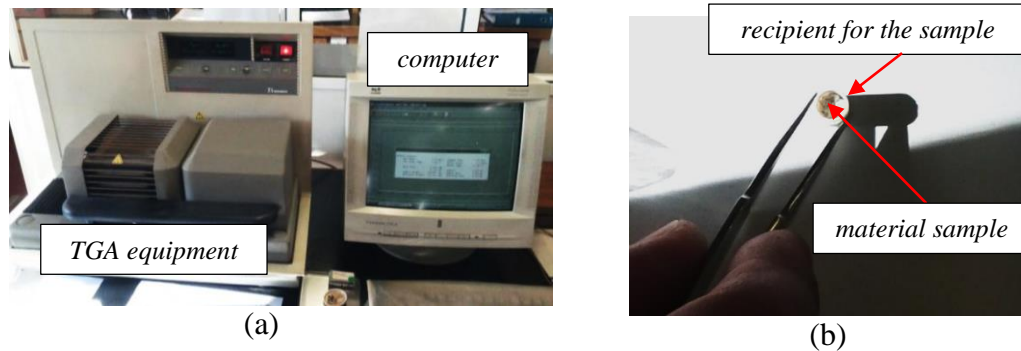


Figure 5-2 – General view of TGA device - (a) TA Instruments TGA 2960 SDT V3.0F / (b) Recipient and example of material sample

For the X-Ray fluorescence, each chemical element has characteristic energy levels for secondary X-ray emission, which has been excited by bombarding with high-energy X-rays. The intensity of emission is characteristic of concentration (Aphane, 2007). In terms of the study of historical mortars, several authors applied this technique for material characterization (Kirca and Erdem, 2004, Arizzi, 2010, Andersen *et al.*, 1999). Further information about the XRF may be found in Jenkins (1999) and Langhoff *et al.* (2006). For this research, a Philips® X'Unique II (TecMinho, 2014, Philips, 1993) unit was used to perform the analyses (see Figure 5-3). This equipment was connected to computer using the SuperQ program (PANalytical, 2015) for data analysis.

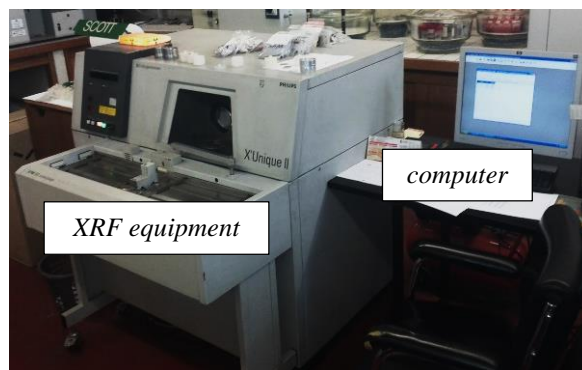


Figure 5-3 – X-Ray Fluorescence Spectroscopy (XRF) - Philips® X'Unique II

5.2.2 Lime

This section presents the characterization of the adopted lime. For this study, micronized quicklime was used. The material was provided by the company *Lusical*[®] (Companhia Lusitana de Cal, S.A.) (Lhoist, 2014). In order to reduce the material contact with the humidity and carbon dioxide, since receiving of the material from the supplier, the lime was stored with an extra protection inside plastic bags.

According to EN 459-1: 2010 (CEN, 2010a), the lime was classified as CL90 Q, thus, in terms of weight, an amount of CaO + MgO larger than 90% was expected. In order to verify this condition, and to study the lime composition, both TGA and XRF were used.

During the TGA test, the lime sample was submitted to a range of temperature from 20 to 1100 °C. The experiment was performed in an inert Argon atmosphere, with a temperature increase rate of 10 °C/min. The sample had the initial weight of 33.56 mg.

In this characterization, X-Ray Fluorescence Spectroscopy (XRF) (Langhoff *et al.*, 2006, Coroado *et al.*, 2010) was also adopted to obtain the chemical composition. The lime sample had a diameter ~4 cm and thickness ~0.5 cm, and it was prepared in a hydraulic press. The results of TGA analysis and the X-Ray Fluorescence Spectroscopy for the studied material are presented in Figure 5-4.

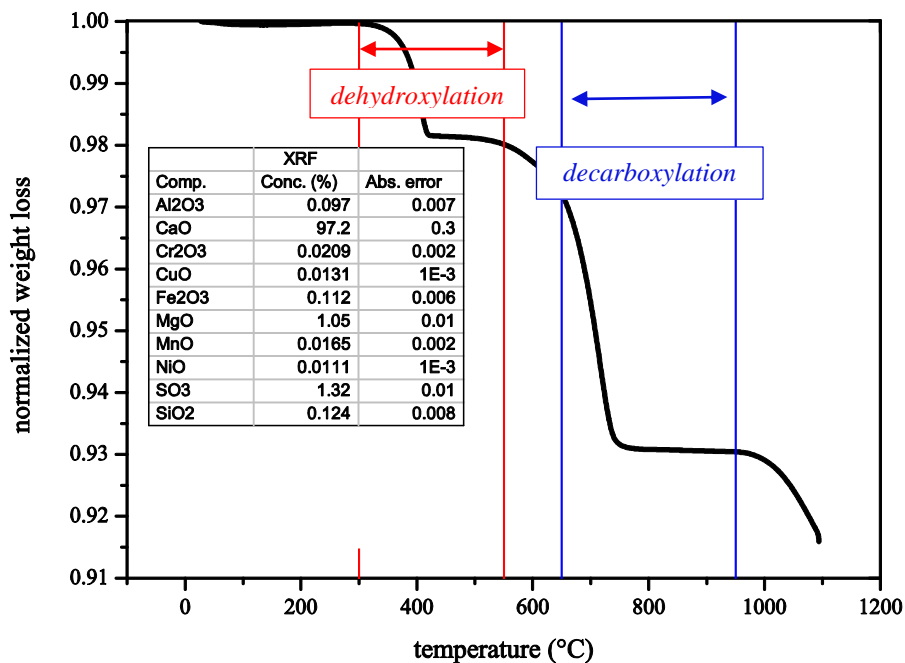


Figure 5-4 – Characterization of lime (TGA+XRF results)

The TGA test on lime allowed identifying the presence of calcium hydroxide and calcium carbonate, even before the mixture. The TGA plot of Figure 5-4 revealed the presence of a certain amount of calcium hydroxide ($\text{Ca}(\text{OH})_2$) (7.5%) and calcium carbonate (CaCO_3) (11.8%). These two percentages were calculated considering the information given in Section 2.5.5. The presence of these two compounds in raw material, might affect the results of TGA for the mortars. In fact, without knowledge of this initial presence of CaCO_3 , one might be induced to consider that all carbonation corresponds to post-mixing phenomena, which would be an overestimation.

The XRF results indicated the presence of 97.2% of CaO, followed by SO_3 (1.32%) and MgO (1.05%). Other compounds were present in small percentage (see Figure 5-4). The sum of the quantity of CaO and MgO was higher than 90% as defined by EN 459-1:2010 (CEN, 2010a) for the class of lime CL90 Q. It is noted that the amount of CaO obtained by XRF testing included the other forms of calcium compounds (Ca), such as CaCO_3 and $\text{Ca}(\text{OH})_2$ (Langhoff *et al.*, 2006, Shackley, 2011, Aphané, 2007), therefore justifying the elevated percentage indicated by XRF in Figure 5-4. Therefore, these two techniques (TGA and XRF) are complementary, and their results should be analyzed together. The presence of the two relevant compounds of calcium, namely CaCO_3 and $\text{Ca}(\text{OH})_2$, was not completely distinguished by the XRF, while in the TGA, the decomposition ranges for those compounds were clearly demonstrated (see Figure 5-4).

5.2.3 Aggregates

This section presents information about the adopted aggregates. Two types/grades of sands were used and herein denominated as fine and coarse. In order to reduce the presence of dross/material impurity that might react with the lime in the mortar, the sands were washed and dried previously to their application. The washing procedure was performed for at least 2 hours. The sands were then placed inside an oven and set at approximately 100 °C for at least 24 hours, for drying. After this period, the material was stored inside plastic containers, covered with a suitable top and plastic foil, to prevent contact with environmental humidity. The washing and drying processes were done according to the evolution of the experimental procedures, and the demand of the material, therefore the storage for the sands was done for a maximum of 60 days.

In order to estimate the water content of the aggregates during their application, representative samples of the materials were weighted and inserted inside the oven with a

temperature ~100 °C, for a period of 24 hour. After that, the sands were weighted again, and the values compared. Table 5-1 indicates the values before and after the drying. The content of water was considered the variation of their mass after this process. Table 5-1 shows, that the water content of both aggregates was less than 1%, thus its influence on the properties of the mortar or the lime/water ratio might be considered negligible.

Table 5-1 – Water content of the aggregates after drying

Sand type	Initial weight (g)	Weight after 24 hours (g)	Weight variation (g)	Water content (%)
<i>fine</i>	700.0	698.5	1.5	0.21
<i>coarse</i>	700.0	699.2	0.8	0.11

TGA and X-Ray fluorescence analyses were also done on both aggregate types. For the fine sand, the initial weight for the TGA testing was of 29.97 mg, whereas, for the coarse sand, the initial weight was 57.63 mg. The test was performed in an inert Argon atmosphere, with a temperature increase rate of 10 °C/min, and a temperature range 20-1100 °C was adopted. For XRF, the sands were crushed and the samples had a diameter ~4 cm and thickness ~0.5 cm, again prepared using a hydraulic press. The normalized curves of TGA weight loss *versus* the temperature, and the X-Ray fluorescence results, for the two types of aggregates are shown in Figure 5-5 .

The results presented in Figure 5-5 suggested that the aggregates, fine and coarse sands, should not induce relevant influence on the results of TGA testing in mortar, for carbonation analyses, since sands do not present any significant weight loss on the ranges of study of both dehydroxylation and decarboxylation of the aerial lime. The XRF studies demonstrated that both sands were composed by silica (SiO₂) at percentages of ~92 and ~89%, respectively, for the fine and coarse sands. It is noted that the temperature of decomposition for silica is much higher (~2000 °C) (Schick, 1960) than the limits considered in this work.

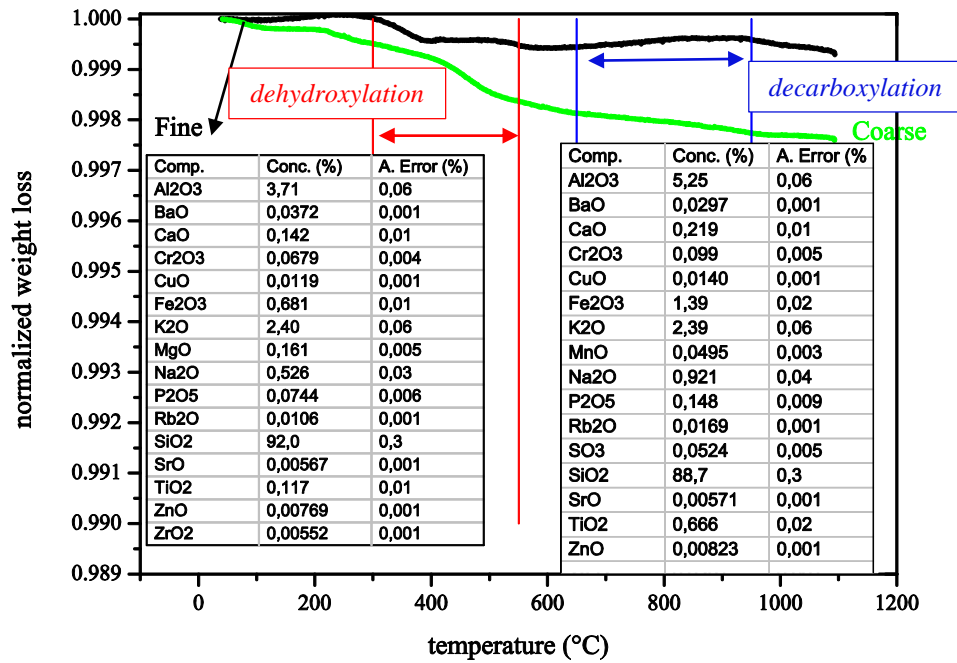


Figure 5-5 – Characterization of aggregates: TGA and X-Ray Fluorescence results

5.3 Mortar composition and preparation

The two types of aggregate (in terms of granulometry) were used for preparing mortar. The final granulometry was a mix of one (1) part of “fine” sand and one (1) part of “coarse”, in terms of volume. The norm for mortar preparation EN-13139 (CEN, 2002) gives limits on the maximum grain size and on the percentage of fines with d smaller than 0.063 mm. The chosen granulometry in the current research respected such limits. Figure 5-6 presents the comparison between the initial granulometry (with mix 1:1 of both types of sand) adopted in the present work and the limits from the norm (dash dot lines).

As the hot-lime mix method (see Chapter 2) can be considered a usual method applied in historic constructions (Margalha *et al.*, 2011, Forster, 2004a, Moropoulou *et al.*, 1996), it was decided to use such method in the context of this research. The hot-lime mix process involves the use of a part of the total amount of water to hydrate lime, whereas another part evaporates (mostly during the mixing period). In fact, the chemical reactions that are induced by the contact of the aerial lime with water are strongly exothermic and may induce very high temperatures (reaching 100°C), which induce strong evaporation during the mixing process (Snow and Torney, 2014). Some trials to establish a suitable amount of water for the mix were performed. Basically, two criteria were followed: (i) the mortar should not exhibit significant shrinkage cracking, and (ii) the mortar should have adequate workability.

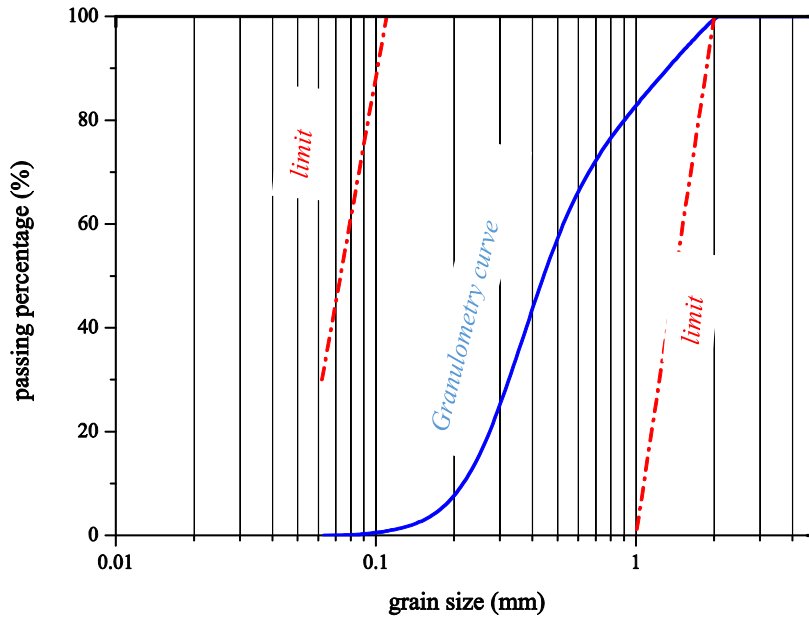


Figure 5-6 – Granulometry of aggregate compared to limits from EN-13139 (CEN, 2002)

The mixing process was carried out as close as possible as the recommendations according to standard procedures for the preparations of mortar mixtures, which can be found in EN 196-1 (CEN, 2005a). The procedure was done by adding the solid part to water and mixing at relatively low speed (~ 40 rpm) for about 300 s. The mixer used was a Würk[®] with a 3 liters capacity bowl with a vertical blade. Details about the blade can be found in EN 196-1 (CEN, 2005a). In terms of casting procedure, immediately after the mixing, the specimens were molded. Since water evaporation after the mixing was noticed, it is worth to remark that the amount of mortar prepared in a single phase was limited, with a maximum volume of ~ 2 dm³.

Standard EN 1015-11 (CEN, 1999b) refer to EN 1015-2 (CEN, 1999a), which gives recommendations about flow table test results according to the mortar density. These recommendations are shown in Table 5-2.

Table 5-2 – Flow table values for mortar according to EN 1015-2 (CEN, 1999a)

Bulk density of fresh mortar (kg/m ³)	Flow value (mm)
> 1200	175 ± 10
> 600 to ≤ 1200	160 ± 10
> 300 to ≤ 600	140 ± 10
≤ 300	120 ± 10

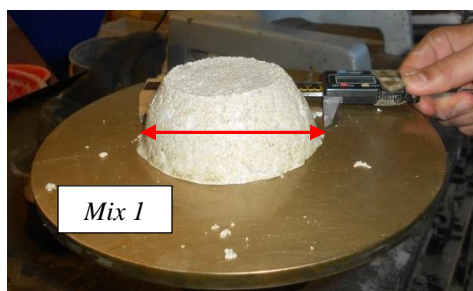
The reference values presented are indicative for different densities (CEN, 1999a). Some pilot specimens were also done for the choice of the final mixing.

Table 5-3 presents the trial mixes and some considerations regarding their consistency and suitability for the experimental work. Before the final mixture (*Mix 4*) was established, three other mixtures were tried (mixture by volume respectively: lime:water:aggregate, *Mix 1* = 1:1:3; *Mix 2* = 1:1.5:3 and *Mix 3* = 1:1.4:3). In particular, *Mix 1* was very dry, thus not workable enough to produce specimens, *Mix 2* presented lack of consistency, and *Mix 3* presented some cracks for longer specimens and high shrinkage. The finally adopted proportion of 1:1:3:3 in *Mix 4* was in agreement with the compositions used in traditional mortar and by other references, see Section 2.4.3.

Table 5-3 – Composition of mixes, flow value and observations

Mix (by volume) lime:water:aggregate	Flow value	Note
<i>Mix 1</i> - 1:1:3	unsuccessful test	mortar had very dry behavior, not workable
<i>Mix 2</i> - 1:1.5:3	173 mm	lack of consistency due to the presence of water
<i>Mix 3</i> - 1:1.4:3	135 mm	cracking of longer specimens
<i>Mix 4</i> - 1:1.3:3	122 mm	suitable and, thus, adopted

All the tried mixes had densities around 1800-2000 kg/m³, thus Table 5-2 shows that the expected flow value for such densities is 175 ± 10 mm. In this case, just the mix richer in water fitted this requirement, while for 1:1.3:3 even it was not fitted with the expected workability, it was identified as final mix as it was suitable in preventing cracking. Similar density values for fresh mortar were found in Seabra *et al.* (2009) and Algarvio (2010).



(a)



(b)

Figure 5-7 – Flow table test: (a) *Mix 1* (b) *Mix 2*

Regarding the shrinkage problem faced in some specimens, for such kind of mortars, the desiccation (water loss) is the major cause (Veiga and Souza, 2004). The chosen mix (*Mix 4*) was initially prepared in terms of volume. For a more accurate mixture, the equivalent composition of the raw materials in terms of weight was finally done. For this purpose, the amounts of materials in terms of volume were weighted and the equivalent proportion expressed as a function of weight was found: 1:1.53:6.14. The materials presented the following values for bulk density (mass divided by the total volume): lime $\approx 0.85 \text{ g/cm}^3$ and sand $\approx 1.74 \text{ g/cm}^3$.

Different references in literature (Teutonico *et al.*, 1993, Baronio *et al.*, 1999, Lawrence, 2006, Lanas and Alvarez, 2003) adopted similar compositions to the mixture chosen here. Lawrence *et al.* (2006a) cited this composition 1:3 (lime/aggregate) as the most common adopted in research (details are given in Section 2.4.3).

5.4 Casting and curing conditions

The specimens were cast with the selected mixture and, in order to reach a similar density, a procedure was followed to fill the mold sequentially by 2cm layers and compacting them with strokes (approximately 10), as to reach an initial target specific mass of $2000 \pm 5\% \text{ kg/m}^3$. Subsequently, the term “*density*” is adopted in the present text for this property. For its calculation, the dimensions of the specimen were measured with a caliper rule and the weight was measured with a balance, providing the density of the material/specimen as its weight per volume. The compacting process was done with the help of a metallic device with a weight of $\sim 250 \text{ g}$ and a contact area of $\sim 12.56 \text{ cm}^2$ or with an auxiliary device with the same weight and a contact area of $\sim 0.79 \text{ cm}^2$.

During the hydration process aerial lime produces a significant amount of heat, and, as stated above, part of the water evaporates during the mixture (Snow and Torney, 2014), meaning that the controlling of density for this kind of mortar is not a simple task. To illustrate the extension of the evaporation process, a test with duration of one day was done, adopting two recipients with same geometry. The first one was filled only with water, and the second with aerial lime mortar, adopting the composition defined in previous section. These two samples were adopted for a comparative study. They were exposed for the same duration and environmental conditions. The tests were done in ambient condition for 24 hours, which was

the adopted reference period. After the period, for this sample around 20% of the initial weight of water used in the mixture had been lost, amounting to ~20 g. In the case of the recipient with water, which had the same exposed area, just ~2 g was evaporated. The evaporation of water was considerably higher for the lime mortar, demonstrating the considerable influence of the heat produced during the hydration process. Therefore, a plausible reason has been found to justify the fact that the consistency, texture and workability of the material changed rapidly during casting. Therefore, the specimens that were cast firstly were easier to prepare. As the time passed by, the specimens cast in sequence exhibited less workability.

After casting, the specimens were stored in controlled conditions. All specimens were kept in a climatic chamber with controlled temperature and relative humidity ($T \sim 20 \pm 2$ °C and $h \sim 60 \pm 5\%$). The average CO₂ concentration for an outdoor environment is around 350 ppm (APA, 2009, Pereira *et al.*, 2013, Saetta and Vitaliani, 2004) and, because of the constant ventilation on the climatic chamber, the concentration inside was assumed equal to the typical value of the external environment. This chamber was simply denominated as “*standard*” conditions.

5.5 *Experiments to study the humidity diffusion process*

5.5.1 *Introduction*

This section describes the experimental aspects adopted to investigate the evolution of the drying process in aerial lime mortar. Since, no reference in literature was found about these tests, the methodology was adapted from the humidity measurement in cementitious based materials presented in literature (Granja *et al.*, 2014, Kim and Lee, 1998, Quincot, 2012). The study can be, thus, considered a pioneer measurement of the humidity profile in aerial lime mortar, involving a learning process and pilot experiments. However, all the results and trials made are not presented here, for the sake of brevity. The summary of the specimens used for each test regarding the study of the humidity flux is presented in Table 5-4.

A prismatic mold was used to simulate 1D flux, with all surfaces sealed, except for one, as to ensure the flux along its 5.0 cm dimension. For the same geometry of the mold, two companion specimens were also cast with all the faces sealed to measure the internal humidity evolution in such conditions. Finally, two different configurations for cylindrical

molds were tested, to reproduce axisymmetric conditions. Further descriptions about the characteristics of the molds, the procedures about the specimens' preparation and the results are given with more detail in the following paragraphs.

Table 5-4 – Summary of specimens for humidity tests

Specimen	Quantity	Dimensions (cm)	Test
mold prismatic (specimen <i>H.MA</i>), isolated (<i>H.MB</i> and <i>H.MC</i>)	3	5.3 × 17.8 × 5 (thickness = 5)	monitoring of humidity with 1D flux
cylinder <i>H-H60-A</i> <i>H-H60-B</i> <i>H-H60-C</i> <i>H-H60-D</i>	4	6 × 12	monitoring of humidity with axisymmetric flux

5.5.2 Prismatic specimens - 5.0 thickness

In this section, information about the prismatic specimens for tests under 1D flux is provided. The prismatic mold, schematically shown in Figure 5-8 was transparent, to check for possible mortar cracking. It was a plastic container, in which three holes were drilled through its bottom surface as to insert the sleeves for posterior introduction of the humidity probe. The mold presented internal dimensions of: 5.3 cm of height, 5.0 cm of thickness and 17.8 cm of length (see Figure 5-8 and Figure 5-9).

The measuring sleeves were introduced as to reach the depth of measurement in which the readings were intended. The sleeves do not disturb the path of moisture between the surface and the measuring point, because they are introduced from the opposite side of the evaporating surface, as it is clearly visible in section A-A of Figure 5-9. For that purpose, plastic tubes with water and vapor proof behavior were adopted. A diameter (~1 cm) was adopted to be suitable to fit with the dimensions of Vaisala *HMI41* humidity sensor (Vaisala, 2004), and to allow fast operation, reducing the environmental exposition.

The bottom parts of the sleeves in contact with the specimen were covered by a GORE-TEX® membrane (Gore, 2014), fixed with hot glue (see Figure 5-9). GORE-TEX® (Gore,

2014) is a special material normally applied in specific types of garments that is impermeable to water in its liquid state, but that allows the water vapor passing through.

The use of this membrane was crucial to ensure adequate protection of the inside of the sleeve, which should be available for insertion of the humidity probe. In fact, according to previous experiences at University of Minho, for instance the work of Granja *et al.* (2014), in which the same procedure was adopted on concrete, the relative humidity measurements through the GORE-TEX® (Gore, 2014) membrane or directly in contact with the specimen are equivalent (see the adopted setup in Figure 5-9).

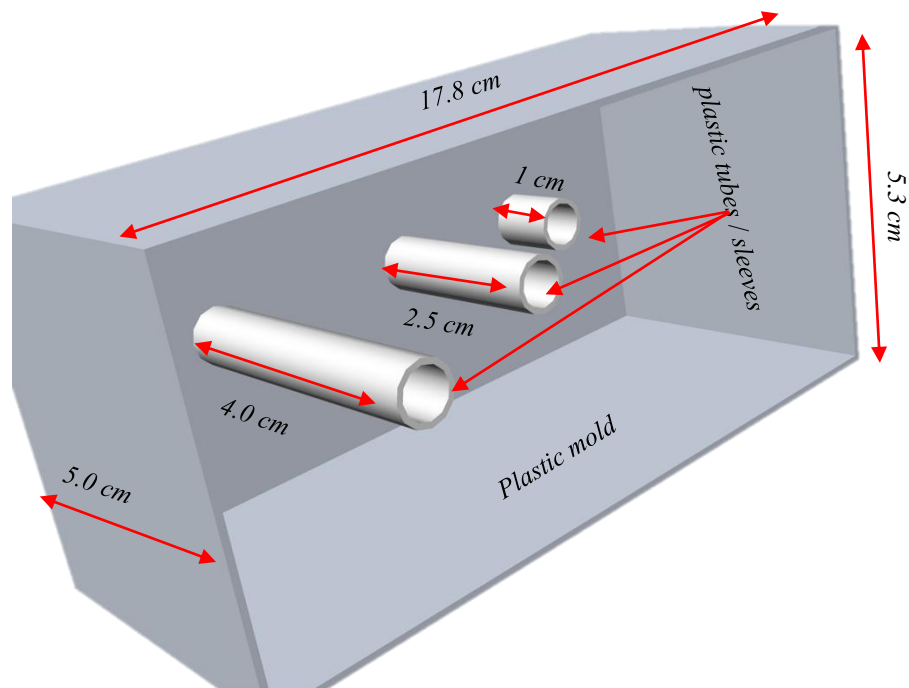


Figure 5-8 – Schematic 3D representation of prismatic mold adopted to study the humidity diffusion process

Other authors also cite the use of such technique in cementitious based materials (Tanabe *et al.*, 2008, Grasley *et al.*, 2006, Quincot, 2012). A view of the prismatic mold adopted and its dimensions used for *HMA* is presented with more details in Figure 5-9.

With the objective to reproduce the 1D humidity flux, for *HMA*, a paraffin layer was applied on the contact edge between the mortar and the plastic container (see Figure 5-9). This procedure was adopted to minimize the effect of the mortar shrinkage, since it could create a free space between the mortar and the mold, creating a preferable path for the humidity flux.

Three prismatic specimens were cast (*HM.A*, *HM.B* and *HM.C*) using the presented mix proportion and the details previous shown (see Sections 5.3 and 5.4). One specimen (*HM.A*) was adopted to simulate the 1D flux, and the two other (*HM.B* and *HM.C*) were adopted to investigate the behavior under sealed conditions. For these experiments, plastic packings (Tupperware®) with the same dimensions and characteristics as presented in Figure 5-9 were used, but in opposition of the previous test, with all the faces sealed. The sealing process was done with the closed packing plastic, auxiliary hot glue and plastic tape. The sealed specimens also were cast with three sleeves inside.

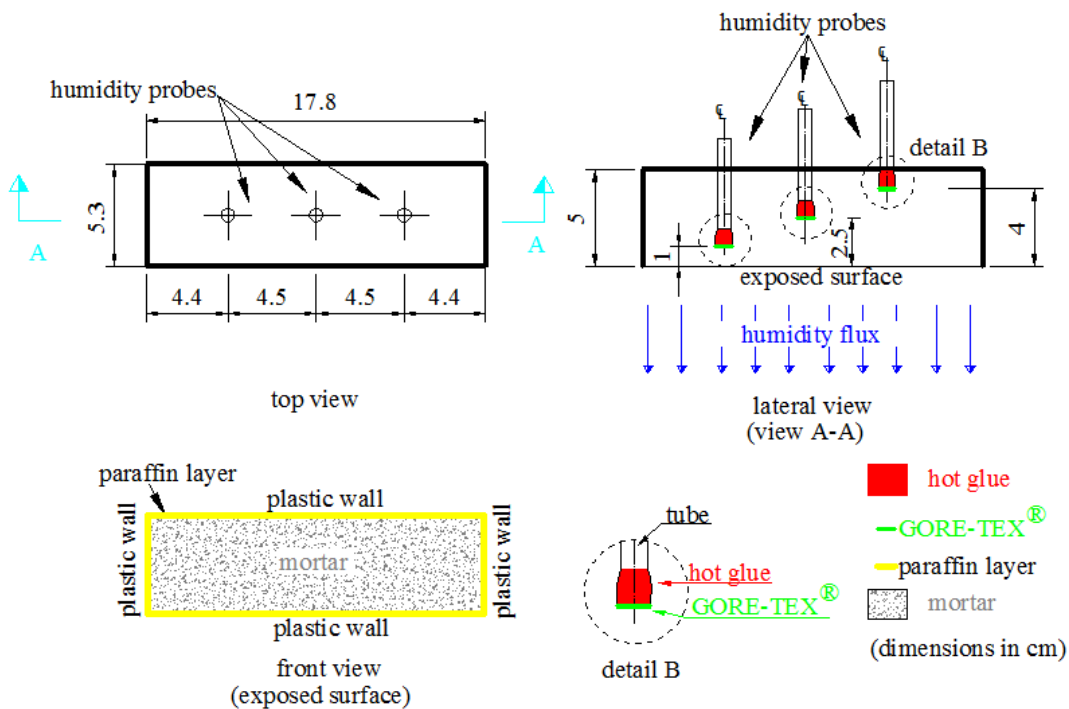


Figure 5-9 – Mold prismatic (specimen *HM.A*)

Regarding the curing conditions, the specimen *HM.A* was exposed since the casting.

- *Results*

For the 1D flux, the results for specimen *HM.A*, for the three monitored depths are presented in Figure 5-10. The values measured at distinct depths from the evaporating surface (1 cm, 2.5 cm and 4 cm) showed a small difference, specially after 30 days. The results for 2.5 cm and 4 cm were similar for all the experiments. These results could be associated with an

elevated diffusion coefficient value for this material, or even with an error related to the measurement device. The humidity sensor presents an error about $\pm 3\%$ and for elevated humidity values ($\sim 95\%$), the error is approximately $\pm 5\%$ (Vaisala, 2004, Meneghini, 2014). The humidity values were similar to the equilibrium with the environment after ~ 50 days for the three studied depths.

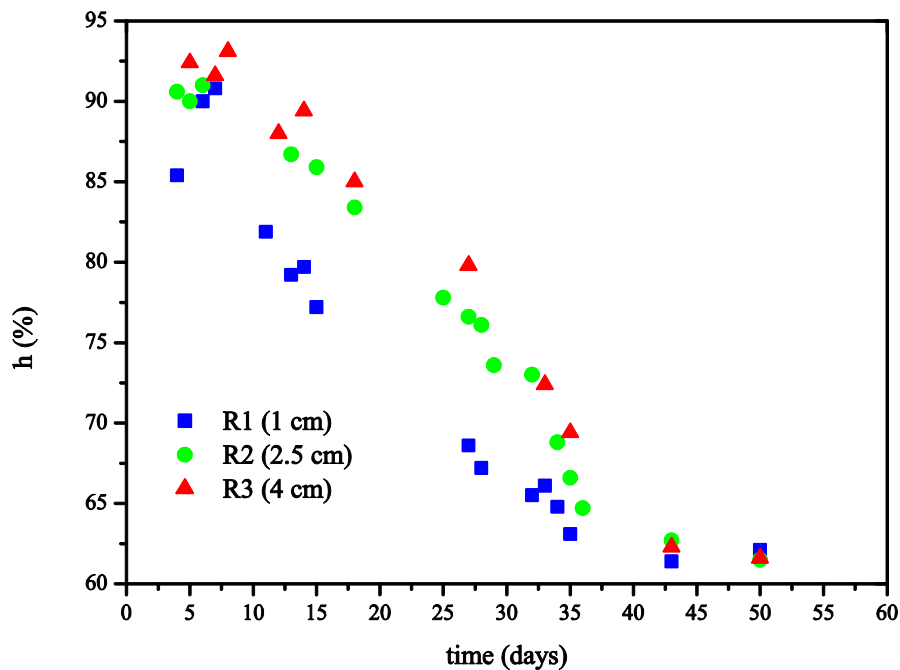


Figure 5-10 – Humidity over time - Specimen *HM.A* (time expressed since casting)

The first measured humidity value for the initial age (~ 2 days) was around 93%, and a higher value would be expected, since just a small parcel of the diffusion should have occurred. The primary possible explanation for this observation is the inaccuracy of the sensor for elevated humidity environments (Vaisala, 2004). Another possible reason for that, could be the elevated water evaporation, during the lime hydration during mortar preparation (Snow and Torney, 2014, Lawrence, 2006).

After the humidity monitoring test, the carbonation depth was also investigated. For this purpose, specimen *HM.A* was broken after 76 days from casting. The specimen presented a density $\sim 1850 \text{ kg/m}^3$, which was a lower value in comparison with the initial one ($\sim 2000 \text{ kg/m}^3$). With the application of phenolphthalein spray, the carbonation depth was measured with a caliper rule (see Figure 5-11). The specimen presented a low carbonation depth ~ 1.3 cm. It is interesting to remark that this very low depth of carbonation coincides with a period at which the entire specimen was already at moisture equilibrium with the surrounding

environment, showing that the humidity field is clearly evolving at a much faster pace than the carbonation field. A detailed analysis of this difference will be discussed in the next chapter.

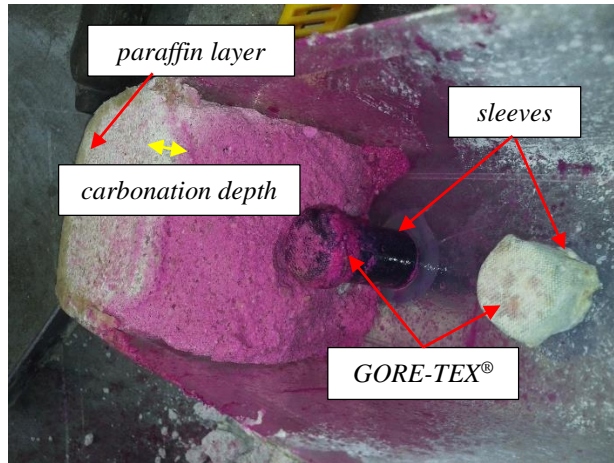


Figure 5-11 – Specimen *HM.A* adopted to study the humidity diffusion - after breaking

The results for the sealed specimens *HM.B* and *HM.C* are shown in Figure 5-9. For the sake of simplicity, and because the results for different depths were similar, for the sealed specimens the position of the probes are not indicated on the final results (see Figure 5-12).

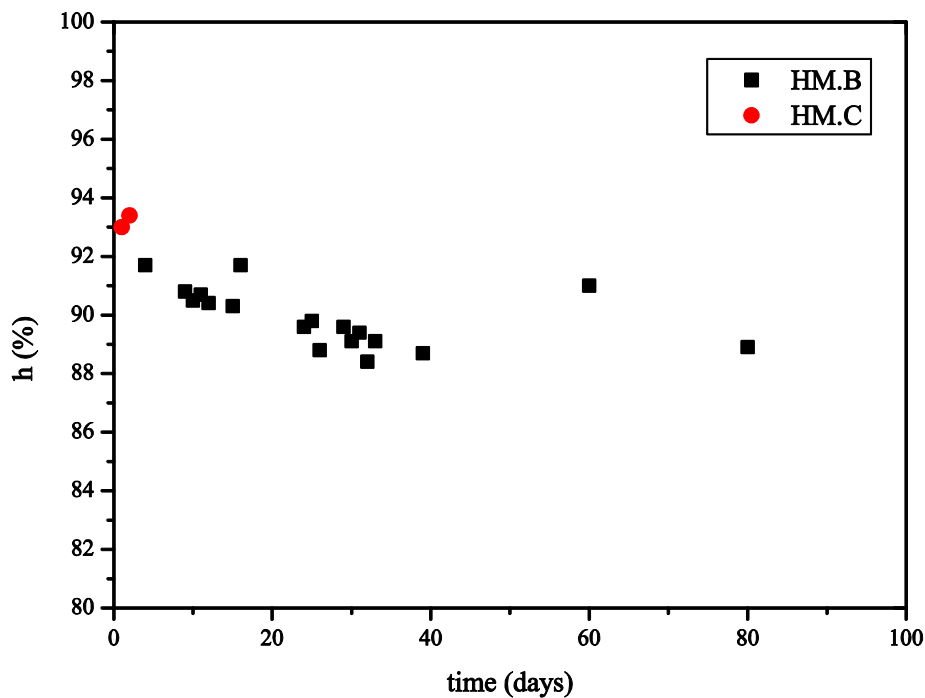


Figure 5-12 – Humidity over time in isolated specimens - self-desiccation (specimens *HM.B* and *HM.C*)

Firstly, with the purpose of analyze the trend, it is necessary to take into account that the adopted device used to measure the humidity was a *HM44* based on the changes in the capacitance of a thin polymer film as it absorbs water molecules (Vaisala, 2004). Thus, the small variations presented in Figure 5-12 could be merely related to variability of the sensor itself. However, looking at the behavior in the entire time interval of measurements, it is reasonable to assume that specimen *HM.B*, after the beginning of the measurements, presented a relatively small decrease of the *h* and the value stabilized around a constant value ~90%. The difference on the results for the two specimens was ~2%, for the initial ages. The objective of the second sealed specimen was to check the maximum value previously obtained. Therefore the test for *HM.C* was interrupted after 3 days. The initially measured values were around 92-93%, even for the sealed specimens. In an analogy with cementitious based materials measurements, a value closer to 100% would be expected (Kang *et al.*, 2012, Kim and Lee, 1999, Kim and Lee, 1998). The initial water evaporation due to the hydration process during casting and the sensor sensitivity can justify these results.

The humidity flux in cementitious material was numerically studied in Chapter 4. The obtained results demonstrated that, with different sizes of specimens simulated, the humidity presented distinct behavior. In view of such knowledge, another specimen simulating the 1D flux with a different geometry was cast to study the influence of the specimen size on the humidity profile. This specimen presented a cross section with dimensions of 9.5 cm × 9.5 cm and a thickness equal to 14.2 cm. Because of experimental problems during the test (damage in the mold later detected) and the unavailability of the humidity sensor in some ages, the test was interrupted and results were discarded. Due to experimental and time limitations, this trial could not be repeated. Therefore, subsequent research focused on the study of cylindrical specimens, as detailed in the next section.

5.5.3 *Cylindrical specimens*

This section presents information about the cylindrical specimens that were adopted to study the humidity flux, for which a summary is presented in Table 5-5. This geometry was intentionally adopted to reproduce axisymmetric conditions, meaning that paraffin layers were applied, in the top and bottom parts, to reduce the water flux in those regions. The cast cylinders had a diameter of ~6 cm and a height of ~12 cm.

For further information about casting conditions and mortar preparation, see Section 5.4.

Table 5-5 – Summary of cylindrical specimens for humidity diffusion tests

Test	Diameter (cm)	Thickness or height (cm)	Environment of exposure	Test ages (days)	Specimen	Amount of specimens	Specimens
humidity profile	~6	~12	standard chamber standard chamber (sealed)	continuous	3+1 (exposed + sealed)	4	<i>H-H60-A</i> <i>H-H60-B</i> <i>H-H60-C</i> <i>H-H60-D</i>

Regarding the mold, a system with a plastic net wrapped inside the polypropylene tube was adopted. Figure 5-13 illustrates, before the casting, the two pieces of the plastic tube that were bound together with adhesive tape. With the objective to keep the external tube's shape, the net was stretched and positioned around the internal diameter of the tube. The specimens were then placed in the climatic chambers and kept in this condition for about 5 hours.

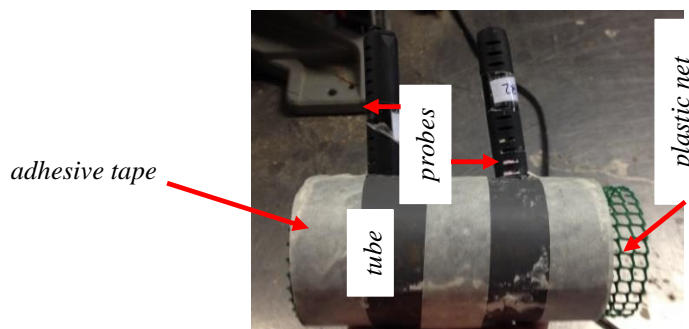


Figure 5-13 – Mold system adopted in the casting of cylindrical specimens - plastic net + tube

After the initial period, the specimens were partially demolded, the adhesive tape was removed (see Figure 5-13), releasing the two plastic tube pieces, and the external mold was removed. The plastic net was used to give the support for the aerial lime mortar on the initial phase, and paraffin layers were applied on the top and on the bottom of the cylinder (see Figure 5-14). In this way, the net was adopted during initial ages, because it allowed the contact mortar-environment (see Figure 5-14). This interaction was essential for the material drying and hardening, since it allowed the humidity flux and the carbonation process.

A general schematic representation of the process is shown in Figure 5-14. The plastic net was removed after a period of 24 hour after casting. After this period, the lateral surfaces of the cylinders were completely exposed to environmental conditions.

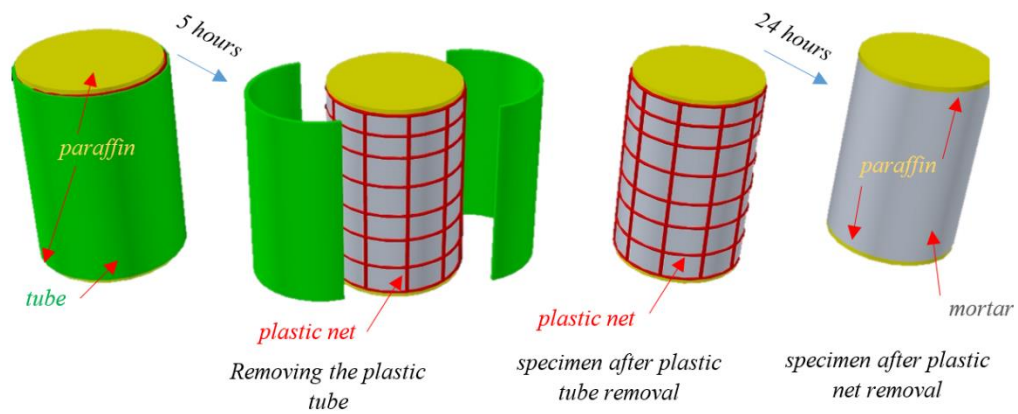


Figure 5-14 – Casting of cylindrical specimens - tube + plastic net

Regarding the sleeves used to study the diffusion process in cylinders, the same procedure to prepare them presented in the previous section was adopted (tubes + GORE-TEX[®] + hot glue). In terms of setup, two configurations were tested, first with the humidity probes on vertical position (see Figure 5-15), and, then, with tubes inserted horizontally (see Figure 5-16). These two configurations (Figure 5-15 and Figure 5-16) were tested with the objective to verify the consistency of the results, and also to check the possible influence of the adopted position for the probes. In summary, three cylinders were analyzed: *H-H60-A*, *H-H60-B* and *H-H60-C* (see Table 5-6).

Table 5-6 – Summary of cylindrical specimens

Specimen name	Probe	Probe positions	Detail
<i>H-H60-A</i>	inserted vertically	1.0 and 3.0 cm	Figure 5-15
<i>H-H60-B</i>	inserted horizontally	1.3 and 3.0 cm	Figure 5-16
<i>H-H60-C</i>	inserted horizontally	1.3 and 3.0 cm	Figure 5-16

Considering the given information, for the first specimen, the final configuration for *H-H60-A* can be seen in Figure 5-15. Two sleeves (*hp-vert-1* and *hp-vert-2*) were inserted vertically, and the top and the bottom of the specimen were sealed with a paraffin layer.

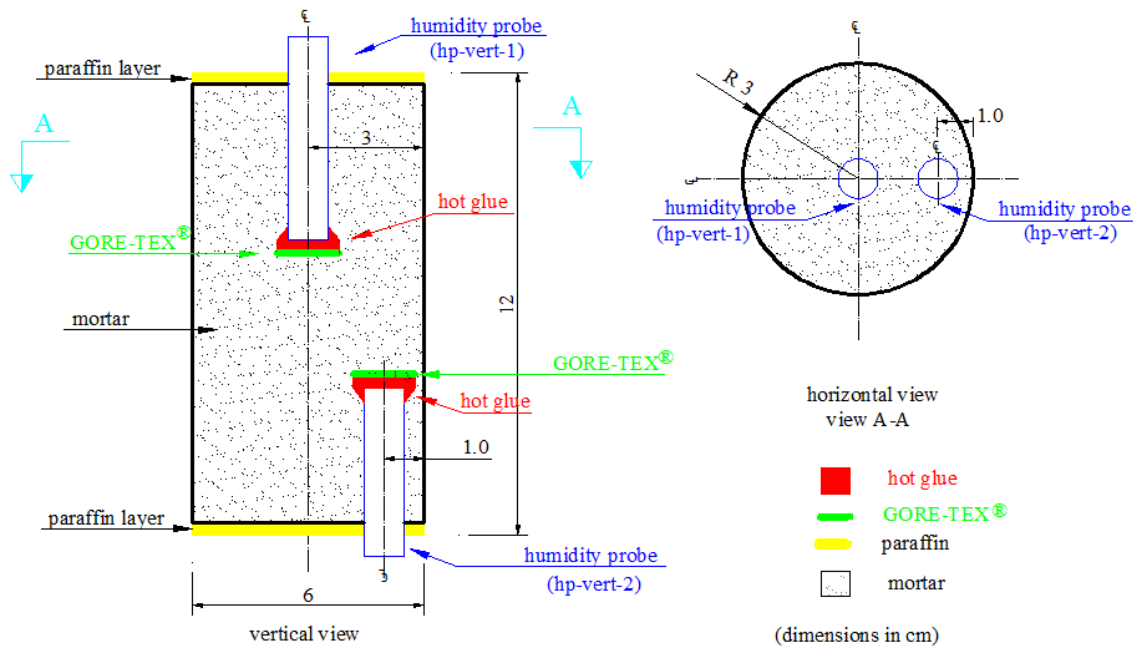


Figure 5-15 – Cylindrical specimen - humidity profile (vertical sleeves) (*H-H60-A*)

The final configuration for *H-H60-B* and *H-H60-C* can be seen in Figure 5-16. For this specimens two sleeves (*hp-hor-1* and *hp-hor-2*) were inserted horizontally. For these specimens, layers of paraffin were placed close to the external region of the cylinder, where the probes were inserted in the mortar, with the objective to reduce the possible liquid escape, as indicated in Figure 5-16 and Figure 5-17.

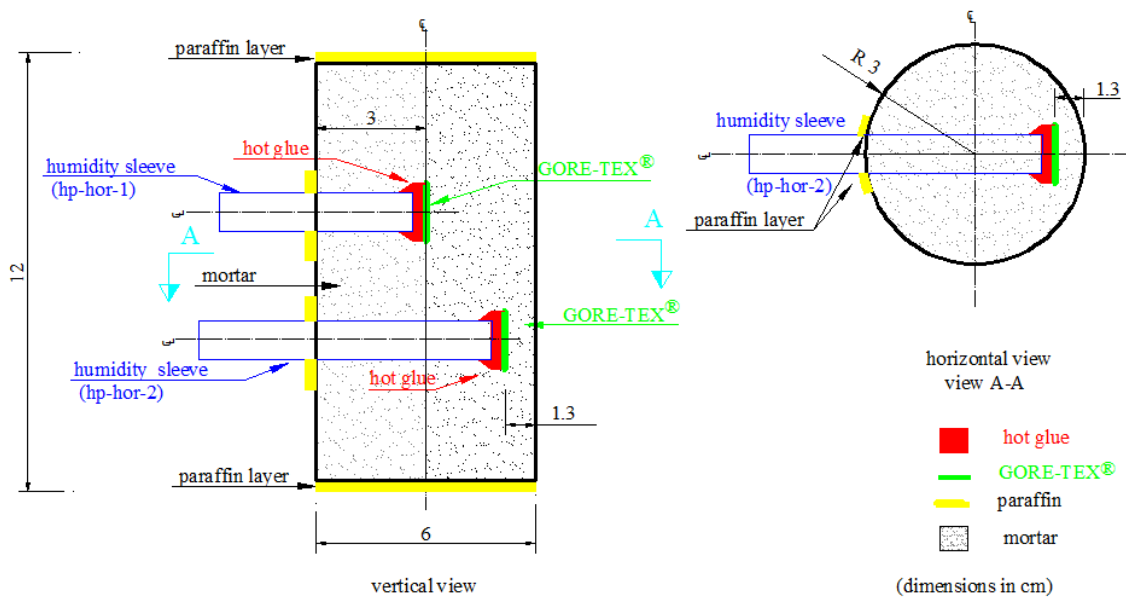


Figure 5-16 – Cylindrical specimen - humidity profile (horizontal sleeves) (*H-H60-B* and *H-H60-C*)

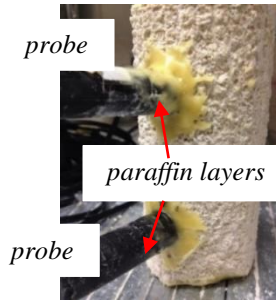


Figure 5-17 – Detail of sleeve and mortar interface in specimen *H-H60-B*, after the removal of the plastic net

The three studied cylinders (*H-H60-A*, *H-H60-B* and *H-H60-C*) presented similar humidity results over time for the same depth (*hp-hor-1* and *hp-vert-1*). A comparative graph with the data for the three tested cylinders for the probe inserted at 3 cm depth is presented in Figure 5-18.

Analyzing the data, the results for the three tested specimen (*H-H60-A*, *H-H60-B* and *H-H60-C*) showed reasonable coherence. At the same age, the maximum difference of the values measured was ~5%, around the eighth day (see Figure 5-18). The dispersion could be again also related to the sensor precision. Therefore, the results stress the feasibility of the experimental setup (at least from the repeatability point of view). Concerning the results for the two tested specimen with horizontal sleeves (*H-H60-B* and *H-H60-C*) for the depth of 1.3 cm (sleeve *hp-hor-2*), the data are shown in Figure 5-19.

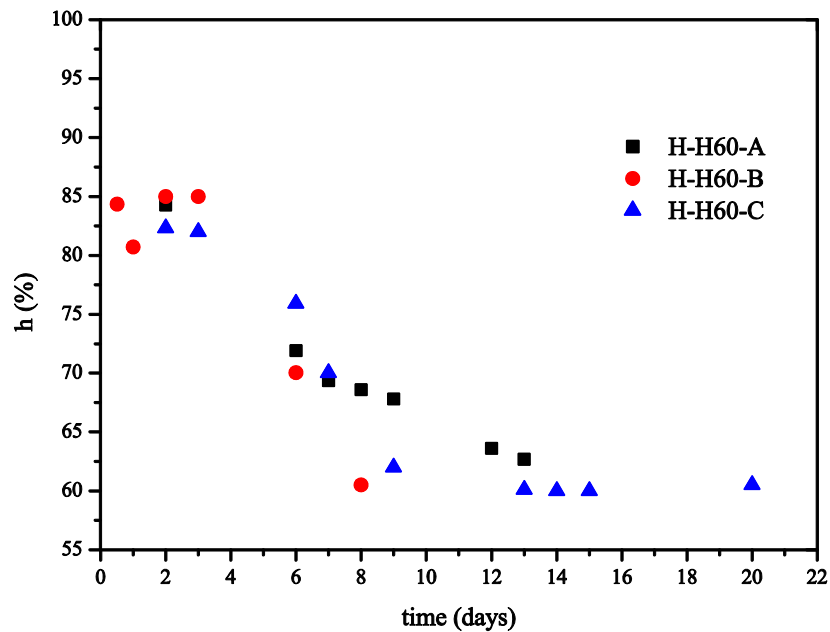


Figure 5-18 – Comparative results for humidity in cylindrical specimens *H-H60-A*, *H-H60-B* and *H-H60-C* (3 cm depth - *hp-hor-1* and *hp-vert-1*)

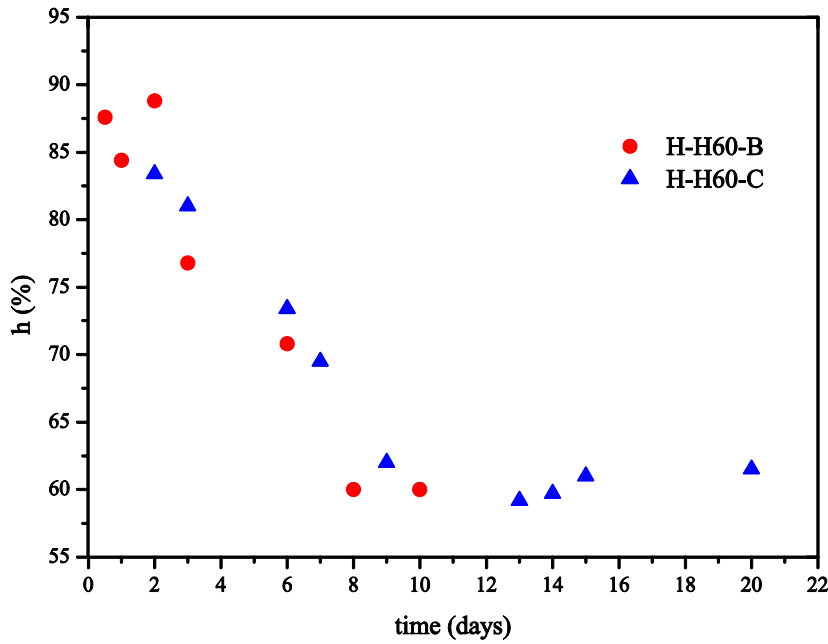


Figure 5-19 – Comparative results for humidity in cylindrical specimens *H-H60-B* and *H-H60-C* (1.3 cm depth, *hp-hor-2*), since the exposure

Considering the results from Figure 5-19, for the initial hours of monitoring, when just a small part of the diffusion happened, the measured values from specimen *H-H60-B* were ~90%. These values were quite similar to the previously measured humidity values for 1D condition with specimen *HM.A* (~93%). With the objective to illustrate the obtained results specifically for cylinder *H-H60-C*, the humidity values on the two measured depths are presented in Figure 5-20. In the second day for the two investigated depths, the measured values were ~83%, these values illustrated the fast humidity decreasing. In a comparative aspect, the values were smaller than the ones measured for two other molds for 1D condition (*HM.A*) for the same age ~90%. This result could be justified by the fact that, for this axisymmetric mold, the drying process occurred faster, because of the geometrical characteristics.

The data presented in Figure 5-20 showed that for the two different depths the humidity presented similar values, meaning that no relevant humidity gradient was measured during the test. This result was in coherence with the data presented in Figure 5-10, with *HM.A*.

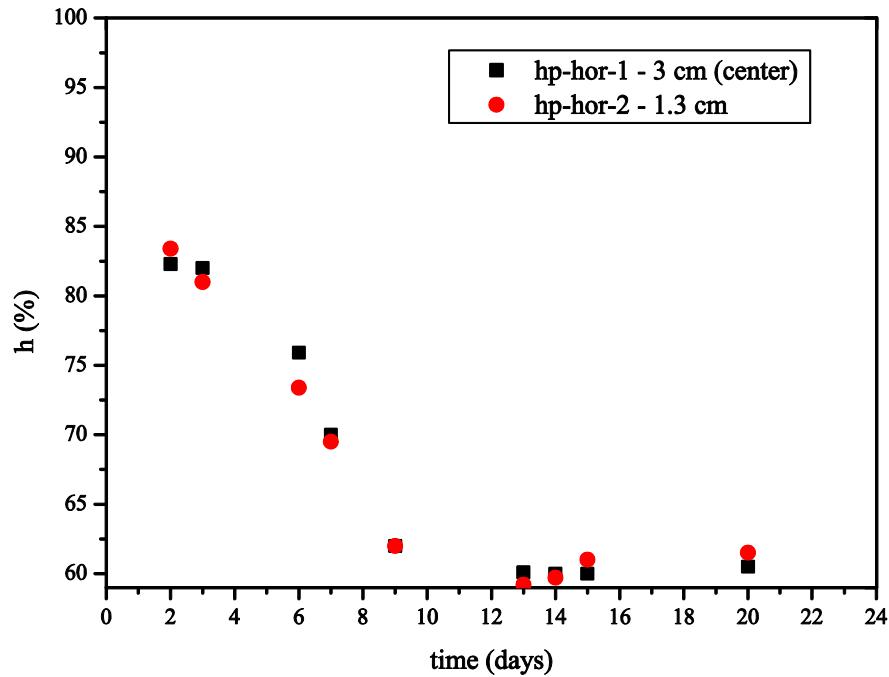


Figure 5-20 – Humidity in cylindrical specimens, *H-H60-C*, since the exposure

With the objective to study the relatively fast humidity decreasing and to validate a possible problem with data obtained from the Vaisala sensor (Vaisala, 2004), another device capable to measure the humidity was adopted. The *SHT75* (Sensorium, 2015) was used to measure the values for some intermediary ages, during the tests with *H-H60-B* and *H-H60-C*. The results obtained with the *SHT75* sensor (Sensorium, 2015) were similar with the data from the Vaisala equipment (Vaisala, 2004), with discrepancies ~2%.

In continuity with the experiments, the self-dissection was analyzed herein once more. The sealing method was done with the use of plastic tubes, paraffin and plastic bags. As previously adopted, two plastic tubes were used as sleeves. The tubes were inserted at two different depths (1.0 and 3 cm) in vertical position (a similar configuration of the sleeves may be seen in Figure 5-15). The humidity values for the two studied depths are shown in Figure 5-21. The presented results showed that the values for the two studied depths were consistent, with differences of less than ~2%. The results were in agreement with the data obtained on the previous tested specimens. The measured values related to humidity in the experiment proposed to investigate the self-consumption were ~90%, and this percentage was almost constant for the complete duration of the test, around 22 days.

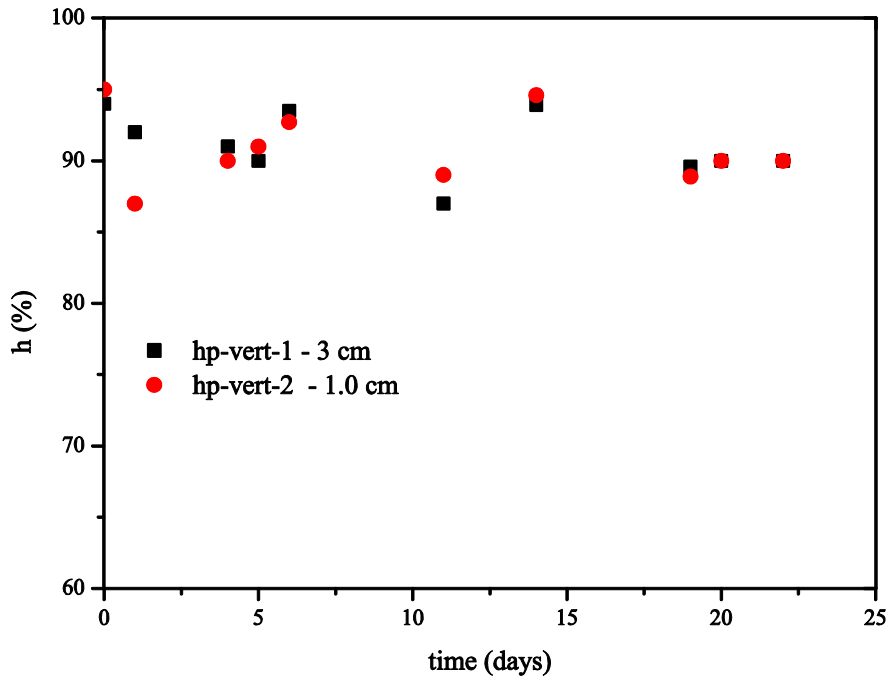


Figure 5-21 – Self- dissection measurement - cylindrical specimen (*H-H60-D*)

5.5.4 A comparative method to measure the humidity

This section presents a different configuration to investigate the humidity. This methodology was chosen to validate the previous method, with probes inside the mortar. The second adopted setup is schematically represented in Figure 5-22, and a similar experimental configuration was used by Nilsson (1980) to measure the humidity in concrete. The samples were extracted from the depth where the humidity was studied. The collected sample of mortar powder was placed inside a tube sealed on the bottom edge (step *II*). Subsequently, the humidity sensor was inserted inside the tube (step *III*), and then the top part of the device was sealed (step *IV*). The sealing process was done with plastic tape and hot glue.

The setup feasibility was tested using a sample of mortar collected from a specimen stored inside an environment with elevated humidity value ($\sim 90 \pm 10\%$). The sample was collected on the surface of the specimen, and, therefore, the humidity of the sample could be assumed similar to the environment ($\sim 90\%$). The sealed device with the sample inside was stored in the “*standard*” climatic chamber. Once the equilibrium humidity between the mortar and the air inside the tube was reached (after ~ 3 hours), the measured value coincided with the expectable 90% of the mortar, despite the fact that the environment around the test tube was at 60%. After the equilibrium (mortar/air inside the tube), the device could keep the mortar

isolated from the influence of external environment, as this test was done continuously for 24 hours.

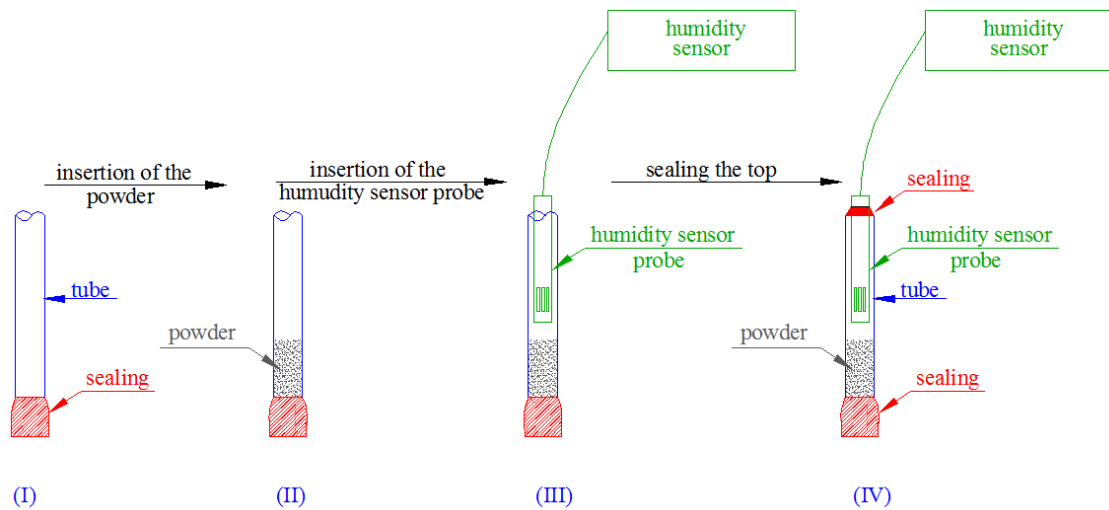


Figure 5-22 – Schematic representation of the adopted experimental setup

After this initial verification, mortar at 1.5 cm depth was collected from specimen *H-H60-B*, with 65 days of age. When the collected sample was placed inside the tube together with the humidity probe, the top part of the device was sealed. This second method showed results that were in agreement with the previous humidity monitoring method ($h_{mortar} \approx 60\%$). The setup is presented in Figure 5-22 and can be considered another method to verify the obtained results from the previous technique, with the insertion of sleeves inside the specimen.

6 EXPERIMENTAL PROGRAM FOR CARBONATION AND MECHANICAL PROPERTIES

6.1 Introduction

The present chapter aimed to extend the experimental work towards the evaluation of carbonation (Figure 6-1 a) and mechanical properties (Figure 6-1 b) of aerial lime. For this reason, the mortar mix defined in the previous chapter was again adopted. The knowledge of carbonation and the evolution of mechanical properties in mortar are considered of relevance for the material study and for obtaining parameters for multi-physics studies. Regarding the carbonation process, which is the first main subject of this chapter, two different techniques were adopted, namely the phenolphthalein indicator and TGA (Figure 6-1 a). The investigation of mechanical properties adopted classical laboratorial techniques for determination of elastic modulus and compressive strength (Figure 6-1 b).

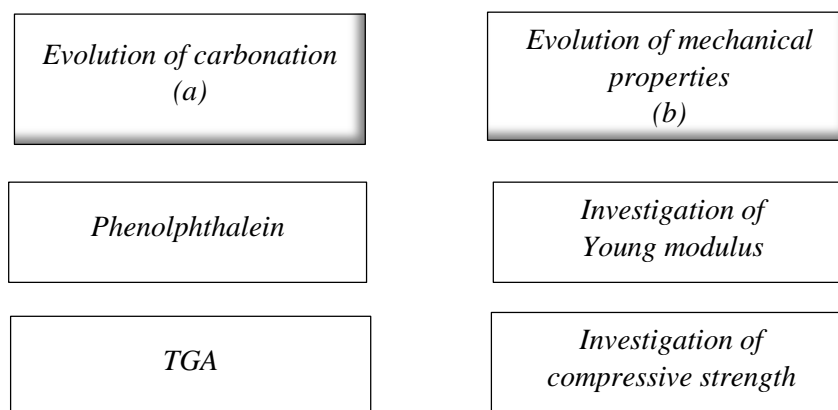


Figure 6-1 – Schematic representation of the studied phenomena and the adopted techniques

The experiments were grouped by similarity and do not necessarily follow a chronological order. Specifically for the study of the evolution of the carbonation process, three main effects were investigated: *(i)* time; *(ii)* environmental conditions; *(iii)* influence of the size of the specimens. A general view regarding the experiments related to carbonation can be seen in Figure 6-2, with the indication of the sections in this chapter where the phenomenon was studied.

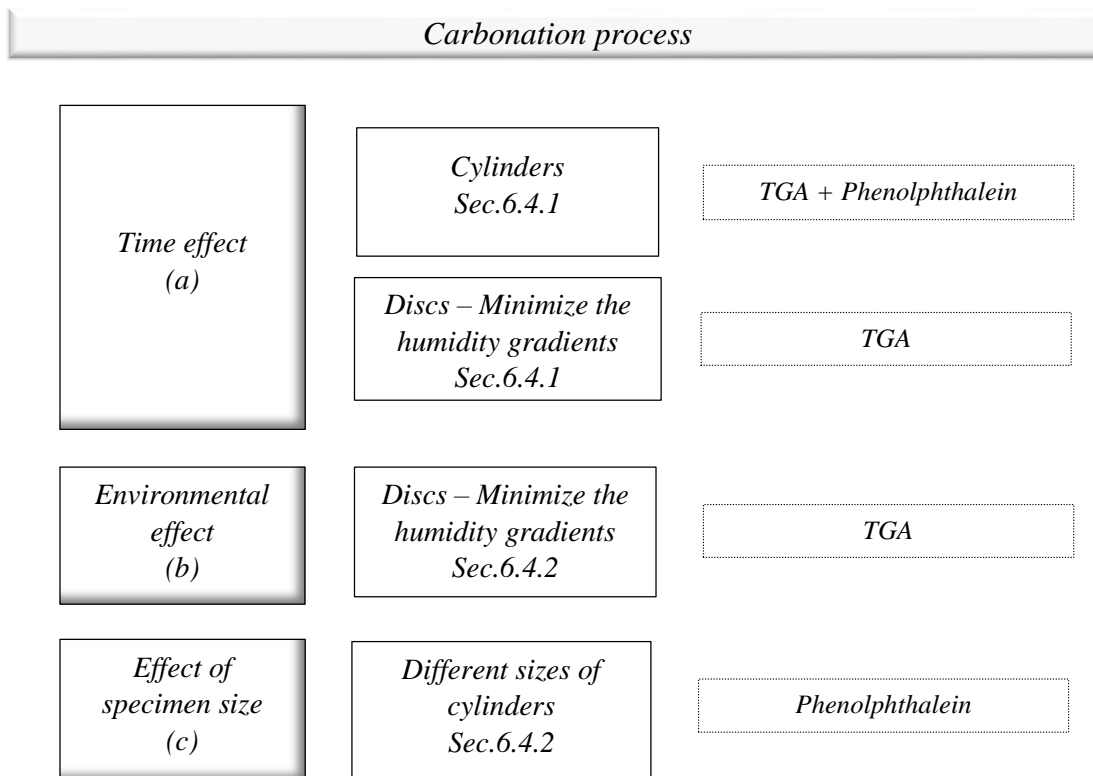


Figure 6-2 – Schematic representation of the experiments regarding the study of carbonation

The carbonation process was measured with phenolphthalein to study the time and size of the specimen effects (Figure 6-2 a and c). With the objective to characterize the material composition and the carbonation process over time and throughout the depth, samples were collected from a transversal section of a cylinder under test at three different depths. The carbonation process was also investigated with TGA analysis in small discs. The first part of this study focused in the evolution of carbonation process over time in specimens with minimized influence of the humidity gradient, thus, justifying the reduced thickness (see Figure 6-2 a). Later, in the second part of the experimental work, the focus was to assess as directly as possible the effects of the environmental conditions on the material (see Figure 6-2 b). The sizes of specimens were equal to the previous discs (see Figure 6-2 b).

Concerning the evolution of mechanical properties over time, the elastic modulus (or e-modulus) evolution was investigated using cylindrical specimens, while for compressive strength, cubes were adopted (see Figure 6-3). In continuity with the integrated experimental work, for the investigation of the elastic modulus, cylinders with the same dimensions as the specimens previously used in the humidity tests and for the study of the time effect in the

carbonation were adopted. The e-modulus study was divided in two parts. An initial one with a preliminary specimen's configuration and curing condition (*part A*, see Figure 6-3 a), and a second with a new setup (*part B*, see Figure 6-3 b). In the second part, the environmental effect was also studied with cylinders stored in a climatic chamber with elevated humidity. For the study of compressive strength, cubes were tested at four different ages in the usual environmental conditions, and at one age in a high humidity chamber (see Figure 6-3 c), to compare with the specimens stored in standard condition.

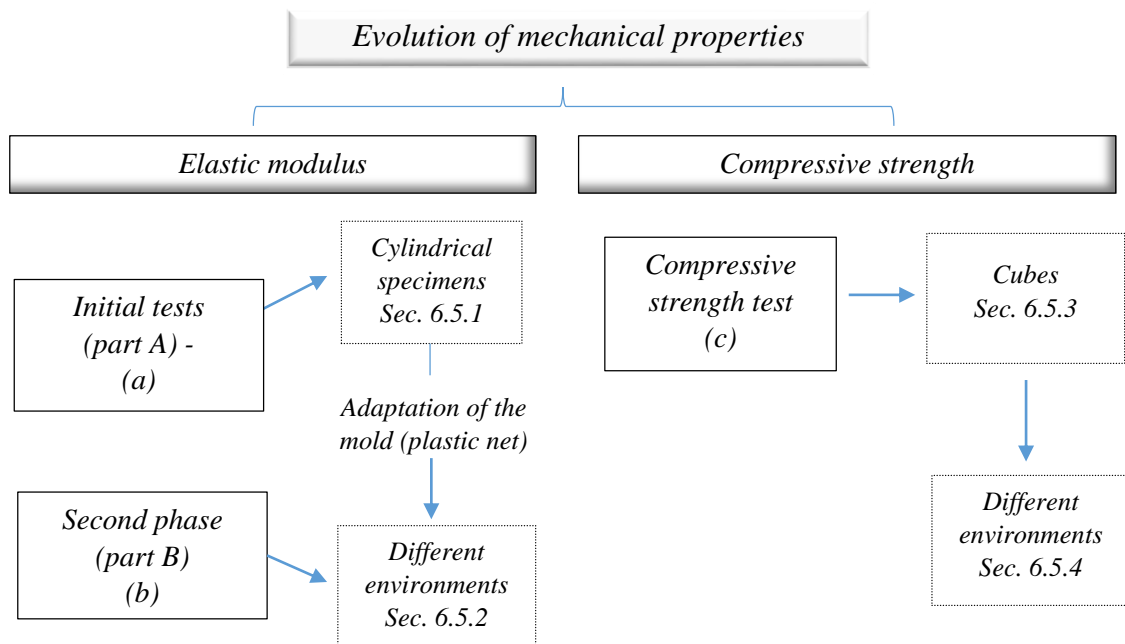


Figure 6-3 – Schematic representation of experiments related to the evolution of mechanical properties

6.2 Specimens types and initial curing conditions

This section describes the types of specimens and initial curing conditions adopted. The mixture and casting procedures followed the previously mentioned characteristics in Section 5.3, with exception of the discs specimens. For these specimens, the density parameter was not controlled. Different times of curing and exposure conditions were adopted, according to the type of specimen studied. A total of four different curing conditions were used, which are schematically shown in Figure 6-4. They were classified as: *ICD*, *ICC*, *IC1* and *IC2*. These conditions were achieved within the learning process discussed before.

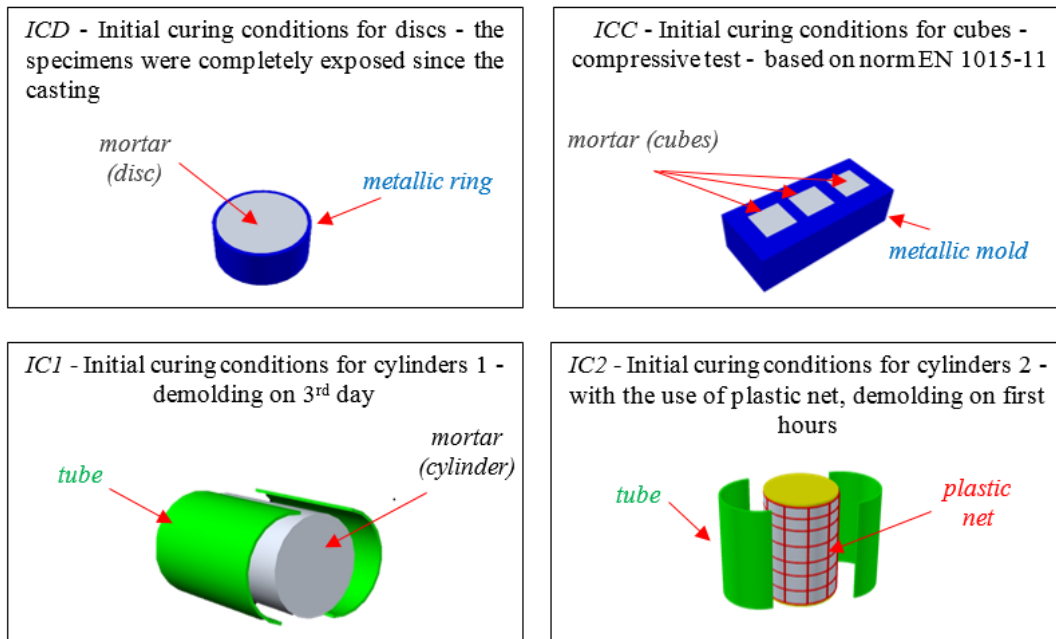


Figure 6-4 – Brief introduction for the different curing conditions and specimens

After this summary introduction, the description with more details for the different initial curing conditions are following presented.

ICD - Initial curing conditions for discs - Discs specimens used for TGA analyses were cast in a little light steel ring mold, which allowed the material to be exposed to environment since the casting, with exception of one specimen that was intentionally sealed. As the aerial lime mortar reacts with the CO_2 , this procedure guarantees the start of the reactions from the curing initiation.

ICC - Initial curing conditions for cubes - For the compressive test, the initial curing procedure according to the norm EN 1015-11 (CEN, 1999b) was adapted: for 5 days, the specimens were molded and stored in a polyethylene bag, simulating an isolated environment with high humidity level (as suggested for the standard, 95% *h*) (see Figure 6-5), then for two days the cubes were exposed to the climatic chamber, but still in the metallic mold. Finally, they were then demolded and kept at the climatic chamber until testing. It is noted that, after the first seven days, the specimens were kept suspended to allow the exposure of all the surfaces during the curing time.



Figure 6-5 – Opening process in the cubic specimens (polyethylene bag)

ICI - Initial curing conditions for cylinders 1 - These cylinders were stored inside the plastic mold and their top and bottom surfaces were exposed during the initial ages. The tube had an internal diameter of ~6 cm and ~12 cm of height. It was cut longitudinally into two pieces to facilitate the demolding process. The specimens were completely demolded with the removal of plastic tube on the 3rd day. This time was necessary for the cylinders to be self-standing without any mold on vertical position and to reduce the damage during the demolding process. In fact, previous attempts to demold at the age of 1 day have resulted in extensive damage to the specimen itself. A schematic view with *ICI* can be seen in Figure 6-6.

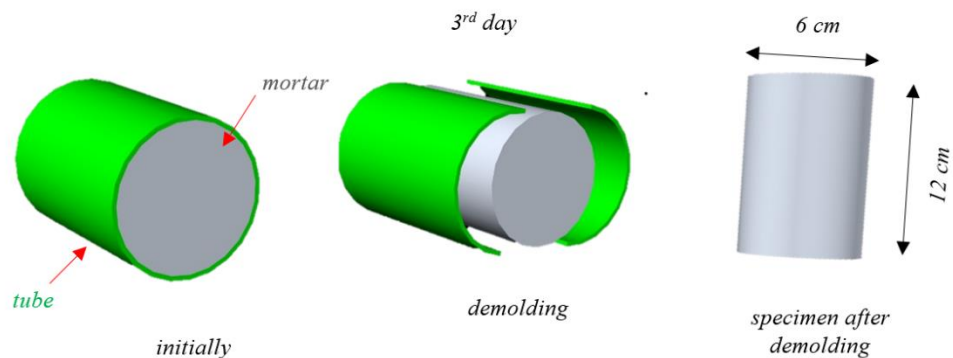


Figure 6-6 – Schematic representation of initial curing conditions for cylinders - *ICI*

The effectiveness of the form in sealing the specimen was assessed through breaking a sample at the age of demolding and performing a phenolphthalein test. It was observed that the carbonated depth at this age and exposure situation was negligible (less than 1 mm). This process of initial curing was primarily adopted for the cylinders for the elastic modulus test in “*part A*”, and for the cylinders used to investigate the effect of the size of the specimen on the carbonation process. This curing procedure was in fact an adaptation of the recommendation presented in EN 1015-11 (CEN, 1999b) for cubic specimens.

IC2 - Initial curing conditions for cylinders 2 - This initial curing condition corresponds to improvements made concerning *IC1*, Details of *IC2* have already been presented in Section 5.5.3. A schematic view presenting the cylinders cast to study the carbonation with TGA profile and for the monitoring of the evolution of the elastic modulus (*part B*), after the plastic net removal is presented in Figure 6-7.



Figure 6-7 – Storage of cylinders (TGA + elastic modulus specimens in *part B*)

- *Environments*

Three different environmental conditions were adopted to study their influence on the results, as summarized in Table 6-1 and detailed further in the text.

Table 6-1 – Different environmental conditions

Name	<i>h</i> (%)	[CO ₂]	Temperature (°C)
<i>standard</i>	60±5	ambient (~0.035%)	20±2
<i>humid</i>	90±10	ambient with low ventilation (~0.05%)	not controlled
<i>high CO₂</i>	60±5	4%	20±2

The first environment was termed as “*standard*” ($h \approx 60 \pm 5\%$, $T \approx 20 \pm 2$ °C and usual CO₂ concentration, as stated in Chapter 5). The second environment was named as “*humid*” ($h \approx 90\%$, low ventilation and uncontrolled temperature). Finally, the third environmental condition was denominated as “*high CO₂*” ($h \approx 60 \pm 5\%$, $T \approx 20 \pm 2$ °C and [CO₂] $\approx 4\%$) (Guimarães, 2014).

Considering the above information, Table 6-2 presents the overall summary of tests, the quantity of specimens, the testing ages, and the environmental conditions adopted in each

experiment. Further information and the results of the tests will be given in the subsequent sections.

Table 6-2 – Summary of specimens, the tests and the curing conditions

Test	Specimen shape	Diameter or side (mm)	Thickness or height (mm)	Environment of exposure	Test ages (days)	Specimen per environment	Amount of specimens
Carbonation time effect phenolphthalein + TGA (IC2)	cylinder	60	120	standard chamber	1 7 14 69	5	5
Carbonation time effect TGA (ICD)	disc	38	8	standard chamber sealed	0 3 7 20 40 47	3 + 1 (standard + isolated)	4
Carbonation environmental effect TGA (ICD)	disc	38	8	wet chamber standard chamber high CO ₂ concentration chamber	1 4 7 14 21 28	2	6
Carbonation specimen size effect phenolphthalein (IC1)	cylinder	40 , 60, 70, 90, 150	80, 120, 140, 180, 150	standard	10 21 90	15	15
E-modulus (IC1)	cylinder	60	120	standard chamber	2 - 38	3	17
E-modulus (part B) (IC2)	cylinder (Part B)	60	120	wet chamber standard chamber	8 15 22	3	6
compressive strength (ICC)	cube	50	50 mm	standard chamber	14 28 120 140	24	24
compressive strength (part B) (ICC)	cube (Part B)	50	50 mm	wet chamber standard chamber	28	3	6
TOTAL				3	Up to 140	-	83

6.3 TGA: Data analysis and experimental methodology

6.3.1 General information

In this section information about the TGA data analysis and the specificities regarding the establishment of the experimental methodology are presented. A brief discussion begins with the reference to the works by Lawrence *et al.* (2006a) and Lawrence (2006) in aerial lime, in which the authors applied a maximum temperature of 700 °C in TGA analysis. With this temperature, Lawrence *et al.* (2006a) could only perform direct assessment of the amount Ca(OH)_2 contained in the samples, as only the dehydroxylation process could be measured. According to the authors, the carbonation degree could be calculated by deducing the amount of carbonated material from the uncarbonated part. Other forms to calculate the reaction degree, not in terms of CaCO_3 , but with the consideration of different theoretical aspects, including the CO_2 concentration may be found in Chang and Chen (2006) and Matsushita *et al.* (2000).

In this thesis, the adopted range of temperature for TGA testing was wide enough to allow the evaluation of both dehydroxylation and decarboxylation phenomena. From the TGA results, the masses of Ca(OH)_2 and CaCO_3 were calculated considering the equations presented in Section 2.5.5. From these results, the formulation to calculate the reaction degree was developed.

In terms of establishment of experimental methodology for TGA testing, efforts are initially made on the influence of the heating rate on the test results, and then considerations are made about sampling issues.

6.3.2 Data analysis

Since the numerical modeling adopted herein was based in the work presented by Ferretti and Bažant (2006a), and the experimental data aimed also to support the simulations, the formula adopted to calculate the carbonation degree, considered the definition of R presented by these authors (see Eq. 3.36). The dependence of the volume of the material in the definition can be disregarded, since it appears in both terms of the equation (numerator and denominator), and it was assumed constant, resulting in the simplified relation for the masses of CaCO_3 and CaCO_{3Max} :

$$R = \frac{Mass_{CaCO_3}}{Mass_{CaCO_3_{Max}}} \quad 6.1$$

where: R is the carbonation degree (%).

Even if, in general, the study of chemical reactions is usually done in terms of moles (Kuriyan *et al.*, 2012), the definition presented by (Ferretti and Bažant, 2006a) and the results from TGA were expressed in terms of mass. Therefore, the formulation adopted was expressed in terms of mass, as also done in Arizzi and Cultrone (2012).

An aspect also to be considered is related with the fact that the TGA tests are typically done in relatively small samples (Villain *et al.*, 2007, Mydin, 2013), and therefore some intrinsic errors can be associated to the heterogeneity of mortar or concrete (Valek *et al.*, 2012, Rogerio-Candelera *et al.*, 2013, Villain *et al.*, 2007). Bearing in mind this information, R was estimated with the TGA results for different ages (and different samples). Both the numerator and denominator of the equation 6.1 needed to be updated for each analysis. This method was also adopted because the raw lime presented calcium carbonate in its composition, and formulations that just consider the dehydroxylation range during the test (Arizzi and Cultrone, 2012, Lawrence, 2006, Lawrence *et al.*, 2006b) could not capture the phenomenon.

In stoichiometric terms, one mole of $Ca(OH)_2$, when completely carbonated, produces one mole of $CaCO_3$ (Kelter *et al.*, 2008, Atkins, 2010). From Eq. 6.1, the term $Mass_{CaCO_3_{Max}}$ can be calculated, converting the mass of $Ca(OH)_2$ to $CaCO_3$ by the consideration of the respective molar masses (Kotz *et al.*, 2009), and the equation for R can be rewritten as:

$$R = \frac{Mass_{CaCO_3}}{Mass_{CaCO_3} + \left(Mass_{Ca(OH)_2} \right) \times \left(\frac{Molar\ mass_{CaCO_3}}{Molar\ mass_{Ca(OH)_2}} \right)} \quad 6.2$$

where: $Mass_{Ca(OH)_2}$ is the measured calcium hydroxide weight (mg) and $Mass_{CaCO_3}$ is the measured calcium carbonate weight (mg), $Molar\ Mass_{CaCO_3}$ is the molar mass of $CaCO_3 \approx 100$ g/mol, and $Molar\ Mass_{Ca(OH)_2}$ is the molar mass of $Ca(OH)_2 \approx 74$ g/mol (Atkins, 2010, Atkins and de Paula, 2014).

The conversion of Ca(OH)_2 to CaCO_3 proceeds slowly (Lieth, 2013, Cizer *et al.*, 2006, Lackner, 2002) and is usually incomplete (Al-Bashaireh, 2008, Daniele and Taglieri, 2015, Montes-Hernandez *et al.*, 2012, Fernandezbertos *et al.*, 2004, Rouchon *et al.*, 2013). The formation of a protective carbonate layer around the reacting particles can explain the incomplete carbonation under isothermal conditions (Montes-Hernandez *et al.*, 2012, Van Balen, 2005, Montes-Hernandez *et al.*, 2010a, Montes-Hernandez *et al.*, 2010b), and usually a percentage smaller than 80% of the total reaction occurs (Montes-Hernandez *et al.*, 2012, Montes-Hernandez *et al.*, 2010a, Montes-Hernandez *et al.*, 2010b).

The normalization of the reaction was done with the above information. The value of R for each test was divided by R_{maximum} (the maximum value of R for each group type of experiments) and this was denominated as $R_{\text{normalized}}$, as shown in Eq. 6.3:

$$R_{\text{normalized}} = \frac{R}{R_{\text{max}}} \quad 6.3$$

where: R_{max} is the maximum value of R for each group of experiments, R is the reaction degree measured in each test, and $R_{\text{normalized}}$ is the normalized reaction degree.

This normalization process aimed to correct the incomplete conversion, and also to allow the comparison of experimental data with the numerical results from the model presented by Ferretti and Bažant (2006a), which assume a R value that can reach 1.

6.3.3 Experimental methodology

This section presents the two main tests regarding the establishment of an experimental methodology for TGA analyses. For all the TGA tests, the procedures were done in an Argon atmosphere, with a temperature increase rate of 10 °C/min, except for the tests that investigate the influence of this parameter in the results. The TGA equipment presented in Section 5.2 was adopted. The maximum temperatures during the TGA tests were 1000 or 1100 °C, as, in some experiments, the lower temperature value (1000 °C) was adopted for simplicity and for faster tests. No significant alteration on the results was observed, because those values are out of the ranges of dehydroxylation/decarboxylation processes.

The influence of the temperature increase rate was assessed, as seven TGA tests were done with values from 5-20 °C/min (5, 7.5 (2×), 10 (2×), 15, 20), with temperatures varying between 20 to 1000 °C. The samples were collected using an existing aged aerial lime mortar specimen and they were taken from the surface of the specimen cast 42 days before the test. The extraction was done with a metallic device with a slender tip to facilitate the material extraction, which was marked as to allow extractions up to depths of 2 mm, Figure 6-8 illustrates the sampling process in disc specimen, which was done adjacent to the specimen surface. A similar procedure was also adopted for the cylindrical specimens.

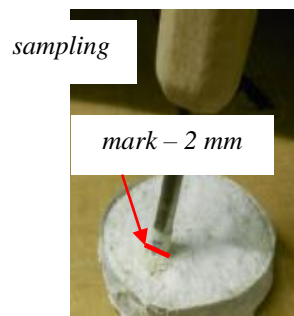


Figure 6-8 – Sampling process

Concerning the experiments with the objective to test the influence of the temperature increase rate on the final results, the weight of each sample is presented in Table 6-3.

Table 6-3 - Amount of tested material at each sample according with the temperature increase rate

Temp. increase rate (°C)	Amount of tested material (mg)
5	64.73
7.5	35.43
7.5 b	50.56
10	47.40
10 b	52.37
15	50.17
20	59.08

The results in terms of normalized weight are shown in Figure 6-9. The adopted rates of temperature increase was similar to the values used by different authors (see Table 2-8).

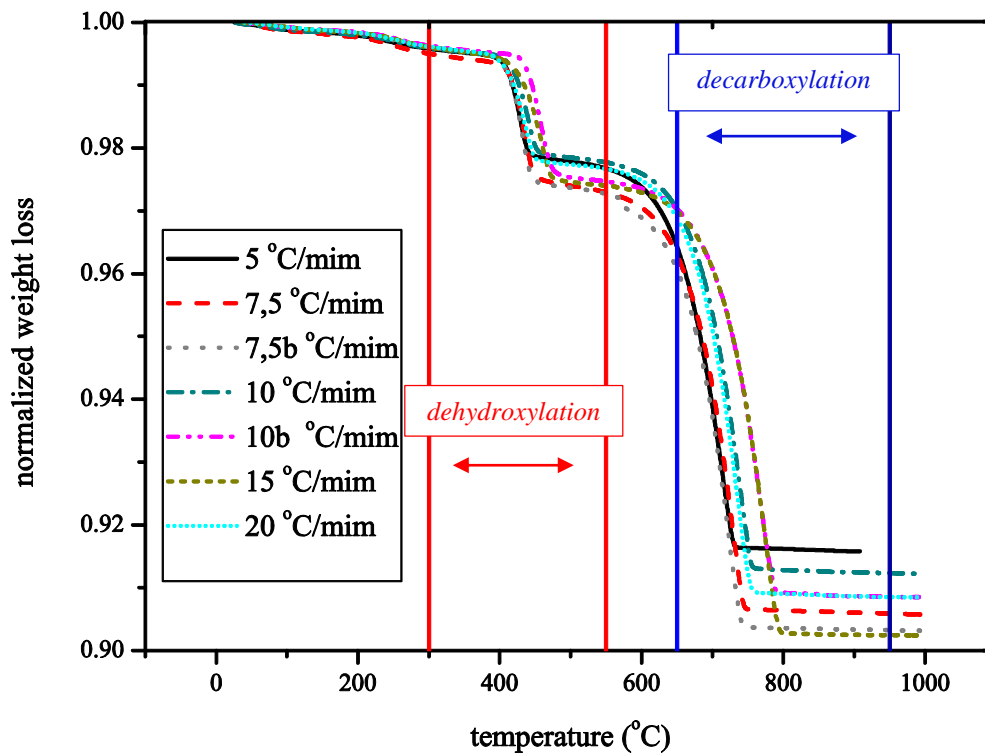


Figure 6-9 – Comparative results, normalized weight vs. temperature - different temperature increase rates - TGA

The curves obtained for different temperature increase rates presented similar results. The data shown in Figure 6-9, demonstrated that for the tested ratios, the final results did not present significant influence of this testing parameter. In terms of reaction degree, the maximum difference of the values was ~5% (for the formulation used to calculate the R , see Eq. 6.2). From these observations, a heating rate of 10 °C/min (an intermediate value) was chosen as standard for the rest of the experiments in this research work. This value was chosen in order to increase the results reliability, even the adoption of higher value would reduce the testing duration. Similar conclusions were obtained by Lawrence *et al.* (2006b), nevertheless the authors adopted a temperature increase rate of 50 °C/min.

Another relevant topic to investigate at this stage was related to accuracy of TGA, according to the representativeness of the samples. Therefore, the influence of the sampling was investigated next. For this study, TGA tests were performed on three samples ($T.A$, $T.B$ and $T.C$) collected from the same mortar specimen at the same age, at 20 days, and with the same sampling procedure. The sampling was done on the surface of the disc. The tested samples

had respectively the initial mass of 54.20 mg (*T.A*), 85.69 mg (*T.B*) and 67.92 mg (*T.C*). The three samples were tested in the range 20-1100 °C, and the results are shown in Figure 6-10.

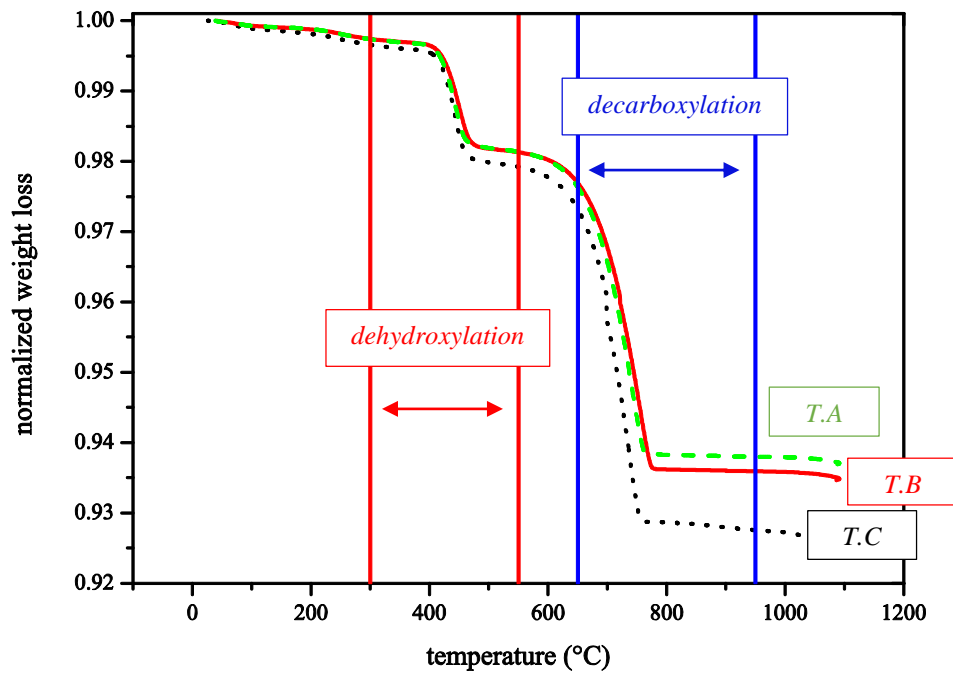


Figure 6-10 – Comparison between three TGA tests - normalized weight vs. temperature (samples collected after 20 days)

The scattering of results could be considered acceptable, since it presented relatively low dispersion in terms of reaction degrees, ~3% (for the formulation used to calculate the *R*, see Eq. 6.2) the values of *R* respectively for *T.A*, *T.B* and *T.C* were respectively ~58%, ~60% and ~61%. This information allowed considering that the sampling process had low influence on the results.

Since the verifications of the influence of the temperature increase rate and the sampling demonstrated to have small influence on the final results, the experimental methodology, in terms of TGA tests, was then considered as fully defined for the purpose of this research.

In order to study the TGA data, the previous results regarding the raw materials compositions should also be mentioned (see Section 5.2.3). The weight loss for the adopted sand composition was smaller than 0.2% of the total weight, in this sense, the influence of the aggregates on the TGA for the mortar, for the adopted mix proportion (1:3) could be disregarded. For the raw lime, it presented an initial CaCO₃ percentage ~11.8%, and this can affect the initial carbonation degree as previously discussed in Section 5.2.3.

6.4 Testing program for carbonation process

6.4.1 Introduction

In this section the testing program for the study of the carbonation process is described. Two (TGA and phenolphthalein) methods to evaluate the carbonation were adopted, and different effects (time, size of the specimens and environmental) were evaluated.

6.4.2 Time effect

The time effect in the evolution of carbonation process on aerial mortar was investigated and is reported in this section. Two different methods to evaluate the phenomenon were applied: phenolphthalein indicator and thermogravimetric analyses. The objective herein was to measure the carbonation and its evolution over time, and also to compare the results from the two methods. For such purpose, an experiment with similarities to the one performed by Lawrence (2006) was done (see also Section 2.5.5).

Herein, the specimens adopted are initially described, followed by the description of results obtained through the phenolphthalein indicator, as well as TGA analyses. A comparison between the two methods, particularly their coherence, is ultimately done in this section.

- *Specimens for phenolphthalein and TGA analyses*

This sub-section presents the procedure and the main information about the specimens adopted to study the carbonation with phenolphthalein spray, together with the comparative TGA profiles. The work aimed to study experimentally different fields and cylinders with the same dimension as presented in Section 5.5.3 were adopted. For each age, the phenolphthalein was sprayed in the broken section. For TGA experiments at each age, three depths were analyzed. The number of samples for each section was associated with experimental limitations, namely the cost inherent to the TGA tests. The chosen section for sampling was located at an intermediary distance between the top and bottom of the specimen, at 6 cm. For this purpose, five specimens were cast (*TGA_H60_1*; *TGA_H60_2*; *TGA_H60_3*; *TGA_H60_4* and *TGA_H60_5*) and the use one specimen per date of test was intended. However, during the course of the experimental program, some of the specimens

presented discrepant densities. In order to preserve the homogeneity of densities in a range up to 5% from the average value, those specimens were discarded (*TGA_H60_3* and *TGA_H60_4*). The densities of the specimens used during the tests are shown in Table 6-4.

Table 6-4 – Density of the specimens

Specimen	Density (kg/m ³)
<i>TGA_H60_1</i>	1893
<i>TGA_H60_2</i>	2019
<i>TGA_H60_5</i>	1954

Different heights of transverse section had to be adopted in the last two sampling procedures. Specimen *TGA_H60_5* was sectioned in half of its height, at ~6 cm depth for the testing age of 14 days. One piece was used in the sampling, while the other one had the sectioned side sealed with paraffin and was kept stored for later analysis, as Figure 6-11 shows.

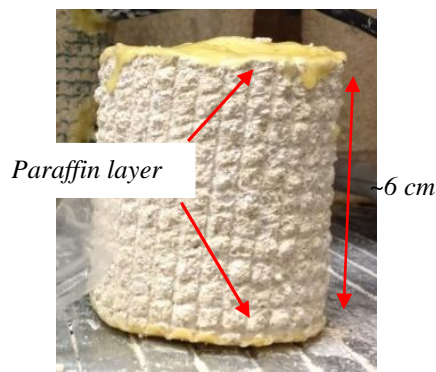


Figure 6-11 - Specimen *TGA_H60_5* after sectioning

For the age of 69 days, the same procedure was conducted, and consequently the sampling occurred at the height of ~3 cm, half of the specimen height (see Figure 6-11). The summary of the specimens used in each age is presented in Table 6-5.

Table 6-5 – Specimen adopted in each age



Specimen	Tested age (days)
TGA_H60_1	1
TGA_H60_2	7
TGA_H60_5	14 and 69

- *Phenolphthalein*

This section presents the results regarding the carbonation measurements with the phenolphthalein indicator. Phenolphthalein in ethanol solution (RILEM, 1988) was sprayed on the fresh-cut interior surfaces of mortar specimens, at different ages. Observations regarding the carbonation depth started at the age of 2 days from casting (see Table 6-6). The investigation of carbonation depth extends to 69 days. After the phenolphthalein spray, the carbonation depth was measured with a caliper rule.

During the casting process, inaccuracies of the molds induced some dispersions on the values of diameters for the different cylinders presented as in Table 6-6. The results in Table 6-6 show the evolution of the carbonation process from the second up to the sixty-ninth day. For the first age, practically no carbonation could be detected, while for the last measurement approximately 12 mm was already carbonated.

Table 6-6 – Results of phenolphthalein staining (specimens stored inside the “standard” chamber)

Specimen	Age (days)	Diameter (mm)	Uncarbonated diameter (mm)	Carbonated thickness (mm)	Aspect
TGA_H60_1	2	54	54	~ 0	
TGA_H60_2	7	56	52	2	


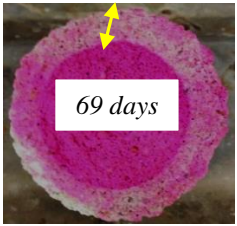
Specimen	Age (days)	Diameter (mm)	Uncarbonated diameter (mm)	Carbonated thickness (mm)	Aspect
TGA_H60_5	14	60	50	5	
TGA_H60_5	69	64	40	12	

Figure 6-12 presents the carbonation depth evolution, which seems to follow a parabolic format. The parabolic format of the curve is typically cited in literature for concrete (Parrott and Killoh, 1989, Parrott, 1994). For aerial lime, as presented in Table 2-7, Lawrence (2006), obtained values ~3 cm for 14 days, ~5 cm for 28 days and 9–14.5 for 90 days. The values obtained in the present work were in agreement with this data.

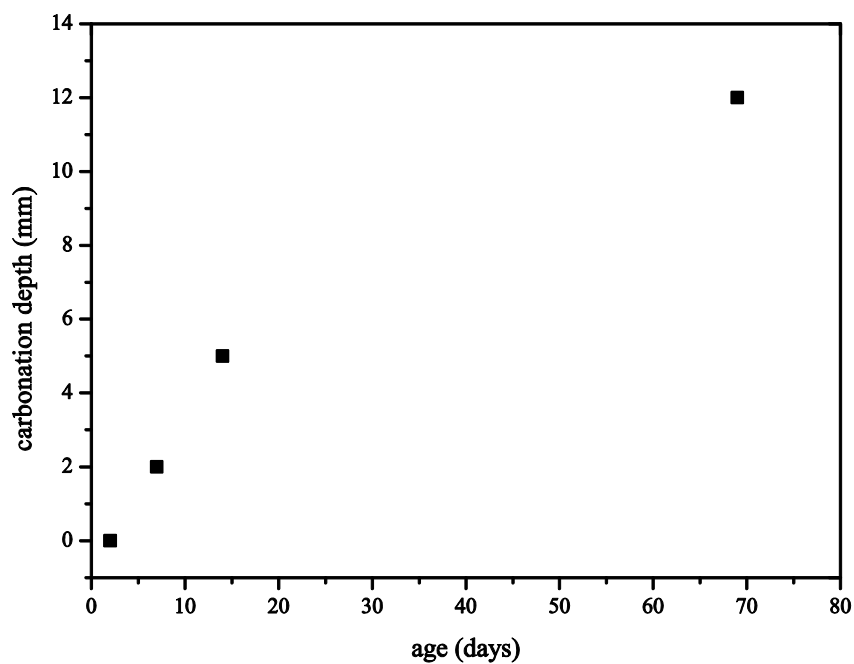


Figure 6-12 – Evolution of carbonation depth - phenolphthalein indicator - IC2

- *TGA analyses*

The objective of this sub-section was to study the carbonation throughout the depth of the cylindrical specimens with TGA testing on gathered samples. For this purpose samples were collected from three points along the radius of the transverse section: *P1* (3.0 cm from the center, thus located at the boundary), *P2* (1.5 cm, middle of the radius) and *P3* (0 cm, center), Figure 6-13 illustrates the positions for these points.

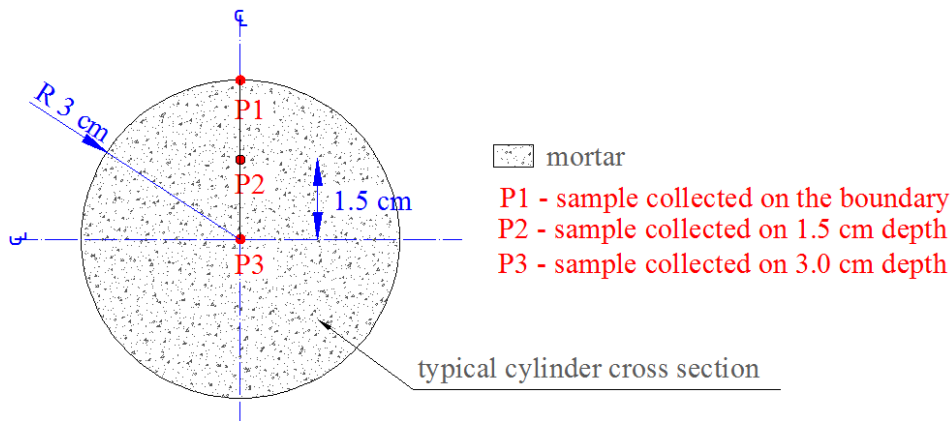


Figure 6-13 – Collected samples for TGA profile

As previously described, analyses were done at four different ages, 1, 7, 14 and 69 days (see Table 6-5). For each age and depth, the weights of the samples for TGA tests are summarized in Table 6-7.

Table 6-7 – Collected samples for TGA in cylindrical specimens at different depths

Age	Sample weight (mg)		
	<i>P1</i>	<i>P2</i>	<i>P3</i>
1 day	44.08	55.34	53.86
7 days	66.84	67.04	70.42
14 days	67.12	66.81	80.02
69 days	79.06	77.02	79.53

During these experiments, a range of temperature from 20-1000 °C was adopted. To illustrate the obtained results, the typical curves with TGA data for the three depths (*P1*, *P2* and *P3*)

after seven days are shown in Figure 6-14. For the sake of brevity, the results for the other studied ages are not presented herein, and the data can be seen in Annex A.

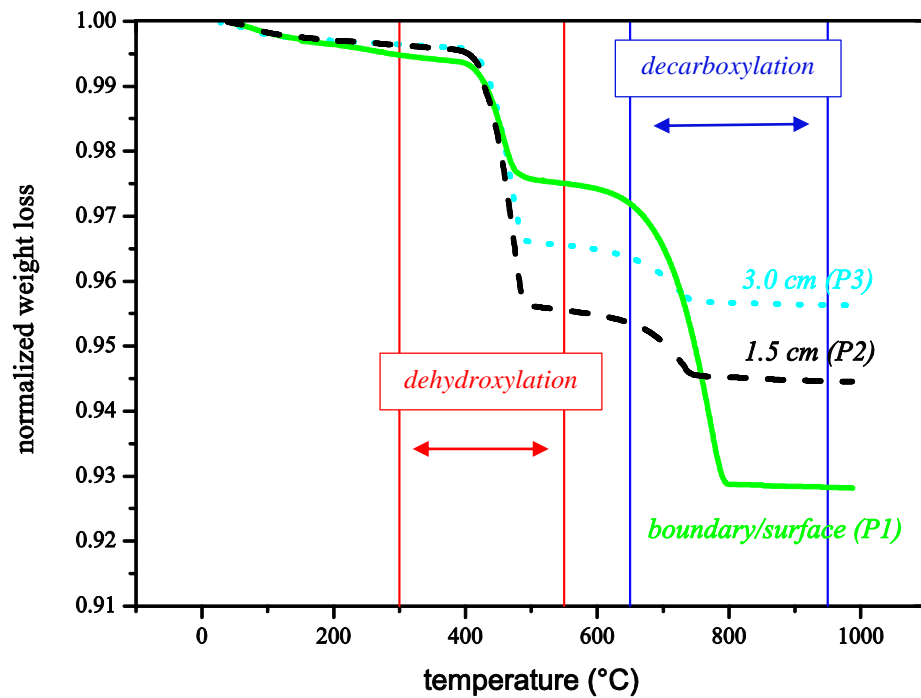


Figure 6-14 – TGA results for cylindrical specimen after 7 days in three depths (*P1*, *P2* and *P3*)

In Figure 6-14, the result for the most external sample, collected on the boundary – *P1*, presented higher amount of CaCO_3 , and, in sequence, the one collect at 1.5 cm (*P2*) and the sample at *P3*. As observed, sample *P3* presented the smallest weight loss on the decarboxylation range. This indicates that almost no carbonation happened (~11%) in the center of the specimen (*P3*), since this percentage was similar to the initial value measured on the fresh mortar (~10%).

With the objective to exemplify the evolution of the calcium carbonate over time, Figure 6-15 shows the different TGA curves for the four studied ages (1, 7, 14 and 69 days) for the samples collected on the boundary/surface of the specimens (*P1*).

The increase of the weight loss in the temperature range for decarboxylation over time could be noticed. The results indicated the evolution of the CaCO_3 content, with the consequent reduction of the Ca(OH)_2 . Another observation from Figure 6-15 was related to the presence of free water. For the first tested age, at 1st day, the results presented a significant reduction (~3%) in the weight for the range of temperature range of 20-100 °C, while for the other ages, this parcel was significantly lower. This decrease for the 1st day started since the initial

temperature of the test, as there was a significant decreasing of the weight from 20 to ~70 °C.

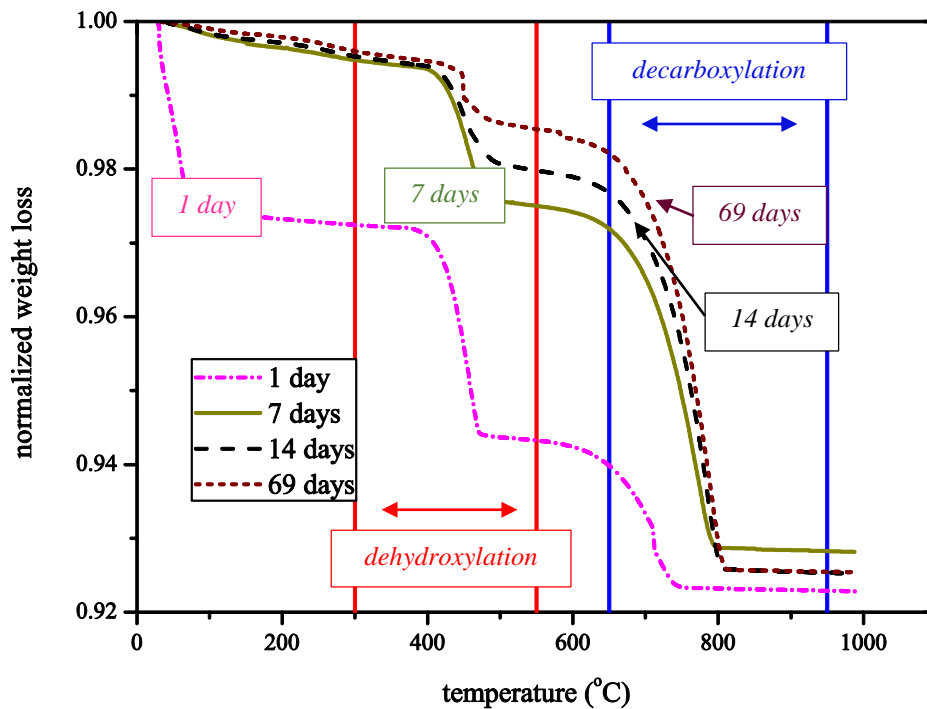


Figure 6-15 – TGA results for cylindrical specimen - *PI*, boundary

In order to study the reaction degree from the TGA data, specifically for this experiment, normalization was done considering the maximum R measured for these tests in the boundary of the specimen after 69 days, $R_{\text{maximum}} \approx 0.73$ or equivalently $R_{\text{maximum}} \approx 73\%$, before the normalization. Considering that the conversion is usually $\leq 80\%$ (Montes-Hernandez *et al.*, 2012, Montes-Hernandez *et al.*, 2010a, Montes-Hernandez *et al.*, 2010b), the results obtained from TGA on the collected sample in the boundary with relatively low presence of $\text{Ca}(\text{OH})_2$, showed an elevated carbonation percentage for 69 days, similar to the cited maximum value in literature.

- *Phenolphthalein and TGA analyses*

Figure 6-16 combines the TGA results at the four ages of testing mentioned above, for the three different depths, and the carbonation depth measured by phenolphthalein. The results for phenolphthalein are indicated by vertical solid lines with different colors varying with the ages, according to the depths provided by the indicator.

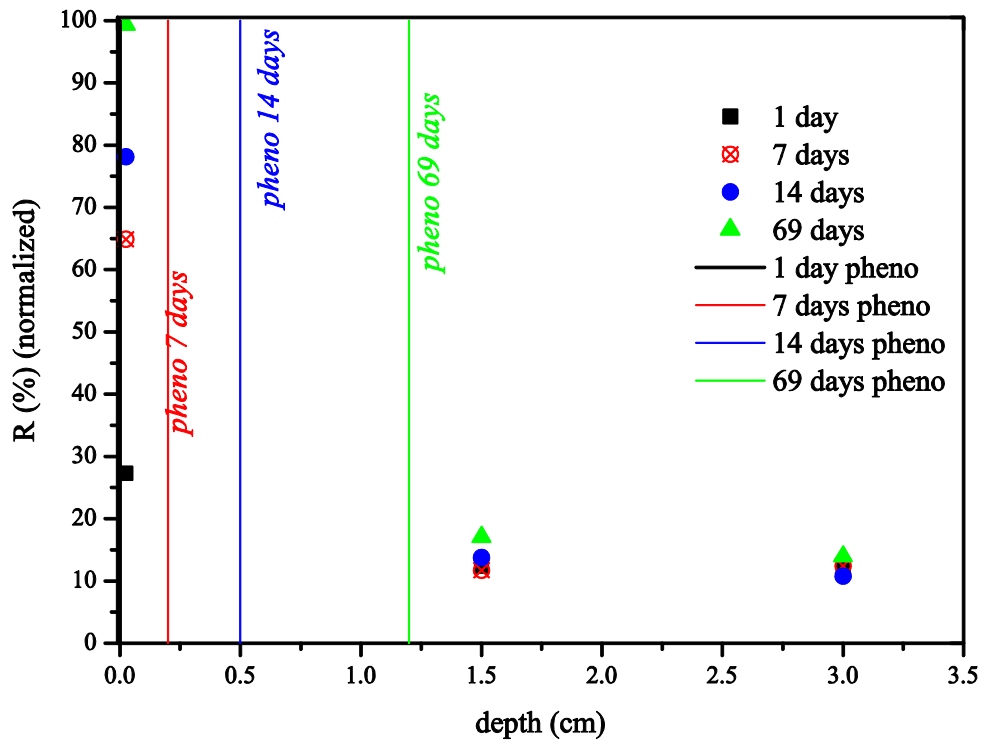


Figure 6-16 – TGA results vs phenolphthalein spray

The TGA results in Figure 6-16 are indicated with symbols, for each day and depth. The data were obtained considering the formulation presented in Eq. 6.2, nevertheless the values presented in Figure 6-16 were normalized (see Eq. 6.3).

In Figure 6-16, visibly for all the studied ages, the most external sample (collected on the boundary) presented higher amount of CaCO_3 and in sequence, the one collect at 1.5 cm.

For the samples collect at 1.5 cm and 3.0 cm, for all the tested ages, the results presented low carbonation percentage (R). Even after 69 days, the samples collected in these depths presented carbonation degrees with similar results of the first day. Considering the relation between the TGA and phenolphthalein indicator, Lawrence (2006) (see Figure 2-17) found values $\sim 60\text{-}75\%$. In the present work, for the sake of simplicity, if a linear approximation was adopted between the TGA results for different points, a range of values $\sim 25\text{-}60\%$ where the equivalent R that intercepted the carbonation depth measured with phenolphthalein indicator for the present work. The results with this linear approximation for the trend-lines (dotted) are presented in Figure 6-17. Parabolic interpolation was also adopted for the trend-lines. Similar observations in terms of equivalent reaction degrees were obtained, and therefore this interpolation is omitted.

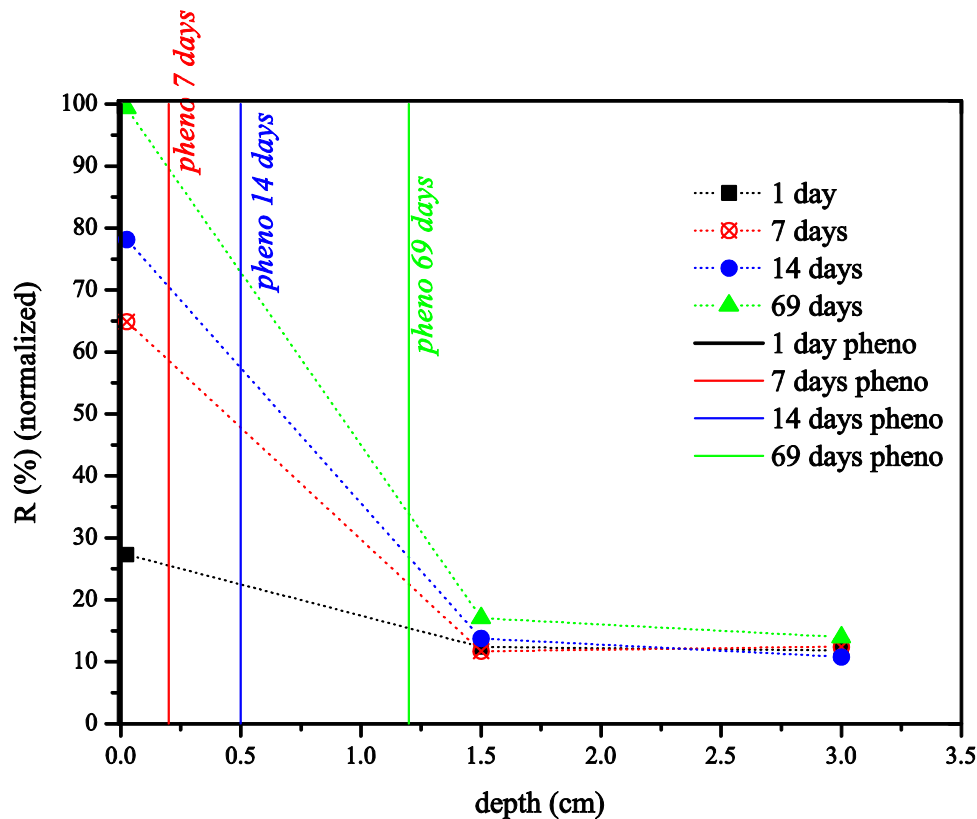


Figure 6-17 – TGA results vs phenolphthalein spray

With these simplified analyses, non-uniform correlations were also found. The results tended to have age dependence. Comparing with the results presented by Lawrence (2006), even with a smaller number of TGA tests done herein, the percentage of reaction that indicated the carbonation depth by phenolphthalein tended to be smaller than the values obtain by this author. The fact that only three depths were studied for each section with TGA should also be considered. Further information about the results from Lawrence (2006) were presented in Section 2.5.5.

- *Phenolphthalein and TGA in a specimen adopted to study the humidity flux*

The cylindrical mortar specimen (*H-H60-B*) used to measure the humidity in Chapter 5, simulating axisymmetric conditions, was also broken after 65 days. The objective to study separately this specimen was to investigate how the carbonation process developed for the cylinder adopted to measure the humidity flux and to compare it with the previous results. This study was done mainly due to fact that the humidity decreased relatively fast, and the carbonation is a slow phenomenon.

As done in the previous section, mortar was also collected at three different depths from the boundary external surface (*P1*), from 1.5 cm depth (*P2*) and from the center (*P3*) (see Figure 6-13). TGA tests were performed on the collected samples, and the results with the normalized weight loss are presented in Figure 6-18. A range of temperature from 20-1000 °C was adopted during the TGA tests. The initial mass of each sample was respectively: 71.14 mg (*P1*), 60.04 mg (*P2*) and 44.60 mg (*P3*).

The humidity values measured at 3.0 cm and 1.5 cm depth were around 60%, indicating the equilibrium with the environment, since the 20th day of monitoring, and the TGA did not measure significant presence of CaCO₃. The tested specimen still presented a carbonation gradient, with a higher amount of CaCO₃ in the boundary and smaller amounts for the other two depths. These results might be an indicative of the low presence of CO₂ in this region, as assumed by Cheng and Chang (2006) for studies in concrete, since the presence of carbon dioxide is essential for the carbonation process (Lawrence *et al.*, 2006a, Chang and Chen, 2006). Nevertheless, this cannot be a conclusive statement because the direct measurement of CO₂ was not possible.

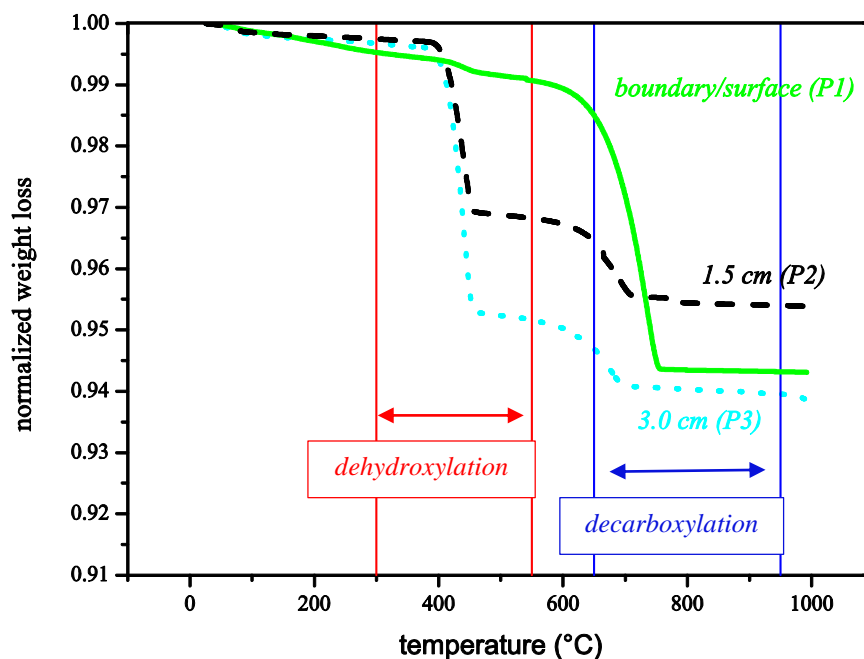


Figure 6-18 – TGA results for *H-H60-B*, after 65 days from casting/exposition - three depths (*P1*, *P2* and *P3*)

In order to validate the previous results, as a second method to evaluate the carbonation, the phenolphthalein indicator was sprayed on the broken surface. After the phenolphthalein

spray, the carbonation depth was measured with a caliper rule. The test showed a carbonation depth ~ 1.3 cm (see Figure 6-19), which is a depth level of great proximity with the depth of sample gathering for TGA testing at 1.5 cm. In TGA, the composition of the sample indicated by thermogravimetric analysis, presented an $R \sim 20\%$. Similar observations in terms of R , and the equivalent carbonation depth measured by phenolphthalein were shown in Figure 6-16. Once more, these experimental results illustrate that the humidity diffusion process tended to occur faster than the carbonation.

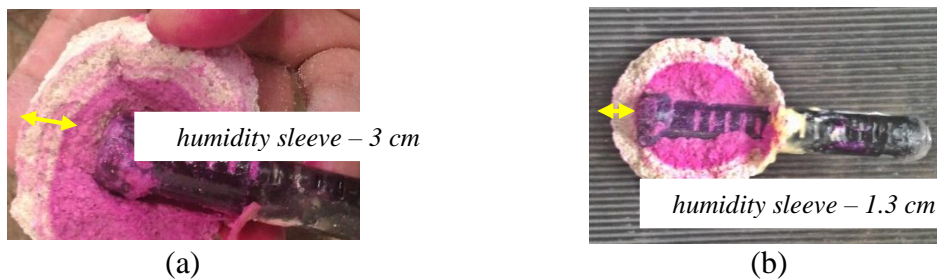


Figure 6-19 – Carbonation in cylinder, specimen *H-H60-B* after break - phenolphthalein indicator - (a) cross section close to the sleeve at 3 cm; (b) cross section close to the sleeve at 1.3 cm.

- *Disc specimens*

This section presents results from TGA data in thin discs filled with mortar. These specimens were proposed with the objective of minimizing the effects of moisture gradients in the behavior of the sample, and thus perform a decoupled study of carbonation (in view of its interaction with humidity). The discs had the dimensions of: diameter ≈ 3.7 cm; thickness ≈ 0.8 cm (see Figure 6-20). The definition of the thickness was related to the maximum size of aggregates used for preparing the mortar. The initially proposed concept was to keep the minimum dimension of the sample around three times higher than the largest diameter of the sand (for granulometry of the sand see Chapter 5).

This condition was adopted in analogy with cementitious materials, in which the representative of the material is desired to preserve the homogeneity level.

The schematic representation of the mortar discs is shown in Figure 6-20. Three specimens were cast, namely *TGA.S.A*, *TGA.S.B* and *TGA.S.ISO* (see Figure 6-21 and Figure 6-22).

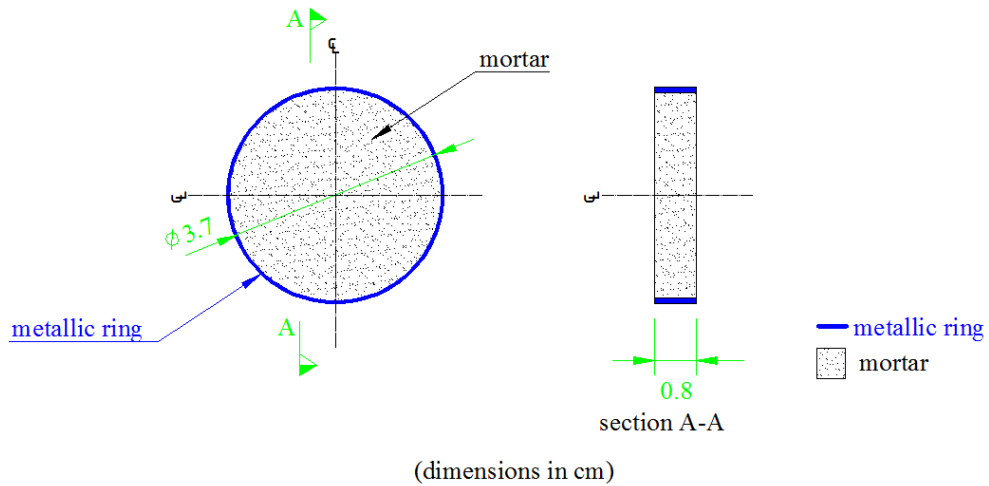


Figure 6-20 – Disc specimens for TGA

For specimens stored and exposed in usual conditions, inside the “*standard*” climatic chamber, the samples and the material extraction can be seen in Figure 6-21. The two discs were stored in vertical position to keep the material in contact with the air, with the objective to allow the carbonation process (see Figure 6-21 a). Samples were collected from the surface of the specimen (see Figure 6-21 a and Figure 6-21 b). *TGA.S.B* (see Figure 6-21 a) was re-wetted, with the objective to study the “*late hydration phenomenon*” as this phenomenon was referred in literature for aerial lime mortar (Pavía *et al.*, 2006). As the name suggests, “*late hydration phenomenon*” is the tardy hydration of CaO (Hughes and Taylor, 2009, Elert *et al.*, 2002, Rodriguez-Navarro *et al.*, 1998).



Figure 6-21 – Discs specimens for TGA (a) storage, (b) after sampling

Specimen, *TGA.S.ISO* was kept isolated (see Figure 6-22 a). The sealing process was done with several plastic layers around the disc. The specimen was cast to study the material behavior with a sealing system that impedes the contact mortar-environment, and to compare the TGA result with the values obtained in the fresh mortar. As Figure 6-22 (a) illustrates, immediately after the opening process, the sealed specimen (*TGA.ISO*) presented a humid

aspect, which was expected in view of the hindered drying process. During the opening process, the disc was broke (see Figure 6-22 a).

Concerning the re-wetting process done in *TGA.S.B*, (see Figure 6-22 b and c), water was sprayed in the specimen until visible mortar saturation. The re-wetting process was done at the thirty-ninth day and the test by TGA at fortieth. These ages were chosen to capture the presence of $\text{Ca}(\text{OH})_2$ and CaCO_3 in the mortar.

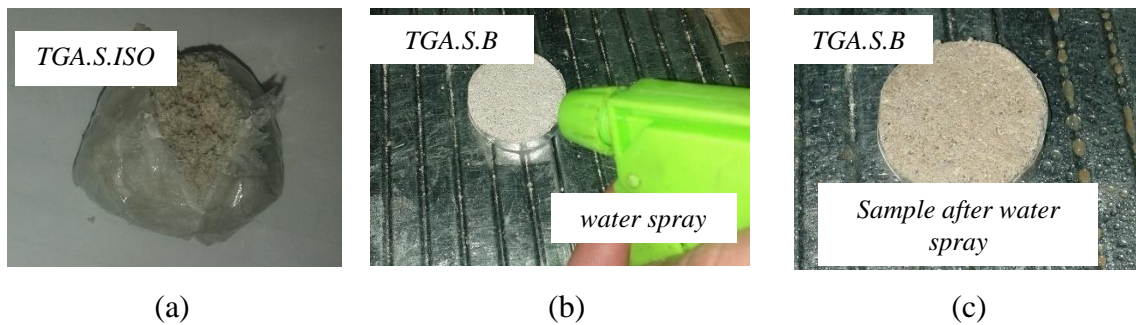


Figure 6-22 – Discs specimens in different conditions (a) isolated, (b) re-wetted specimen - water spray (c) re-wetted, after water spray

Considering the specimens described, for each tested sample, in different ages, the amount of material collected for the TGA tests is presented in Table 6-8, together with the used specimen.

Table 6-8 – Amount of material tested in TGA at each age

Age (days)	Specimen	Amount of tested material (mg)
0	<i>TGA.S.A</i>	51.06
3	<i>TGA.S.A</i>	35.43
7	<i>TGA.S.A</i>	50.56
20/TA (*)	<i>TGA.S.A</i>	54.20
20/TB (*)	<i>TGA.S.A</i>	85.68
20/TC (*)	<i>TGA.S.A</i>	67.92
40	<i>TGA.S.A</i>	64.51
40 re-wetted	<i>TGA.S.B</i>	60.56
47 (isolated)	<i>TGA.S.ISO</i>	78.12

(*) for the test done at 20 days, the obtained curves with the TGA results were presented in Section 6.3.

The TGA data from the samples stored in ordinary conditions are presented in Figure 6-23, based on the formulation presented in Eq. 6.2. The R value for the twentieth day was the average of the three TGA tests, and the maximum dispersion found in the results for these samples was ~3% (the TGA curves were shown in Figure 6-10).

A tendency for carbonation increase was observed during the first days. The decreasing of the values after the 3rd day was relatively small, however unexpected, since a continuous evolution over time for the R was expected and mentioned in Lawrence et al. (2007) and Lawrence (Lawrence, 2006). The peak of measured R occurred at this age. One possible explanation for the alterations of the trend for R , increasing after the 3rd day, might be the sampling or repeatability issues, as presented in Figure 6-10. These tests were adopted with the objective of learning the TGA capabilities to study the material and its carbonation process.

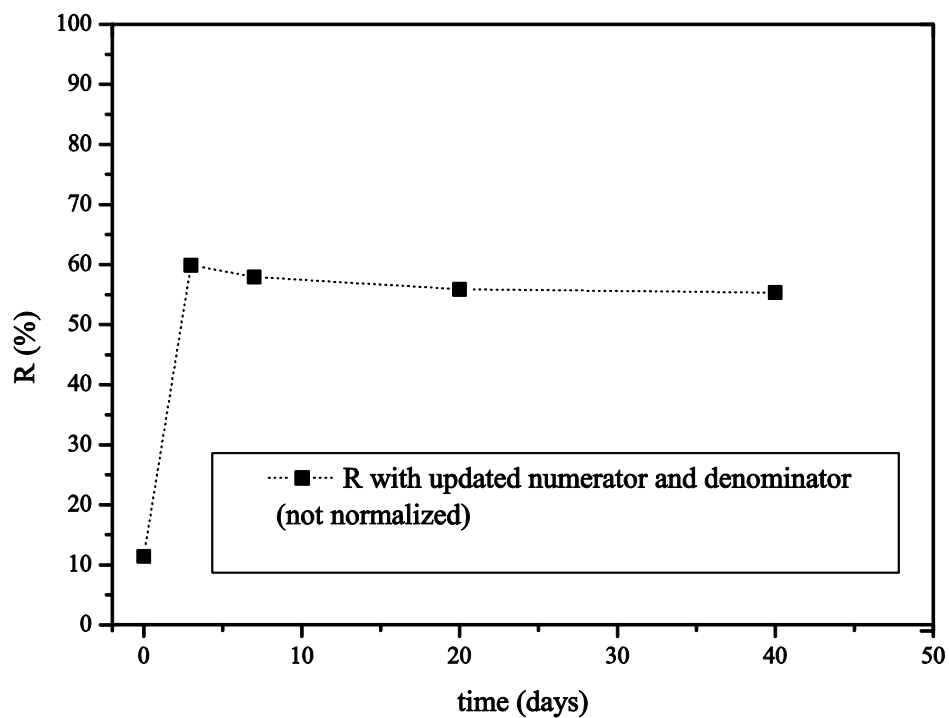


Figure 6-23 – Carbonation percentages - TGA results in thin discs - TGA.S.A

The results presented in Figure 6-23 were not normalized because they presented a relatively low R (~60%). In fact, the results of this section were the first TGA tests done chronologically. Comparing the values of R herein, with the reaction degree obtained in other tests, with the same environmental conditions, the values obtained in the present set of experiments were lower, as, previously, maximum values for R ~70-75% were measured.

The lower values occurred due to the reduced conversion of Ca(OH)_2 to CaCO_3 . This phenomenon could indicate that, for some unexpected reason, the remaining fraction of Ca(OH)_2 will be converted later or experimental errors occurred.

Still, the unexpected increase of the Ca(OH)_2 detected in some samples after the 3rd day was studied, as it could be associated with a “late hydration” phenomenon. From the tests and comparing the results, the re-wetted sample *TGA.S.B*, shown with dashed line in Figure 6-24, presented a similar percentage of Ca(OH)_2 (dehydroxylation range) with the data of the ordinary disc, displayed with solid line in Figure 6-24.

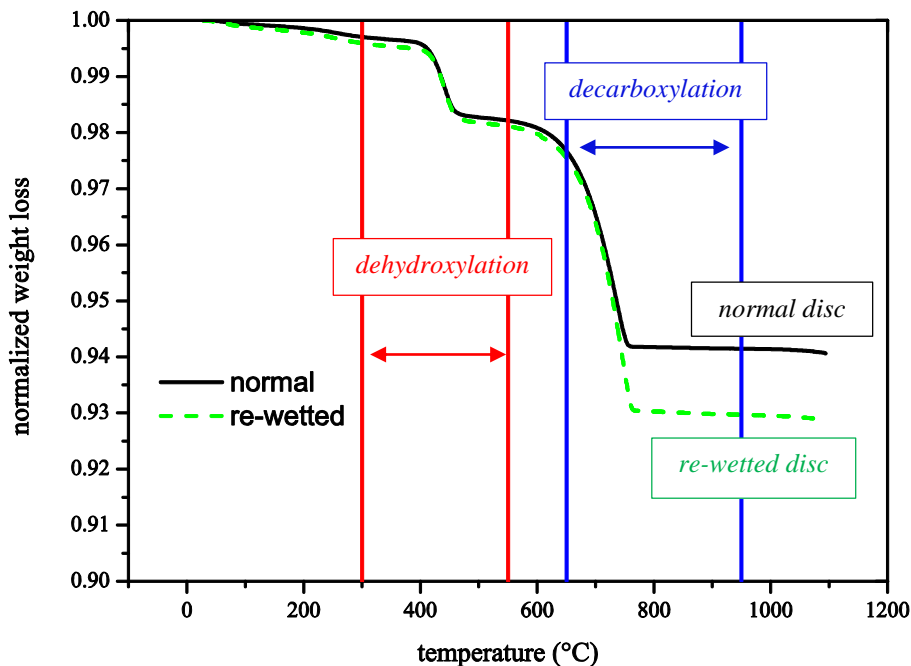


Figure 6-24 – Comparative results between the re-wetted (*TGA.S.B*) and ordinary samples (*TGA.S.A*) (tests were done after 40 days)

From the TGA data, the difference in *R* for the normal (*TGA.S.A*) and the re-wetted discs (*TGA.S.B*), was around 5%, as the results were: 56% for the ordinary sample and 61% for the re-wetted one. These results were in agreement with references in literature, which state that, the “late hydration phenomenon” is usually more common in dolomite (MgO), than in calcium lime (CaO) (Hughes and Taylor, 2009, Elert *et al.*, 2002, Rodriguez-Navarro *et al.*, 1998). These results illustrated that for the conditions studied just a small extension of the “late hydration phenomenon” occurred due to the addition of water. The results also indicated that the amount of water used in the mortar preparation could not be considered a limitation factor for the hydration process, since the measured values for the dehydroxylation

were similar (see Figure 6-24). The results presented in Figure 6-23, with the increase of the amount Ca(OH)_2 were probably not linked with this “*late hydration phenomenon*”.

The last experiment proposed in this section aimed at comparing the TGA data from the tests done in fresh mortar and the sealed specimen. The results of these tests are presented in Chapter 7 (numerical study of the experiments).

6.4.3 Environmental effect in discs

An important aspect in the study of carbonation is the fact that the tests can be performed with experiments in accelerated or natural environments, and the influence of the concentration of CO_2 was studied in Chapter 2. Experiments in accelerated conditions are often adopted due to the slowness of the phenomenon. Sanjuán *et al.* (2003) claim that the accelerated tests modify the microstructure of concrete and recommend this type of experiment only as an auxiliary tool. The applicability and study of the carbonation process in environments with elevated CO_2 concentration in specimens with large dimensions is still a controversial aspect. Considering this, in the present work, the accelerated carbonation was just applied for comparison with ordinary conditions in thin and small discs. This comparison had the objective to observe the behavior supporting the numerical modeling. This section presents the results regarding the environmental effects in discs with the same geometry as previously presented (see Figure 6-20). The mortar discs were used to investigate the evolution of carbonation process in different environments. For this study, three different environments were adopted, as presented in Table 6-1. The discs were also stored in vertical position as presented in Figure 6-21 a. Due to the results found previously, the focus of the study was on early ages (1, 4, 7, 14, 21 and 28 days). For each age and environmental conditions, the weights of the samples for the TGA tests are summarized in Table 6-9.

Table 6-9 – Collected samples for TGA in disc specimens

Age	Sample weight (mg)		
	<i>standard</i>	<i>humid</i>	<i>high CO₂</i>
1 day	62.82	55.67	57.52
7 days	73.85	70.42	62.65
14 days	61.39	80.02	58.28

Age	Sample weight (mg)		
	<i>standard</i>	<i>humid</i>	<i>high CO₂</i>
21 days	69.18	68.37	77.24
28 days	71.94	56.44	67.55

Again, during the tests, a range of temperature from 20-1000 °C was adopted with an increase rate of 10 °C/min. The obtained data after normalization for the three different environmental conditions and six ages are presented in Figure 6-25. Analyzing the trend presented, the calcium carbonate content showed a global increase over time, with the consequent increase of R , for the three scenarios. The tendency of the carbonation rate for the specimen stored in the “*humid*” chamber was significantly slower for the first ages (~6 days) in comparison with the observed values in disc stored in the “*standard*” condition, then, it was accelerated until ~21 days. This behavior can be explained with the concept that elevated humidity values made difficult the initial CO₂ ingress, retarding the carbonation process at first ages (Houst, 1996, Lawrence, 2006). As could be observed, the peak of the normalized value (see Eq. 6.3) occurred at the age of 14 days for the specimens stored in the chamber with elevated CO₂ concentration, and at 21 days for the discs stored inside the two other environmental conditions. These points are marked with arrows in Figure 6-25. Before the normalization, the maximum reaction degrees were: $R_{max} \approx 70\%$ at 14 days for the specimen stored in the “*high CO₂*” chamber; $R_{max} \approx 70\%$ in the same age for the specimen in standard condition, and $R_{max} \approx 99\%$ for the disc inside the humid environment.

Since the specimens were stored in different environmental conditions, the normalization was done considering the maximum R for each group/each condition studied during the tests. For the specimen stored in the climatic chamber with 4% CO₂, the results showed a fast carbonation in the initial ages, approximately until the 4th day, indicating that most of the carbonation occurred by such age. Analyzing the extension of reaction before the normalization, for the specimen stored inside the “*humid*” chamber, the percentage was higher and the sample tested at 21 days presented a $R \approx 99\%$. In fact, the measured value was significant larger than the others, because of the small amount of Ca (OH)₂ detected at that age. In all the TGA tests done, this result was the only one in which the R was close to 100% before the normalization. The value could be an outlier, since the results for the test immediately after, at 28th day showed a smaller percentage of CaCO₃ and higher percentage of calcium hydroxide, and a consequently decreasing of the carbonation degree, $R \approx 0.87$.

Another possibility to explain the result is the presence of higher humidity values inside the chamber induced a conversion percentage more elevated. In this sense, Dheilily *et al.* (2002) stated that in environment with elevated humidity, relatively low levels of CO₂ and temperatures (~10 °C) favored the carbonation.

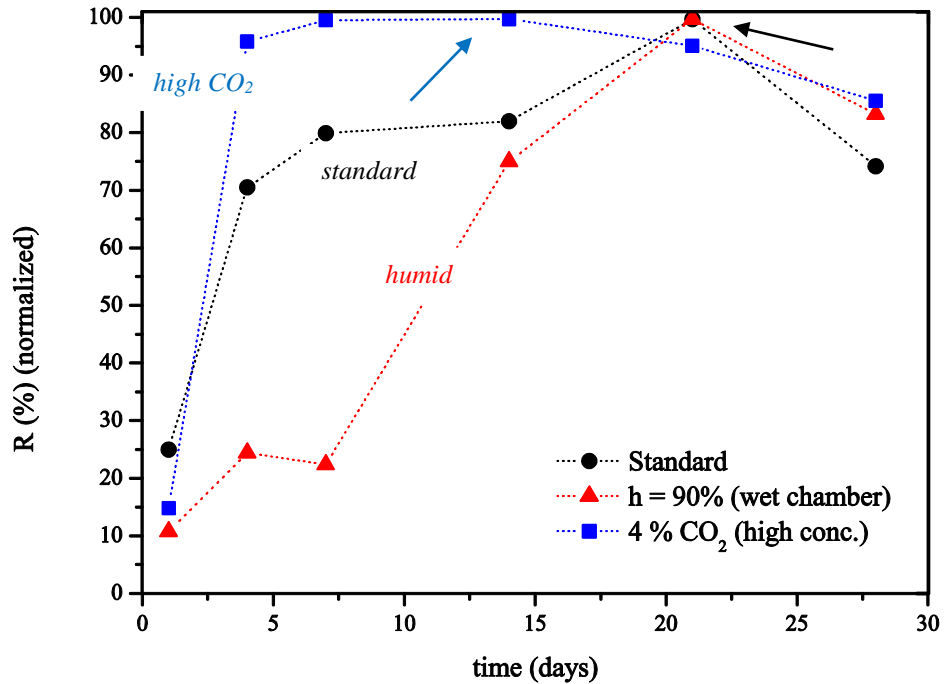


Figure 6-25 – Results of TGA in discs specimen for different environmental conditions (considering the normalized R)

In comparative terms, for the carbonation processes in natural and in elevated concentration of CO₂, different conclusions in literature were found (see Chapter 2). Evaluating the data from the specimens stored in the two other conditions, similar values for the maximum reaction were obtained, $R_{max} \approx 70\%$ at 14 days for the specimen stored in the “*high CO₂*” chamber; and ~76% in the same age for the specimen stored inside the “*standard*” one. Comparable percentages of the total reaction are found in literature for natural carbonation process (Montes-Hernandez *et al.*, 2012, Montes-Hernandez *et al.*, 2010a, Montes-Hernandez *et al.*, 2010b). The results obtained in the present study showed a faster carbonation for the specimen in the chamber with 4% of CO₂.

6.4.4 Effect of the size of the specimens

Another comparative test was performed with the objective to detect a possible effect due to the size of the specimens on the evolution of their carbonation profiles. With this objective, cylindrical specimens with five different dimensions denominated as series *S.A*, *S.B*, *S.C*, *S.D* and *S.E* were cast (see Table 6-10), ranging from ~3.6 cm diameter (*S.A*) to 15 cm diameter (*S.E*). The groups of cylinders *S.A*, *S.B*, *S.C* and *S.D* had the diameter/height ratio ~1:2 (see Table 6-10).

Table 6-10 – Study of the effect of the size of the specimens for the carbonation depth measured with phenolphthalein

Age	Specimen	Height (mm)	Diameter (mm)	Density (kg/m ³)	Carbonation depth (mm)
10 Days	<i>S.A10</i>	79	36	1761	~3.9
	<i>S.B10</i>	112	60	1820	~2.7
	<i>S.C10</i>	155	71	1852	~2.4
	<i>S.D10</i>	181	86	1852	~1.8
	<i>S.E10</i>	Not tested			
21 Days	<i>S.A21</i>	83	37	1820	~6.0
	<i>S.B21</i>	119	60	1858	~5.9
	<i>S.C21</i>	153	72	1856	~5.8
	<i>S.D21</i>	179	87	1850	~5.9
	<i>S.E21</i>	150	150	1860	~6.0
90 Days	<i>S.A90</i>	80	36	1831	~12.3
	<i>S.B90^(a)</i>	~ 60	~ 60	~ 1858	~12.1
	<i>S.C90^(a)</i>	~ 76	~ 72	~ 1856	~11.9
	<i>S.D90^(a)</i>	~ 90	~ 87	~ 1850	~12.1
	<i>S.E90^(a)</i>	~ 75	~ 150	~ 1860	~12.0

(a) Phenolphthalein did not provide consistent results in some specimens tested at 90 days, because of experimental limitations. Therefore, some specimens previously tested at 21 days were re-used at 90 days. In terms of the minimum distance from the sectioning to the extremities of the specimens (top and bottom parts of the cylinders), these specimens had a distance longer than 3 cm. The effect of this change in the final results should be marginal, since the measured carbonation depths for 90 days were around 1.2 cm

In specimens of series *S.E*, due to cracking, the geometry had to be adapted and they finally presented a diameter/height ratio $\sim 1:1$.

The specimens were tested at 10, 21 and 90 days after demolding, keeping the period for the demolding process (*ICI* see Section 6.2). These ages were chosen in order to understand the distinct behavior over time (see Table 6-10). Some specimens tested at 21 days were re-used also at 90 days. For the casting procedure, more information was presented in Section 5.4.

During the tests, the measured densities of the specimens were $\sim 1800\text{-}1860\text{ km/m}^3$, for the three ages, except for the specimen *S.A10*, which presented a density $\sim 1761\text{ km/m}^3$, after 10 days. The latter value was lower, probably due to a fast drying process. The initial density for the specimens was $\sim 2000\text{ km/m}^3$.

In Table 6-10, for the age of 10 days, there was a tendency of the increase of the density with the diameter, which indicate a slower drying process for that specimen and a smaller variation in the density for the cylinders with larger dimension.

The dimensions presented in Table 6-10 are the average of measured values during the tests, considering a minimum of three measurements for each dimension, adopting a caliper rule. With the objective to illustrate the results for 21 days, a general view of the carbonation depths for the five cylinders after the phenolphthalein spraying is presented in Figure 6-26.

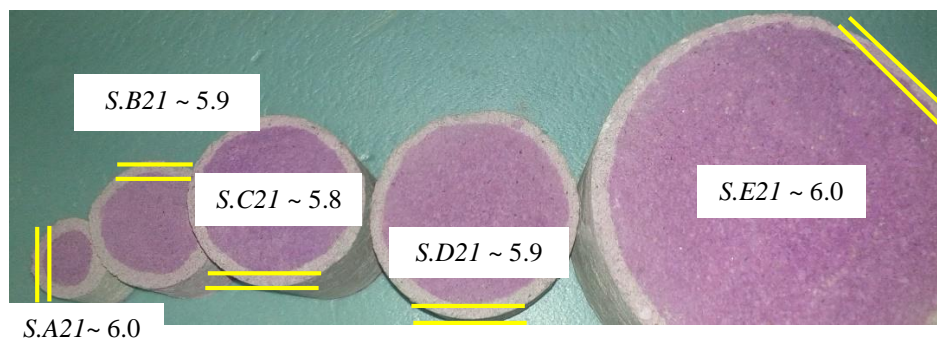


Figure 6-26 - Carbonation depth for all the specimen for 21 days (after demolding)

The carbonation evolution, specifically for specimens of series *S.A* is exemplified in Figure 6-27 with photographs for the three tested aged. For the first measurement, at age of 10 days (*SA.10*), a carbonation depth around 3.9 mm was measured (Figure 6-27 a), while for 21 days a value of 6.0 mm was found (*SA.21*, Figure 6-27 b), and finally for 90 days, 12.2 mm was measured (*SA.90*, Figure 6-27 c).

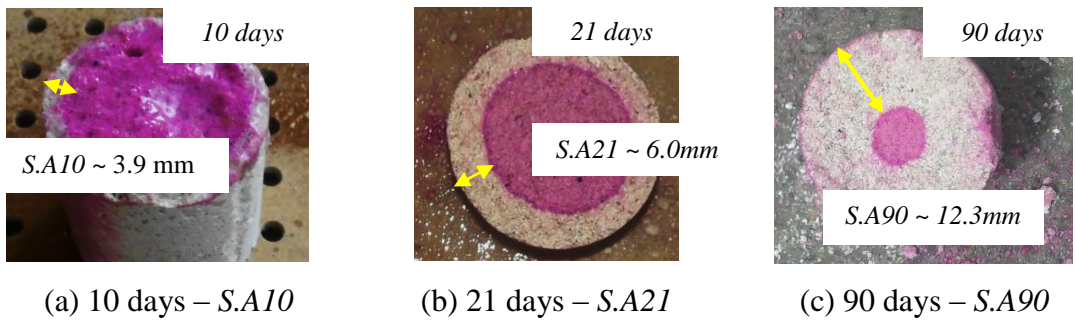


Figure 6-27 - Evolution of carbonation over time for specimens of series S.A, days from demolding: a) 10 days, b) 21 days and c) 90 days

In summary, the phenomenon of the carbonation depth increasing over time was observed for all the specimens' sizes. This evolution, for the five series of specimens is shown in Figure 6-28.

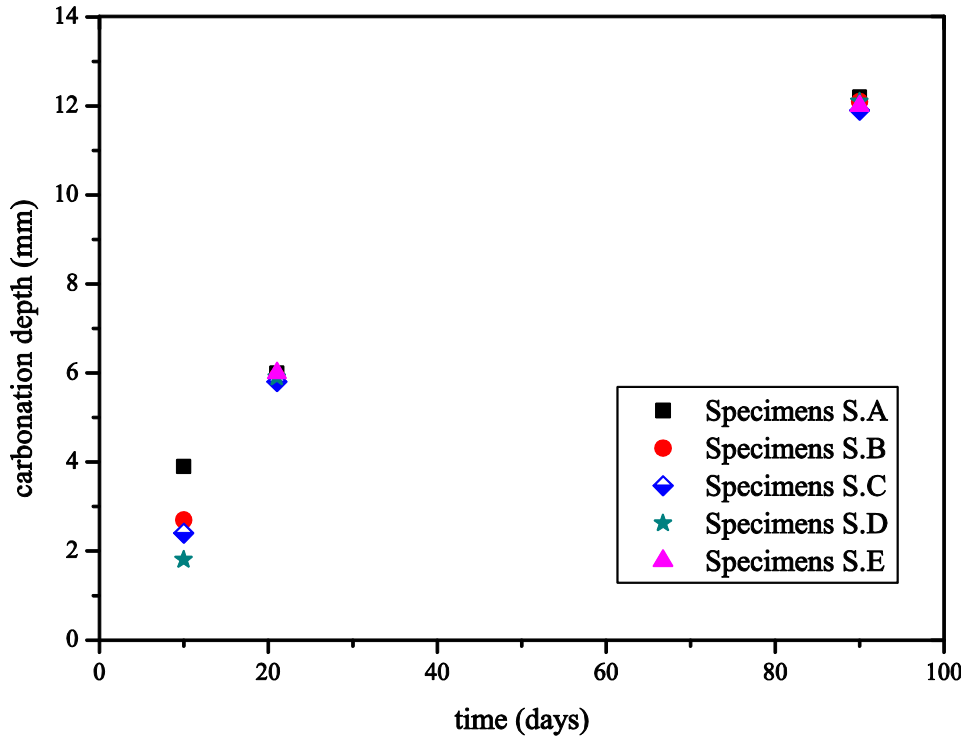


Figure 6-28 – Evolution of carbonation depth over time for different specimens – days after demolding

Considering the data from Table 6-10 and Figure 6-28, at the first age of testing, an effect related with the size of the specimens was noticeable. For instance, in specimens of series S.D, for 10 days (S.D10), which had dimensions of height and diameter around two times larger the specimen of series S.A (S.A10), the carbonation front progressed inward the

specimen ~2.2 times less than the smaller one. At longer ages, the effect in terms of carbonation depth tended to be less remarkable. In fact, at 21 days, all specimens had carbonation depths of ~5 mm and, at 90 days, the carbonation depths were all approximately equal to 12 mm.

Assuming a correlation between the humidity and the carbonation process, as mentioned by (Lawrence, 2006, Houst, 1996, Van Balen, 2005, Van Balen and Van Gemert, 1994), one possible explanations for the results obtained in those experiments can be linked with the fact that, at first ages, the humidity decreased faster for the smaller specimens, while for the larger ones, it stayed with higher levels for longer period, because the inner parts supplied water for the external ones. Those higher values of humidity in specimens with larger dimensions, might limit carbonation, possibly due to the smaller ingress of CO₂ in higher humidity conditions. For relatively early ages, the humidity for the cylinders with different diameter were in equilibrium with the environment, as experimentally it was observed that the influence of the internal humidity in the carbonation process tended to reduce over time.

6.4.5 TGA in lime paste

This section presents the results for TGA test in lime paste (lime + water). This test was proposed since previous results indicated a competition between the evaporation of water (reduction of the material weight) and the carbonation (increasing the weight). The TGA equipment was available for a longer period and this condition was essential for the experiment. The tested paste preparation followed the same proportion in terms of weight of lime:water, adopted in the mixing process for the mortar (1:1.3). The sample was tested inside the same thermogravimetric device (see Section 5.2) for 25 days in an atmospheric condition with ambient CO₂ concentration ($h \approx 60\%$). The test was done during the summer period, therefore the environment presented a higher average temperature, $T_{average} \sim 30$ °C, in comparison with the standard temperature.

The analyzed sample presented an initial weight of ~105 mg, which was measured by the balance of the TGA device immediately after the insertion of the material. Before the experiment could be initiated, a fast decreasing in the weight of the sample was observed. This variation could be associated with the exothermic reaction during the hydration of aerial lime. Thus, this initial weight variation is considered to have been related to the evaporation of water. The material inside the TGA device lost ~40 mg in approximately 90 minutes. After this initial period, the weight of the sample did not present significant variation in the

very short term range of '*minutes*'. Thereafter, the TGA test registered the weight variation over time, within a continuous monitoring process (see Figure 6-29).

The results presented in Figure 6-29 indicated a general tendency of a continued and progressive increasing of weight over time, as expected, due to the carbonation process. These results indicate that there was a predominance of carbonation in relation to evaporation process. The steps related to the increasing of the weight of the material were divided in 3 segments: 1, 2 and 3, as presented in Figure 6-29. An initial steep branch (1), with the increasing weight variation until ~5 days was observed, followed by a slower rate (2). This decrease in the rate was maintained until ~20 days, when a faster rate was subsequently observed, after this age until the ending of the test, with the step 3, from ~21 to 25 days.

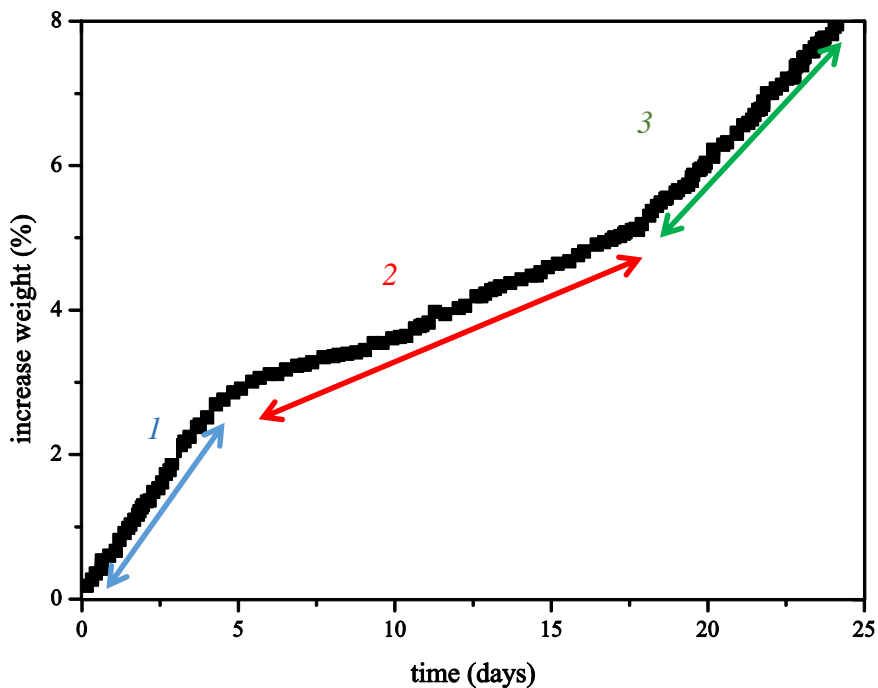


Figure 6-29 – TGA result for the carbonation process in lime paste over 25 days

The lower weight increase rate observed in segment 2 could be associated with the hydration of CaO compound and the later conversion to CaCO₃, which would prevent deeper penetration of the CO₂, as proposed by Van Balen (2005) and Montes-Hernandez *et al.* (2012). Comparatively, the densities of calcium hydroxide and carbonate are usually lower than the density of calcium oxide (Ek *et al.*, 2009), which would provide the formation of external hydroxide and carbonate layers around the aerial lime particles (CaO).

Therefore, the carbonation process could be correlated to the progressive deposit of calcium carbonate, as the hydration with the calcium hydroxide. These phenomena might be associated with the origin of external layers. The CaCO_3 layer, in particular, may exhibit a smaller porosity that could present a reduced diffusivity to the CO_2 penetration (Montes-Hernandez *et al.*, 2012, Van Balen, 2005). However, considering these effects, the deposition of compound formed during the carbonation process (CaCO_3) around the CaO particles apparently occurred to a limit ~20 days. From this age, a higher conversion rate could be once more observed (see Figure 6-29). This observed behavior might be explained by considering a possible rupture on the more external layers. The nature of the rupture could be linked with a possible shrinkage, and this phenomenon probably might be connected with the water evaporation. Considering these assumptions, the possible alteration of the impermeable layer could foster again an easier penetration of carbon dioxide (step 3 in Figure 6-29), thus the conversion of the non-carbonated material with a higher increasing weight rate was once more observed (step 3 in Figure 6-29).

6.5 *Testing program for evolution of mechanical properties*

6.5.1 *General aspects*

This last section of Chapter 6 regards the investigation of the evolution of mechanical properties of aerial lime mortars, namely the elastic modulus and the compressive strength. The knowledge of e-modulus may be considered fundamental, for instance, for the stress distribution in real scale structures, and the compressive strength allows to study the load capacity (Hibbeler, 2011). The measurements of e-modulus herein reported were made in two distinct experimental setups/procedures, being the second procedure (*Part B*) an evolution/improvement of the first one (*Part A*). Compressive strength testing was performed on cubic specimens, using as initial reference the recommendations presented in EN 1015-11 (CEN, 1999b).

6.5.2 *Preliminary measurement of e-modulus evolution over time – Part A*

This section presents information about the preliminary test to monitor the evolution of static elastic modulus over time. Cylinders with the dimensions used before, for humidity and carbonation studies, were herein analyzed. As presented in Section 2.6, different authors

have studied the mechanical properties of aerial lime. However, the elastic modulus evolution is usually investigated with measurements done by resonance frequency (Margalha *et al.*, 2011). In this section, cylinders with the curing condition *ICI* (see Section 6.2) were tested. Limitations related to cracking of specimens of greater dimensions, as well as the load capacity the precision of the hydraulic testing machine, guided the choice of the specimen size. The specimens were cast with the mixture and conditions presented in Section 5.4.

Before the test was initiated, a pre-load of 100 N was applied. In sequence five cycles of loading with ramps of amplitude ~ 300 N were performed, applied with a loading speed rate ~ 20 N/s. The maximum load value was estimated considering a percentage $\sim 30\%$ of the initial compressive strength of the material.

In terms of strain measurement, three linear variable differential transformer (*LVDTs*) were used to measure the displacements. The *LVDTs* were placed externally around the specimens, and they were positioned at an angle $\sim 120^\circ$. They were connected to the cylinder specimen through two metallic rings, as shown in Figure 6-30. The ring located on the upper part presented holes, in which the *LVDTs* were inserted, while the second ring was positioned below, supporting the extremities of the *LVDTs*. Screws were adopted to fix the *LVDTs* inside upper metallic ring (“*screw a*” in Figure 6-30), in sequence the set was attached to the specimen with screws (“*screw b*” in Figure 6-30), as also done for the bottom ring (see Figure 6-30 and Figure 6-31). With the objective to clarify the experimental setup, a schematic 3D view of the apparatus is shown in Figure 6-30.

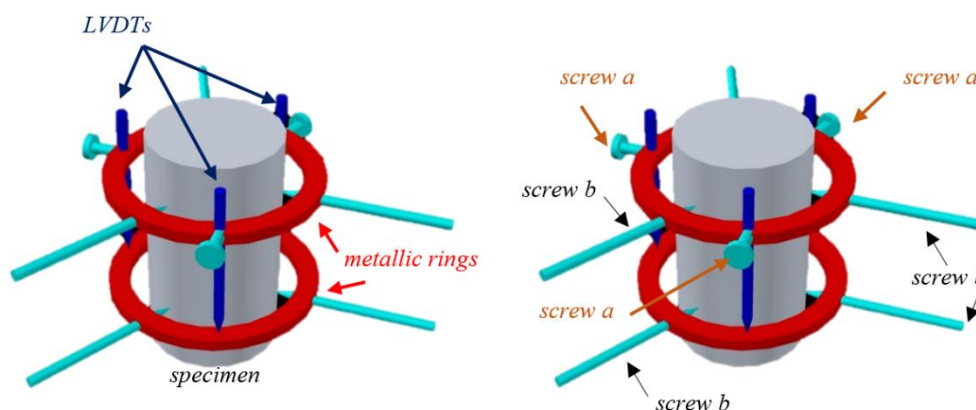


Figure 6-30 – 3D view of the experimental setup for elastic modulus test (“*screw a*” - connection *LVDT*/metallic ring – “*screw b*” - connection metallic ring/specimen)

The metallic rings should be well fixed on the specimens to avoid movements during the tests. The rings were positioned around 3 cm from the top and bottom parts of the cylinder (see Figure 6-30 and Figure 6-31).

During the tests, on the top of specimen a metallic device was placed with the objective to apply mostly compressive load, and to reduce the possible effect of bending related eccentricities. This accessory operated as a hinge (see Figure 6-31). The experiments were done using a hydraulic testing machine, connected to an acquisition data system, which recorded the load applied and the displacements (see Figure 6-31).

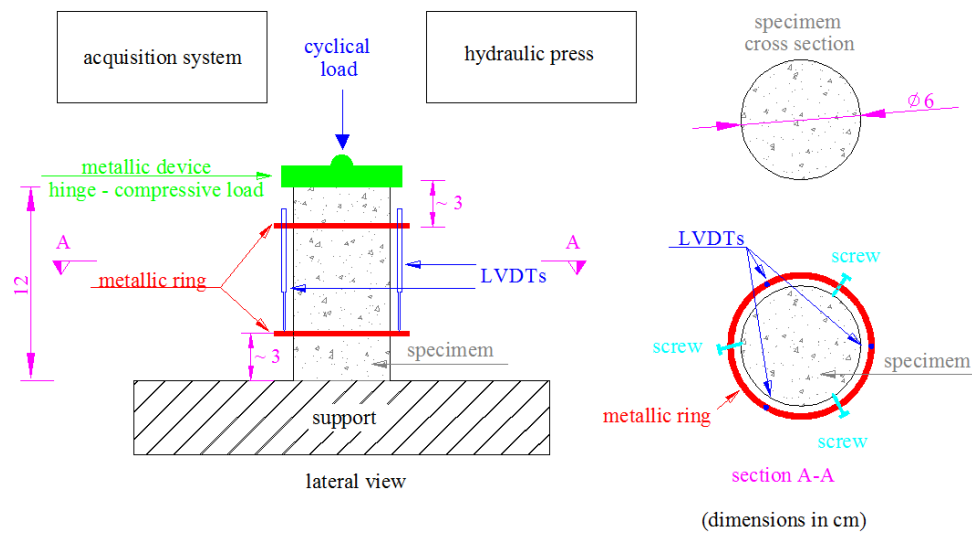


Figure 6-31 – Experimental setup for elastic modulus testing

Regarding the experimental challenges, a frequent problem was the cracking of specimens, and the detaching and rupture in the region close to the bottom and top surfaces of the cylinder (some specimens were broken during the tests). Figure 6-32 illustrates the fragility of the material.

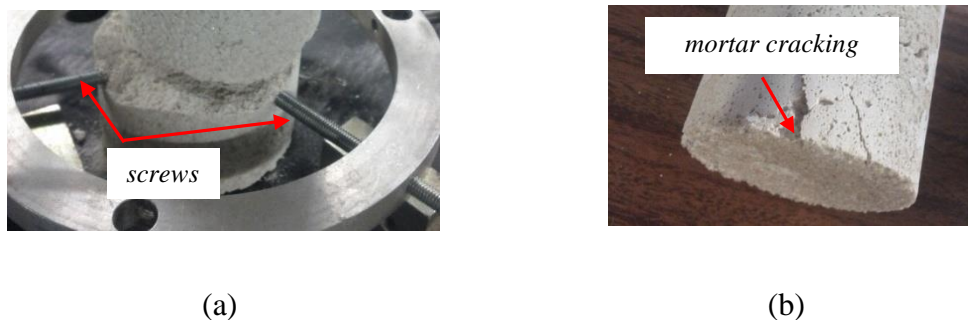


Figure 6-32 – Problems during the e-modulus test (a) break due to screws - (b) cracks in the specimen

The first load cycle was not considered for the calculations of the elastic modulus. During the test, some seating and time dependent effects were experimentally observed, meaning that, for the final analyses of the results, the data stress vs strain of the first cycle were discarded. Figure 6-33 shows a typical curve stress vs strain of the measurements, from the second to the last cycle.

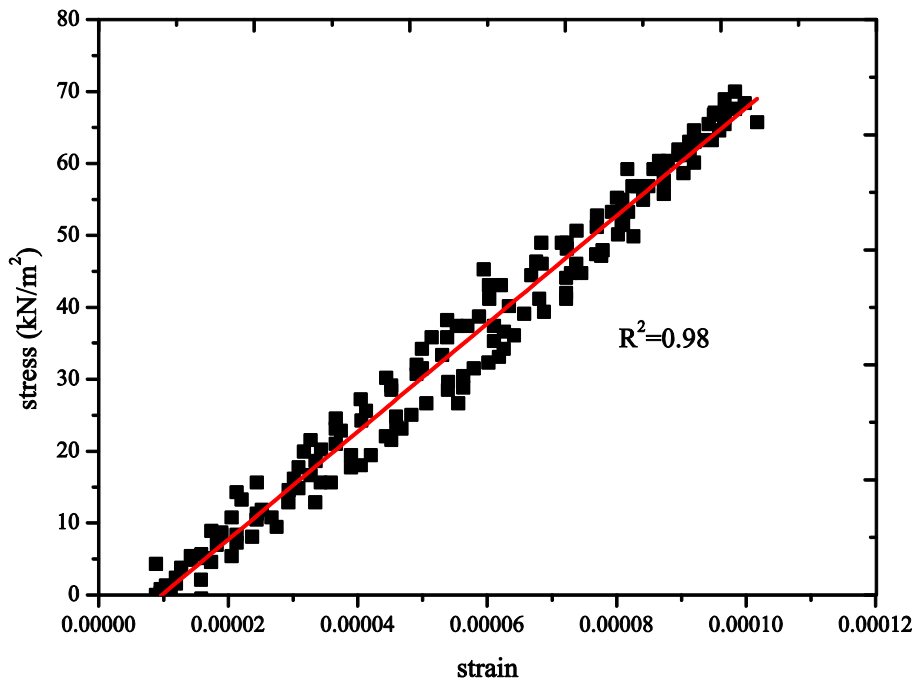


Figure 6-33 – Typical curve: stress vs strain from the second cycle and linear approximation – specimen after five days from casting – *ICI*

The linear correlation presented in Figure 6-33 graphically represents the elastic modulus. Specifically for this example, an elevated R^2 coefficient was obtained ($R^2=0.98$), demonstrating the elastic linear behavior of the material for the range of tested load. For the sake of the brevity, and because the aspect of the curves obtained were similar, the graph for other specimens and ages are not shown. Considering the experimental tests for elastic modulus done at different ages, the results are summarized in Table 6-11. The data were grouped according with the specimen adopted.

In chronologic terms, these tests were the first experiments done, therefore, the problem related to the non-uniform density for different specimens was more evident. Some specimen presented smaller densities (such as *EI-C* or *EI-I*), as, probably, they were cast when the hydration process was still occurring (exothermic reaction). Therefore, the initial density was reduced because of water evaporation. The average of e-modulus measured for different

specimens, were grouped in terms of ages, without any distinctions for different densities. Considering the entire measurements, there was a trend of increase over time, which was more evident for the measurements done at 4-5 days to 7-11 days (~150% see Figure 6-34).

Table 6-11 – Results of elastic modulus test – *ICI*

Specimen	Time from casting (days)	Density (kg/m ³)	E modulus (GPa)
<i>El-A*</i>	4	1825	0.75
<i>El-B*</i>	4	1850	0.67
<i>El-B*</i>	5	1850	0.93
<i>El-C*</i>	5	1777	0.84
<i>El-D</i>	7	1754	2.23
<i>El-D</i>	28	1771	2.70
<i>El-D</i>	38	1783	2.84
<i>El-E</i>	11	1793	1.51
<i>El-E</i>	25	1801	2.42
<i>El-E</i>	28	1801	2.44
<i>El-F</i>	25	1755	2.27
<i>El-F</i>	35	1770	3.41
<i>El-G</i>	18	1732	2.60
<i>El-G</i>	35	1734	3.30
<i>El-H*</i>	18	1740	2.71
<i>El-I</i>	7	1817	2.03
<i>El-I</i>	28	1830	3.04
<i>El-I</i>	35	1859	3.11
<i>El-J</i>	7	1848	2.71
<i>El-L</i>	7	1851	2.21
<i>El-L</i>	21	1861	3.51
<i>El-L</i>	28	1863	3.57
<i>El-L</i>	35	1865	3.86

Specimens marked with * were tested only for one age, since they were too fragile to repeat the test.

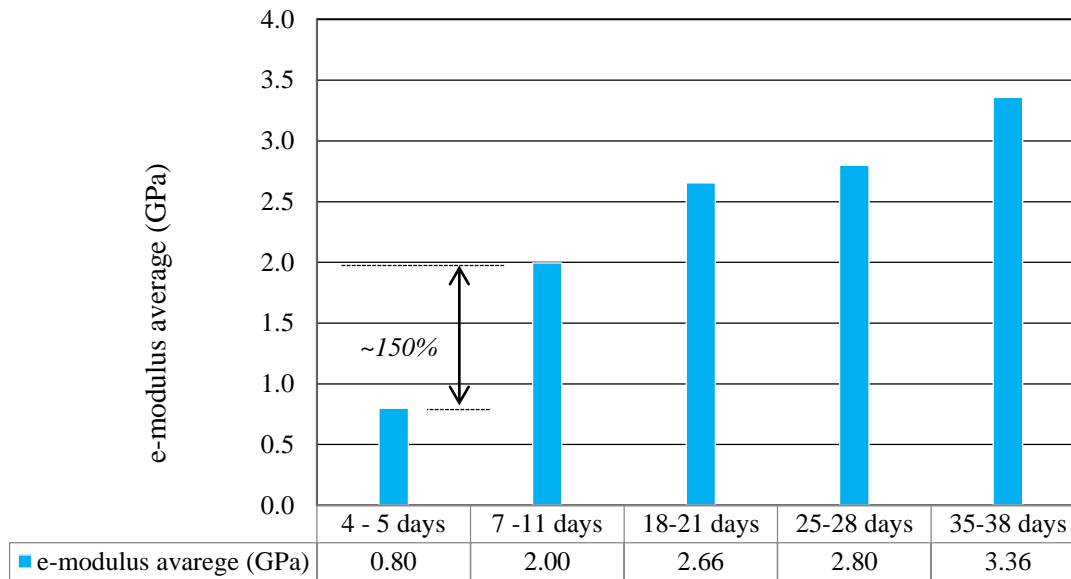


Figure 6-34 – E-modulus results grouped by ages for different specimens (days from casting)

The results presented in Table 6-11 indicated a general tendency of density dependency. For instance, the specimen *El-L* with density of 1865 kg/m^3 , after 31 days of demolding presented the e-modulus equal to 3.86 GPa, while the specimen *El-I*, with density = 1734 kg/m^3 , presented, for the same age, an e-modulus equal to 3.30 GPa. The difference of the densities for the two specimens was $\sim 6\%$, while for the elastic modulus results was $\sim 16\%$. This behavior could also be observed for other specimens. With the objective to study the influence of the density of the specimens on the results, the values presented in Table 6-11 were grouped considering four different density ranges $1700\text{-}1750$; $1750\text{-}1800$; $1800\text{-}1850$ and $1850\text{-}1900 \text{ kg/m}^3$ (see Figure 6-39).

In Figure 6-35, even if the data presented a certain scattering, a general tendency is clear, as specimens with a higher densities reached larger e-modulus values. These results were comparable to those obtained by Margalha *et al.* (2011) (modulus of elasticity measured by resonance frequency in $40 \text{ mm} \times 40 \text{ mm} \times 160 \text{ mm}$ specimens). The authors used specimens with 1:5 and 1:13 lime:aggregate by weight and mortar matured for 7 days before casting. They reached a value for e-modulus at 28 days a value of $\sim 3 \text{ GPa}$ and the e-modulus at 90 days was $\sim 4.6 \text{ GPa}$ (Margalha *et al.*, 2011). The densities of the specimens are not specified by the authors. The results obtained herein were in the same range of values, $\sim 2\text{-}3 \text{ GPa}$ after 7 days.

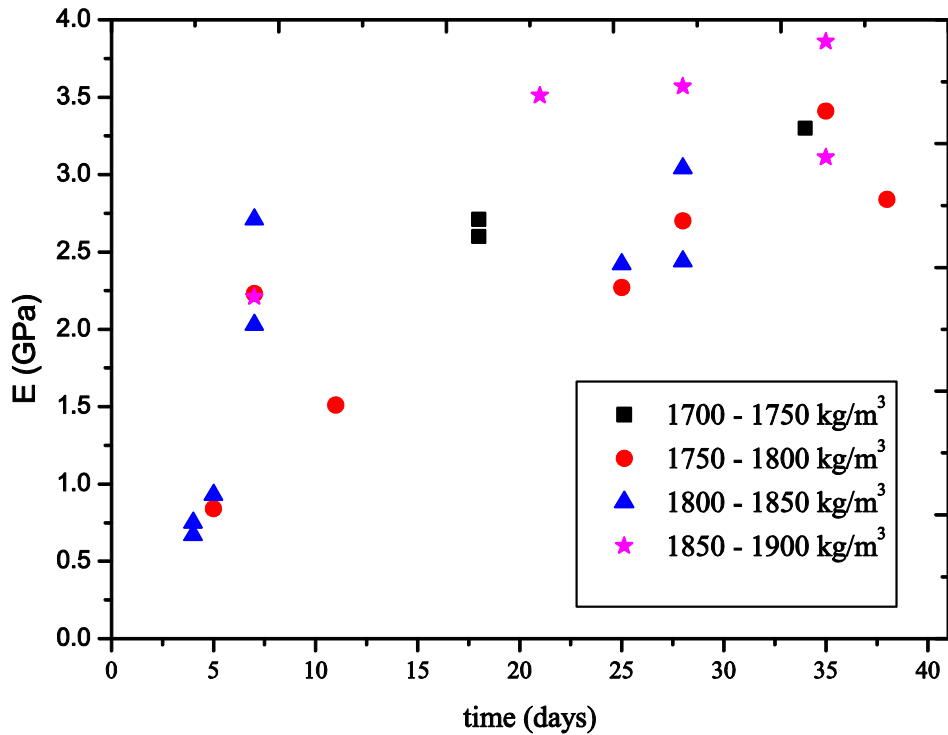


Figure 6-35 – E-modulus results grouped by ranges of densities (days from casting)






- *Carbonation depth in cylinders used to study the elastic modulus*

In continuity with the study, and using the same cylinders, with *ICI* curing conditions, the carbonation depth was measured, as already adopted in another part of this work, phenolphthalein in ethanol solution was used (RILEM, 1988). After the phenolphthalein spray, the carbonation depth was measured using a caliper rule. These tests were done at four different ages: 0, 4, 14, 21 and 36 days after the demolding process, and the results are summarized in Table 6-12.

The results presented in Table 6-12 showed an increase of the carbonation depth over time. This phenomenon was in conformity with the increase of the elastic modulus.

For the first day, the phenolphthalein sprayed in the specimen did not indicate the presence of carbonation, while for the last measurement, after 36 days it presented ~9.8 mm. These results were in coherence with the data presented in Figure 6-12.

Table 6-12 – Carbonation depth in cylindrical specimens - elastic modulus test (time expressed after the demolding)

Time (days)	Carbonation depth (mm)	Carbonation depth (picture)
0	~ 0	
4	1.2	
14	5.5	
21	6.2	
36	9.8	

In Figure 6-36 is shown the evolution of the carbonation depth.

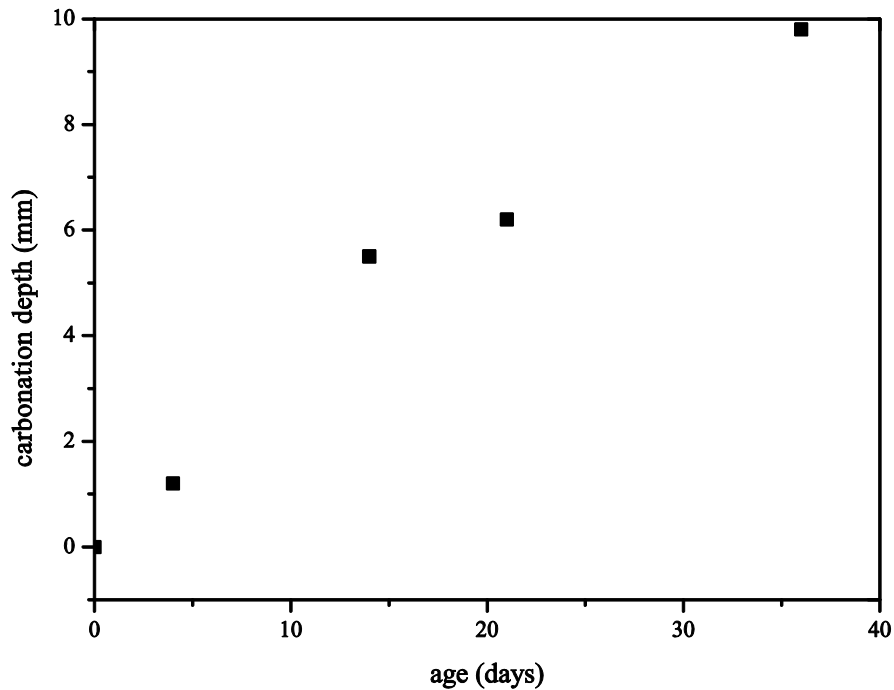


Figure 6-36 – Evolution of the carbonation depth for cylinders used to investigate the elastic modulus evolution – *IC1*

As summary of the experimental program done in this section, these experiments were preliminary tests. In this stage, one aspect to consider is the fact that the top and bottom surfaces of cylinders were not isolated from the environmental contact. In this sense, a new experimental setup, in terms of initial curing conditions is presented next.

6.5.3 Elastic modulus in cylinders with sealed top and bottom faces (part B)

This section presents the *part B* of the investigation of the e-modulus evolution. Comparing with the method used on the previous study, some advances were introduced, especially regarding the initial curing condition with the use of plastic net as previous described in Section 6.2 (*IC2*). The influence of the environmental humidity on the evolution of the elastic modulus was also studied with an additional environmental condition.

Two sets of specimens were cast, one stored in the “*standard*” climatic chamber ($h_{chamber} \approx 60\%$) and another stored in an environment with elevated humidity, “*humid*” chamber ($h_{chamber} \approx 90\%$), see Table 6-1. The mixture procedure was detailed in Section 5.4. Table 6-13 presents the densities for the different specimens according with the ages.

Table 6-13 – Summary of densities of specimens

<i>h_{chamber} ≈ 90%</i>		
Time (days)	<i>EM-H90-2</i>	<i>EM-H90-3</i>
	Density (kg/m ³)	Density (kg/m ³)
8	2032	2039
15	1941	1982
21	1873	1956
<i>h_{chamber} ≈ 60%</i>		
Time (days)	<i>EM-H60-6</i>	<i>EM-H60-7</i>
	Density (kg/m ³)	Density (kg/m ³)
8	1863	1855
15	1853	1857
22	1823	1813

The specimens stored in the “*humid*” climatic chamber presented more elevated density values. This phenomenon could be explained with the fact that they probably presented slower water flux, since the environment presented elevated humidity.

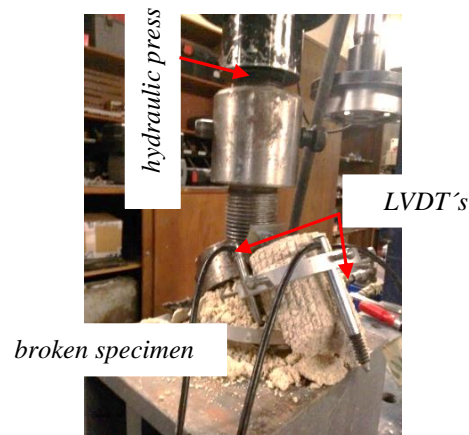


Figure 6-37 – Damage in specimen *EM_H90_1* after testing

Regarding the elastic modulus tests, for the specimens stored in the “*standard*” chamber, a cyclical load was applied as presented in previous section (~300 N). The specimens stored in the “*humid*” chamber did not resist the applied load during the test (see Figure 6-37). Due to this reason, the cyclical load applied was reduced to the amplitude of ~100 N.

Even with the reduction of the applied load, during the tests the cylinders stored in the “*humid*” chamber presented a residual displacement for each load step, as can be seen in Figure 6-38.

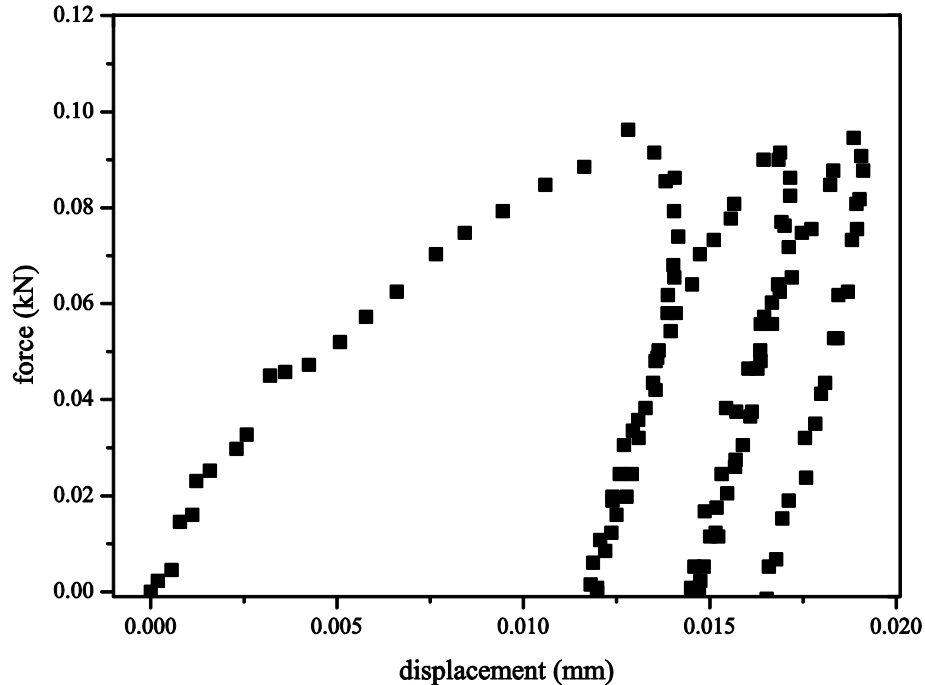


Figure 6-38 – Example of curve: force vs displacement for cylinder stored inside the “*humid*” climatic chamber

The evolution of the elastic modulus for specimens stored in the two environments is presented in Figure 6-39. The results of cylinders stored on the climatic chamber with $h = 90\%$ should be considered with special attention. The values presented are the average of the results, since as shown in Figure 6-38, the modulus for those specimens changed during the test. Because of limitations regarding the equipment availability, the last tests were done at different ages, respectively, 22 and 21 days for the specimens stored in the “*standard*” and “*humid*” chambers.

The relatively low number of results presented was associated with the fact that some specimens were discarded to keep a range of homogeneity for density values ($\sim 5\%$), and because some cylinders presented damage during the tests. Comparing the results for the specimens stored in the two environments, at the age of 8 days the average of e-modulus for the cylinders stored inside the chamber with $h \approx 60\%$ was ~ 3 GPa; while for $h \approx 90\%$, values ~ 0.8 GPa were obtained, a difference of $\sim 73\%$. A similar variation was also obtained for the

age of 15 days with values ~ 3.5 GPa and 1.0 GPa respectively for the “standard” and “high humidity” chambers.

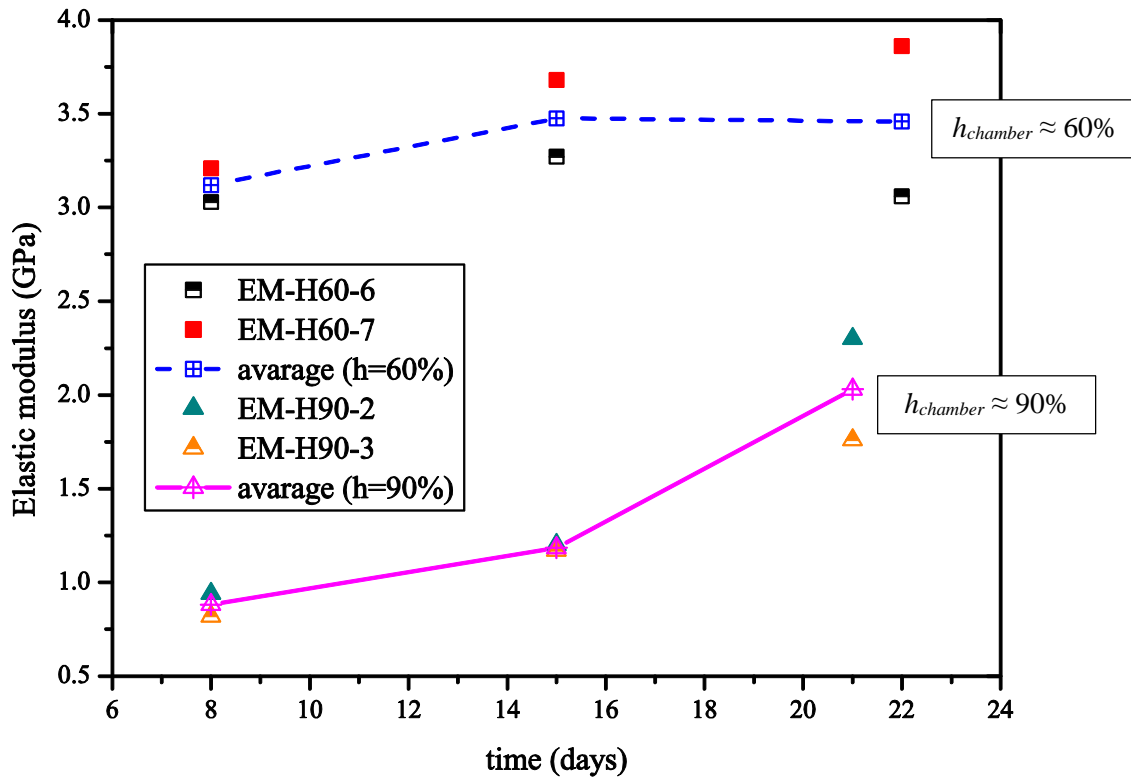


Figure 6-39 – Evolution of elastic modulus for the two studied environments ($h_{chamber} \approx 60\%$ and $h_{chamber} \approx 90\%$)

The average of e-modulus for specimens stored at 60% h reached 3.5 GPa at 22 days, a value that was comparable with the preliminary tests (see Section 6.5.2). The results for the specimens in the previous section, for similar ages indicated the average of values around 3 GPa considering the results between the ages of 21 to 25 days. At the age of 22 days, the cylinders stored inside the chamber with $h \approx 60\%$ presented a higher dispersion. In fact, this result was not expectable and the scattering made the average of e-modulus for the age of 15 to 22 days nearly constant. This effect was observed because the value of the e-modulus for *EM-H60-6* for the 22th day decreased in comparison with the result for the fifteenth day.

The difference on the results according with the environment is explained with a simplified analogy with a soil material, in which macroscopic properties depend on particle interactions (Scholtès *et al.*, 2009, Aysen, 2002), and the elevated water content may affect the interaction between grains, influencing the cohesion of the material (Das and Sobhan, 2009). This phenomenon could also be linked with the results presented in Figure 6-39. In fact,

different authors, for instance, Callebaut (2000), Lanas *et al.* (2004a), Ngoma (2009) and Izaguirre *et al.* (2011), also cite similar influence of the humidity for lime based mortar. Considering the presented concepts, the elevated humidity inside the mortar would result in a lower capacity to resist the applied loads during the tests, with a consequently lower stiffness. The elevated humidity also could be associated with a smaller extension of the carbonation process in comparison with the cylinders stored in the environment with $h_{chamber} \approx 60\%$, since it could difficult the CO_2 ingress (see Section 2.5.3).

6.5.4 Evolution of compressive strength

This section describes the methodology and the results obtained by test to evaluate the compressive strength. The procedure for casting adopted in this work, are different from the procedure presented in the standard EN 1015-11 (CEN, 1999b) for determination of flexural and compressive strength. Firstly, since the flexural strength was not studied herein, cubic specimens were adopted and casted. According to EN 1015-11 (CEN, 1999b), specimens with $16 \text{ cm} \times 4 \text{ cm} \times 4 \text{ cm}$ should be cast, for flexural test, and the compressive strength of the mortar is determined on the two parts resulting from the flexural strength experiment. Herein, the recommendation was not adopted because experimental problems were faced during the casting and demolding process, for instance, cracking and experimental limitations. The compressive test was carried out in cubic specimens $5 \text{ cm} \times 5 \text{ cm} \times 5 \text{ cm}$. The procedure for casting presented in the norm EN 1015-11 (CEN, 1999b) was also not followed, in which the use of cotton gauze and absorbent filter paper is suggested. This may represent a suggestion to reproduce the absorbent behavior of bricks (Meneghini, 2014). For the sake of simplicity a simple casting in the steel molds took place (see Section 5.4). Information about the initial curing condition were presented in Section 6.2. After this initial time, during the demolding process, some cubes were damaged or completely broken (see Figure 6-40), and these specimens were discarded.

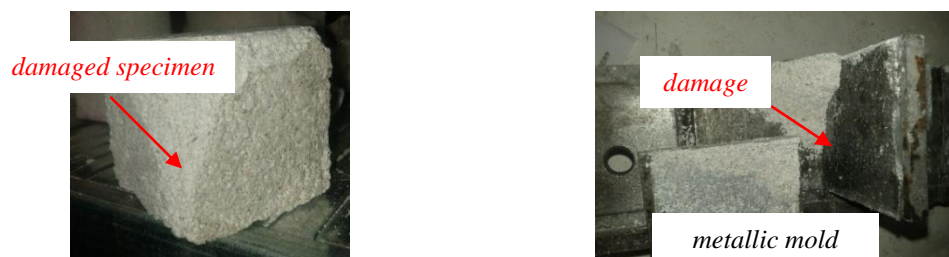


Figure 6-40 – Example of damaged cubic specimen

For the experiments at each age, six cubes were prepared. For the ages of 14 and 28 days, all the specimens were tested in the hydraulic testing machine, while, for the evaluation of the carbonation at longer ages, for 120 and 140 days, 5 cubes were used to estimate the compressive strength, and one specimen was broken to measure the carbonation depth. During the experiments, the cubes were submitted to an increasing compressive load at the rate of 50 N/second, up to the failure (CEN, 1999b). The typical curves load vs displacement obtained from compressive strength test at four different tested ages are presented in Figure 6-41.

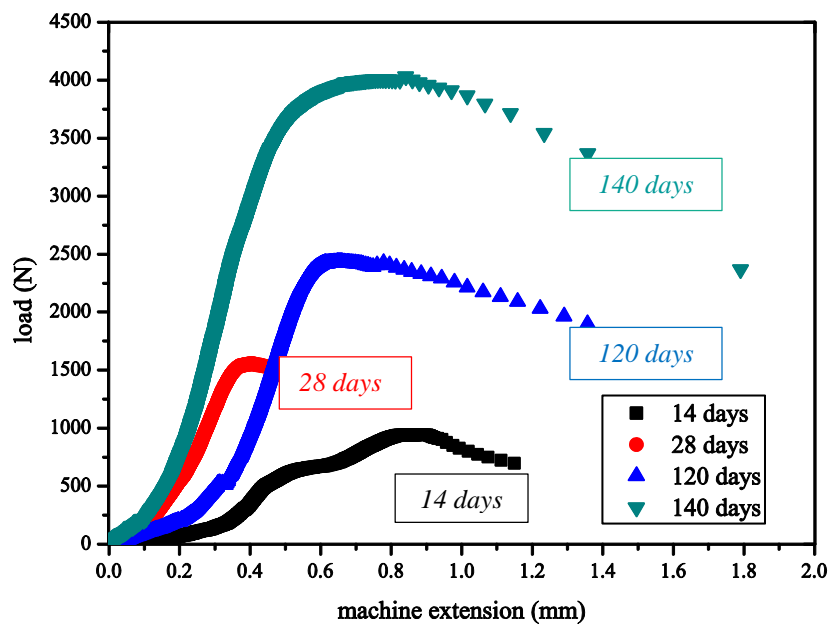


Figure 6-41 – Typical curves for compressive strength test, ages: 14, 28, 120 and 140 days

The aspect of the curves presented approximately the same form for the four tested ages (see Figure 6-41). An initial slope (due to seating of the specimen, adjusting to the steel plates) was then followed by a second inclination until the load capacity peak. After this, there was a decrease of the applied load by the testing machine, and a significant displacement.

The summary of the experimental results are shown in Table 6-14.

The density values presented in Table 6-14 are the average for all the six cubes for the ages of 14, 28, 120 and 140 days. Since for each tested age, the specimens presented a relatively small variation on the densities values (~3%), the data were grouped.

Table 6-14 – Summary of results of compressive strength test

Time (days)	Average compressive failure stress (MPa)	Standard deviation	Average density (kg/m ³)	Carbonation depth (mm)
14	0.37 (6 cubes)	0.03	1820	~2.2
28	0.49 (6 cubes)	0.10	1840	~4.5
120	1.16 (5 cubes)	0.22	1835	~16.0
140	1.61 (5 cubes)	0.13	1850	~20.0

Phenolphthalein was applied once more to investigate the carbonation depth, and the typical results at four different studied ages are presented in Figure 6-42.

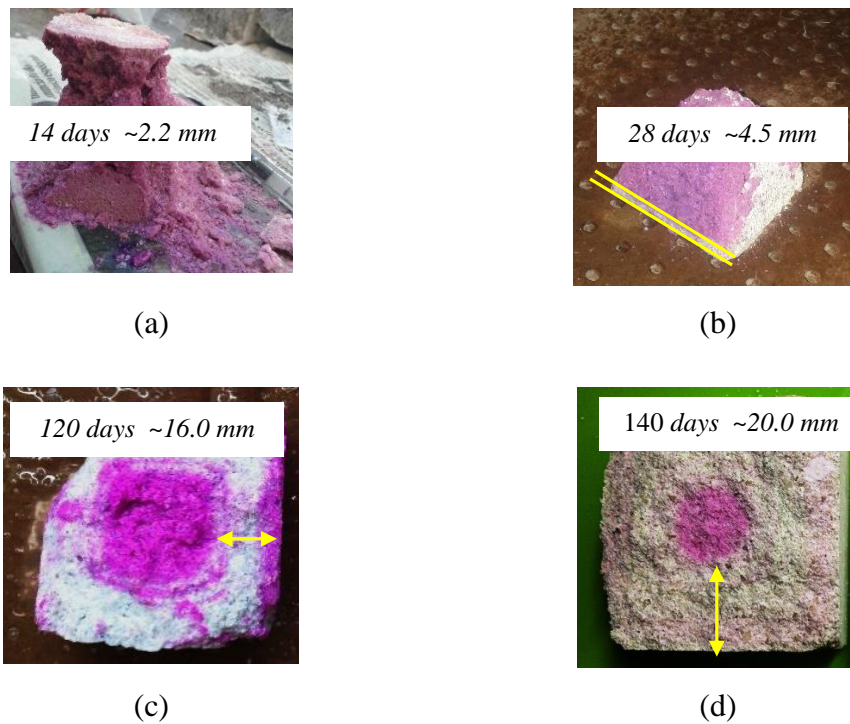


Figure 6-42 – Carbonation depth in cubes (a) 14 days, (b) 28 days, (c) 120 days and (d) 140 days

As shown, the compressive strength values increased continually, as the carbonation depth. The average of compressive strength for 140 days was almost five times higher than for 14 days, while the carbonation depth was approximately nine times larger when the results for the same ages were compared. For the current experiments, the standard deviation presented higher value for the cubes tested at 120 days (~0.22), because the results for this age showed more scattering, while for the other ages the values were smaller (see Table 6-14).

With the objective to compare values from the literature with the results of the current work some references are cited. In the research of Lanas and Alvarez-Galindo (2003), in which the authors adopted a 1:3 lime:aggregate ratio, dry hydrated lime and silicate sand, the results showed values for 14 days around 0.45 MPa and 0.6 MPa, depending on the type of the silicate sand adopted (Lanas and Alvarez, 2003). At 28 days the compressive strength was around 0.5 to 0.9 MPa (Lanas and Alvarez, 2003). The compressive strength was measured by Moropoulou *et al.* (2005) with 1:1.5 and 1:1.8 lime:aggregate ratio, using both lime putty and dry hydrated lime, and the authors obtained a value ~0.69–0.90 MPa after 30 days. The range of values found in the present work was in coherence with both references. Experimental observations showed the presence of carbonations rings, especially for cubes tested at the age of 140 days, to illustrate, the Liesegang patterns are indicated with arrows in Figure 6-43.

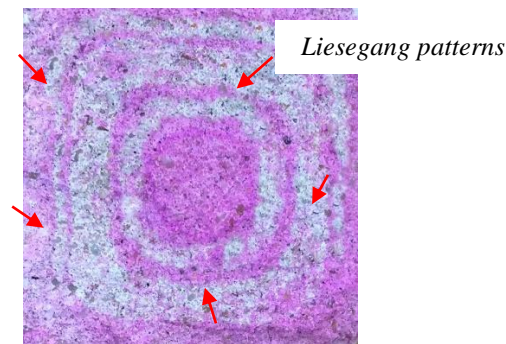


Figure 6-43 – Liesegang patterns in cubic specimen indicated with arrows - measurement after 140 days

The Liesegang phenomenon is a quasi-periodic self-organized occurring in the wake of a moving reaction front (Rodríguez-Navarro *et al.*, 2002). Liesegang patterns present generally the shapes of rings or spheres (Rodríguez-Navarro *et al.*, 2002), although there are more complex patterns such as spirals (Rodríguez-Navarro *et al.*, 2002, Henisch, 1988). In spite of their abundance, Liesegang patterns are formed only under specific physical-chemical conditions (García-Ruiz *et al.*, 1996). According to Rodríguez-Navarro *et al.* (2002), the moving of the carbonation front towards the center of the specimen results in their occurrence. The location of the patterns is determined by the spatial and temporal arrangement of the crystallization conditions (Rodríguez-Navarro *et al.*, 2002). In addition to the previous cited references, more information about this phenomenon can be found in literature (Arizzi and Cultrone, 2013, Lawrence *et al.*, 2006a, Lawrence, 2006).

6.5.5 Evolution of compressive strength in standard and high humidity environments

This part of the work presents the results for two series of cubes specimens with the same dimensions as presented in previous section. The main purpose was to compare the compressive strength for 28 days, for specimens stored in the standard conditions and inside the “*humid*” chamber. The same initial curing conditions and compressive load increasing rate of the previous tests were adopted. The tests were conducted on three specimens exposed to each of the climatic chambers, and the results can be seen in Table 6-15.

Table 6-15 - Compressive strength results for specimens stored inside the “*standard*” and the “*humid*” chambers (specimens tested at 28 days after casting)

Chamber	Average density (kg/m ³)	Average compressive strength (MPa)	Standard deviation
<i>h_{chamber} ≈ 60%, standard</i>	1821	0.73	0.13
<i>h_{chamber} ≈ 90%, humid</i>	1835	0.40	0.10

Considering the initial density of fresh mortar (~2000 kg/m³), a decreasing tendency in both environments could be observed, and this reduction was also observed in other experiments. For the specimens stored inside the “*standard*” chamber, the results for 28 days after casting, when compared with the tests presented in the previous section, for the same age and conditions, presented an increase of the average values from 0.49 MPa to 0.73 MPa. This discrepancy could be associated with some inaccuracies during the experiments, for instance related with a faster decrease of the humidity inside the specimen or an increase in the carbonation, since these two processes might affect the material strength.

For the specimens stored inside the “*standard*” climatic chamber, the average value for compressive strength was ~0.73 MPa, and for the “*humid*” chamber, ~0.40 MPa. Therefore, the specimens maintained inside the chamber with higher environmental humidity presented a value ~45% smaller than the ones kept in the standard conditions.

In terms of compressive strength, the data trend was compatible with the obtained results for e-modulus, with specimens exposed to the same conditions. In terms of mechanical behavior, the specimens stored in wetter condition tended to present smaller values of strength/stiffness. The reduced strength, as previously mentioned, could be associated to prolonged contact with the higher environmental humidity. This phenomenon is linked with

the excess of water inside the specimen, that would reduce the interaction between the grains, and also it could reduce the carbonation, since it limits the CO₂ ingress.

7 NUMERICAL SIMULATIONS OF EXPERIMENTS

7.1 Introduction

This chapter describes the numerical simulations concerning the experiments presented in Chapters 5 and 6, regarding humidity, carbonation and mechanical properties. There has been no previous attempt for multi-physics simulation of aerial lime mortar, thus bringing added difficulties in ascertaining the feasibility of the modelling parameters and strategies adopted herein.

The work reported in this chapter is leveraged in previous knowledge generated from experiments that have been reported in previous chapters of this thesis. Chapters 3 and 4, related to the humidity flux in cementitious materials, was the basis of the numerical implementation. The deployment of the multi-physics model was made in the framework of Chapter 4 and finally the parameter/model oriented experimentation reported in Chapters 5 and 6 provide closure to the integrated knowledge brought upon the present chapter. Specimens with the same composition were tested, and their results were adopted in the simulations for the present chapter, which are outlined in Figure 7-1 and briefly described in the following paragraphs.

The work reported in this chapter follows a sequence of parameters achievement, from the simplest to the more sophisticated model. This chapter is mainly focused in the simulation of different aspects regarding the specimens with cylindrical shape, which was a common geometry among the several experiments that have been conducted.

The working strategy initially consisted in merely evaluating the necessary simulation parameters for humidity field simulations, under the simplifying assumption that the humidity field could be decoupled from the remaining physical fields (carbon dioxide, carbonation and mechanical fields) - see Figure 7-1 a. With the set of parameters obtained from the humidity tests, the coupled model could be applied. In continuity with the study, the multi-physics coupled model was then applied in the set of experimental results. Based on the model and parameters presented by Ferretti and Bažant (2006a), the experiments regarding carbonation processes were simulated (see Figure 7-1 b). Firstly, the results obtained through TGA testing on samples collected from cylinders at three different depths and different ages were adopted to calibrate the multi-physics model with a set of parameters. With this set of initial parameters, the cylinders used to study the carbonation process with

phenolphthalein were simulated. These analyses were carried out in an integrated way, considering the two experiments (TGA + phenolphthalein).

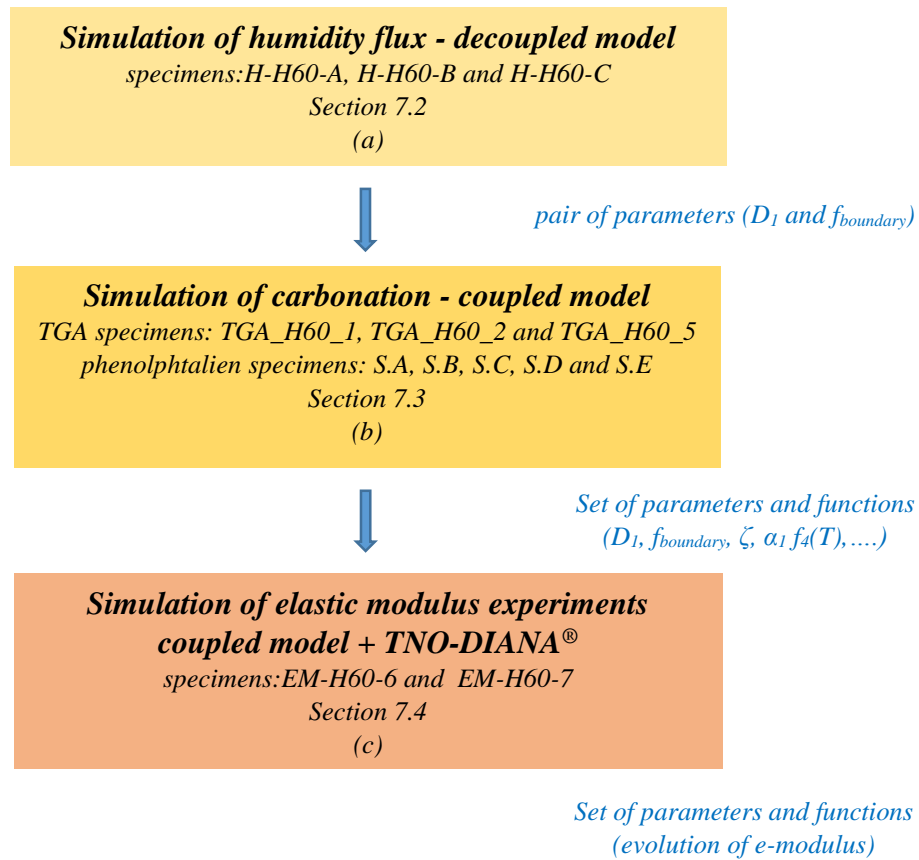


Figure 7-1 – Sequence of modeling and simulations

The results from the coupled hygro-carbo model (implemented in Matlab®) were then exported to TNO-DIANA® (TNO-DIANA-BV, 2010) (see Figure 7-1 c) in order to perform the mechanical analyses. Such studies intended to simulate the experiments in which the e-modulus of aerial lime mortars were tested (at several ages). The full hygro-carbo-mechanical numerical framework was adopted to simulate the evolution of the material properties over time. Considerations are made about the evolution of the elastic modulus as a function of the carbonation reaction itself, together with the effect of internal humidity reduction.

7.2 Humidity field

In the absence of previous research works focused on the determination of moisture diffusion parameters for humidity simulation in aerial lime, the work reported herein followed a similar strategy to the one presented in Chapter 4 in the scope of concrete humidity simulation. Therefore, the same finite difference code was deployed in order to simulate and obtain the best pair of relevant model parameters (D_1 and $f_{boundary}$) for the humidity flux on aerial lime mortar. As the experiments to simulate pertained to cylinders subject to drying in the outer surfaces (and sealed on top/bottom), the axisymmetric models described in Chapter 4 were adopted and a pair of $f_{boundary}$ and D_1 to simulate the experimental results was obtained. In the absence of proposals targeted to aerial lime, the parameters α , n and h_c were chosen with basis on the recommendations presented by the Model Code (CEB–FIP, 2010) for concrete.

The self-desiccation of aerial lime mortar that was measured experimentally and reported in Chapter 5, was also considered on the simulations. In this way the algorithm considered an initial reduction of humidity for each node as experimentally measured ~10% in Section 5.5.3: the actual initial condition for internal humidity was therefore of 90%. A Neumann formulation (Azenha, 2009, Oliveira *et al.*, 2015) for the boundary condition with a specified boundary coefficient and a constant environmental humidity equal to 60% was considered in correspondence to the humidity of the climatic chamber in which the drying experiments took place.

For the following analyses of humidity diffusion process, both the space and time discretizations were constant: 0.25 cm; $\Delta t = 0.001$ days. A range of values for D_1 from 10 to 70 mm²/day with increments of 5 mm²/day was tested. For the boundary coefficient, $f_{boundary}$, values from 5×10^{-4} to 100×10^{-4} m/day with an increment of 10×10^{-4} m/day were adopted in an iterative process. These values were estimated considering the experience assimilated in Chapter 4.

The simulation was carried out in view of specimens *H-H60-A*, *H-H60-B* and *H-H60-C*, which test results are shown in section 5.5.3. The R^2 (coefficient of determination) for the parametric simulation results, as compared to experimental values was calculated, and the corresponding results for each specimen are shown in Figure 7-2. The selection of the best pair D_1 and $f_{boundary}$ values was made based on the maximization of the maximum sum of R^2 for the results of the three specimens ($R^2_{H-H60-A} + R^2_{H-H60-B} + R^2_{H-H60-c}$). Consequently, the

best pair of values was: $D_1 = 60 \text{ mm}^2/\text{day}$, $f_{\text{boundary}} = 25 \times 10^{-4} \text{ m/day}$. With these parameters, the values for R^2 were: 0.68, 0.74 and 0.86 respectively for *H-H60-A*, *H-H60-B* and *H-H60-C*.

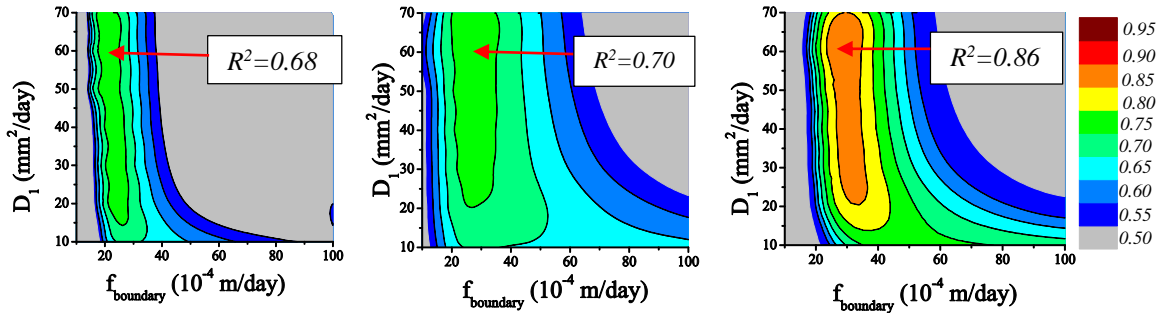


Figure 7-2 – Determination coefficient for numerical results from the simulations of the three specimens (*H-H60-A*, *H-H60-B* and *H-H60-C*)

As can be seen in Figure 7-2, the iso-curves for R values assume almost vertical position, meaning that the D_1 factor has very small influence on the results, as opposed to the case of f_{boundary} . This behavior is in opposition to the one observed in Chapter 4 for concrete specimens, in which both parameters (D_1 and f_{boundary}) had significant influence on the calculated humidity fields. Herein, possibly because of the reduced size of the specimen studied, for a fixed value of f_{boundary} the influence of the diffusivity was reduced.

In sequence, the numerical results adopting the pair of D_1 and f_{boundary} previously obtained are presented. For cylinder *H-H60-A*, the results are shown in Figure 7-3. Small dispersions were observed, specially after the 10th day. A discrepancy ~5% between the numerical and experimental results was observed for the age of 15 days.

Continuing with study, the results of the simulation for the cylinder *H-H60-B* and *H-H60-C* are respectively presented in Figure 7-4 and Figure 7-5. An intermediary decrease observed in *H-H60-B* and *H-H60-C*, around the 8th day, (Figure 7-4 and Figure 7-5) was not completely captured by the model. The inherent experimental scatter might be cited, and also the simplified adopted modeling. In general, the observed dispersion might be considered acceptable.

When comparing the values for D_1 and f_{boundary} with the values obtained in Chapter 4 for concretes, the diffusivity for aerial lime was in the range of the previous obtained data, while for the f_{boundary} , the maximum value in mortar was approximately five times higher than the highest one used for concrete ($25 \times 10^{-4} \text{ m/day}$ as opposed to $5.5 \times 10^{-4} \text{ m/day}$). The value of

$f_{boundary}$ for aerial lime mortar might be related to the larger values of porosity as compared to concrete.

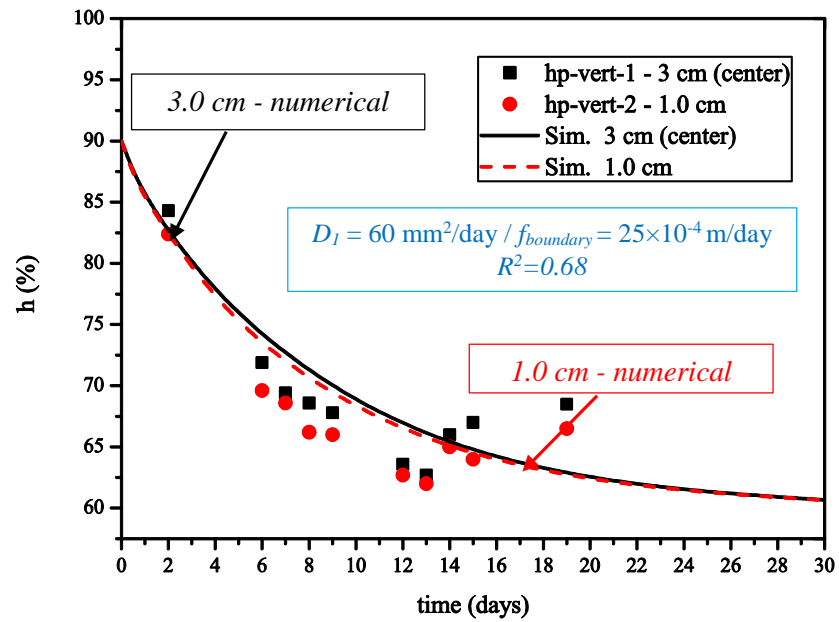


Figure 7-3 – Comparative results for humidity experimental and numerical simulation (cylindrical specimen - axisymmetric conditions - H-H60-A)

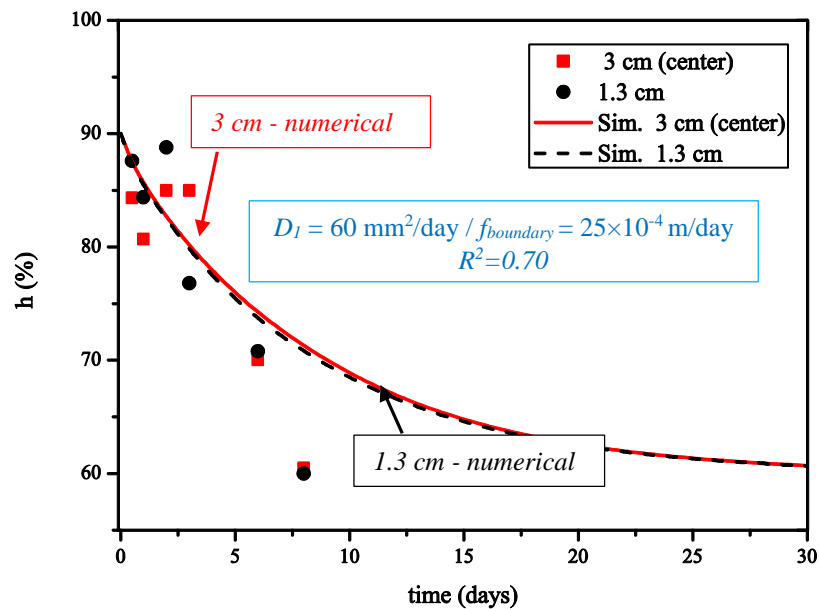


Figure 7-4 – Comparative results for humidity experimental and numerical simulation (cylindrical specimen - axisymmetric conditions - H-H60-B)

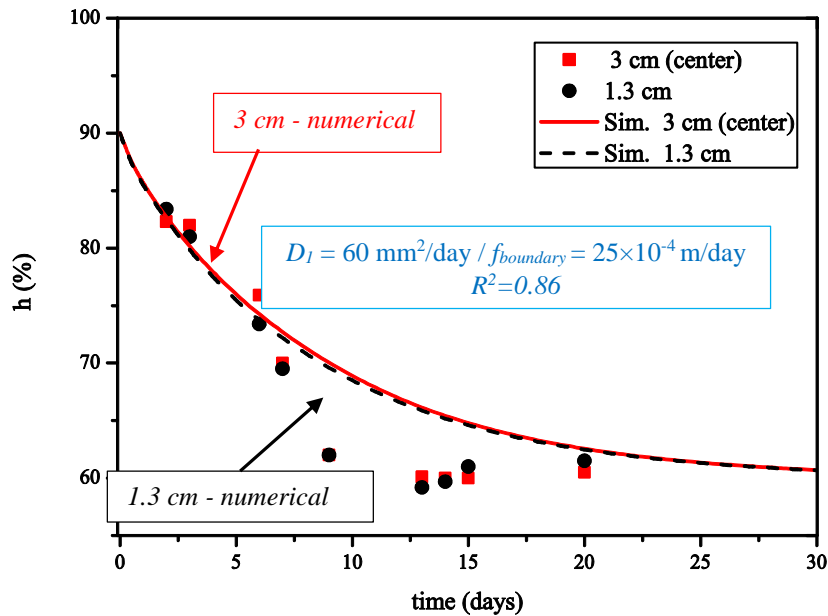


Figure 7-5 – Comparative results for humidity experimental and numerical simulation (cylindrical specimen - axisymmetric conditions - *H-H60-C*)

In this section, the simulations adopted a decoupled model that solely contemplated the humidity field and did not explicitly account for carbonation effects. Experimentally, the humidity diffusion process demonstrated to be faster than the carbonation (see Chapter 5 and 6). The reaction occurred slowly, and assuming that the carbonation process affects the material pore structure (more information can be seen in Section 2.5.4), the resulting reduction of the porosity during the testing duration is likely to have had a relatively small contribution, rendering feasibility to the decoupled modelling simplification adopted.

7.3 Carbonation

7.3.1 General aspects

This section presents the main considerations and the results for the simulation with the multi-physics model implemented in Chapter 4 (Ferretti and Bažant, 2006a). The results for the cylinders tested with TGA presented in Section 6.4.2 were simulated first (see Figure 7-6 a). A pilot simulation with the direct application of the model by Ferretti and Bažant (2006a) was the starting point for the modeling, but the formulation did not present satisfactory results. These authors did their simulations based in a set of parameters by assuming

similarity of aerial mortar with a concrete of low compressive strength, without any experimental support. Therefore, an optimization process was done. The pair of parameters previously obtained for the humidity field were adopted, together with modifications in different parameters regarding the carbon dioxide and the reaction fields.

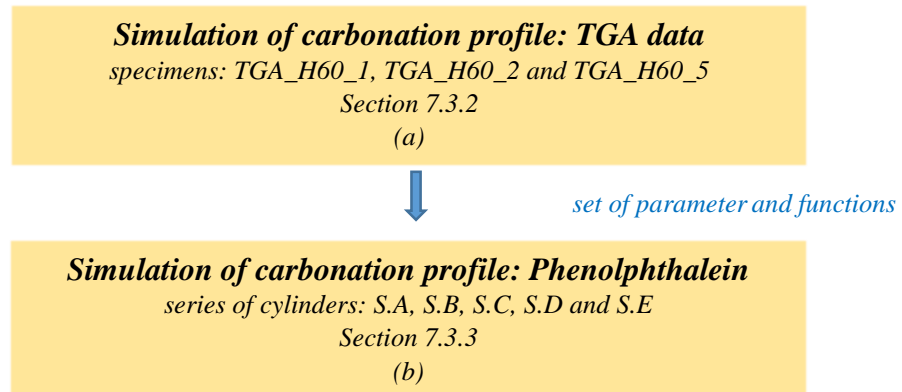


Figure 7-6 – Strategy for the simulation of carbonation process

From the functions and parameters' calibration obtained from the simulation of the carbonation in cylinders with TGA data, the set of values was in sequence applied on the study of the specimens with different sizes, with the carbonation depths measured by the phenolphthalein indicator (see Section 6.4). This study had the objective to verify the capability of the model to simulate the data from specimens of different sizes (see Figure 7-6 b).

7.3.2 Simulation of the TGA results :Parameters and proposals for model modification

The original parameters and functions for the multi-physics modeling were presented in Section 3.3.2. For the following numerical analyses, constant time and spatial discretizations were adopted: time step (Δt) = 0.002 days or equivalently 2.88 min, and nodal space (Δx) = 0.1 cm.

- *Initial carbonation degree*

Considering the experimental data from TGA, an initial carbonation percentage was found in the studied mortar. To illustrate the results, the TGA curve for fresh mortar is presented

with solid line in Figure 7-7 and, for the results using the sealed disc specimen, is shown with dashed line (specimen *TGA.ISO* was tested after 47 days, for more details see Section 6.4.2). For the fresh mortar, the TGA test showed the presence of calcium carbonate in a percentage $\sim 10\%$, a similar value was obtained for the sealed specimen, with a percentage $\sim 11\%$.

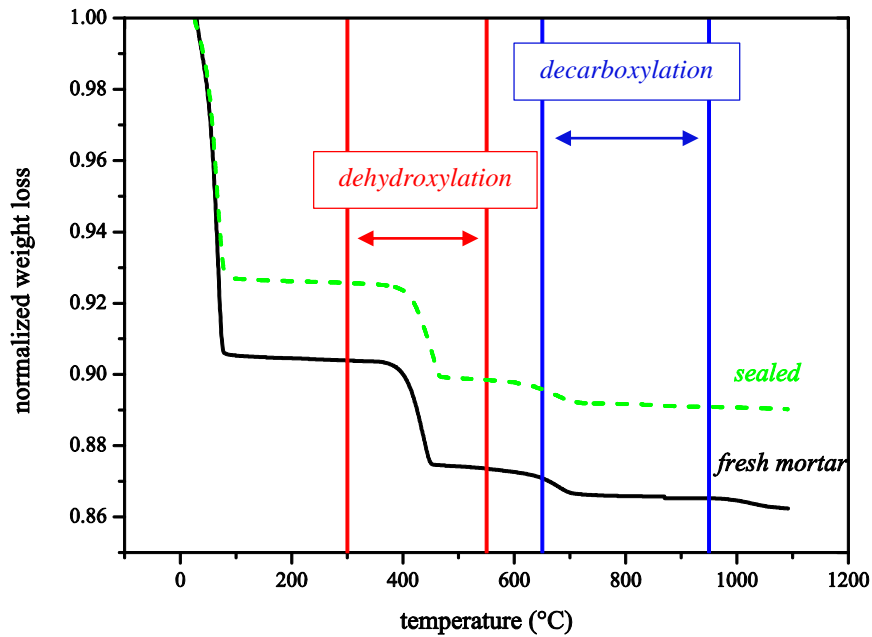


Figure 7-7 – TGA on fresh mortar ($R \approx 10\%$) and sealed specimen ($R \approx 11\%$) (test done after 47 days for the specimen in sealed condition)

The sample was stored in sealed conditions to avoid contact with external environment, particularly the carbon dioxide present in air (for the results, see Figure 7-7). These percentages ($\sim 10\%$) could be related to presence of CaCO_3 on the raw aerial lime and/or a fast initial carbonation that happened during the mixture and casting procedure.

The results at 1.5 and 3 cm depths at first day of TGA test also indicated a similar reaction percentage ($\sim 10\text{-}13\%$) as evidenced in Section 6.4.2. In view of these observations, it was decided to consider an initial carbonation degree of 10% in the numerical simulations.

- *Considerations about the coefficient ζ*

According to Eq. 3.39 in Section 3.3.2, the coefficient zeta (ζ) correlates the carbon dioxide diffusivity with the reaction degree. It is associated with the reduction of porosity after the

carbonation and can vary from 0 to 1 (Saetta *et al.*, 1995, Saetta and Vitaliani, 2004, Ferretti and Bažant, 2006a).

The transformation of $\text{Ca}(\text{OH})_2$ to CaCO_3 is a complex phenomenon, and depends of different factors (see Chapter 2). The final product (CaCO_3) can occur in different molecular arrangements, which imply the existence of distinct pore structures for the material (see Section 2.5.4). In the absence of direct evidence or indications about the values to consider for zeta, a range of values from 0.1 to 0.99 was tested, with increments equal to 0.1.

- *Considerations about the initial diffusivity for carbon dioxide*

As presented in Chapter 2 several complexities are involved in the CO_2 diffusivity, and the measurement of such parameter is not simple (Park *et al.*, 2012). Differently from the direct measurement of CO_2 diffusivity for instance done in concrete by Houst and Wittmann (1986), wherein the authors adopted an elevated CO_2 concentration (~2%), herein the value was obtained indirectly by an iterative process and in a natural CO_2 concentration.

As the model adopted by Ferretti and Bažant (2006a) and Saetta and Vitaliani (2005, 2004) assumes a direct relation between the carbonation degree and the concentration of CO_2 , the use of a reduced diffusivity value might be justified with the significant low carbonation degree found in the experiments with TGA (see Section 6.4.2). For these simulations, a range of values from 100 to 1200 mm^2/day was tested, with variations of 100 mm^2/day . After an iterative process, the adopted value for the initial diffusivity of CO_2 was equal to 200 mm^2/day , as it could reproduce the experimental R for the depths of 1.5 cm and 3.0 cm. The adoption of higher value would implicate a higher R for the two cited depths. The initial diffusion value of CO_2 was around 10 times smaller the value used by Ferretti and Bažant (2006a). The adopted value presented the same order of magnitude as the one adopted by Steffens *et al.* (2002) and by Muntean *et al.* (2011) for concrete. Houst and Wittmann (2002) also found low values for the CO_2 diffusivity in cement mortar, as a function of the percentage of aggregates.

- *Considerations about the boundary coefficient for CO_2*

In the work presented by Ferretti and Bažant (2006a), the authors adopted a imposed boundary condition for humidity and carbon dioxide flux (Dirichlet formulation). In

similarity with the humidity flux, a boundary coefficient (f_{carbo}) was applied to simulate the carbon dioxide field. The adopted value was $f_{carbo} = 10 \times 10^{-3}$ m/day. Since there is no information about the parameter in literature, the estimated value was around four times higher than the one adopted for humidity ($f_{boundary} = 25 \times 10^{-4}$ m/day), in agreement with the proportionality of the diffusivity values for both fields.

- *Considerations about the reaction parameter $\alpha_l f_4^*(T)$*

The $\alpha_l f_4^*(T)$ parameters can be found in Eq. 3.35, and it is related with the reaction field. Because the temperature was assumed constant during the experiments, and for sake of simplicity, the multiplication $\alpha_l f_4^*(T)$ was adopted a single parameter, as done by Ferretti and Bažant (2006a). The parameter α_l is related to material propensity to react, and $f_4^*(T)$ expresses the influence of the temperature. A range of values for $\alpha_l f_4^*(T)$ from 0.001 to 0.2 was tested, with increments equal to 0.05. To properly replicate the experimental data, with elevated carbonation degree in the boundary, the value $\alpha_l f_4^*(T) = 0.18$, was adopted. The parameter was around nine times higher than the adopted by Ferretti and Bažant (2006a).

- *Simulation with the presented proposal*

For a preliminary simulation, the TGA data for the depth of 1.5 and 3.0 cm after 69 days were initially disregarded, since they presented very low carbonation degree (the points are marked with a circle and arrow in Figure 7-8). Considering the parameters already presented, which represent the best fitting scenario disregarding the last experimental data, the experimental and numerical results are shown in Figure 7-8.

Since the samples of mortar collected in surface regions were extracted in a small depth of the specimen, for the numerical results presented, the values for the depth named as “boundary” were obtained with a simple average of R for the nodes at 0 and 1 mm (respectively first and second nodes).

As Figure 7-8 presents, for the experimental data on the boundary, the model already could simulate reasonably the test results, as also for the depths of 1.5 and 3 cm, with exception to the last age, with a considerable overestimation. The humidity diffusion process occurred faster as shown in Section 7.2, due to this fact in the coupled model, the ingress of CO_2 was accelerated and consequently the carbonation, because, as presented in Chapter 3 and 4,

these two fields are directly linked. The diffusivity of CO₂ was adopted as a relatively low value, and even with an additional reduction, the model was still not able to properly reproduce the experimental data.

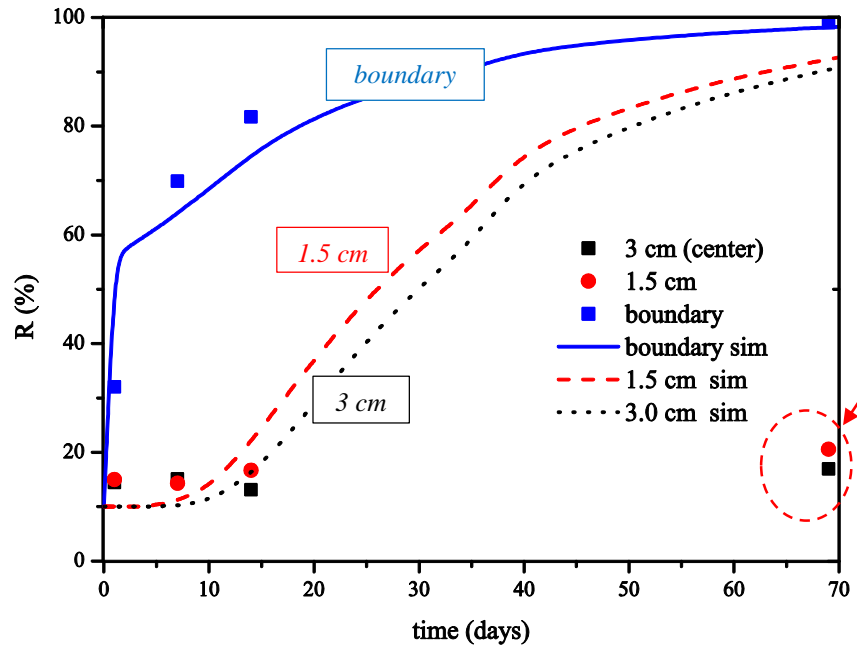


Figure 7-8 – TGA profile - experimental and numerical results for the degree of carbonation reaction (normalized values for experimental data) - results for three depths disregarding the last measurements, at 69 days

Because of those reasons, and with the objective to simulate more appropriately the experimental data for all the ages, a new function that correlates the carbon dioxide diffusion with the humidity was proposed.

- *New proposed function F1*

There is no unified model that correlates the diffusion of CO₂ with the humidity (Papadakis *et al.*, 1991a, Steffens *et al.*, 2002, Ishida *et al.*, 2007). The present adaptation is related with the exponent of the Eq. 3.43, which is related with that effect. The function was modified from the original equation used by Ferretti and Bažant (2006a), where the exponent adopted by the authors was equal to 2.5. The new proposed formulation is shown in Eq. 7.1:

$$F_1(h) = (1 - h)^{7.5} \quad 7.1$$

where: h is the humidity.

The new proposed function (Eq. 7.1) with the modified exponent was adopted after a large number of numerical simulation attempts (parametric analyses). For the cited coefficient, a range of values from 2 to 8 was tested, with increments of 0.5.

- *Results from the proposed model*

Herein, the numerical results considering the proposed model are presented. Figure 7-9 shows the comparative result for experimental measurement and numerical simulations, for specimens investigated with TGA, considering all the cited information. The experimental values of reaction presented in Figure 7-9 were normalized considering the maximum measured R during the experiments, for further information see Section 6.4.2.

The numerical data shown in Figure 7-9 were obtained from several analyses performed in an iterative process as previously mentioned for different parameters. In general, the model could reproduce the experimental data.

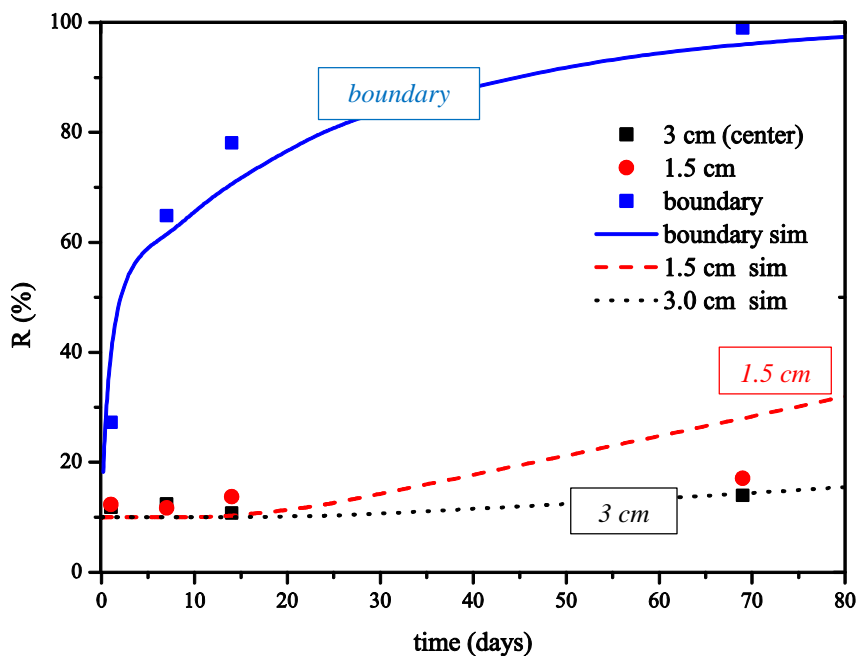


Figure 7-9 – TGA profile results for three depths - experimental and numerical data with all the optimizations (normalized values for experimental data)

For the boundary, the largest discrepancy was observed at 14 days, ~5%, for the depth of 1.5 cm it was for the measurement of 69 days, the experiments showed a $R \approx 17\%$ and the numerical model calculated a $R \approx 25\%$. The difference might be assumed relatively low, considering the uncertainties, simplifications and inaccuracies involved in both results. After these simulations, the summary of the set of parameters / function is presented in Table 7-1.

Subsequently the presented simulations, the relevance of coupling term of humidity and reaction ($\alpha_2(\partial R/\partial t)$), and the influence of the reaction on the diffusivity the terms was tested. These were initially disregarded in Section 7.2 with the decoupled model. The influence in the final results was small (< 1%), since the evolution of the reaction field was relatively slow and the parameter α_2 presents a reduced value ~0.0017 (Ferretti and Bažant, 2006a). In this sense, the initial assumption could be considered appropriated.

Table 7-1 – Proposed set of parameters / function

Parameter / function	Proposed value
Boundary coefficient for humidity - $f_{boundary}$	25×10^{-4} m/day
Initial diffusivity for humidity - D_I	60 mm ² /day
Initial diffusivity for CO ₂ - D_{c0}	200 mm ² /day
Boundary coefficient for CO ₂ - f_{carbo}	10×10^{-3} m/day
$\alpha_{if_4}^*(T)$	0.18
Initial carbonation degree	10%
$F_1(h)$	$(1-h)^{7.5}$
Coefficient ζ	0.8

7.3.3 Simulations of carbonation results from phenolphthalein indicator, effect of the size of the specimens

This section presents the numerical simulation of the five series of cylinders studied in Section 6.4.4 to study the effect of the specimen's size. As shown in Chapters 2 and 6, the carbonation percentage that corresponds to the carbonation depth (threshold) measured by phenolphthalein indicator was not clearly defined, and can change over time (Lawrence, 2006).

In terms of numerical modeling, Saetta and Vitaliani (2005, 2004) adopted a $R = 0.1$ (or equivalently $R = 10\%$), as the degree of reaction equivalent to the carbonation depth for the

study of concrete carbonation, but the different experimental observations, including, results from literature, and also of the data obtained in Chapter 6 for aerial lime mortar showed higher percentages (~20 to 60%). Therefore, for numerical simulations five different carbonation ratios were considered ($R = 0.2$, $R = 0.3$, $R = 0.4$, $R = 0.5$ and $R = 0.6$). The set of parameters previously obtained (see Table 7-1) were adopted to simulate the cylinders, more details about the experiments can be seen in Section 6.4.4.

- *Numerical simulation of cylindrical specimens: series S.A*

This part of the work presents the numerical simulation for the cylinders of series S.A (diameter ≈ 3.6 cm). The experimental and numerical results considering different carbonation degrees as corresponding to the threshold of phenolphthalein coloring are presented in Figure 7-10.

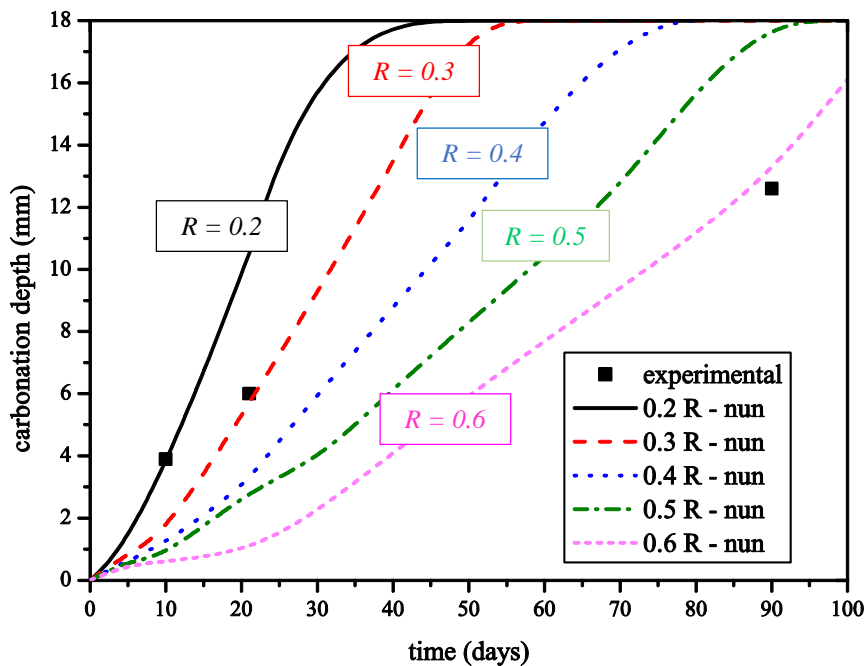


Figure 7-10 – Specimens of series S.A - diameter ≈ 3.6 cm - carbonation depth measured with phenolphthalein indicator and results from numerical simulation - days after casting

For 10 days the curve with $R = 20\%$ was the closest to the experimental data. However, for 21 days the model fitted the experimental data for $R = 30\%$. The numerical results for 90 days indicated that the entire specimen was already carbonated for the mold with $R 0.2 - 0.5$, and the phenolphthalein indicator showed a carbonation depth around 12 mm. The numerical model with $R = 0.6$ fitted more accurately the measured carbonation at 90 days.

- *Numerical simulation of cylindrical specimens: series S.B*

Continuing with the simulations, for series *S.B*, the numerical and experimental results are presented in Figure 7-11

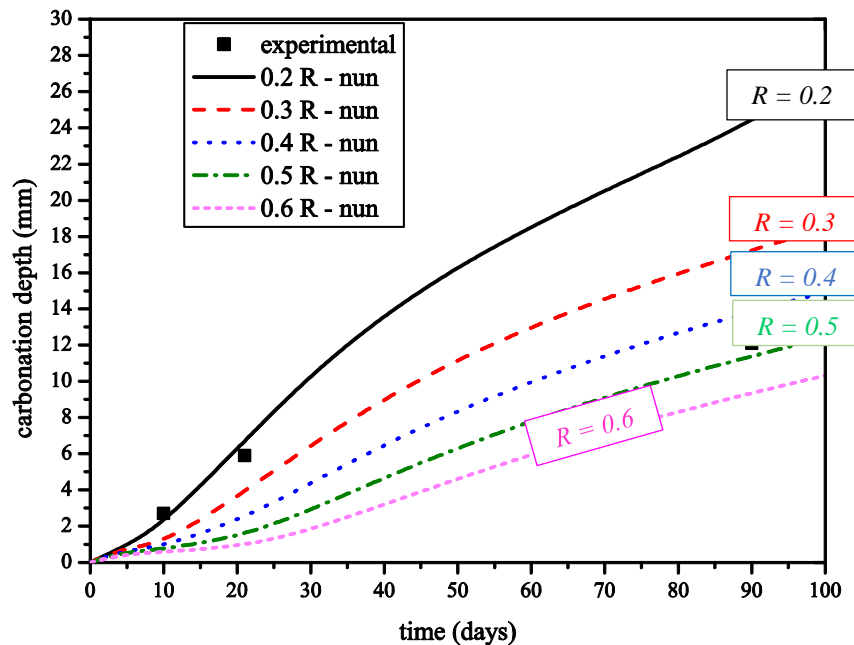


Figure 7-11 – Specimens of series *S.B* - diameter ≈ 6.0 cm - carbonation depth measured with phenolphthalein indicator and results from numerical simulation - days after casting

For the first ages, the best simulations were obtained with the curve of $R = 0.2$ or equivalently 20%. However, for the age of 90 days, the reaction rate adopted was 50%, which presented numerical results similar to the value observed experimental. The curves presented in Figure 7-11 might be in a simplified analysis, divided in two segments, the first one, where the carbonation was significant low, because of low concentration of carbon dioxide, until the age ~ 20 days. In sequence, the second part could be seen with a faster reaction.

- *Numerical simulation of cylindrical specimens: series S.C*

Two different series of cylindrical specimens were already simulated (*S.A* and *S.B*). Next, the study was focused in specimens of series *S.C*. The experimental and numerical data are shown in Figure 7-12.

Analyzing the results presented in Figure 7-12, the following conclusion could be stated. For the first ages (10 and 21 days) the tendency was that the model with $R = 20\%$ fitted the

experimental data, while for 90 days the experimental result are between the curves with $R = 40/50\%$. Once more, the curves obtained numerically might be in a simplified way divided in two segments, the first one, until the age ~ 15 days, in sequence the second fragment, when the carbonation tended to occur faster.

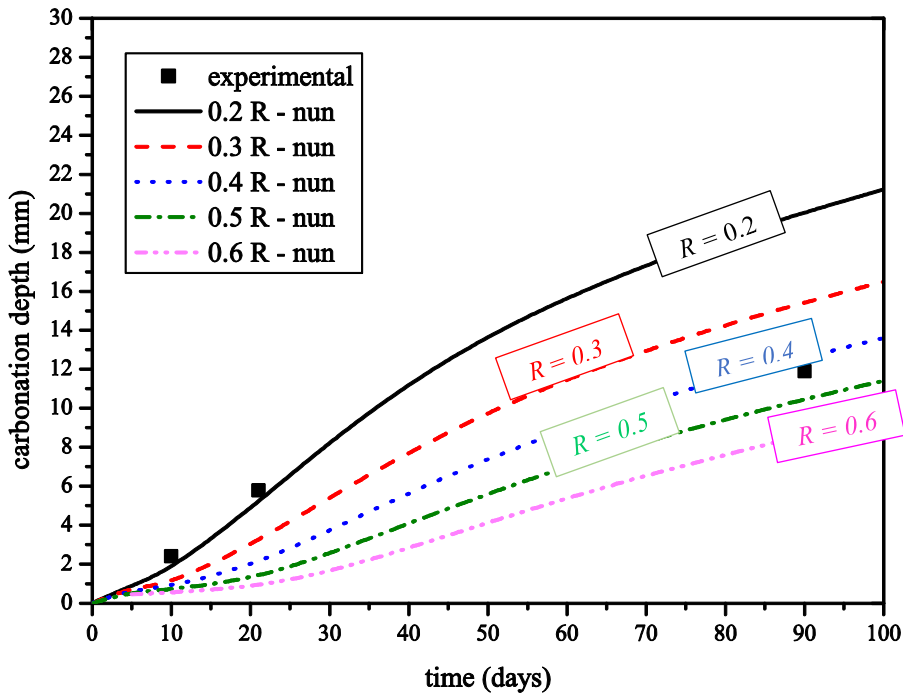


Figure 7-12 – Specimens of series *S.C* - diameter ≈ 7.2 cm - carbonation depth measured with phenolphthalein indicator and results from numerical simulation - days after casting

- *Numerical simulation of cylindrical specimens: series S.D*

The fourth series of cylinders (*S.D*, with diameter ≈ 9.0 cm) was also simulated. The results experimental and numerical are presented in Figure 7-13.

For 10 and 21 days, the curve with $R = 0.2$ or $R = 20\%$ fitted more appropriately the experimental results. Even for 21 days, there was a difference of about 1 mm, in terms of experimental and numerical results. While, for 90 days the experimental result was similar to the curve with $R = 40\%$.

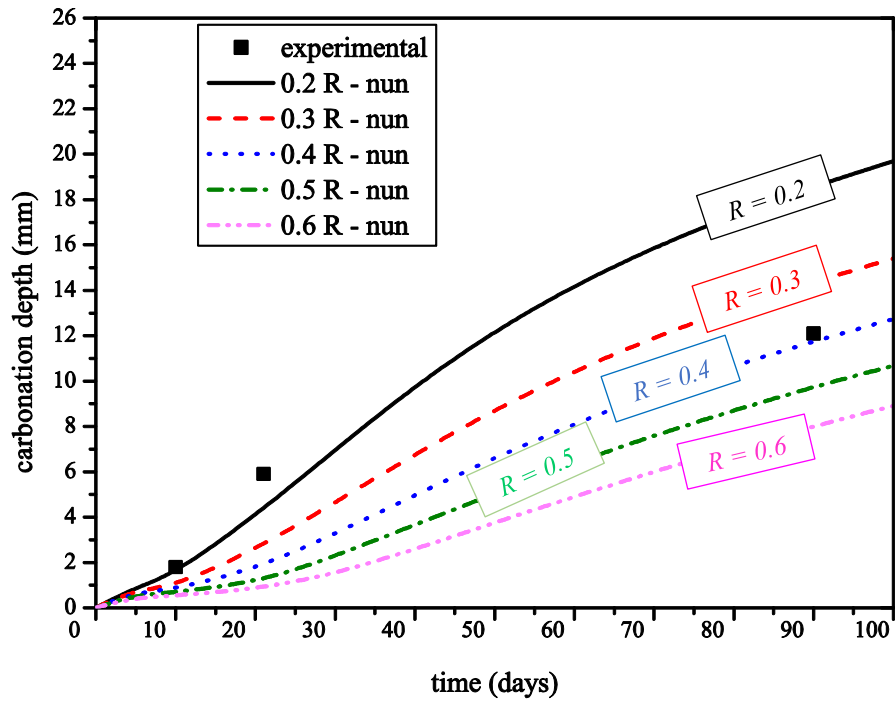


Figure 7-13 – Specimens of series *S.D* - diameter ≈ 9.0 cm - carbonation depth measured with phenolphthalein indicator and results from numerical simulation - days after casting

- Numerical simulation of cylindrical specimens: series *S.E*

For cylinders of series *S.E*, the experimental and numerical data are presented in Figure 7-14.

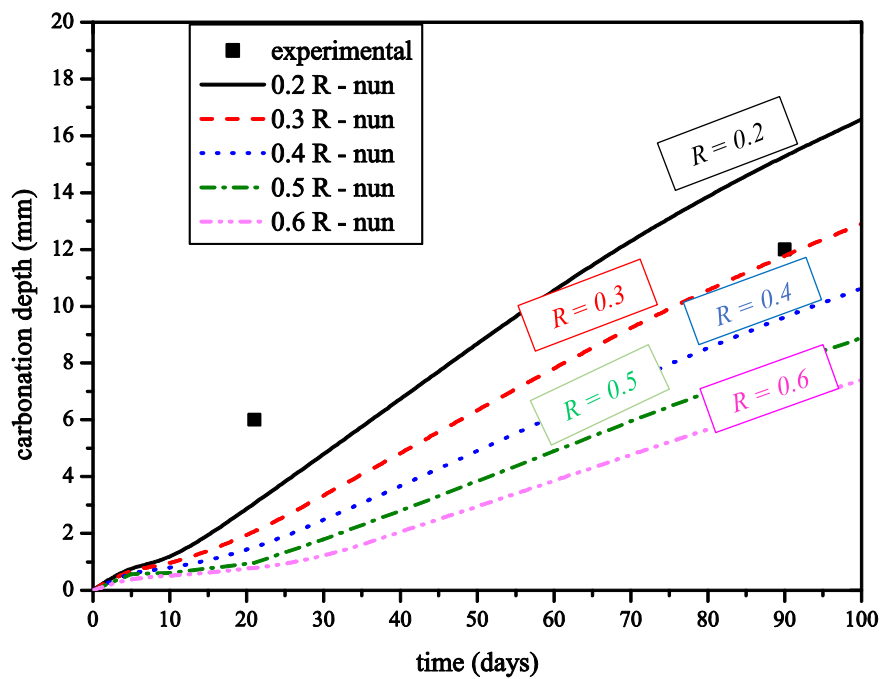


Figure 7-14 – Specimens of series *S.E* - diameter ≈ 15.0 cm - carbonation depth measured with phenolphthalein indicator and results from numerical simulation - days after casting

As shown in Figure 7-14, for 21 days all the adopted curves tend to underestimate the carbonation depth with phenolphthalein, while for 90 days, the carbonation depth was simulated more appropriately with the curve of $R = 30\%$.

- *General observations*

After the simulation of five series of specimens, the main integrated observations are herein highlighted. As different authors in literature recognize, the use of phenolphthalein indicator for the measurement of the carbonation depth implies precision limitations (Chang and Chen, 2006, Lawrence, 2006, Parrott and Killoh, 1989, Pacheco Torgal *et al.*, 2012), therefore experimental measuring errors can be implicit in the technique (Parrott and Killoh, 1989, Villain *et al.*, 2007, Houst and Wittmann, 2002). Even with this limitation, in general, the model was able to simulate the experimental results for different sizes of specimens, though for some ages the model could not reproduce exactly the experimental values, and, for different ages, there was a variation with the R that fitted with the measurements.

In the adopted coupled formulation, with interaction between the fields, the humidity results affects the carbonation field, for instance for the cylinders with larger dimensions the higher values of humidity for longer ages difficult the diffusion of CO_2 . This phenomenon might be associated with the smaller carbonation depth in those specimens. The behavior of the numerical results for the series *S.A*, the smallest cylinders, was the opposite, as it presented a faster drying and carbonation. The typical aspect of the empirical curve for concrete carbonation over time presented in literature (El-Reedy, 2007, Richardson, 2003), usually has the shape of a function depending on the time with an exponent 0.5. This curve format was obtained more clearly for specimens with intermediary diameters, with 9 and 7.2 cm.

Summarizing the results obtained, Figure 7-15 presents the different data for the five specimens, and the equivalent reaction from the numerical model that best fitted the experiments. For the plotted values in Figure 7-15, the corresponding names of the specimens are indicated inside the text boxes.

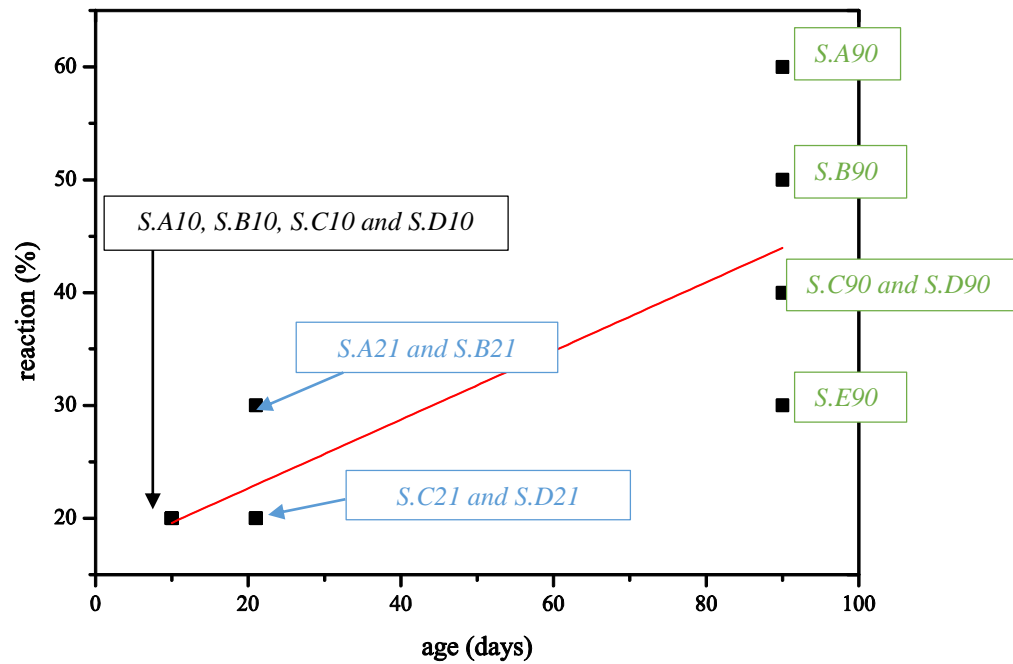


Figure 7-15 – Equivalent reaction vs carbonation depth with phenolphthalein for different ages

As presented in Figure 2-17, (Lawrence, 2006) experimentally obtained different values in terms of R that fit the carbonation depth with phenolphthalein. It is important to stress that the author only measured in the TGA tests only the dehydroxylation process. In the present work, variations were also obtained in the experiments presented in Section 6.4. Limitation related with the numerical model may be cited, as experimental inaccuracies. A tendency of increase in the equivalent reaction over time was noticeable. For the first ages, the R was around 20-30%, for 90 days the results presented a scattering, with R varying from 30 to 60% (see Figure 7-15).

7.4 Elastic modulus

7.4.1 General considerations

In the previous sections, experiments associated to the humidity flux and the evolution of the carbonation were simulated. Considering all the results until this stage, and the reasonable degree of confidence in the models and parameters under use, the evolution of the elastic modulus was also studied. Considering the experimental work presented in Chapters 5 and 6, and based on the literature, two major mechanisms may be identified as the main phenomena affecting the material stiffness: (i) the water loss, as evidenced by the

initial rigidity of the material (Izaguirre *et al.*, 2011, Callebaut, 2000, Ngoma, 2009), (ii) the carbonation process generating precipitates that contribute to the densification of the solid skeleton (Lawrence, 2006, Lawrence *et al.*, 2006b)

To start the study, an association of concepts is proposed. In analogy with the physical concept of two parallel springs, wherein the equivalent stiffness is the summation of the two individual parcels (Crandall, 2012), a simplified modelling to simulate the elastic modulus was adopted. In concrete science, this kind of strategy can be seen in the parallel model, which is a simple modelling to consider the contribution of different phenomena or material properties on the evolution of the elastic modulus (Yoshitake *et al.*, 2012, Monteiro, 1995, Topcu and Ugurlo, 2007). Other models to consider different phenomena can be found in literature (Brandt, 1994, Monteiro, 1995, Tenchev and Purnell, 2005, Alexander and Mindess, 2010).

Considering the cited aspects for the parallel model, two curves were proposed, the first one correlating the evolution of the elastic modulus with the internal humidity (E_h) and a second curve that is associated to the reaction field (E_R) (see Figure 7-16). The modeling considered explicitly separately the influence of both phenomena on the mechanical properties (see Figure 7-16).

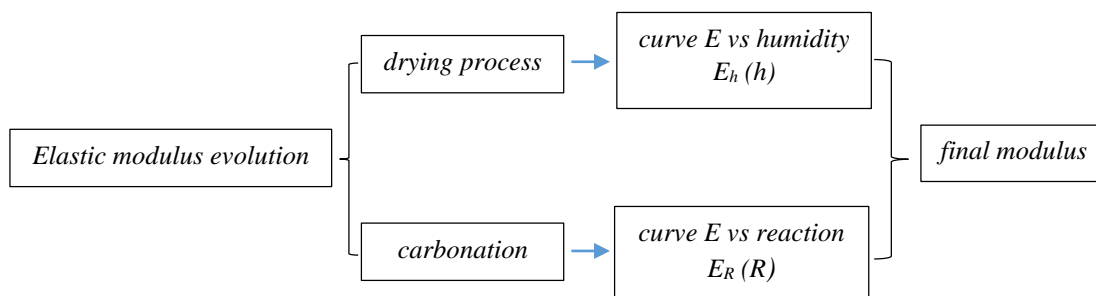


Figure 7-16 – Study of the elastic modulus evolution – carbonation and drying processes

7.4.2 Proposed model for e-modulus evolution

In this section, the proposed modelling is presented. The first aspect studied was related to the evolution of the e-modulus with the reaction/carbonation, and afterwards the evolution of e-modulus as a function of humidity will be discussed.

The carbonation process occurs from the external part to the interior of the material, as shown in Figure 7-17 a that schematically depicts the gradients of carbonation in a cylindrical specimen. With the carbonation progress, there is also the modification of mechanical

properties, namely the elastic modulus (see Figure 7-17 b). These processes evolve over time (see Figure 7-17 c and d), and throughout the depth of the material/specimen. The most external part presents higher carbonation degree, when compared with the interior and with that assumption also higher values for the E (Figure 7-17 b and d). Therefore, for aerial lime mortar, a non-uniform elastic modulus distribution over the section is expected to occur. Other references that deal with the evolution of concrete mechanical properties can be found in Kanstad *et al.*, (2003) or the formulation cited in Model Code 2010 (CEB–FIP, 2010). However, for the sake of brevity, they are not shown here. Because of the similarity of phenomena, herein an association of parameters was proposed. While for concrete, the model (Rostásy *et al.*, 2001) correlates the evolution of the mechanical properties with the degree of hydration, for aerial lime mortar, the adaptation for the degree of reaction/carbonation was done.

In concrete, the evolution of mechanical properties, such as compressive strength (f_c), tensile strength (f_{ct}) and elastic modulus (E) may be expressed by a general equation, as the one indicated and experimentally validated by Rostasy *et al.* (2001). For the general property X_i (which may be f_c , f_{ct} or E), at a degree of hydration α , as a function of the hypothetical value of $X_{i,1}$ upon full hydration development $X_i(\alpha = 1)$, the initial degree of hydration $\alpha = 0$ and a parameter η_i (with the recommended values of $\eta_i = 1.5$ for f_c ; $\eta_i = 1.0$ for f_{ct} ; $\eta_i = 0.5$ for E) (Azenha, 2009, Rostásy *et al.*, 2001). The generic formulation can be seen in Eq. 7.2.

$$X_i(\alpha) = X_{i,1} \times \left(\frac{\alpha - \alpha_0}{1 - \alpha_0} \right)^{\eta_i} \quad 7.2$$

The generic formulation presented in Eq. 7.2, can be rewritten specifically for the study of elastic modulus as Eq. 7.3.

$$E(R) = E_1 \times \left(\frac{R - R_0}{1 - R_0} \right)^\eta \quad 7.3$$

where: $E(R)$ is the generic value for the elastic modulus, R is the reaction degree, and R_0 is the initial reaction degree, E_1 is the maximum value for the elastic modulus of upon full carbonation development ($R = 1$), and η is an exponent, which was adopted with the value $\eta = 0.5$ as a starting point, in similarity to the value proposed for concrete (Rostásy *et al.*, 2001).

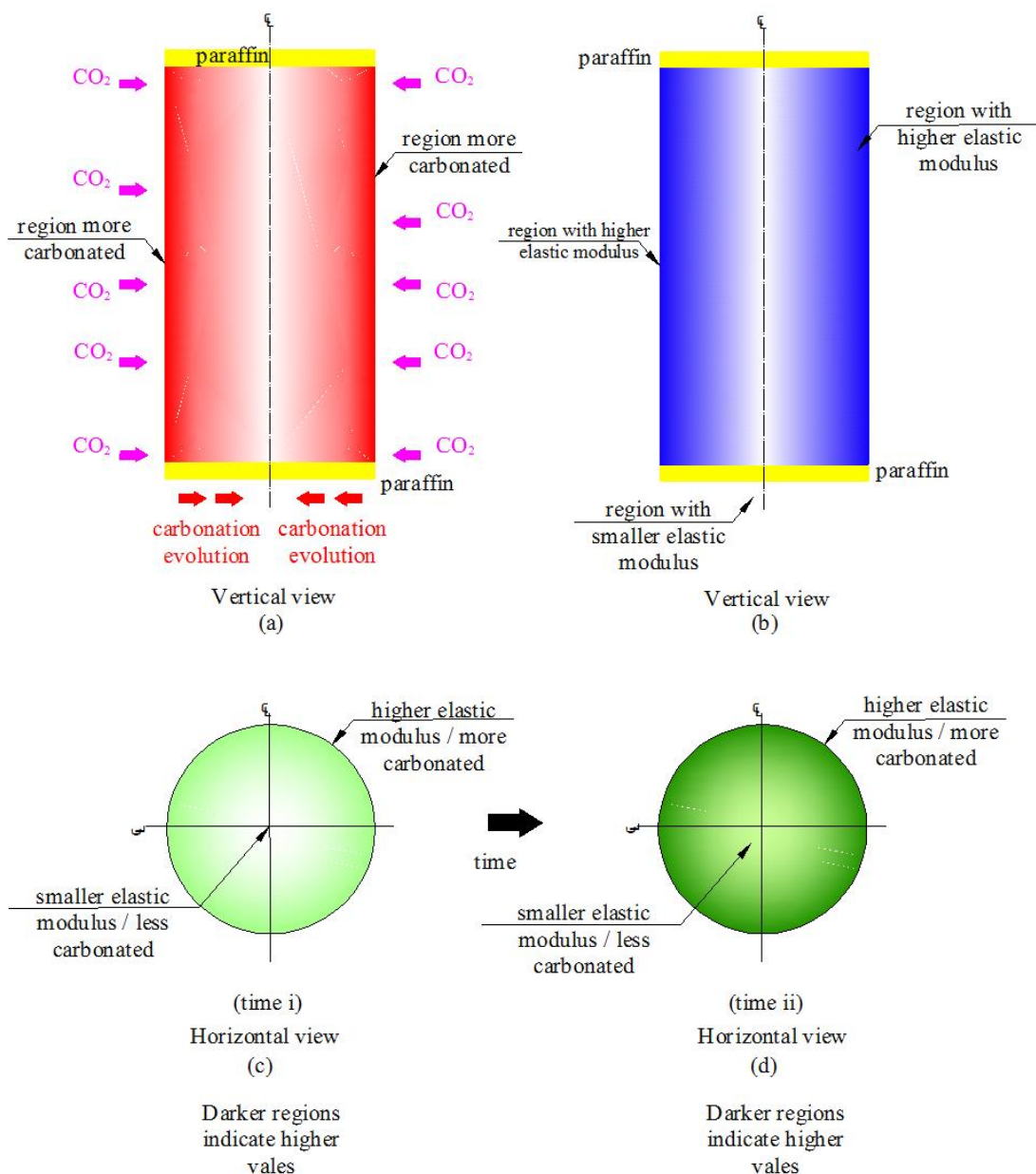


Figure 7-17 – Schematic representation of carbonation and elastic modulus evolution
 (a) vertical view, carbonation profile, (a) vertical view, e-modulus profile, (c) cross section, carbonation and e-modulus profiles for earlier age (d) cross section, carbonation and e-modulus profiles for latter age

The initial degree was also adopted as, $R_0 = 0.10$, because the TGA results indicated the early presence of CaCO_3 for the fresh mortar and for the sealed specimen of aerial lime (~10%). A comparative graph with the elastic modulus evolution (E/E_{final}) for the adapted formulation of Rostásy *et al.* (2001) with two different initial reaction degrees ($R_0 = 0$ and $R_0 = 0.10$) can be seen in Figure 7-18.

The best value of E_I to simulate the experimental results was found by an iterative process. A range of values from 2 to 8 GPa was tested, and the final value adopted was: $E_I = 3.2$ GPa. Therefore, the final proposed equation for $E_R(R)$ may be written as:

$$E_R(R) = 3.2 \times \left(\frac{R - 0.1}{1 - 0.1} \right)^{0.5} \quad 7.4$$

Considering the previous information, Figure 7-19 shows the graphical representation of Eq 7.4.

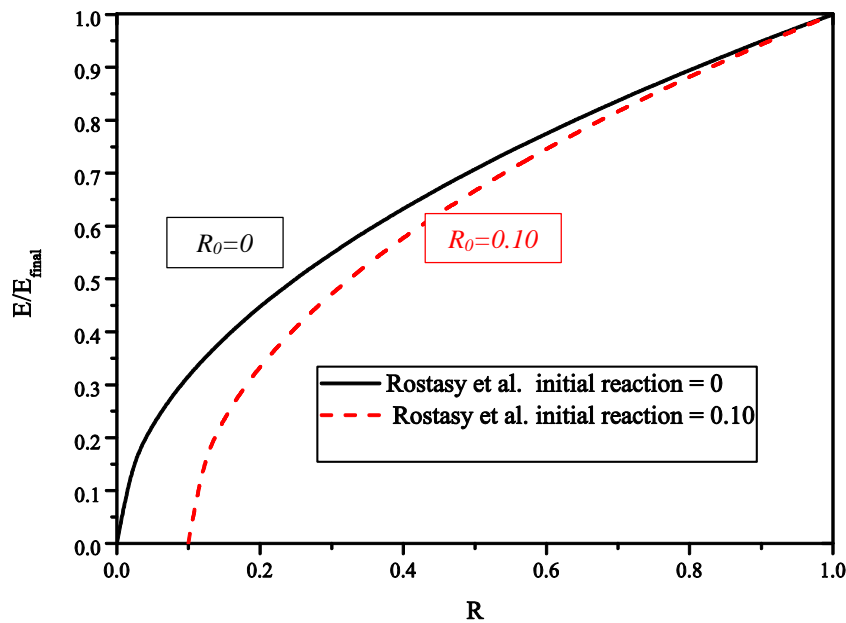


Figure 7-18 – Comparison of elastic modulus evolution with two different R_0 (Rostásy *et al.*, 2001)

After the description of the formulation on the evolution of the e-modulus with the reaction, the study about the influence of the humidity is presented. Regarding the drying process in aerial lime mortar, as cited by authors such as Callebaut (2000), Lanás *et al.* (2004a), Ngoma (2009) and Izaguirre *et al.* (2011), for the initial ages, it may be considered the major phenomenon for the material strength and stiffness. For the definition of the curve that correlated the elastic modulus with humidity, an association of concepts with the behavior of clay soil material was done. This association was assumed because clay soils tend to present a mechanical behavior dependent of the moisture content (Khalili *et al.*, 2014, Hammouda and Mihoubi, 2014, Lu, 2013, Bravo *et al.*, 2012). Many authors (Khalili *et al.*,

2014, Hammouda and Mihoubi, 2014, Lu, 2013, Bravo *et al.*, 2012) show a tendency of increasing of e-modulus with the reduction of the water content.

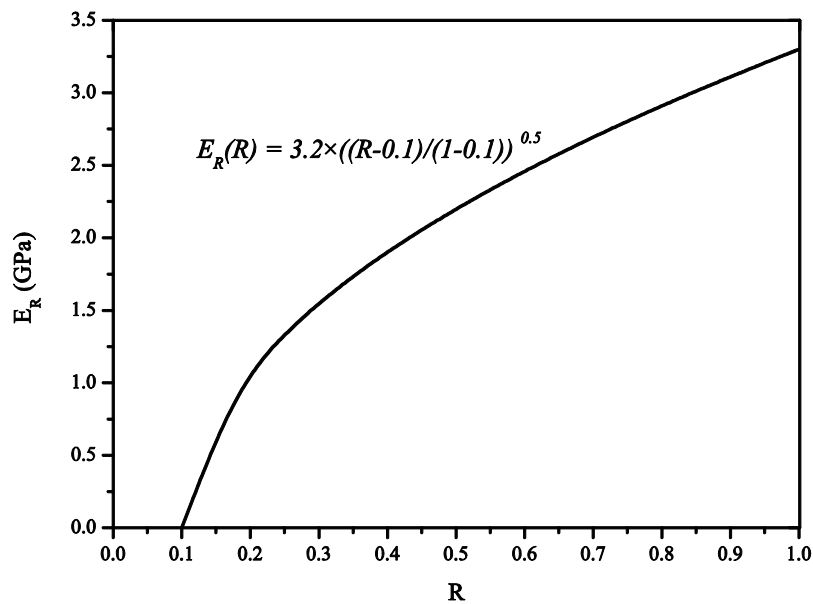


Figure 7-19 – Proposed formulation of the elastic modulus, evolution with R (E_R)

In terms of formulation, Lu and Kaya (2014) and Lu (2013) proposed a power law for the evolution of the elastic modulus of clay with the water content, considering different experimental results from literature (Ng *et al.*, 2009, Schuettpelez *et al.*, 2010). The principle of the formulation presented by Lu and Kaya (2014) and Lu (2013) is similar with the equation presented by Rostásy *et al.* (2001) (Eq. 7.3), therefore, for simplicity and because no other reference specific for aerial lime could be found, the concept was extended to the humidity variable for aerial lime mortar.

The values for the curve that correlated the evolution of the elastic modulus with the humidity were defined considering the experimental data available, by an iterative process. The model here proposed assumes that for $h = 90\%$, the elastic modulus presents a low value, which increases with the reduction of the humidity until the maximum is reached for $h = 60\%$. The value for the e-modulus for $h = 90\%$, was estimated considering the previous results of Chapter 6, in which a low value of E for this environmental condition was obtained (see Section 6.5.3). Even though the observed value varied over the experiment for different loading steps (see Section 6.5.3), it was decided to adopt the minimum value of ~ 0.5 GPa. The maximum E was adopted for $h = 60\%$, and this value represented the environmental humidity inside the “*standard*” climatic chamber. The adopted formulation for humidity vs

elastic modulus was based on the proposals presented by Rostásy *et al.* (2001) together with the equation of Lu and Kaya (2014) and Lu (2013) (see Figure 7-20).

For the sake of simplicity, and because no other reference could be found specific for aerial lime mortar, the exponent was adopted equal to 0.5 as also suggested for the modelling in soil (Lu and Kaya, 2014). For the factor that multiplies the term related with the humidity decreasing, a range of values from 1 to 4 GPa was tested, and the value of 2.5 GPa fitted more appropriately the results.

The final proposed equation for $E_h(h)$ may be written as:

$$E_h(h) = 0.5 + 2.5 \times \left(\frac{0.9 - h}{0.9 - 0.6} \right)^{0.5} \quad 7.5$$

The tendency of the proposed curve is in agreement with the previous obtained results in Chapter 6, in which the specimens stored inside the climatic chamber with higher humidity presented lower e-modulus than cylinders stored in the “*standard*” chamber (see Section 6.5.3)

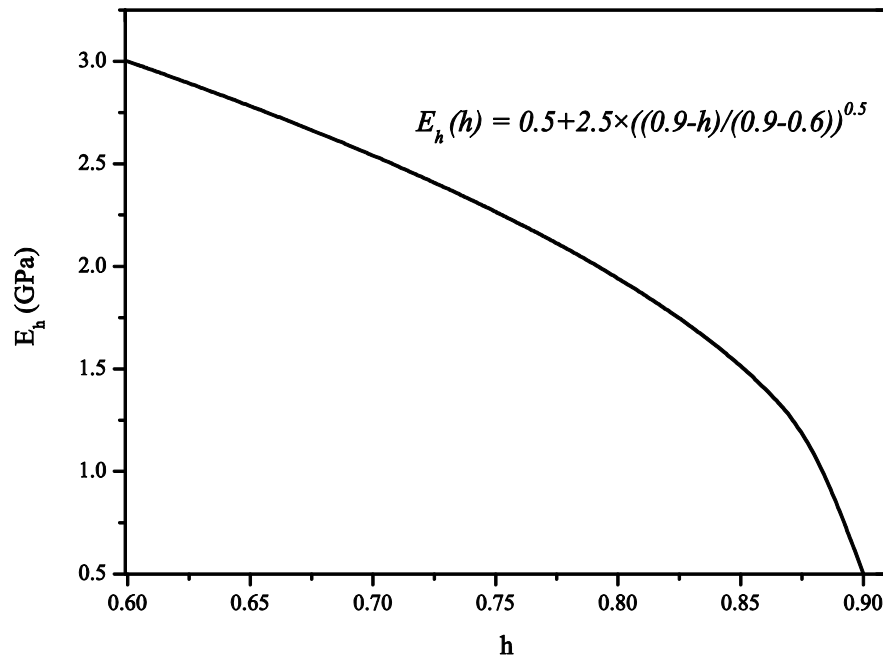


Figure 7-20 – Proposed formulation for the elastic modulus evolution with the reduction of humidity (E_h)

7.4.3 Multi-physics numerical modelling

Aspects related with the strategy adopted in the multi-physics numerical modeling are presented herein. Considering the curves shown in the last section, correlating the elastic modulus with the humidity and the reaction degree, as well as the calculated humidity and carbonation fields, the parcels of E were calculated ($E_{humidity}$ and $E_{Reaction}$, see Figure 7-21). From the hygro-carbo model, a table associating the equivalent reaction field with E for each node was given to the FEM program, so that it could compute the stress/strain distribution.

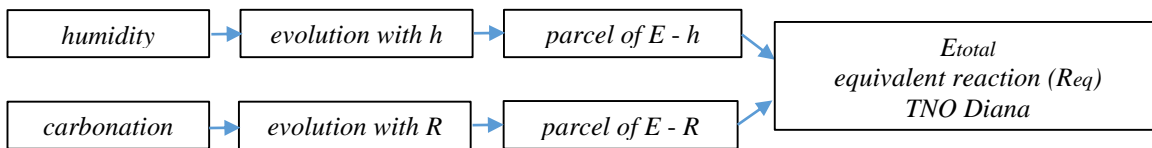


Figure 7-21 – Framework considering the different parcels for the calculus of elastic modulus

Regarding the numerical model in FEM, two materials were adopted. The first one with an elevated elastic modulus (around 10^5 times higher than the elastic modulus of mortar), to numerically simulate the steel plate positioned on the top of the specimen during the experiments, and a second material to replicate the mortar, presenting mechanical properties with evolution over time. The model presented an axisymmetric condition, therefore, the cylinder was simulated with a section as shown in Figure 7-22. The simulated section had, in horizontal direction (x axis), the dimension of the cylinder radius = 3 cm, and, in vertical direction, the (y axis) height = 12 cm (see Figure 7-22).

The mesh adopted is also displayed in Figure 7-22, with elements with $1 \text{ cm} \times 1.5 \text{ cm}$ respectively in horizontal (x axis) and vertical (y axis) directions. The geometry of elements was chosen to reduce the possible distortion on the elements/ results. A four-node isoparametric axisymmetric element with a quadrilateral shape was adopted. It is based on linear interpolation and Gauss integration. A linear relation between stress/strain was also adopted.

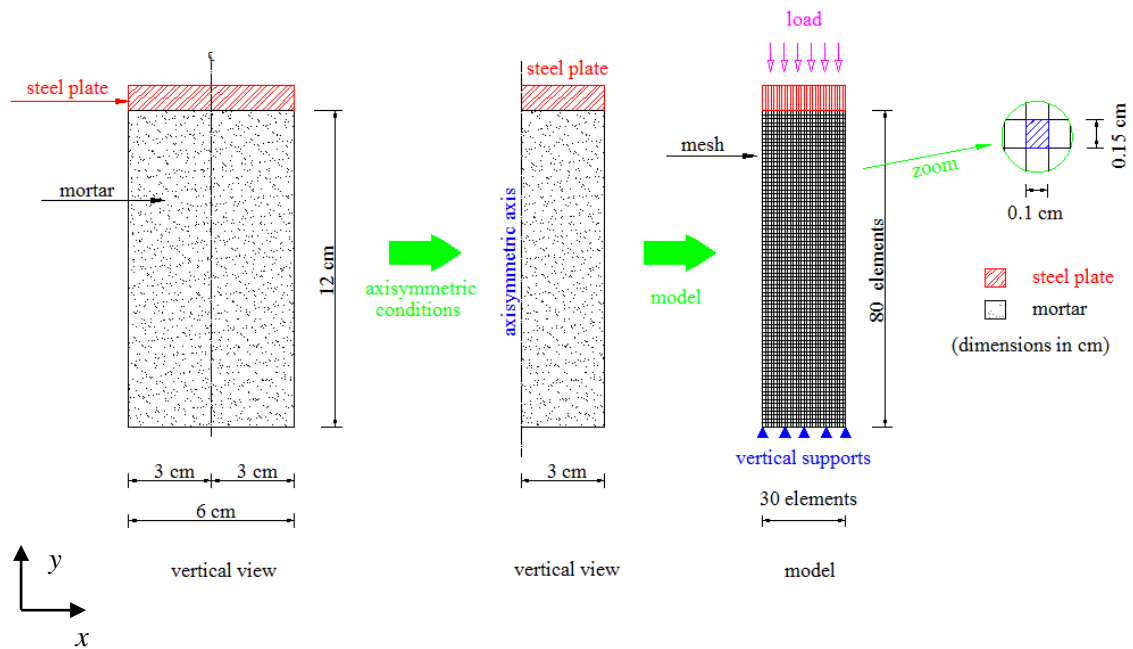


Figure 7-22 – Adopted modeling for the simulation of elastic modulus in cylindrical specimens

On the basis of the model (bottom part), vertical supports were adopted to simulate the experimental apparatus (the basis of the hydraulic testing machine) as presented in Figure 7-22. The numerical analyses were done for the discrete ages of 1, 2, 4, 8, 15 and 22 days. A loading cycle was applied, considering 25%, 50%, 75% and 100% of the maximum load adopted during the experiments (~300N). The Poisson ratio equal to 0.19 was adopted based on literature values (Ferretti and Bažant, 2006b, Arizzi and Cultrone, 2013).

7.4.4 Calculated strain fields

Considering the previous given information, Figure 7-23 presents the results for the strain (ϵ) in vertical direction (y axis) for the simulation of 8, 15 and 22 days for the maximum load in y direction (~ -300 N).

The strain data presented uniform distribution for each age, with exception of the top of the cylinder, where the load was applied, where a small perturbation was observed. For the maximum load in vertical direction (y axis) the values for strain, respectively for 8, 15 and 22 days were: $\sim -3.5 \times 10^{-5}$, $\sim -3.0 \times 10^{-5}$ and $\sim -2.7 \times 10^{-5}$. The negative values indicate compression. With the increase of the elastic modulus over time, there was a consequently reduction of the vertical strain, for the maximum applied load.

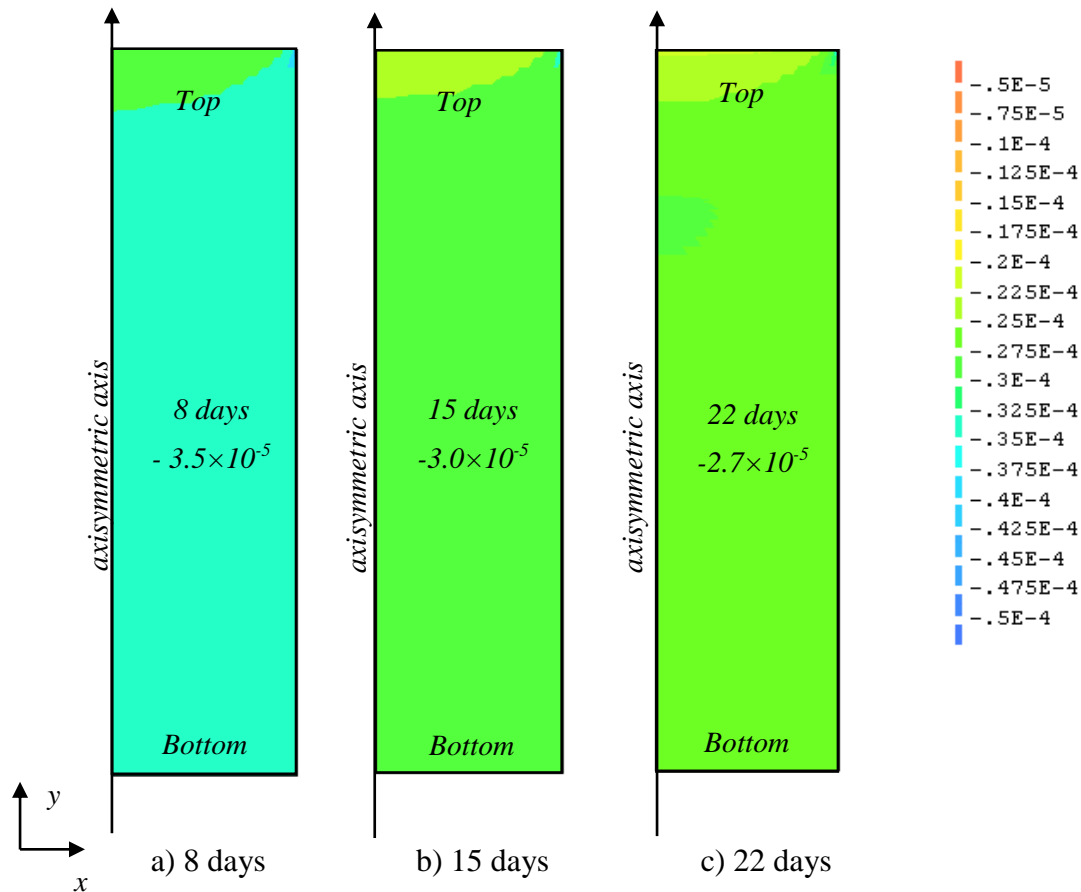


Figure 7-23 – Strain for the maximum load in y direction (~ -300 N) a) 8 days, b) 15 days and c) 22 days

7.4.5 Calculated stress fields

This section presents the numerical results for the stress fields. Initially a simple formulation to calculate the stress is shown for comparison of results. The simple uniform vertical stress (in y direction), results from the F_y (the maximum force in y direction ~ -300 N), divided by the area perpendicular to the force (in this case it represented the circular area of cylinder: $A=2827\text{mm}^2$). Applying this simple consideration, it would result in a constant vertical stress (y axis) ~ -0.106 N/mm².

In opposition to this simple formulation that assumed homogeneous e-modulus at cross-sectional level, the numerical simulations were done considering the non-uniform elastic modulus distribution across the section, and with evolution over time. The results for testing at 8 days are shown in Figure 7-24 a, with the maximum absolute value of load adopted in the modeling (~ -300 N). The non-uniform distribution of stress may be seen, with the vertical stress concentration (y direction) on the region indicated with horizontal arrows in

Figure 7-24. This resulted from a higher carbonation percentage/smaller humidity in that region, and consequently higher e-modulus. The peak stress ($\sigma \approx -0.2 \text{ N/mm}^2$) in Figure 7-24 a, considering absolute values was around 2 times higher than the results assuming the uniform stress distribution ($\sigma \approx -0.106 \text{ N/mm}^2$) (see Figure 7-24 a). The negative values indicated compressive stress (direction in opposition of the y axis). The stress distribution for testing at 15 days is shown in Figure 7-24 b. As already showed on the previous age, once more there was a stress concentration on the region close to boundary (region nearby the right side of the figure and indicated with horizontal arrows). Figure 7-24 represents the stress distribution for testing at 22 days, and similar observations to those previously mentioned can be extended to this age.

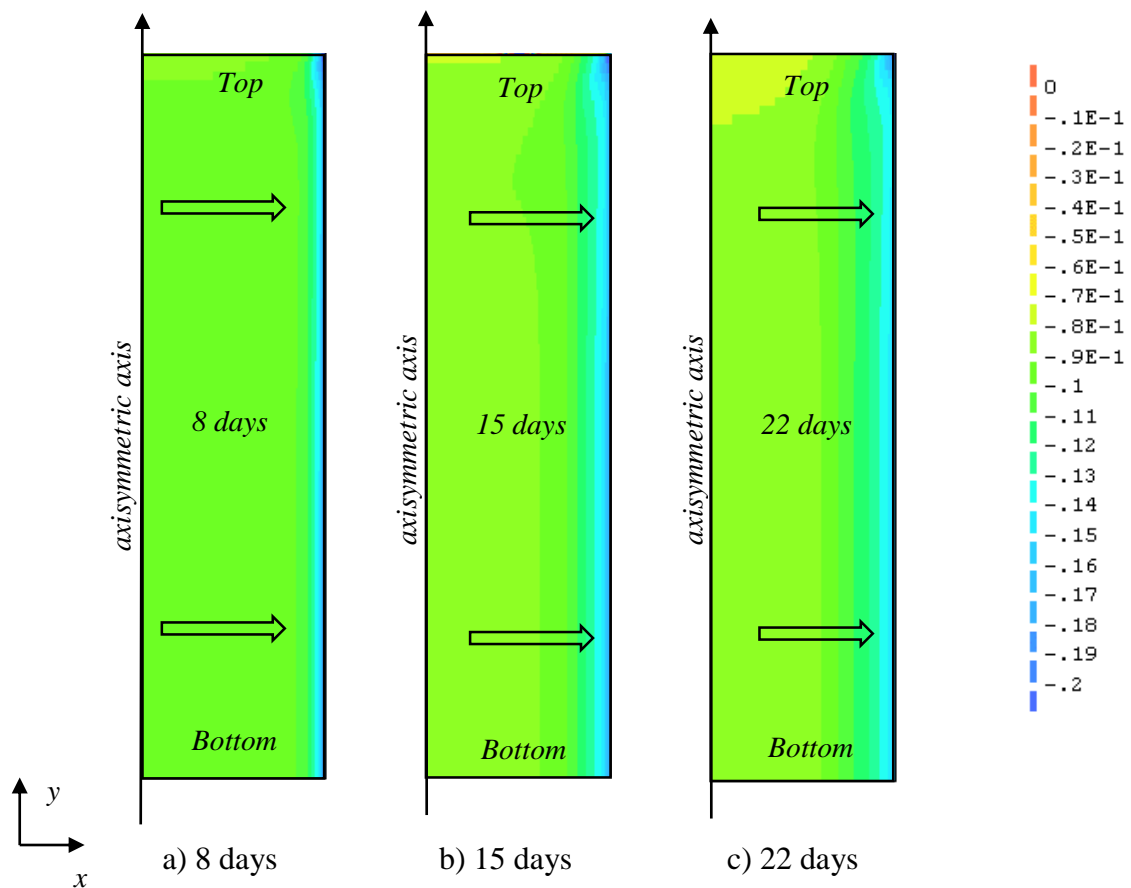


Figure 7-24 – Vertical stress for the maximum load (N/mm^2) - a) 8 days, b) 15 days and c) 22 days (horizontal arrows were adopted to indicate the regions with stress concentration)

There was a spreading of the region with stress concentration over time, this effect might be seen comparing the results from Figure 7-24 a, b and c. For the first age, this region was smaller, and consequently the peak in terms of absolute value was higher (the maximum

values can be seen in Figure 7-29), with the increase of the elastic modulus in that region over time, the area enlarged (see Figure 7-24 and Figure 7-29).

In sequence, the stress distribution was analyzed through a line of elements in the middle of the specimen height, the position of the adopted section can be seen in Figure 7-25.

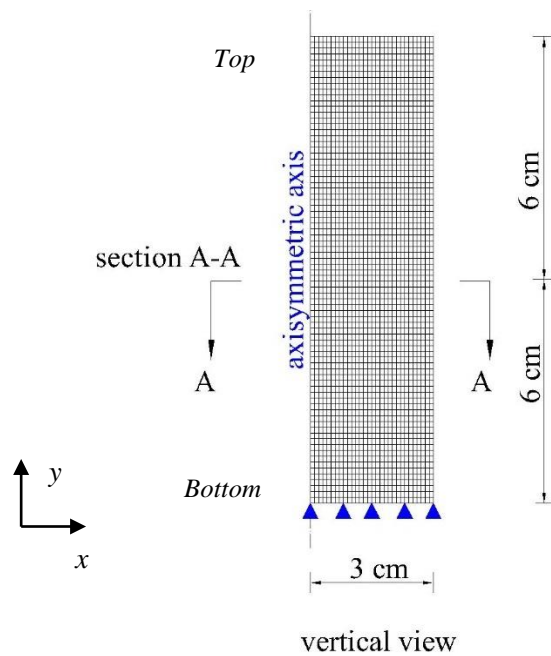


Figure 7-25 – Section A-A adopted to study the stress/strain profiles (positioned in the middle of the specimen height)

The profiles for reaction and humidity fields of the nodes from section A-A are presented respectively in Figure 7-26 and Figure 7-27.

The reaction profiles presented larger values for the most external part, as expected, since the carbonation occurred faster in that region. The humidity profiles were almost constant over the length of the specimen for the ages of 15 and 22 days, while for 8 days it presents a gradient. The modification over time for the profiles in both fields can be noticed comparing the different ages. Considering the two proposed formulation correlation the elastic modulus with the reaction (Eq. 7.4) and humidity (Eq. 7.5) fields, the final elastic modulus profile is shown in Figure 7-28.

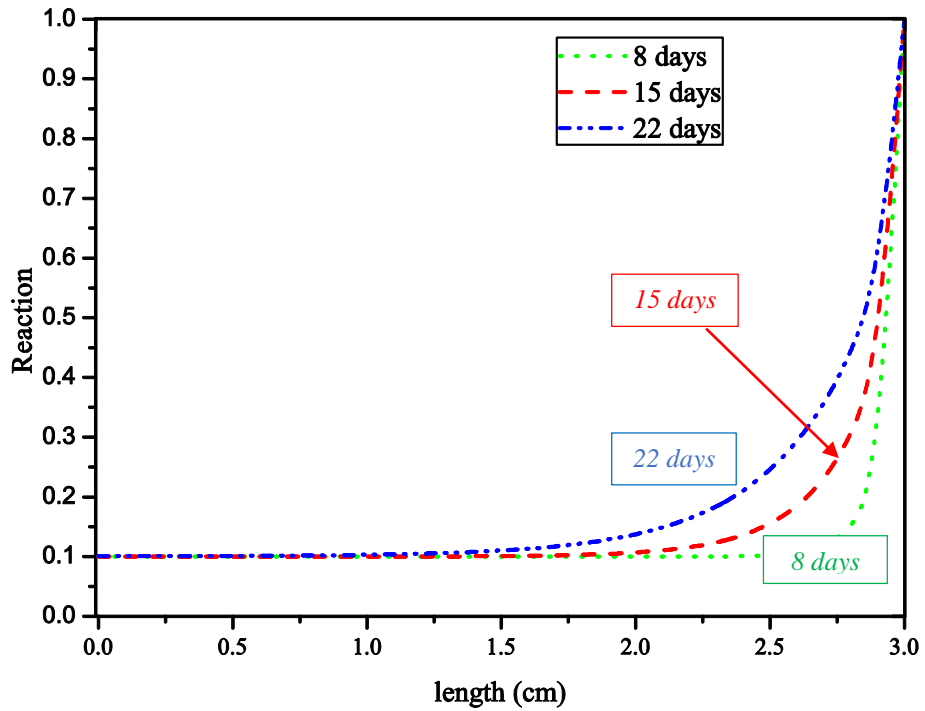


Figure 7-26 – Reaction profile for the three ages, 8, 15 and 22 days

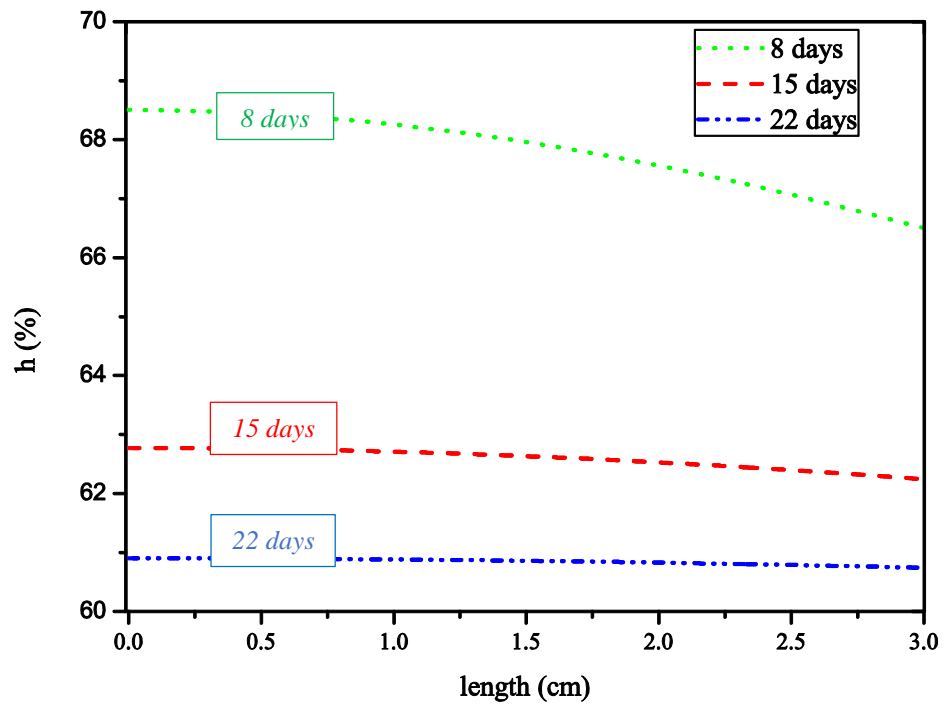


Figure 7-27 – Humidity profile for the three ages, 8, 15 and 22 days

The profiles of the stress values obtained in the numerical analyses from elements of section A-A, for the three ages are shown in Figure 7-29, together with a uniform stress distribution, considering the simple relation for stress, as presented in the beginning of the present section.

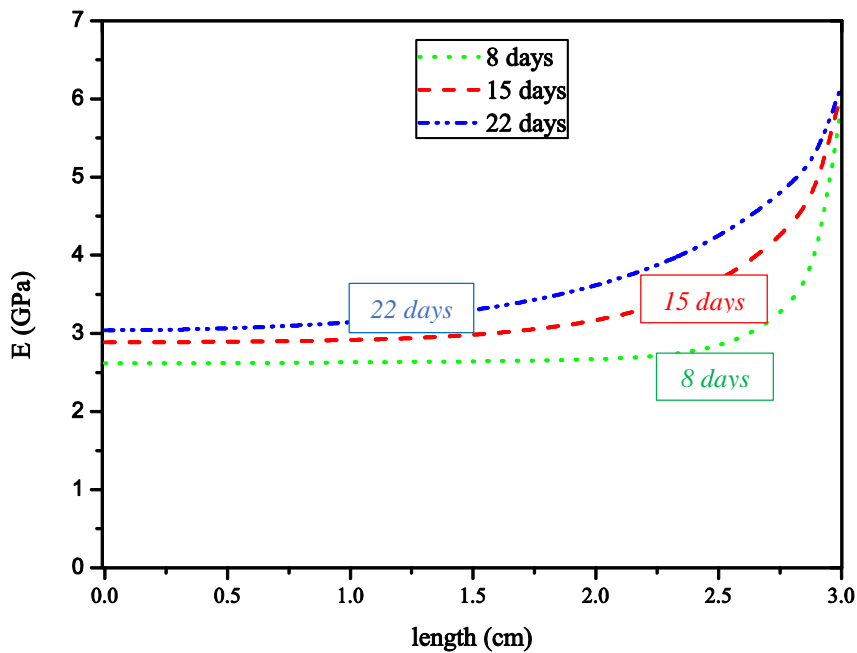


Figure 7-28 – E-modulus profile for the three ages, 8, 15 and 22 days

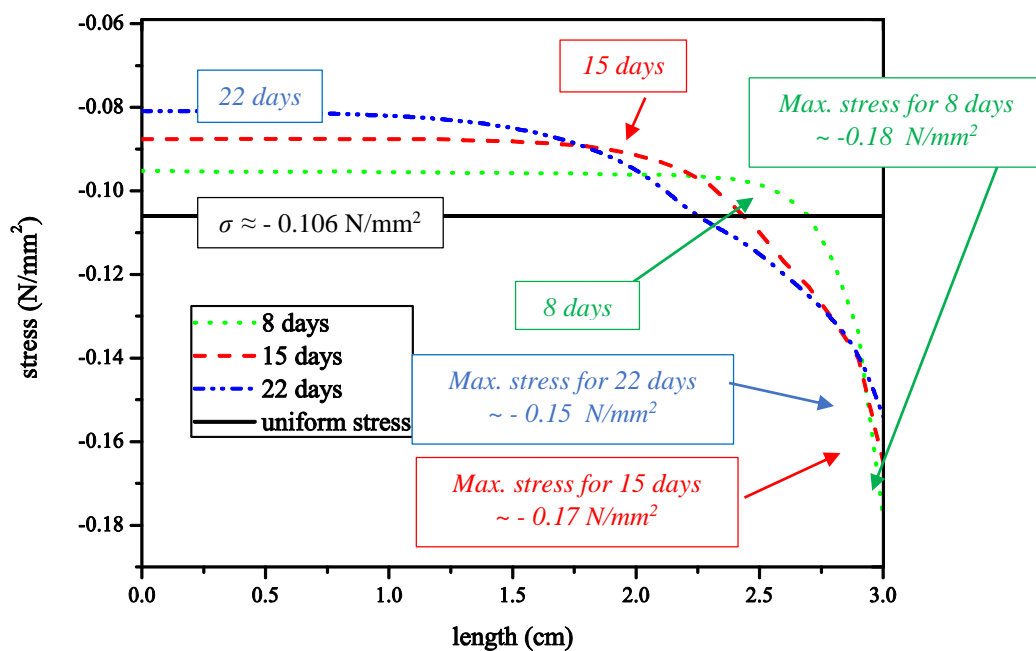


Figure 7-29 – Vertical stress distribution for the three ages (averaged values for each element) and the uniform stress (σ) (N/mm^2)

Analyzing the data presented in Figure 7-29, it can be seen that the maximum stress reduced over time, for 8 days it was equal to $\sim -0.18 \text{ N/mm}^2$, for 15 days $\sim -0.17 \text{ N/mm}^2$ and for 22 days $\sim -0.15 \text{ N/mm}^2$. As already shown in Figure 7-24 and confirmed in Figure 7-29, there was a spreading of the region with stress concentration over time, for instance for 8 days,

this region was located around the first 0.5 cm, while for 22 days it extended ~1.5 cm for the external part of the specimen. The stress distribution (see Figure 7-29) is in agreement with the elastic modulus profile presented in Figure 7-28, regions with higher values of E , presented also higher stresses.

7.4.6 Evolution of elastic modulus

This section presents the numerical results for the computed global e-modulus that can be inferred from the simulated tests on the specimen. The parameter was calculated considering the linear relation between stress and strain. For the calculation of stress/strain curves, a range of values was adopted for the applied vertical force, from 0 to -300 N (maximum absolute value during the experiments), the inclinations of the global response curves represented the values of the elastic modulus. For each age, the strain was obtained from the elements in section A-A as presented in Figure 7-25. As previously shown in Figure 7-23 a homogeneous strain distribution was obtained and it occurred for different load values. Considering the given information, the obtained data for the e-modulus for the three ages studied experimentally can be seen in Figure 7-30 (for the sake of simplicity the data for stress and strain are presented with absolute values).

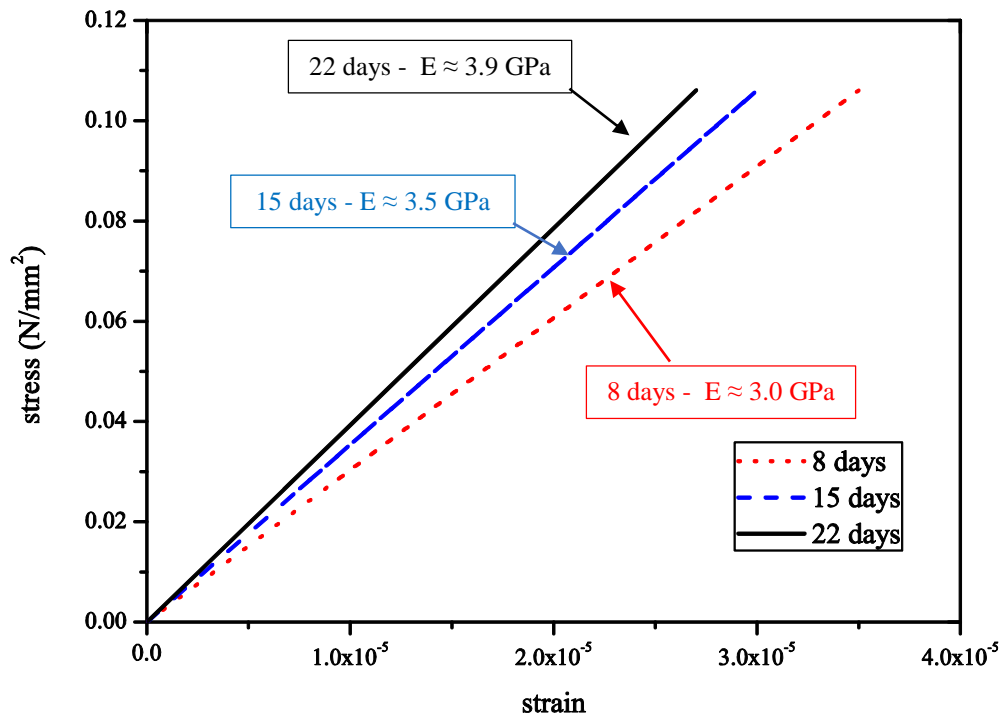


Figure 7-30 – Stress vs strain curves for the three ages experimentally studied

The values for the e-modulus respectively for 8, 15 and 22 days were: ~3.0 GPa, ~3.5 GPa and ~3.9 GPa. For different ages, the comparison of experimental and numerical simulations for the proposed formulation is presented in Figure 7-31.

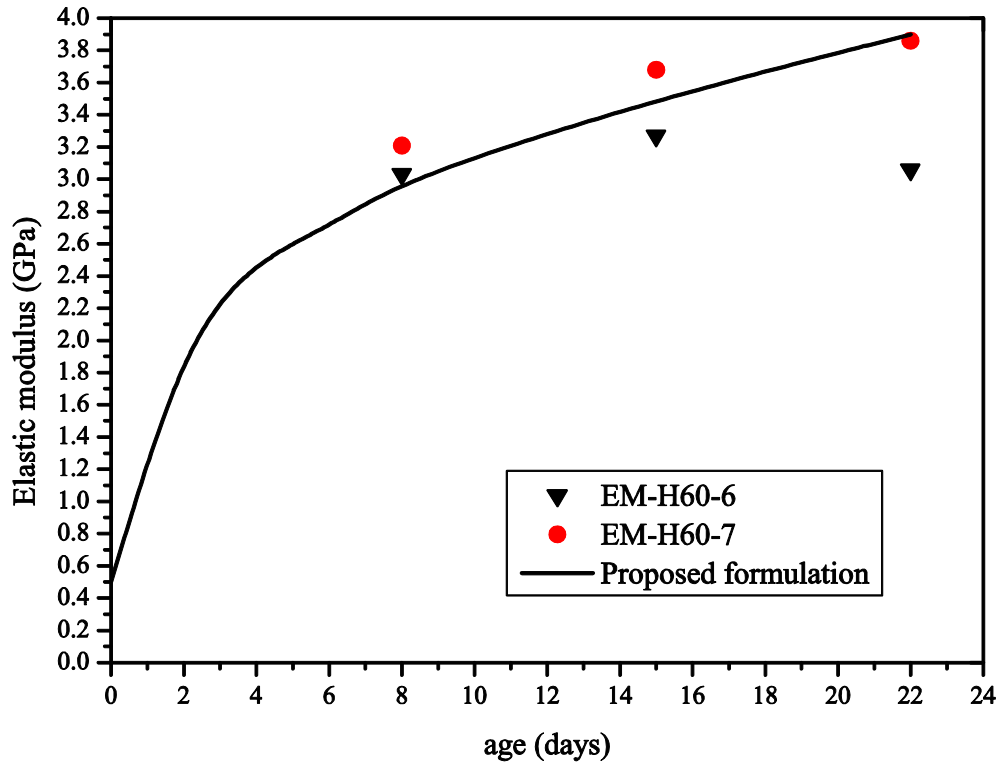


Figure 7-31 – Experimental and numerical results for elastic modulus

In summary, as shown in Figure 7-31, the simplified adapted formulation from the original models presented by Rostasy *et al.* (2001) and Lu and Kaya (2014) for the e-modulus presented a continuous evolution over time. In this approach, different complex iterations and models were simplified, namely with the explicit sum of the contribution for the two parcels: humidity and carbonation. The values for the curves that correlated the e-modulus with the humidity and reaction (Eqs. 7.3 and 7.4) were obtained by a fitting process. The resulting simulated e-modulus that corresponds to the global behavior of the specimen was able to very closely simulate the observed values obtained through experimental testing.

The mechanical simulations presented in the work of Ferretti and Bažant (2006b) did not consider the evolution of the mechanical properties over time. Also, as already mentioned in Ferretti and Bažant (2006a), no experiments were presented by the authors. Considering the research presented in this thesis, with experimental and numerical simulation regarding the study aerial lime, no other similar reference in literature could be found about this subject.

As a pioneer study, the focus of the research was to investigate several of the different phenomena involved. The scale of the specimens studied herein was relatively small, nevertheless the experiments and simulation presented diverse challenges. The application in real scale structures should also be considered.

8 CONCLUSIONS AND RECOMMENDATIONS FOR FURTHER WORK

8.1 Conclusions

In this thesis, a methodology for hygro-carbo-mechanical analyses of aerial lime mortars was presented, based on the proposal of Ferretti and Bažant (2006a). The originality of the presented work is related to the pioneering connection between experimentation and multi-physical simulation in the scope of aerial lime mortars. Significant emphasis was given to an adequate characterization of the raw materials and mortars in order to back sustained choices on models and modelling parameters. Particular attention was also given to the conduction of validation experiments and simulations.

In several aspects, the existing knowledge about concrete and cementitious-based materials gave a relevant initial support, in view of the near-absence of specific references for the topic of research of this thesis. Experiments, numerical implementations and the corresponding simulations were described throughout the thesis. The present section highlights the main conclusions of the developed work.

- *Humidity field and multi-physics model*

The main objective was to understand, study and implement numerical models presented in literature. The work initially focused on the simulation of humidity fields, particularly in a well-known and widely studied material such as concrete. The formulation adopted by Model Code 2010/1990 (CEB–FIP, 2010, CEB–FIP, 1993) was implemented through the Finite Difference Method (FDM) for 1D/axisymmetric simulations. Data was collected from the literature concerning several experiments in which humidity profiling was carried out. Then, several parametric/sensitivity analyses were conducted on the implemented model. These analyses allowed to establish a strategy for parameter testing and further allowed making a proposal of extension of the models of MC2010/1990 to include a factor for boundary effects.

Continuing with the numerical implementation, the hygro-carbo model presented by Ferretti and Bažant (2006a) was implemented in 1/2D and axisymmetric conditions in FDM. The

implemented coupled hygro-carbo model in 1D was verified with the results of these authors. This capacity to replicate the results of Ferretti and Bažant, which were the only ones to publish about multi-physical simulation of aerial lime mortars, was considered a cornerstone for the developments to be conducted with this thesis. Sensitivity analyses were done with the 1D model, mainly focused on the influence of carbon dioxide diffusivity and the effect of the thickness of the wall. The initial CO₂ diffusivity is one of the parameters that mostly affects the carbonation profile. A range from one hundred times higher and smaller times the value adopted from Ferretti and Bažant (2006a) was considered, and different results for carbonation were obtained according with the values of that parameter. The carbonation front after 50 years was ~5 cm of the wall, for the diffusivity, $D_{c,rif} = 24 \text{ mm}^2/\text{day}$ the smallest value; while for the highest one, $D_{c,rif} = 240000 \text{ mm}^2/\text{day}$, the wall presented ~80 cm carbonated. Similar conclusions were obtained for other ages.

For the effect of the thickness of the wall, three thicknesses were studied (1, 2 and 4 m). The results indicated that the carbonation occurred faster for thinnest wall.

- *Experimental program: mortar composition studies and humidity measurements*

This experimental work had the purpose of defining a suitable mortar composition for further study, as well as establishing and testing methodologies for conditioning and conducting humidity profiling measurements in aerial lime mortar specimens. The campaign started with the characterization of the raw materials and the definition of a suitable mix out of four different compositions tested. One of the largest challenges was to overcome the cracking proneness that the mortars had when relatively large specimens were prepared. The finally adopted mix was able to adequately perform in the intended geometry sizes, and was coherent with compositions cited in literature and used in practical applications, 1:1.3:3 (lime:water:sand) in terms of volume.

A prismatic mold to experimentally test 1D humidity fluxes in aerial lime mortar specimens was established, with simultaneous testing of totally sealed specimens for assessment of mortar self-desiccation. No reference was found in literature about the monitoring of the humidity in aerial lime mortar, therefore the study was pioneer. The humidity was monitored at three different depths. Around fifty days after the exposure, the specimen was in equilibrium with the environment. Similar humidity values were obtained for the three studied depths, which was unexpected as, for concrete, usually the humidity is different

according with the analyzed depth. These results could be linked with an elevated material diffusivity. The self-desiccation measurements indicated a stabilized final humidity value of ~90%, meaning that there was a reduction of ~10% as compared to the saturated state in which the material is initially mixed.

Following the initial experiments in prisms, the humidity was experimentally investigated in axisymmetric conditions, which correspond to the common geometry studied along the entire span of the thesis. For this study, cylinders were cast and two different configurations for the insertion of humidity probes were tested, parallel and perpendicular to the flux. The humidity diffusion study in cylinder specimen showed coherent result in terms of initial values with the previous prismatic tested molds (1D), however demonstrating a faster decreasing. The humidity decrease due to self-desiccation was again measured for one cylindrical mold, and the sealed specimens presented once more $h \approx 90\%$ at the end of the experiment. Another important fact to cite, for all the specimens studied, the first measured humidity values measured at ages as early as one day were $h \approx 90-93\%$, even in the sealed specimens, meaning that a significant part of the self-desiccation happened somewhere between the mixing and the age of 2 days. This was a far more pronounced pace of self-desiccation than for concrete (at least normal-strength concrete with relatively high water-to-cement ratio). Taking into account the elevated temperatures that the aerial lime mortar endures during mixing, which reach $90^{\circ}-300^{\circ}\text{C}$ (Snow and Torney, 2014), it is speculated that this apparent self-desiccation may be strongly related to evaporation mostly during mixing, which affects the material of all specimens.

This study was important to support the humidity field for the multi-physics modeling. In literature, regarding the study of humidity diffusion process, no references or experiments specifically for aerial lime mortar could be found, indicating the pioneer character of the study.

- *Experimental program for carbonation and mechanical properties*

For the second phase of experimental campaign, important experience and knowledge acquired from the previous testing was applied, particularly about the use of the mixture and preservation of the cylindrical specimen size. This extensive study that preserves important features at all its stages is a strong support to the integrated modelling envisaged as a final contribution.

The carbonation process was evaluated with two different techniques: phenolphthalein and TGA. The phenolphthalein indicator was sprayed in cylindrical specimens and cubes (after breaking at selected ages), while TGA was applied in samples taken from thin discs and cylinders. Both methods showed the expectable increase of carbonation over time. During the TGA experiments, the ranges of temperature adopted allowed the measurement of the two main phenomena involved in aerial lime carbonation, the dehydroxylation and the decarboxylation. In literature, different works adopted the in TGA tests a maximum temperature capable to evaluate only the dehydroxylation, inferring the reaction percentage from this measurement. Here, a formulation correlating the data from the experiments considering the dehydroxylation and the decarboxylation to calculate the carbonation degree was presented, in agreement with the definition used in the model by Ferretii and Bažant (2006a).

Concerning the time effect, and based on the comparison of the results from the TGA profiles, with the carbonation depths measured by phenolphthalein indicator, it was not possible to find a precise correlation between the percentage of CaCO_3 , measured through thermogravimetric analyses and the carbonation depth measured by phenolphthalein. A scattering of results could be seen. Adopting a linear approximation, a range of values ~20-60% was the equivalent R that intercepted the carbonation depth measured with the phenolphthalein indicator. As recognized in literature, the use of this pH indicator should be considered carefully.

Regarding the use of TGA in the study of cylindrical specimens, the results demonstrated a carbonation front with a very low percentage of CaCO_3 in the depths of 1.5 and 3.0 cm from the surface, even for ages when the humidity values were already stabilized with the surrounding environment (at 69 days of exposure time).

In order to be able to study the carbonation process without direct interaction with humidity diffusion processes, samples were taken from mortar discs with small dimensions for TGA testing. This investigation was done in two stages, initially with the study of the carbonation evolution in the “*standard*” chamber ($60\pm 5\%$, $T \approx 20\pm 2$ °C and environmental CO_2 concentration). These tests had the objective to study the time effect and also to evaluate the use of that technique. The results indicate that the carbonation process mainly occurred on the first ages, ~7 days, as the data were almost constant after this. The results also showed an incomplete carbonation reaction for these experiments.

Subsequently, the TGA tests were once more adopted, but with the addition of two other environments: the first one with elevated humidity ($h_{chamber} \sim 90\%$), and the second one with

high carbon dioxide concentration (concentration of CO_2 $\sim 4\%$). The calcium carbonate content showed a global increasing propensity over time, with the consequent increase of R , for the three scenarios. Comparing the results for the disc in the standard environment with the specimen stored in the environment with higher humidity, the main conclusions were: initially, the water tended to block the carbonation to occur, and this phenomenon was coherent with other results presented in literature; over time, the disc stored inside the humid chamber presented a higher carbonation percentage, and this observation was also in coherence with some results in literature (Dheilly *et al.*, 2002). The influence of CO_2 environmental concentration tended to be of little relevance in terms of the maximum reaction percentage, comparing the results for the samples stored in natural and elevated CO_2 concentrations, however the specimen inside the elevated CO_2 chamber presented an initial faster reaction rate.

The possible existence of an effect associated with the size of the specimen was investigated with five cylinders of different diameters, which were analyzed through partial breakage and tested with phenolphthalein indicator at three different ages. The phenomenon was more evident for the initial ages (10 days), and it tended to reduce over time. In fact, for the ages of 21 and 90 days the carbonation depths were similar, independently of the diameter.

Mechanical tests were done studying the e-modulus and compressive strength. Initially a preliminary e-modulus set-up was developed. During the test, some experimental problems were faced, namely related to cracking and fragility of the specimens. In this stage, the top and bottom surface of cylinder were not isolated from the environment. The first measurements indicated values ~ 0.7 GPa for the initial ages, such as 4 days, while for ~ 30 days the values were ~ 3.4 GPa, the tendency of increase was noticed over time. The results also indicated a general tendency of density dependency. For instance, comparing two specimens with difference of the densities $\sim 6\%$, the results for elastic modulus at the same age were $\sim 16\%$.

Continuing with the study, the introduction of a new setup to simulate the axisymmetric condition since the early ages could be considered a relevant aspect. Using the new configuration, the influence of the environmental humidity on the evolution of elastic modulus was investigated. Cylinders were stored in two different environments ($h_{chamber} \approx 60\%$ and $h_{chamber} \approx 90\%$). The obtained results of elastic modulus for the specimens stored in the climatic chamber with lower humidity presented higher values.

Comparing the e-moduli results for the specimens stored inside the two environments, at the age of 8 days the average for the cylinders stored inside the chamber with $h \approx 60\%$ was ~ 3

GPa; while for $h \approx 90\%$, values ~ 0.8 GPa were obtained, a difference of $\sim 73\%$. For 15 days, a similar variation was obtained with values ~ 3.5 GPa and 1.0 GPa respectively for the “*standard*” and “*high humidity*” chambers. Because of experimental limitation, the last tests were done at 22 and 21 days and the results average were 3.5 GPa and 2.0 GPa for the specimens respectively stored inside the “*standard*” and “*high humidity*” chamber.

The compressive strength was investigated in cubes. Initially the test was done at four different ages. For the ages 14, 28, 120 and 140 days, the average compressive failure stress was respectively: 0.37 , 0.49 , 1.16 and 1.61 MPa; and for the carbonation depth ~ 2.2 , 4.5 , 16.0 and 20.0 cm. In sequence, the influence of the environmental humidity was analyzed. As done for cylindrical specimens, the cubes were also stored in two different humidity environments. They were tested after 28 days, for the specimens stored inside the “*standard*” climatic chamber, the average value for compressive strength was ~ 0.73 MPa, and for the “*humid*” chamber, ~ 0.40 MPa. Consequently, the specimens maintained inside the chamber with higher environmental humidity presented a value $\sim 45\%$ smaller.

In general, terms, both mechanical properties presented an evolution over time for the two studied environments. As expected, the environmental humidity also affected the final results, the specimens stored inside the environment with lower humidity tended to present higher values for both mechanical properties.

- *Simulation of experiments with the multi-physics framework*

The main results of the experimental simulations obtained were compared with numerical simulations. Initially the simulations started with the humidity field, and were afterwards followed by multi-physics modelling, including the explicit modelling of carbonation and stiffness development, as well as the resulting mechanical response.

For the humidity field, in general, the numerical model based on the concrete Model Code approach was able to reasonably simulate the experiments in aerial lime mortar. Initially for the humidity field, the results were obtained considering the decoupled model, in an extensive campaign of simulations. This approach was focused in obtaining a pair of values for D_1 and $f_{boundary}$ by a similar approach to that adopted previously. Three experiments in axisymmetric conditions were simulated. The pair of D_1 and $f_{boundary}$ with the maximum R^2 for the specimens was adopted, $D_1 = 60 \text{ mm}^2/\text{day}$ and $f_{boundary} = 25 \times 10^{-4} \text{ m/day}$. The humidity

diffusion process for the specimens studied was mainly controlled by the $f_{boundary}$. This phenomenon was mainly associated with the relatively small diameter of the cylinders. After the study of the humidity field, the research focused on the simulation of the carbonation. The direct application of the model presented by Ferretti and Bažant (2006a), with the set of parameter adopted by the authors on the TGA results did not yield satisfactory results. Therefore, an optimization procedure was done. From the numerical simulation of TGA results at three different depths, the set of parameter that best simulated the carbonation was obtained. Even with extensive modifications and sensitivity analyses on the parameter values, the modeling was not capable to reproduce the experimental data, especially for the last measurement done after 69 days. From the proposed model by Ferretti and Bažant (2006a), an adaptation related to the function that correlates the diffusion of CO₂ with the humidity was done. For this equation, a different exponent was proposed (7.5). With this proposed adaptation the modeling could reproduce more appropriately the experimental data for all the tested age. From this step, the cylindrical specimens used to study the possible effect related with the size of the specimen in the carbonation phenomenon were also simulated.

After these simulations, the work was focused on the modelling for the elastic modulus evolution over time. For this stage, the multi-physics model (hygro-carbo) was coupled with a software for mechanical analyses (TNO-DIANA[®]). A formulation for correlating the evolution of the elastic modulus with the reaction degree and the humidity was proposed. These correlations were inspired in original models presented in literature for other materials, such as concrete (Rostásy *et al.*, 2001) and soil (Lu and Kaya, 2014). In general, terms, the coupled model could well reproduce the evolution of the elastic modulus, even providing insights into the expectable kinetics at very early ages. The analysis of results of the mechanical model also allowed having an interesting insight into the stress distribution within the tested specimens along time, highlighting the stress concentration near the outer regions of the specimen that are in direct contact with the environment and thus subjected to stronger carbonation.

8.2 *Further work*

The current study experienced some limitations, in both main aspects, experimental and numerical. Therefore, from the mentioned conclusions, the following issues are suggested for the development of further works:

- Because of the exothermic reaction and consequently heat generated during lime hydration, a precise controlling of the casting procedure is important. In future works, this challenge should be explicitly considered.
- The direct measuring of carbon dioxide concentration within inner parts of mortar specimens could allow a more precise quantification of the diffusion of this gas within the material. Some trial experiments were done here, but the results were not conclusive.
- The storage of specimens in environments with humidity lower than the 60% could provide further information on the behavior of the mortar in conditions with reduced humidity, and it would be a possible way to compare the influence of the field.
- Research regarding the humidity diffusion process in aerial lime mortar may be studied with more experiments, namely adopting specimens with different geometry and stored in diverse environments.
- The experimental study of sorption/desorption isotherms for aerial lime mortar may be important to study the behavior under realistic conditions in which the environmental humidity varies throughout the year.
- A test related to the evaluation of porosity of mortar in different ages is important. One example of technique that can be possible used is mercury intrusion. When performed in specimens submitted to different environmental and storage conditions, the results could provide more information about the alteration of the pore structure, due to the evolution of the carbonation process. This information is important for the multi-physics modeling.

- The study of the carbonation process for longer ages and the use of different techniques of measurement, with comparative analyses may be important for the study of this phenomenon. Thus, a research program involving calibration and subsequent comparison of different techniques is required to evaluate the carbonation, together with TGA and phenolphthalein. This would provide more information about the evolution of the carbonation process and the applicability of other methods to measure the phenomenon.
- Monitoring of the mechanical proprieties, such as compressive strength and elastic modulus, for longer ages, could give important information for the application in real structures.
- The study of the influence of the environmental temperature on different phenomena may bring information about the relevance of the thermal field.
- Regarding TGA tests, the adoption of a smaller distance between the collect samples, together with the study for a larger number of ages may provide results with a higher precision.
- The performing of TGA tests in specimens with different sizes of specimens may provide important information about the carbonation process, and the possible influence of the specimen size on the final results.
- The collection of samples in real ancient masonry structures may provide relevant information in existing buildings, even with the practical difficulties involved.
- The experimental investigation of creep, cracking and shrinkage in aerial lime mortar may give support for the study of long term behavior.
- An experimental monitoring in a real scale, or even in an ancient existing structure, coupling different fields in terms of experiments (humidity, carbonation, mechanical, etc.), may be relevant for a better understanding of ancient structures based in aerial lime mortar.

- Some trials were done with the objective to create a climatic chamber with reduced humidity value ($h_{chamber} < 60\%$). In these attempts, different methods to control the humidity were adopted, such as the use of silica gel, a dehumidifier, also the coupling of the two methods. However, the system was not able to keep the humidity value inside the chamber constant. Another possibility was the use of salts (Granja *et al.*, 2014), however, they were not adopted, because of the possible influence of the material on the carbonation process. The adoption of an environment with lower humidity, and the study of the possible influence of the salts may bring important contribution.

Regarding the numerical limitations, the main point can be considered the application of relatively simple models. These models summarize complex phenomena in a simplified form. Considering these limitations, some reflections are cited:

- The implementation of the humidity model done in this thesis is valid only for isothermal conditions, which is not realistic in view of real structures. This is a point that requires further development. The numerical study of the humidity flux considering more complex models may also give important contributions for the simulation of the process in aerial lime mortar.

- The hygro-carbo model was implemented in 1D, axisymmetric and 2D conditions, and it can be relatively easily extended to 3D conditions. However, the 2D program demanded long time in processing, due to the large dimensions of the involved matrixes and their complex couplings, which induced strong non-linearity. This can also compromise the proper functioning of the 3D modeling. More developments or the adoption of commercial software (advanced solution algorithms and use of parallel computing) to solve the coupled problem may be needed.

- Regarding the aspects about the multi-physics numerical modeling, simulations considering other models, including more complex formulations that the ones adopted can bring important contributions. Noticeably, this adoption would require a more extensive experimental program and further development in numerical aspects.

- The applicability of the proposed set of parameters and models in the present work should also be tested in specimens with larger dimensions or even in real scale structures.

- The numerical coupling with others phenomena such as creep, shrinkage and cracking may be important, especially in the study for long term behavior of real structures.

- Upon stabilized understanding of the multi-physical behavior of aerial lime mortars and achievement of the capability to adequately simulate the several physical fields involved, it is necessary to step up to the scale of the structure in the mechanical analysis and evaluate real masonry elements, with careful judgement about the redistribution of internal stresses along the years in masonry due to causes related to the mortar itself.

REFERENCES

- ACI (1992). "Guide to durable concrete, ACI 201.2R-92." American Concrete Institute. Farmington Hills, Michigan: ACI Committee 201.
- ACI (2006). "Guide for concrete slabs that receive moisture-sensitive flooring materials." A 302.2R-06. American Concrete Institute.
- Adam, J. P., (2005). "Roman Building: Materials and Techniques." 1st edition. Taylor & Francis.
- Adams, J., Dollimore, D. and Griffiths, D. L., (1998). "Thermal analytical investigation of unaltered Ca(OH)₂ in dated mortars and plasters." *Thermochimica Acta*, 324 (1-2), 67-76.
- Adams, J., Kneller, W. and Dollimore, D., (1992). "Thermal analysis (TA) of lime and gypsum-based medieval mortars." *Thermochimica Acta*, 211 (10), 93-106.
- Adriano, P., Santos Silva, A., Veiga, R., Mirão, J. and Candeias, A. E., (2009). "Microscopic characterisation of old mortars from the Santa Maria Church in Évora." *Materials Characterization*, 60 (7), 610-620.
- Agnew, N., (2010). "Conservation of Ancient Sites on the Silk Road: Proceedings of the Second International Conference on the Conservation of Grotto Sites, Mogao Grottoes, Dunhuang, People's Republic of China, June 28 - July 3, 2004." Getty Conservation Institute.
- Akita, H., Fujiwara, T. and Ozaka, Y., (1997). "A practical procedure for the analysis of moisture transfer within concrete due to drying." *Magazine of Concrete Research*, 49 (197), 129-137.
- Al-Bashaireh, K. S., (2008). "Chronology and technological production styles of Nabatean and Roman plasters and mortars at Petra (Jordan)." PhD Thesis, The University of Arizona.
- Al-Fadhala, M. and Hover, K. C., (2001). "Rapid evaporation from freshly cast concrete and the Gulf environment." *Construction and Building Materials*, 15 (1), 1-7.
- Al-Khaiat, H. and Fattuhi, N., (2002). "Carbonation of concrete exposed to hot and arid climate." *Journal of Materials in Civil Engineering*, 14 (2), 97-107.
- Alexander, M. and Mindess, S., (2010). "Aggregates in Concrete." 1st edition. Taylor & Francis.
- Algarvio, M. P. R. P. (2010). Influence of water/lime ratio on the characteristics of lime mortars for use as substitution renders in ancient buildings, Extended Abstract. Available:
<https://fenix.tecnico.ulisboa.pt/downloadFile/395142119584/Resumo%20alargado.pdf> [Accessed 10-02-2015].

- Alvarez De Buergo, B., M., Garcia Calleja, M. A., Gonzalez Limon, T. and Soriano Carrillo, J., (1994). "Estudio de la eficacia y durabilidad de los tratamientos de conservacion aplicados a los materiales petreos del Claustro de San Juan de Duero en Soria (in Spanish)." *Ingenieria Civil (Madrid)*, 96, 89-97.
- Alvarez, J. I., Navarro, I. and Garcia Casado, P. J., (2000). "Thermal, mineralogical and chemical studies of the mortars used in the cathedral of Pamplona (Spain)." *Thermochimica Acta*, 365 (1-2), 177-187.
- Anderberg, A. and Wadsö, L., (2008). "Method for simultaneous determination of sorption isotherms and diffusivity of cement-based materials." *Cement and Concrete Research*, 38 (1), 89-94.
- Andersen, H. D., Zimmermann, H. D., Friis, H. and Schnell, U., (1999). "Examination of hydraulic lime mortars of medieval churches in Denmark." In: C. Groot and J. J. Hughes P. Bartos, ed. *International RILEM Workshop on Historic Mortars: Characteristics and Tests*, 1999, Paisley, Scotland. RILEM Publications, 37 - 42.
- Andrejkovicova, S., Ferraz, E., Velosa, A. L., Silva, A. S. and Rocha, F., (2012). "Air Lime Mortars with Incorporation of Sepiolite and Synthetic Zeolite Pellets." 9 (1), 79-91.
- Angelo, P. C. and Subramanian, R., (2008). *Powder Metallurgy: Science, Technology and Applications*. Eastern Economy Edition. PHI Learning.
- Anzani, A. and Binda, L. (2013). Evolution of the crack-pattern as a visible effect of long term damage. Available: <http://www.gruppofrattura.it/ocs/index.php/ICF/ICF11/paper/viewFile/10598/9946> [Accessed 12-11-2013].
- Anzani, A., Binda, L. and A., T., (2005). "Application of a dam-age model to the study of the long term behaviour of ancient towers." In: *1st Canadian Conference on Effective Design of Structures*, 2005, Ontario, Canada.
- Anzani, A., Binda, L. and Roberti, G. M., (2000). "The effect of heavy persistent actions into the behaviour of ancient masonry." *Materials and Structures*, 33 (4), 251-261.
- Anzani, A., Binda L., Saisi, A. and Roberti, G. M., (2002). "Historic Structures." In: R. O. Ritchie I. Milne, and B. Karihaloo (ed.) *Comprehensive Structural Integrity*. Elsevier Science Ltd.
- Anzani, A., Garavaglia, E. and Binda, L., (2009). "Long-term damage of historic masonry: A probabilistic model." *Construction and Building Materials*, 23 (2), 713-724.
- APA. (2009). Air quality in interior spaces - A technical guide (in Portuguese). *Ministério do Ambiente, Ordenamento do Território e Energia* [Online]. Available: http://www.apambiente.pt/_zdata/Divulgacao/Publicacoes/Guias%20e%20Manuais/manual%20QArInt_standard.pdf [Accessed 05-04-2015].

- Aphane, M. E., (2007). *"The hydration of magnesium oxide with different reactivities by water and magnesium acetate."* Mastes Thesis, University of South Africa.
- Arandigoyen, M., Bernal, J. L. P., López, M. A. B. and Alvarez, J. I., (2005). "Lime-pastes with different kneading water: Pore structure and capillary porosity." *Applied Surface Science*, 252 (5), 1449-1459.
- Arandigoyen, M., Bicer-Simsir, B., Alvarez, J. I. and Lange, D. A., (2006). "Variation of microstructure with carbonation in lime and blended pastes." *Applied Surface Science*, 252 (20), 7562-7571.
- Arandigoyen, M., Lanas, J. and Alvarez, J. I., (2004). "Carbonation of limecement mortars: a description of this process through the fractal dimension. In: D. Kwiatkowski and R. Lifvendahl, eds. Proceedings of the 10th International congress on deterioration and conservation of stone." In: *ICOMOS*, 2004, Stockholm, Sweden. 1057–1064.
- Arizzi, A., (2010). "Characterization of Lime Mortars for their use in Restoration of Cultural Heritage and in Modern Construction." *Revista de la Sociedad Española de Mineralogía*, 12, 78-79.
- Arizzi, A. and Cultrone, G., (2012). "The difference in behaviour between calcitic and dolomitic lime mortars set under dry conditions: The relationship between textural and physical–mechanical properties." *Cement and Concrete Research*, 42 (6), 818-826.
- Arizzi, A. and Cultrone, G., (2013). "The influence of aggregate texture, morphology and grading on the carbonation of non-hydraulic (aerial) lime-based mortars." *Quarterly Journal of Engineering Geology and Hydrogeology*, 46 (4), 507-520.
- Arizzi, A., Martínez Martínez, J., Cultrone, G. and Benavente, D., (2011). "Mechanical Evolution of Lime Mortars During the Carbonation Process." *Key Engineering Materials*, 465, 483-486.
- Ashurst, J. and Ashurst, N., (1988). *"Practical building conservation. English heritage technical Handbook."* Gower Technical Press, Ltd.
- ASTM (2011). *"C51-11 - Standard Terminology Relating to Lime and Limestone (as used by the Industry)."* Subcommittee: C07.08. ASTM International American Society for Testing and Materials.
- Atkins, P., (2010). *"Shriver and Atkins' Inorganic Chemistry."* 5th edition OUP Oxford.
- Atkins, P. and de Paula, J., (2014). *"Atkins' Physical Chemistry."* 9th edition. OUP Oxford.
- Aysen, A., (2002). *"Soil Mechanics: Basic Concepts and Engineering Applications."* Taylor & Francis.
- Azenha, M., (2004). *"Behaviour of concrete at early ages. Phenomenology and thermomechanical analysis. (in Portuguese)."* MSc Thesis, Univeristy of Porto.

- Azenha, M., (2009). "Numerical simulation of the structural behaviour of concrete since its early ages." PhD Thesis, University of Porto, University of Tokyo.
- Azenha, M., Maekawa, K., Ishida, T. and Faria, R., (2007a). "Drying induced moisture losses from mortar to the environment. Part I: experimental research." *Materials and Structures*, 40 (8), 801-811.
- Azenha, M., Maekawa, K., Ishida, T. and Faria, R., (2007b). "Drying induced moisture losses from mortar to the environment. Part II: numerical implementation." *Materials and Structures*, 40 (8), 813-825.
- Baccaro, M. L. P., Balzi, S., Del Chiaro, L. and Vannucci, S., (2000). "The effects of the strong use of cements in restoration: the case of Barga Duomo (northern Tuscany)." In: V. Fassina, ed. *Proceedings of the 9th International Congress on deterioration and conservation of stone 2*, 19-24 June 2000, Venice, Italy. 3-12.
- Bakolas, A., Biscontin, G., Moropoulou, A. and Zendri, E., (1998). "Characterization of structural byzantine mortars by thermogravimetric analysis." *Thermochimica Acta*, 321 (1-2), 151-160.
- Balcerowiak, W., (2000). "Phase Analysis of High-calcium Lime by TG." *Journal of Thermal Analysis and Calorimetry*, 60 (1), 67-70.
- Bard, A. J. and Faulkner, L. R., (1980). "Electrochemical Methods: Fundamentals and Applications." New York, USA: Wiley.
- Baroghel-Bouny, V., (2007). "Water vapour sorption experiments on hardened cementitious materials: Part I: Essential tool for analysis of hygral behaviour and its relation to pore structure." *Cement and Concrete Research*, 37 (3), 414-437.
- Baroghel-Bouny, V., Mainguy, M., Lassabatere, T. and Coussy, O., (1999). "Characterization and identification of equilibrium and transfer moisture properties for ordinary and high-performance cementitious materials." *Cement and Concrete Research*, 29 (8), 1225-1238.
- Baroghel-Bouny, V., (1996). "Concrete: From material to structure." In: J.P. Bournazel and Y. Malier, eds. *Proceedings of the International RILEM Conference*, September 11-12 1996, Arles, France. 144-165.
- Baronio, G., Binda, L. and Saisi, A., (1999). "Mechanical and physical behaviour of lime mortars reproduced after the characterisation of historic mortar." In: C. Groot and J. J. Hughes P. Bartos, ed. *International RILEM Workshop on Historic Mortars: Characteristics and Tests*, 1999, Paisley, Scotland. RILEM, 307-325.
- Bartos, P., Groot, C. and Hughes, J. J., (2000). "PRO 12: International RILEM Workshop on Historic Mortars: Characteristics and Tests." RILEM Publications.
- Bary, B. and Sellier, A., (2004). "Coupled moisture-carbon dioxide-calcium transfer model for carbonation of concrete." *Cement and Concrete Research*, 34 (10), 1859-1872.

- Basheer, L., Kropp, J. and Cleland, D. J., (2001). "Assessment of the durability of concrete from its permeation properties: a review." *Construction and Building Materials*, 15 (2–3), 93-103.
- Bazant, M. Z. and Bažant, Z. P., (2012). "Theory of sorption hysteresis in nanoporous solids: Part II Molecular condensation." *Journal of the Mechanics and Physics of Solids*, 60 (9), 1660-1675.
- Bažant, Z. P., (1972). "Thermodynamics of hindered adsorption and its implications for hardened cement paste and concrete." *Cement and Concrete Research*, 2 (1), 1-16.
- Bažant, Z. P., (1988). "*Mathematical modeling of creep and shrinkage of concrete.*" Chichester, John Wiley & Sons, Inc., xxii, 459 s.
- Bažant, Z. P. and Baweja, S., (2000). "Creep and shrinkage prediction model for analysis and design of concrete structures: model B3." In: Adam Neville A. Al-Manaseer, ed. *Symposium: Creep and Shrinkage—Structural Design Effects, ACI SP-194*, 2000, Farmington Hills, Michigan. American Concrete Institute, 1–83.
- Bažant, Z. P. and Chern, J. C., (1985). "Concrete creep at variable humidity: constitutive law and mechanism." *Materials and Structures*, 18 (1), 1-20.
- Bažant, Z. P., Hauggaard, A. B. and Baweja, S., (1997a). "Microprestress–solidification theory for concrete creep: II. Algorithm and verification." *Journal of Engineering Mechanics, ASCE*, 123 (11), 1195–1201.
- Bažant, Z. P., Hauggaard, A. B., Baweja, S. and Ulm, F. J., (1997b). "Microprestresssolidification theory for concrete creep: I. Aging and drying effects." *Journal of Engineering Mechanics, ASCE*, 123 (11), 1188–1194.
- Bažant, Z. P. and Najjar, L. J., (1971). "Drying of concrete as a nonlinear diffusion problem." *Cement and Concrete Research*, 1 (5), 461-473.
- Bažant, Z. P. and Najjar, L. J., (1972). "Nonlinear water diffusion in nonsaturated concrete." *Matériaux et Construction*, 5 (1), 3-20.
- Bažant, Z. P. and Oh, B. H., (1983). "Crack band theory for fracture of concrete." *Matériaux et Construction*, 16 (3), 155-177.
- Beck, C. W., (1950). "Differential thermal analysis curves of carbonate minerals." *American Mineralogist*, 35 (1-2), 985–1013.
- Benboudjema, F., Meftah, F. and Torrenti, J. M., (2005). "Interaction between drying, shrinkage, creep and cracking phenomena in concrete." *Engineering Structures*, 27 (2), 239-250.
- Bentur, A., (2002). "Cementitious Materials—Nine Millennia and A New Century: Past, Present, and Future." *Journal of Materials in Civil Engineering*, 14 (1), 2-22.

- Bentz, D. P., (1997). "Three-Dimensional Computer Simulation of Portland Cement Hydration and Microstructure Development." *Journal of the American Ceramic Society*, 80 (1), 3-21.
- Bianchini, G., Marrocchino, E. and Vaccaro, C., (2004). "Chemical and mineralogical characterisation of historic mortars in Ferrara (northeast Italy)." *Cement and Concrete Research*, 34 (8), 1471-1475.
- Biggs, D. T., (2007). "Hybrid Masonry Structures." In: *Tenth North American Masonry Conference*, June 3-6 2007, St. Louis, USA. The Masonry Society, 13.
- Binda, L., (2003). "Compatibility between safety and authenticity: The experience of Noto Cathedral." In: *WTA Colloquium on Authenticity in the Restoration of Monuments*, 2003, Katholieke Universiteit Leuven.
- Binda, L., (2008). *"Learning from failure: Long-term behaviour of heavy masonry structures."* Wessex Institute of Technology: WIT Press.
- Binda, L., Anzani, A., Saisi, A. and Mirabella Roberti, G., (2003). "1.02 - Historic Masonry Structures." In: I. Karihaloo, R. O. Milne and B. Ritchie (eds.) *Comprehensive Structural Integrity*. Oxford: Pergamon.
- Binda, L., Folli, T. and Roberti, G. M., (2000a). "Survey and investigation for the diagnosis of damaged masonry structures: the "Torrazzo of Cremona"." In: *2th International Brick/Block Masonry Conference*, 2000a, Madrid, Spain. 237–257.
- Binda, L., Gatti, G., Manano, G., Poggi, C. and Sacchi Landriani, G., (1992). "The collapse of the Civic Tower of Pavia: a survey of the materials and structure." *Masonry International*, 6 (1), 11-20.
- Binda, L. and Saisi, A., (2001). "Non destructive testing applied to historic buildings: The case of some Sicilian Churches." In: P.B. Lourenço and P. Roca, ed. *Historical Constructions*, 2001, Guimarães, Portugal. 29–46.
- Binda, L. and Saisi, A., (2002). "State of the Art of Research on Historic Structures in Italy." In: *Proceedings of 11th Advanced Research Initiation Assisting and Developing Networks in Europe (ARIADNE)*, May 20-26 2002, http://www.arczip.cz/w11/w111_binda.pdf,
- Binda, L. and Saisi, A. (2004). State of Art of Research on Historical Structures in Italy. Available: http://www.arcchip.cz/w11/w11_binda.pdf [Accessed 10-12- 2013].
- Binda, L. and Saisi, A., (2009). "Application of NDTs to the diagnosis of Historic Structures " In: *NDTCE'09, Non-Destructive Testing in Civil Engineering* June 30th – July 3rd 2009, Nantes, France.
- Binda, L., Saisi, A., Messina, S. and Tringali, S., (2001). "Failure due to long-term behaviour of heavy structures: the Pavia Civic Tower and the Noto Cathedral." *Wessex Institute Online*, WIT Press 10.
- Binda, L., Saisi, A. and Tiraboschi, C., (2000b). "Investigation procedures for the diagnosis of historic masonries." *Construction and Building Materials*, 14 (4), 199–233.

- BLA. (2015). British Lime Association Available: http://www.britishlime.org/lime_uses/construction.php [Accessed 07-04-2015].
- Böke, H., Çizer, Ö., İpekoğlu, B., Uğurlu, E., Şerifaki, K. and Toprak, G., (2008). "Characteristics of lime produced from limestone containing diatoms." *Construction and Building Materials*, 22 (5), 866-874.
- Boutin, F. and Bromblet, P., (2000a). "Durability of materials used in the replacement of sculptures in historical monuments." In: *CANMET/ACI International conference on durability of concrete*, June 4-9, 2000a, Barcelone, Spain. 647-661.
- Boutin, F. and Bromblet, P., (2000b). "Evaluation of materials used in the replacement of sculptures in historical monuments, Weathering of natural stone: causes, mechanism and measurement of stone damage." In: *9th International Congress on Deterioration and Conservation of Stone*, 2000b, Venice, Italy. 31-39.
- Boynton, R. S., (1984). *"Lime and limestone in Encyclopedia of Chemical Technology."* New York: Wiley.
- Brandon, C. J., Hohlfelder, R. L., Jackson, M. D. and Oleson, J. P., (2014). *"Building for Eternity: the History and Technology of Roman Concrete Engineering in the Sea."* Illustrated edition. Oxbow Books.
- Brandt, A. M., (1994). *"Cement-based Composites: Materials, Mechanical Properties and Performance."* Second edition. Taylor & Francis.
- Bravo, E. L., Suárez, M. H., Cueto, O. G., Tijssens, E. and Ramon, H., (2012). "Determination of basic mechanical properties in a tropical clay soil as a function of dry bulk density and moisture." *Revista Ciencias Técnicas Agropecuarias*, 21 (3), 5-11.
- Brooks, J. J. and Bakar, B. H. A., (2004). "Shrinkage and creep of masonry mortar." *Materials and Structures*, 37 (3), 177-183.
- Brunauer, S., (2007). *"The Adsorption of Gases and Vapors."* Reprinted in 2007 by Brunauer Press. Brunauer Press.
- Bruni, S., Cariati, F., Fermo, P., Pozzi, A. and Toniolo, L., (1998). "Characterization of ancient magnesian mortars coming from northern Italy." *Thermochimica Acta*, 321 (1-2), 161-165.
- Bruno, P., Calabrese, D., Di Pierro, M., Genga, A., Laganara, C., Manigrassi, D. A. P., Traini, A. and Ubbriaco, P., (2004). "Chemical-physical and mineralogical investigation on ancient mortars from the archaeological site of Monte Sannace (Bari—Southern Italy)." *Thermochimica Acta*, 418 (1-2), 131-141.
- Buenfeld, N. R. and Hassanein, N. M., (1998). "Life prediction of concrete structures using neural networks." In: *Proceedings of the ICE - Structures and Buildings*, 1998, 38-48.
- Bunte, D. and Rostasy, F., (1994). "Ingenieurmodell zur Vorhersage der Dauerhaftigkeit gegen karbonatisierungsinduzierte Korrosion der Bewehrung (in Germany)." In:

12 *Internationale Baustofftagung (ibausil)*, 1994, Weimar, Germany. *Wissenschaftliche Zeitschrift der Hochschule für Architektur und Bauwesen Weimar*, 169–172.

- Burkan Isgor, O. and Razaqpur, A. G., (2004). "Finite element modeling of coupled heat transfer, moisture transport and carbonation processes in concrete structures." *Cement and Concrete Composites*, 26 (1), 57-73.
- Cabeza, L. F., Barreneche, C., Miró, L., Morera, J. M., Bartolí, E. and Inés Fernández, A., (2013). "Low carbon and low embodied energy materials in buildings: A review." *Renewable and Sustainable Energy Reviews*, 23 (0), 536-542.
- Cadoni, E., Labibes, K., Albertini, C., Berra, M. and Giangrasso, M., (2001). "Strain-rate effect on the tensile behaviour of concrete at different relative humidity levels." *Materials and Structures*, 34 (1), 21-26.
- Callebaut, K., (2000). "*Characterisation of Historical Lime Mortars in Belgium: Implications for Restoration Mortars.*" PhD Thesis, Katholieke Universiteit.
- Callebaut, K., Elsen, J., Van Balen, K. and Viaene, W., (2001). "Nineteenth century hydraulic restoration mortars in the Saint Michael's Church (Leuven, Belgium): Natural hydraulic lime or cement?" *Cement and Concrete Research*, 31 (3), 397-403.
- Carino, N. J. and Lew, H. S., (1984). "The maturity method: theory and application." *Cement, Concrete, and Aggregates*, 6 (2), 61-73.
- Carran, D., Hughes, J., Leslie, A. and Kennedy, C., (2011). "A Short History of the Use of Lime as a Building Material Beyond Europe and North America." *International Journal of Architectural Heritage*, 6 (2), 117-146.
- Cazalla, O., Navarro, C. R., Sebastian, E. and G., C., (2000). "Aging of lime putty: Effects on traditional lime mortar carbonation." *Journal of American Ceramic Society*, 83 (5), 1070–1076.
- CEB–FIP (1993). "*Model Code 1990.*" CEB–FIP: Comité Euro–International Du Béton.
- CEB–FIP (2010). "*Model Code 2010, V1.*" CEB–FIP: Comité Euro–International Du Béton.
- CEN (1999a). "*CEN-EN-1015-2: Bulk sampling of mortars and preparation of test mortars - Part 2.*" European Committee for Standardization.
- CEN (1999b). "*CEN-EN-1015-11 - Methods of test for mortar for masonry. Determination of flexural and compressive strength of hardened mortar.*" Part 11. European Committee for Standardization.
- CEN (2002). "*CEN-EN-13139:2002 - Aggregates for mortar.*" European Committee for Standardization.
- CEN (2004). "*CEN-EN 14146:2004 - Natural stone test methods. Determination of the dynamic elastic modulus of elasticity (by measuring the fundamental resonance frequency.*" European Committee for Standardization.

- CEN (2005a). "*CEN-EN-196-1-Methods of testing cement. Determination of strength.*" European Committee for Standardization.
- CEN (2005b). "*CEN-EN 14580:2005 - Natural stone test methods. Determination of static elastic modulus.*" The British Standards Institution.
- CEN (2010a). "*CEN-EN 459-1.*" Part 1: Definitions, specifications and conformity criteria. European Committee for Standardization.
- CEN (2010b). "*CEN-EN 459-2 - Building lime. Test methods - Part 2.*" European Committee for Standardization.
- Chang, C.-F. and Chen, J.-W., (2006). "The experimental investigation of concrete carbonation depth." *Cement and Concrete Research*, 36 (9), 1760-1767.
- Chen, M., Wang, N., Yu, J. and Yamaguchi, A., (2006). "Preparation of slaking resistant CaO aggregate from lightweight CaCO₃ with oxide addition." *Materials Letter*, 61 (1), 45-49.
- Christensen, R., (1979). "*Mechanics of composite materials.*" Second edition reprinted in 2005. New York: Wiley Interscience.
- Christidis, G. E., (2011). "*Advances in the Characterization of Industrial Minerals.*" European Mineralogical Union.
- Cizer, O., (2009). "*Competition between carbonation and hydration on the hardening of calcium hydroxide and calcium silicate binders.*" PhD Thesis, K. U. Leuven.
- Cizer, Ö., Van Balen, K., Elsen, J. and Van Gemert, D., (2012). "Real-time investigation of reaction rate and mineral phase modifications of lime carbonation." *Construction and Building Materials*, 35, 741-751.
- Cizer, O., Van Balen, K. and Van Gemert, D. (n. d). Components presents in aerial lime mortar during the carbonation. *Sustainable Materialization of Residues from Thermal Processes into Products - SMaRT-Pro²* [Online]. Available: http://web.abo.fi/fak/tkf/vt/aceme10/6-3%20%20C3%96zlem%20Cizer_ACEME10.pdf [Accessed 10/11/2014].
- Cizer, O., Van Balen, K. and Van Gemert, D., (2006). "Carbonation reaction of lime hydrate and hydraulic binders at 20°C." In: The Royal Society, ed. *First International Conference on Accelerated Carbonation for Environmental and Materials*, 12-14 June 2006 London, UK.
- Cliver, E. B., (1974). "Tests for the Analysis of Mortar Samples." *Bulletin of the Association for Preservation Technology*, 6, 68-73.
- Colleparidi, M., (1990). "Degradation and restoration of masonry walls of historical buildings." *Materials and Structures*, 23 (2), 81-102.
- Como, M., (2012). "*Statics of Historic Masonry Constructions.*" Second edition. Springer-Verlag Berlin Heidelberg: Springer Berlin Heidelberg.

- Conciatori, D., Grégoire, É., Samson, É., Marchand, J. and Chouinard, L., (2014). "Statistical analysis of concrete transport properties." *Materials and Structures*, 47 (1-2), 89-103.
- Coroado, J., Paiva, H., Velosa A. and Ferreira, V. M., (2010). "Characterization of renders, joint mortars and adobes from traditional constructions in Aveiro-(Portugal)." *International Journal of Architectural Heritage*, 4 (2), 102-114.
- Cowan, H. J., (1978). "The Master Builders: A History of Structural and Environmental Design from Ancient Egypt to the Nineteenth Century." *Technology and Culture*, 19 (3), 525-528.
- Cowper, A. D., (1998). "*Lime and lime mortars.*" Reprint of 1927 edition, Illustrated edition. Donhead: Shaftsbury: Donhead Publishing Ltd.
- Crandall, S. H., (2012). "*An Introduction to Mechanics of Solids.*" Tata McGraw-Hill Education Private Limited.
- Crank, J., (1979). "*The Mathematics of Diffusion.*" 2nd edition. OUP Oxford.
- Croci, G., (1998). "*The Conservation and Structural Restoration of Architectural Heritage.*" Computational Mechanics Publications.
- Croft, D. R. A. and Lilley, D. G., (1977). "*Heat Transfer Calculations Using Finite Difference Equations.*" London: Applied Science Publishers LTD.
- Cultrone, G., Sebastián, E. and Huertas, M. O., (2005). "Forced and natural carbonation of lime-based mortars with and without additives: Mineralogical and textural changes." *Cement and Concrete Research*, 35 (12), 2278-2289.
- D'Ayala, D. and Fodde, E., (2008). "*Structural analysis of historical construction: Preserving safety and significance.*" Taylor & Francis.
- Daniele, V. and Taglieri, G., (2015). "Ca(OH)₂ Nanoparticle Characterization: Microscopic Investigation Of Their Application On Natural Stones." In: C. A. Brebbia A. A. Mammoli, and A. Klemm, ed. *Materials Characterisation V*, 22 - 24 April 2015, Valencia, Spain. 12.
- Das, B. M. and Sobhan, K., (2009). "*Principles of Geotechnical Engineering.*" 8th Edition. CL Engineering, Cengage Learning.
- Degryse, P., Elsen, J. and Waelkens, M., (2002). "Study of ancient mortars from Sagalassos (Turkey) in view of their conservation." *Cement and Concrete Research*, 32 (9), 1457-1463.
- Dewaele, P. J., Reardon, E. J. and Dayal, R., (1991). "Permeability and porosity changes associated with cement grout carbonation." *Cement and Concrete Research*, 21 (4), 441-454.
- Dheilly, R. M., Tudo, J. and Quéneudec, M., (1998). "Influence of climatic conditions on the carbonation of quicklime." *Journal of Materials Engineering and Performance*, 7 (6), 789-795.

- Dheilly, R. M., Tudo, J., Sebaïbi, Y. and Quéneudec, M., (2002). "Influence of storage conditions on the carbonation of powdered $\text{Ca}(\text{OH})_2$." *Construction and Building Materials*, 16 (3), 155-161.
- Di Luzio, G. and Cusatis, G., (2009a). "Hygro-thermo-chemical modeling of high-performance concrete. II: Numerical implementation, calibration, and validation." *Cement and Concrete Composites*, 31 (5), 309-324.
- Di Luzio, G. and Cusatis, G., (2009b). "Hygro-thermo-chemical modeling of high performance concrete. I: Theory." *Cement and Concrete Composites*, 31 (5), 301-308.
- Dodge, H., (1984). "*Building Materials and Technique in the Eastern Mediterranean from the Hellenistic Period to the Fourth Century AD.*" PhD Thesis, University of Newcastle upon Tyne. .
- DOI, (2004). "*Department of Interior - The Preservation of Historic Architecture: The U.S. Government's Official Guidelines for Preserving Historic Homes.*" Globe Pequot.
- Dupas, M., (1981). "Methodes d'analyse chimique appliques a l'etude de l'alteration et de la conservation des materiaux pierreux." In: Centro conservazione sculture al'aperto, ed. *The conservation of stone*, 1981, Bologna. 45-464.
- Duran, A., Perez-Maqueda, L. A., Poyato, J. and Perez-Rodriguez, J. L., (2010). "A thermal study approach to roman age wall painting mortars." *Journal of Thermal Analysis and Calorimetry*, 99 (3), 803-809.
- E.C. (2014). European Commission, Tourism statistics. *Eurostat information* [Online]. Available: http://ec.europa.eu/eurostat/statistics-explained/index.php/Tourism_statistics [Accessed 06-09-2014].
- E.C. (2015). Climate Action. *European Commission* [Online]. Available: <http://ec.europa.eu/clima/policies/brief/eu/> [Accessed 07-04-2015].
- Earnest, C. M., (1988). "The modern thermogravimetric approach to the compositional analysis of materials." In: C.M. Earnest, ed. *Compositional analysis by Thermogravimetry*, 1988, Philadelphia: American Society for Testing and Material, 1-18.
- Ek, M., Gellerstedt, G. and Henriksson, G., (2009). "*Pulping Chemistry and Technology.*" Walter de Gruyter.
- El-Reedy, M., (2007). "*Steel-Reinforced Concrete Structures: Assessment and Repair of Corrosion.*" CRC Press.
- Elert, K., Carlos Rodriguez-Navarro, Eduardo Sebastian Pardo, Eric Hansen and Cazalla, O., (2002). "Lime Mortars for the Conservation of Historic Buildings." *International Institute for Conservation of Historic and Artistic Works*, 47 (1), 62-75.

- Elliot, C. D., (1992). *"Technics and architecture: The development of materials and systems of buildings."* First Editio. Cambridge, Massachusetts, USA: The MIT Pres.
- Elsen, J., (2006). "Microscopy of historic mortars-a review." *Cement and Concrete Research*, 36 (8), 1416-1424.
- Erdly, J. L. and Schwartz, T. A., (2004). *"Building Facade Maintenance, Repair, and Inspection."* Edition Illustrated n.º 1444. ASTM International.
- Ewertson, C. and Petersson, P. E., (1993). "The influence of curing conditions on the permeability and durability of concrete. Results from a field exposure test." *Cement and Concrete Research*, 23 (3), 683-692.
- Faria, P., Henriques, F. and Rato, V., (2008). "Comparative evaluation of lime mortars for architectural conservation." *Journal of Cultural Heritage*, 9 (3), 338-346.
- Faria, P. and Martins, A., (2011). "Influence of Curing Conditions on Lime and Lime-Metakaolin Mortars." In: *International Conference on Durability of Building Materials and Components*, 12-15 April 2011, Porto, Portugal. 8.
- Faria, P. and Martins, A., (2013). "Influence of Lime Type and Curing Conditions on Lime and Lime-metakaolin Mortars." In: eds. V. Freitas & J. Delgado, ed. *Durability of Building Materials and Components, Building Pathology and Rehabilitation. Berlin and Heidelberg*, 2013, Springer, 105-26.
- Fattuhi, N. I., (1988). "Concrete carbonation as influenced by curing regime." *Cement and Concrete Research*, 18 (3), 426-430.
- Fernandezbertos, M., Simons, S., Hills, C. and Carey, P., (2004). "A review of accelerated carbonation technology in the treatment of cement-based materials and sequestration of CO₂." *Journal of Hazardous Materials*, 112 (3), 193-205.
- Ferretti, D. and Bažant, Z. P., (2006a). "Stability of ancient masonry towers: Moisture diffusion, carbonation and size effect." *Cement and Concrete Research*, 36 (7), 1379-1388.
- Ferretti, D. and Bažant, Z. P., (2006b). "Stability of ancient masonry towers: Stress redistribution due to drying, carbonation, and creep." *Cement and Concrete Research*, 36 (7), 1389-1398.
- Festa, D. and Colombo, P., (2006). *"Materiali per l'Ingegneria Civile (in Italian)."* Edizioni Libreria Progetto. Progetto Libreria.
- FIB, (2013). *"Code-type models for concrete behaviour: State-of-the-art Report."* International Federation for Structural Concrete, FIB - Fédération Internationale du Béton, Bulletin 70.
- Forster, A., (2004a). "Hot-Lime Mortars: A Current Perspective." *Journal of Architectural Conservation*, 10 (3), 7-27.
- Forster, A. M., (2004b). "The Scottish Experience of Lime Mortars, Renders and Harling." *International Journal for Restoration*, 10 (6), 637-647.

- Friedman, D., (2010). *"Historical Building Construction: Design, Materials, and Technology."* Second Edition. W. W. Norton & Company.
- Frizot, M., (1981). "Mortars, cements and grouts used in the conservation of historic buildings. Mortiers, ciments et coulis utilisés dans la conservation des bâtiments historiques. ." In: *Symposium*, 3-6 Nov 1981, Rome.
- Gadja, J. (2001). *"Absorption of Atmospheric Carbon Dioxide by Portland Cement Concrete."* Skokie, Illinois, USA,: Portland Cement Association.
- Gambhir, M. L. and Jamwal, N., (2014). *"Building and Construction Materials."* McGraw Hill Education.
- Gameiro, A., Santos Silva, A., Faria, P., Grilo, J., Branco, T., Veiga, R. and Velosa, A., (2014). "Physical and chemical assessment of lime–metakaolin mortars: Influence of binder:aggregate ratio." *Cement and Concrete Composites*, 45, 264-271.
- Gameiro, A., Santos Silva, A., Veiga, R., Velosa, A. and Faria, P., (2012). "Lime-Metakaolin Mortars for Historical Buildings Repair: Study of the Hardening Reaction." In: *ICDS12 - International Conference Durable Structures: from Construction to Rehabilitation*, 31 May - 1 June 2012, Lisbon, Portugal 12.
- Garavaglia, E., Anzani, A. and Binda, L. (2003). *"A probabilistic model for the assessment of historic buildings under permanent loading."* Milano, Italy: Department of Structural Engineering, Politecnico di Milano.
- Garavaglia, E., Anzani, A. and Binda, L., (2006). "Probabilistic Model for the Assessment of Historic Buildings under Permanent Loading." *Journal of Materials in Civil Engineering*, 18 (6), 858-867.
- García-González, C. A., el Grouh, N., Hidalgo, A., Fraile, J., López-Periago, A. M., Andrade, C. and Domingo, C., (2008). "New insights on the use of supercritical carbon dioxide for the accelerated carbonation of cement pastes." *Journal of Supercritical Fluids*, 43 (3), 500-509.
- García-Ruiz, J. M., Rondón, D., García-Romero, A. and Otálora, F., (1996). "Role of Gravity in the Formation of Liesegang Patterns." *The Journal of Physical Chemistry*, 100 (21), 8854–8860.
- Gawin, D., Pesavento, F. and Schrefler, B. A., (2002a). "Modelling of hygro-thermal behaviour and damage of concrete at temperature above the critical point of water." *International Journal for Numerical and Analytical Methods in Geomechanics*, 26 (6), 537-562.
- Gawin, D., Pesavento, F. and Schrefler, B. A., (2002b). "Simulation of damage-permeability coupling in hygro-thermo-mechanical analysis of concrete at high temperature." *Communications in Numerical Methods in Engineering*, 18 (2), 113-119.
- Gawin, D., Pesavento, F. and Schrefler, B. A., (2003). "Modelling of hygro-thermal behaviour of concrete at high temperature with thermo-chemical and mechanical

material degradation." *Computer Methods in Applied Mechanics and Engineering*, 192 (13-14), 1731-1771.

- Gawin, D., Pesavento, F. and Schrefler, B. A., (2006). "Hygro-thermo-chemo-mechanical modelling of concrete at early ages and beyond. Part I: hydration and hygro-thermal phenomena." *International Journal for Numerical Methods in Engineering*, 67 (3), 299-331.
- Gawin, D., Schrefler, B. A. and Galindo, M., (1996). "Thermo-hydro-mechanical analysis of partially saturated porous materials." *Engineering Computations*, 13 (7), 113-143.
- Genestar, C. and Pons, C., (2003). "Ancient covering plaster mortars from several convents and Islamic and Gothic palaces in Palma de Mallorca (Spain). Analytical characterisation." *Journal of Cultural Heritage*, 4 (4), 291-298.
- Gimbert, S. J., (2008). "A Combined Empirical and Computational Approach to Creep in Replicas of Historic Mortar." Masters Thesis, Pennsylvania State University at University Park.
- Glasser, F. P., Marchand, J. and Samson, E., (2008). "Durability of concrete - Degradation phenomena involving detrimental chemical reactions." *Cement and Concrete Research*, 38 (2), 226-246.
- Gonçalves, A. P. A., (2011). "Corrosion Prevention in Historic Concrete - Monitoring the Richards Medical Laboratories." Masters Thesis, University of Pennsylvania.
- Gonen, T. and Yazicioglu, S., (2007). "The influence of compaction pores on sorptivity and carbonation of concrete." *Construction and Building Materials*, 21 (5), 1040-1045.
- Gore, W. L. A. (2014). Gore-Tex [Online]. Available: <http://www.gore-tex.com/en-us/home> [Accessed 10/02/2014].
- Granger, L., (1996). "Comportement differe du beton dans les enceintes de centrales nucleaires. Analyse et modelisation." PhD Thesis, LCPC.
- Granger, L., Torrenti, J. M. and Acker, P., (1997). "Thoughts about drying shrinkage: Scale effects and modelling." *Materials and Structures*, 30 (2), 96-105.
- Granja, J. L., Azenha, M., Sousa, C., Faria, R. and Barros, J., (2014). "Hygrometric assessment of moisture fields in concrete: Practical application issues." *Journal of Advanced Concrete Technology - J-Stage*, 12 (12), 250-265.
- Grasley, Z., Lange, D. and D'Ambrosia, M., (2006). "Internal relative humidity and drying stress gradients in concrete." *Materials and Structures*, 39 (9), 901-909.
- Groot, C., Ashall, G. and Hughes, J., (2007). "Report 28: Characterisation of Old Mortars with Respect to their Repair - State-of-the-Art Report of RILEM Technical Committee 167-COM." RILEM Pub. SARL.

- Groot, C. J. W. P., (2010). "Performance and repair requirements for renders and plasters." In: J. Valek, Groot, C. & Hughes, J. , ed. *International Workshop on 'Repair Mortars for Historic Masonry*, 2010, Prague, Czech Republic. RILEM TC 203-RHM, RILEM Publications SARL, 1359–1363.
- Gualtieri, A. F., Viani, A. and Montanari, C., (2006). "Quantitative phase analysis of hydraulic limes using the Rietveld method." *Cement and Concrete Research*, 36 (2), 401-406.
- Guimarães, E. T., (2014). "*Parametrical Studies of the Behavior of Aerial Lime Mortars.*" MSc Dissertation University of Minho.
- Hall, C. and Hoff, W. D., (2004). "*Stone and Concrete.*" 2nd Edition. London: E. & F.N.Spon.
- Hammouda, I. and Mihoubi, D., (2014). "Thermodynamic and mechanical characterisation of kaolin clay." *Polish Journal of Chemical Technology*, 16 (1), 28–35.
- Han, J. and Zhou, Z., (2013). "Dynamics of Soil Water Evaporation during Soil Drying: Laboratory Experiment and Numerical Analysis." *The Scientific World Journal*, 2013 (ID 240280), 10.
- Han, Y. S., Hadiko, G., Fuji, M. and Takahashi, M., (2005). "Effect of flow rate and CO₂ content on the phase and morphology of CaCO₃ prepared by bubbling method." *Journal of Crystal Growth*, 276 (3-4), 541-548.
- Hansen, E., Van Balen, K. and Rodriguez-Navarro, C., (2005). "Variations in high-calcium lime putty and mortar properties resulting from the use of freshly slaked quicklime and commercial dry hydrated lime." In: *Proceedings of the 2005 International Building Lime Symposium*, 9-11 March 2005, Orlando, Florida, USA. National Lime Association,
- Hansen, K. K. (1986). "*Sorption Isotherm, A Catalogue, Technical Report 162/86.*" Lyngby, Denmark: The Technical University of Denmark.
- Harrison, D. J. (1993). Industrial Minerals Laboratory Manual, Limestones - Technical Report. *British Geological Survey* [Online]. Available: https://www.bgs.ac.uk/research/international/dfid-kar/WG92029_col.pdf [Accessed 12-11-2014].
- Hendry, A. W., (1981). "*Structural Brickwork.*" New York: Wiley.
- Henisch, H. K., (1988). "*Crystals in gels and Liesegang rings.*" Cambridge University Press.
- Henriques, F. M. A., Rato, V. M. and Charola, A. E., (2004). "The influence of grain size distribution on the performance of mortars." In: eds D. Kwiatkowski and R. Lifvendahl, ed. *Proceedings of the 10th international congress on deterioration and conservation of stone*, 27 June - 2 July 2004, Stockholm: ICOMOS. 1001-1008.
- Hewlett, P., (2003). "*Lea's Chemistry of Cement and Concrete.*" 4th Edition. Elsevier Science.

- Heyman, J., (1997). *"The Stone Skeleton: Structural Engineering of Masonry Architecture."* Cambridge University Press.
- Hibbeler, R. C., (2011). *"Structural Analysis "* 8th Edition. Prentice Hall.
- Hillel, D., (1980). "5 - Evaporation from Bare-Surface Soils." In: Daniel Hillel (ed.) *Applications of Soil Physics*. Academic Press.
- Hobbs, D. W., (2001). "Concrete deterioration: causes, diagnosis, and minimising risk." *International Materials Reviews*, 46 (3), 117–144.
- Hogewoning, S., Wolter, A. and Schmidt, S. O., (2008). "Dependence of hard burn potential on limestone properties (Part 1)." *ZKG International*, 61 (6), 54-60.
- Holický, M., Vladislava, N., Gottfried, R., Kronika, M., Marková, J., Sýkora, M. and Jung, K. (2013). *"Basics for assessment of existing structures "* Prague Klokner Institute, Czech Technical University in Prague
- Holmes, S. and Wingate, M., (1997). *"Building with Lime."* London: Intermediate Technology Publications.
- Hosokawa, Y., Yamada, K., Johannesson, B. and Nilsson, L.-O., (2011a). "Development of a multi-species mass transport model for concrete with account to thermodynamic phase equilibriums." *Materials and Structures*, 44 (9), 1577-1592.
- Hosokawa, Y., Yamada, K., Johannesson, B. and Nilsson, L., (2011b). "A Coupled System of Thermodynamic Phase Equilibrium and Multi Species Mass Transfer Models Reproducing the Combined Deterioration of Chloride Attack and Carbonation." In: *13th International Congress on the Chemistry of Cement*, 2011b, Madrid. 11.
- Houst, Y. F., (1996). "The role of moisture in the carbonation of cementitious materials." *International Journal for Restoration of Buildings Monuments*, 2 (1), 49–66.
- Houst, Y. F., Sadouki, H. and Wittmann, F. H., (1993). "Influence of aggregate concentration on the diffusion of CO₂ and O₂." In: RILEM Proceedings Proceedings 18, ed. *Interfaces in Cementitious composites*, 1993, Toulouse. London, etc: E & F SPON, 279-288.
- Houst, Y. F. and Wittmann, F. H., (1986). "The diffusion of carbon dioxide and oxygen in aerated concrete." In: F. H. eds Wittmann, ed. *2nd International Colloquium: Materials Science and Restoration*. WTA, 1986, Esslingen, Germany. 629-634.
- Houst, Y. F. and Wittmann, F. H., (1994). "Influence of porosity and water content on the diffusivity of CO₂ and O₂ through hydrated cement paste." *Cement and Concrete Research*, 24 (6), 1165-1176.
- Houst, Y. F. and Wittmann, F. H., (2002). "Depth profiles of carbonates formed during natural carbonation." *Cement and Concrete Research*, 32 (12), 1923-1930.

- Huang, N. M., Chang, J. J. and Liang, M. T., (2012). "Effect of plastering on the carbonation of a 35-year-old reinforced concrete building." *Construction and Building Materials*, 29, 206-214.
- Hughes, J. J. and Taylor, A. K., (2009). "Compressive and flexural strength testing of brick masonry panels constructed with two contrasting traditionally produced lime mortars." In: C. Groot, ed. *International RILEM Workshop Repair Mortars for Historic Masonry*, 2009, RILEM Publications SARL, 162 - 177.
- ICCROM. (2014). International Centre for the Study of the Preservation and Restoration of Cultural Property. Available: <http://www.iccrom.org/> [Accessed 10-10-2014].
- Incropera, F. P., Dewitt, D. P., Bergman, T. L. and Lavine, A. S., (2007). *Introduction to Heat Transfer*. 5th Edition. John Wiley & Sons.
- Ingo, G. M., Fragalà, I., Bultrini, G., de Caro, T., Riccucci, C. and Chiozzini, G., (2004). "Thermal and microchemical investigation of Phoenician–Punic mortars used for lining cisterns at Tharros (western Sardinia, Italy)." *Thermochimica Acta*, 418 (1–2), 53-60.
- Ishida, T. and Li, C., (2008). "Coupling of Mass Transport and Equilibrium in Micro–pore Structure of Concrete." *Journal of Advanced Concrete Technology - J-Stage*, 6 (2), 303–316.
- Ishida, T. and Maekawa, K., (2001). "Modeling of pH profile in pore water based on mass transport and chemical equilibrium theory." *Concrete Library of JSCE*, 37, 151-166.
- Ishida, T., Maekawa, K. and Kishi, T., (2007). "Enhanced modeling of moisture equilibrium and transport in cementitious materials under arbitrary temperature and relative humidity history." *Cement and Concrete Research*, 37 (4), 565-578.
- Ishida, T., Maekawa, K. and Soltani, M., (2004). "Theoretically identified strong coupling of carbonation rate and thermodynamic moisture states in micropores of concrete." *Journal of Advanced Concrete Technology - J-Stage*, 2 (2), 213-222.
- Izaguirre, A., Lanas, J. and Álvarez, J. I., (2010). "Ageing of lime mortars with admixtures: Durability and strength assessment." *Cement and Concrete Research*, 40 (7), 1081-1095.
- Izaguirre, A., Lanas, J. and Álvarez, J. I., (2011). "Characterization of aerial lime-based mortars modified by the addition of two different water-retaining agents." *Cement and Concrete Composites*, 33 (2), 309-318.
- Janoo, V., Korhonen, C. and M., H., (1999). "Measurement of water content in Portland cement concrete." *Journal of Transportation Engineering*, 125 (3), 245–249.
- Jedrzejewska, H., (1960). "Old Mortars in Poland: A New Method of Investigation." *Studies in Conservation*, 5 (4), 132-138.
- Jenkins, R., (1999). *X-Ray Fluorescence Spectrometry*. 2nd edition. Wiley.

- Jennings, H. M., Bullard, J. W., Thomas, J. J., Andrade, J. E., Chen J. J. and W, S. G., (2008). "Characterization and modeling of pores and surfaces in cement paste: correlations to processing and properties." *Journal of Advanced Concrete Technology - J-Stage*, 6 (1), 5-29.
- Johannesson, B., Hosokawa, Y. and Yamada, K., (2009). "Numerical calculations of the effect of moisture content and moisture flow on ionic multi-species diffusion in the pore solution of porous materials." *Computers & Structures*, 87 (1-2), 39-46.
- Johannesson, B. and Utgenannt, P., (2001). "Microstructural changes caused by carbonation of cement mortar." *Cement and Concrete Research*, 31 (6), 925-931.
- Jung, S. H., Lee, M. K. and Oh, B. H., (2011). "Measurement Device and Characteristics of Diffusion Coefficient of Carbon Dioxide in Concrete." *Materials Journal*, 108 (6), 589–595.
- Kamiya, K., Tohmoto, M., Yada, M. and Nasu, H., (1986). "Recovery of calcium from waste concrete and fixation of carbon dioxide gas by carbonation reaction." *Journal of the Ceramic Society of Japan*, 106 (7), 719–723.
- Kang, S., Kim, J., Lee, Y., Park, Y. and Kim, J. K., (2012). "Moisture Diffusivity of Early Age Concrete Considering Temperature and Porosity." *KSCE, Journal of Civil Engineering*, 16 (1), 179-188.
- Kanstad, T., Hammer, T. A., Bjøntegaard, Ø. and Sellevold, E. J., (2003). "Mechanical properties of young concrete: Part II: Determination of model parameters and test program proposals." *Materials and Structures*, 36 (4), 226-230.
- Key, R., (1972). *"Drying. Principles and practice."* Oxford, New York: Pergamon Press.
- Kelley, C. T., (1987). *"Solving Nonlinear Equations with Newton's Method (Fundamentals of Algorithms)."* Society for Industrial and Applied Mathematics.
- Kelter, P. B., Mosher, M. D. and Scott, A., (2008). *"Chemistry: The Practical Science."* Houghton Mifflin.
- Khalili, K., Heydari, M. and Khalili, M. S., (2014). "Drying Clay Bricks with Variable Young's Modulus." *Procedia Technology*, 12, 382-387.
- Khunthongkeaw, J. and Tangtermsirikul, S., (2005). "Model for Simulating Carbonation of Fly Ash Concrete." *Journal of Materials in Civil Engineering*, 17 (5), 570-578.
- Kim, J.-K. and Lee, C.-S., (1999). "Moisture diffusion of concrete considering self-desiccation at early ages." *Cement and Concrete Research*, 29 (12), 1921-1927.
- Kim, J. K. and Lee, C. S., (1998). "Prediction of differential drying shrinkage in concrete." *Cement and Concrete Research*, 28 (7), 985-994.
- Kim, U. J., (2006). *"Vibrational modes and thermal transformation of purified single walled carbon nanotubes."* PhD Thesis, The Pennsylvania State University.

- Kingery, W. D., Bowen, H. K. and Uhlmann, D. R., (1976). *"Introduction to Ceramics."* 2nd edition. John Wiley & Sons .
- Kingery, W. E. (1988). *"Introduction: Some aspects of the history of ceramic processing - Ultrastructure Processing of Advanced Ceramic."* Mackenzie and Ulrich: John Wiley.
- Kirca, O. and Erdem, T. K., (2004). "An experimental study on the construction materials of the Ankara Citadel." In: C. Modena, P. B. Lourenco and P. Roca, eds. *4th International Seminar on Structural Analysis of Historical Constructions*, 2004, Padova, Italy. Taylor & Francis, 223-230.
- Klemm, A. J. and Klemm, P., (1997). "The effects of the alternate freezing and thawing cycles on the pore structure of cementitious composites modified by MHEC and PVA." *Building and Environment*, 32 (6), 509-512.
- Klysz, G. and Balayssac, J. P., (2007). "Determination of volumetric water content of concrete using ground-penetrating radar." *Cement and Concrete Research*, 37 (8), 1164-1171.
- Kobayashi, K., Suzuki, K. and Uno, Y., (1994). "Carbonation of concrete structures and decomposition of C-S-H." *Cement and Concrete Research*, 24 (1), 55-61.
- Kontturi, K., Murtomäki, L. and Manzanares, J. A., (2008). *"Ionic transport processes: In electrochemistry and membrane science."* Oxford.
- Kotz, J., Treichel, P. and Townsend, J., (2009). *"Chemistry and Chemical Reactivity, Enhanced Edition."* Cengage Learning.
- Kourkoulis, S. K., (2006). *"Fracture and failure of natural building stones."* Springer Netherlands.
- Kubo, J., (2007). *"Methods of remedial treatment for carbonation-induced corrosion of reinforced concrete."* PhD Thesis, University Of Leeds, School of Civil Engineering.
- Kubo, J., Sawada, S., Page, C. L. and Page, M. M., (2007). "Electrochemical injection of organic corrosion inhibitors into carbonated cementitious materials: Part 2. Mathematical modelling." *Corrosion Science*, 49 (3), 1205-1227.
- Kuriyan, J., Konforti, B. and Wemmer, D., (2012). *"The Molecules of Life: Physical and Chemical Principles."* Taylor & Francis Group.
- Lackner, K. S., (2002). "Carbonate Chemistry for Sequestering Fossil Carbon." *Annual Review of Energy and the Environment*, 27, 193-232.
- Lagerblad, B. (2006). *"Carbon dioxide uptake during concrete life, Sate of the art."* Nordic Innovation Centre project.
- Lanas, J. and Alvarez, J. I., (2003). "Masonry repair lime-based mortars: factors affecting the mechanical behavior." *Cement and Concrete Research*, 33 (11), 1867-1876.

- Lanas, J., Arandigoyen, M. and Alvarez, J. I., (2004a). "Mechanical behavior of masonry repair mortars: aerial and hydraulic lime-based mixtures." In: *10th International Congress on Deterioration and Conservation of Stone*, 2004a, Stockholm. 9.
- Lanas, J., Pérez Bernal, J. L., Bello, M. A. and Alvarez Galindo, J. I., (2004b). "Mechanical properties of natural hydraulic lime-based mortars." *Cement and Concrete Research*, 34 (12), 2191-2201.
- Lanas, J., Sirera, R. and Alvarez, J. I., (2005). "Compositional changes in lime-based mortars exposed to different environments." *Thermochimica Acta*, 429 (2), 219-226.
- Lanas, J., Sirera, R. and Alvarez, J. I., (2006). "Study of the mechanical behavior of masonry repair lime-based mortars cured and exposed under different conditions." *Cement and Concrete Research*, 36 (5), 961-970.
- Landsberg, D. v., (1992). "The history of lime production and use from early times to the industrial revolution." *Zement-Kalk-Gips*, 8 (ID 859879), 192–203.
- Langenbach, R., (2010). "Rescuing the Baby from the Bathwater: Traditional Masonry as Earthquake-Resistant Construction " In: *8th International Masonry Conference 2010*, 2010, Dresden, Germany. .
- Langenbach, R. D., (1994). "Architectural issues in the seismic rehabilitation of masonry buildings." In: US–Italy workshop on guidelines for seismic evaluation and rehabilitation of unreinforced masonry buildings, ed. *Abrams and G. Calvi (eds)*, 20 July 1994, Buffalo, N.Y, USA. Technical report NCEER-94-0021, National Center for Earthquake Engineering Research,, 3-16.
- Langhoff, N., Simionovici, A., Arkadiev, V., Knüpfer, W., Čechák, T., Leonhardt, J. and Chavanne, J., (2006). "Handbook of Practical X-Ray Fluorescence Analysis." In: B. Beckhoff, Kanngießner, B., Langhoff, N., Wedell, R., and Wolff, H. (ed.): Springer-Verlag Berlin Heidelberg.
- Larkin, D. E., (1988). "Compositional analysis by thermogravimetry: the development of a standard method." In: C.M. EARNEST, ed. *Compositional analysis by Thermogravimetry*, 1988, Philadelphia. American Society for Testing and Material,, 28-37.
- Lawrence, R. M. H., (2005). "A critical review of techniques used for the assessment of carbonation in lime mortars." In: *2005 International Building Lime Symposium*, 9-11 March 2005, Orlando, Florida, USA. National Lime Association, 15.
- Lawrence, R. M. H., (2006). "*A Study of Carbonation in Non-Hydraulic Lime Mortars.*" Doctor of Philosophy, PhD Thesis, University of Bath.
- Lawrence, R. M. H., Mays, T. J., Rigby, S. P., Walker, P. and D'Ayala, D., (2007). "Effects of carbonation on the pore structure of non-hydraulic lime mortars." *Cement and Concrete Research*, 37 (7), 1059-1069.
- Lawrence, R. M. H., Mays, T. J., Walker, P. and D'Ayala, D., (2006a). "Determination of carbonation profiles in non-hydraulic lime mortars using thermogravimetric analysis." *Thermochimica Acta*, 444 (2), 179-189.

- Lawrence, R. M. H., Mays, T. J., Walker, P. and D'Ayala, D., (2006b). "The use of tg to measure different concentrations of lime in non-hydraulic lime mortars." *Journal of Thermal Analysis and Calorimetry*, 85 (2), 377-382.
- Laycock, E. A., (2002). "Ten years of frost testing at Sheffield Hallam University." *Construction and Building Materials*, 16 (4), 195-205.
- Lea, F. M., (1970). *"The Chemistry of Cement and Concrete,."* 3. London: Edward Arnold, Ltd.
- LeVeque, R., (2007). *"Finite Difference Methods for Ordinary and Partial Differential Equations: Steady-State and Time-Dependent Problems."* Society for Industrial and Applied Mathematics (SIAM).
- Lewis, D. W. and McConchie, D., (1994). *"Analytical sedimentology."* 2. New York: Chapman & Hall.
- Lhoist. (2014). Lusical - Companhia Lusitana de Cal, S.A. Available: http://www.lhoist.com/pt_pt [Accessed 12-10-2014].
- Li, Y. and Ren, S., (2011). *"Building Decorative Materials."* Elsevier Science.
- Lieth, R. M. A., (2013). *"Preparation and Crystal Growth of Materials with Layered Structures."* Springer Netherlands.
- Lindvall, A., (2003). *"Environmental actions on concrete expose in marine and road environments and its response – Consequences for the initiation of chloride induced reinforced corrosion."* PhD Thesis, Chalmers University of Technology.
- Liu, L. H., Hashida, T., Teramura, S. and Karino, K., (2003). "Development of a method for CO₂ solidification of glass and concrete waste composites." *Journal of Ceramic Society*, 111 (5), 357-361.
- Lo, Y. and Lee, H. M., (2002). "Curing effects on carbonation of concrete using a phenolphthalein indicator and Fourier-transform infrared spectroscopy." *Building and Environment*, 37 (5), 507-514.
- Lotfi, H. and Shing, P., (1994). "Interface Model Applied to Fracture of Masonry Structures." *Journal of Structural Engineering*, 120 (1), 63-80.
- Loukili, A., Khelidj, A. and Richard, P., (1999). "Hydration kinetics, change of relative humidity, and autogenous shrinkage of ultra-high-strength concrete." *Cement and Concrete Research*, 29 (4), 577-584.
- Lourenço, P. B., (1996). *"Computational strategies for masonry structures."* PhD Thesis, Delft University of Technology.
- Lourenço, P. B., (1998). "Experimental and numerical issues in the modelling of the mechanical behaviour of masonry, Structural analysis of historical constructions." In: *CIMNE*, 1998, Barcelona, Spain. 57-91.

- Lourenço, P. B., (2001). "Analysis of historical constructions: From thrust-lines to advanced simulations." In: P. Roco and P.B. Lourenço, eds. *Structural Analysis of Historical Constructions*, 2001, Guimarães, Portugal. 91-116.
- Lourenço, P. B., (2002). "Computations on historic masonry structures." *Progress in Structural Engineering and Materials*, 4 (3), 301-319.
- Lourenço, P. B., (2004). "Analysis and restoration of ancient masonry structures. Guidelines and Examples, in Innovative Materials and Technologies for Construction and Restoration " In: *IMTCR04*, 2004, Lecce (Italy).
- Lourenço, P. B., Luso, E. and Almeida, M. G., (2006). "Defects and moisture problems in buildings from historical city centres: a case study in Portugal." *Building and Environment*, 41 (2), 223-234.
- Lourenço, P. B., Mendes, N., Ramos, L. F. and Oliveira, D. V., (2011). "Analysis of Masonry Structures Without Box Behavior." *International Journal of Architectural Heritage*, 5 (4-5), 369-382.
- Lourenço, P. B., Oliveira, D. V. and Milani, G., (2010). "Computational Advances in Masonry Structures: From Mesoscale Modelling to Engineering Application Developments and Applications in Computational Structures Technology." In: B.H.V.; Topping, J.M.; Adam, F.; Pallarés and M. L. Bru. J. R. and Romero (eds.): Saxe-Coburg Publications.
- Lu, N., (2013). "A Power Law for Elastic Moduli of Unsaturated Soil." In: Qiang Yang, Jian-Min Zhang, Hong Zheng and Yangping Yao (eds.) *Constitutive Modeling of Geomaterials*. Springer Berlin Heidelberg.
- Lu, N. and Kaya, M., (2014). "Power Law for Elastic Moduli of Unsaturated Soil." *Journal of Geotechnical and Geoenvironmental Engineering*, 140 (1), 46-56.
- Lu, X., (1997). "Application of the Nernst-Einstein equation to concrete." *Cement and Concrete Research*, 27 (2), 293-302.
- Luciano, R. and Sacco, E., (1997). "Homogenization technique and damage model for old masonry material." *International Journal of Solids and Structures*, 34 (24), 3191-3208.
- Ma, Y. F., Gao, Y. H. and Feng, Q. L., (2010). "Effects of pH and temperature on CaCO₃ crystallization in aqueous solution with water soluble matrix of pearls." *Journal of Crystal Growth*, 312 (21), 3165-3170.
- Macchi, G., (1998). " Problems related to the original conception– the case of Pavia Cathedral." In: P.Roca et al., ed. *Structural Analysis of Historical Constructions II. CIMNE*, 1998, Barcelona. 39–56.
- MacLaughlin, D. and Estrada, H., (2009). *Structural Steel Drafting and Design*. Cengage Learning.
- Maekawa, K., Chaube, R. and Kishi, T., (1999). "Modelling of Concrete Performance." E&FN SPON.

- Maekawa, K., Ishida, T. and Kishi, T., (2003). "Multi-scale modeling of concrete performance-integrated material and structural mechanics." *Advanced Concrete Technology*, 1 (2), 91-119.
- Maekawa, K., Ishida, T. and Kishi, T., (2008). "*Multi-Scale Modeling of Structural Concrete*." illustrated edition. Taylor & Francis.
- Magalhães, A. and Veiga, R., (2009). "Physical and mechanical characterisation of historic mortars. Application to the evaluation of the state of conservation." *Materiales de Construcción*, 59 (295), 61-77.
- Mahdi, T., (2015). "Seismic Vulnerability of Arches, Vaults and Domes in Historical Buildings." In: pp. P.G. Asteris & V. Plevris Publisher Editors: (ed.) *Handbook of Research on Seismic Assessment and Rehabilitation of Historic Structures (2 Volumes)*. IGI Global.
- Mainguy, M., Coussy, O. and Baroghel-Bouny, V., (2001). "Role of Air Pressure in Drying of Weakly Permeable Materials." *Journal of Engineering Mechanics*, 127 (6), 582-592.
- Malinowski, E. S. and Hansen, T. S., (2011). "Hot Lime Mortar in Conservation—Repair and Replastering of the Façades of Läckö Castle." *Journal of Architectural Conservation*, 17 (1), 95-118.
- Maravelaki-Kalaitzaki, P., Bakolas, A., Karatasios, I. and Kilikoglou, V., (2005). "Hydraulic lime mortars for the restoration of historic masonry in Crete." *Cement and Concrete Research*, 35 (8), 1577-1586.
- Maravelaki-Kalaitzaki, P., Bakolas, A. and Moropoulou, A., (2003). "Physico-chemical study of Cretan ancient mortars." *Cement and Concrete Research*, 33 (5), 651-661.
- Margalha, G., Veiga, R., Silva, A. S. and de Brito, J., (2011). "Traditional methods of mortar preparation: The hot lime mix method." *Cement and Concrete Composites*, 33 (8), 796-804.
- Marshall, A. L., (1990). "*Marine Concrete*." 1st edition. Springer US.
- Martínez-Ramírez, S., Zamard A., Thompson G. E and E., M. B., (2002). "Organic and inorganic concrete under SO₂ pollutant exposure " *Building and Environment*, 37 (10), 933-93.
- Martínez, I., Castillo, A., Martínez, E. and Castellote, M., (2013). "Physico-chemical material characterization of historic unreinforced masonry buildings: The first step for a suitable intervention." *Construction and Building Materials*, 40 (0), 352-360.
- Martinez, M. C. I. and Carro, G. A., (2007). "Ancient building requirements and the evaluation of different lime-cement mortars compositions." In: *2 Congresso Nacional de Argamassas de Construção, Associação Portuguesa dos Fabricantes de Argamassas de Construção*, 22 - 23 November 2007, Lisbon, Portugal.

- Martinola, G. and Sadouki, H., (1998). "Combined experimental and numerical study to assess shrinkage cracking of cement-based materials." *Internationale Zeitschrift für Bauinstandsetzen / Restoration of Buildings and Monuments*, 4 (5), 479–506.
- Martys, N. S. and Ferraris, C. F., (1997). "Capillary transport in mortars and concrete." *Cement and Concrete Research*, 27 (5), 747-760.
- Masel, R. I., (1996). "*Principles of Adsorption and Reaction on Solid Surfaces.*" Volume 3, Wiley Series in Chemical Engineering. Wiley.
- Mason, E. A. and Malinauskas, A. P., (1983). "*Gas transport in porous media: the dusty-gas model.*" Elsevier.
- Matsushita, F., Aono, Y. and Shibata, S., (2000). "Carbonation degree of autoclaved aerated concrete." *Cement and Concrete Research*, 30 (11), 1741-1745.
- Mehta, P. and Monteiro, P. J. M., (2005). "*Concrete: Microstructure, Properties, and Materials.*" McGraw-Hill Education.
- Mehta, P. K., (1997). "Durability-critical issues for the future." *Concrete International*, 19 (7), 27-32.
- Meier, S. A., Peter, M. A., Muntean, A. and Böhm, M., (2007). "Dynamics of the internal reaction layer arising during carbonation of concrete." *Chemical Engineering Science*, 62 (4), 1125-1137.
- Meland, I. (1985). "*Karbonatisering i flygaskement og standard portland sement med og utan silika.*" *SINTEF Rapport, STF A85049*. Trondheim, Norge:
- Meneghini, A., (2014). "*Experimental Characterization of Aerial Lime Mortars in View of Multiphysics Modelling.*" Master Thesis, University of Padova, Università Degli Studi di Padova.
- Mensi, R., Acker, P. and Attolou, A., (1998). "Drying of Concrete: Analysis and Modelling. Sechage du Beton: Analyse et Modelisation." 21 (121), 3–12.
- Midgley, H. G., (1979). "The determination of calcium hydroxide in set Portland cements." *Cement and Concrete Research*, 9 (1), 77-82.
- Miller, T. C. (1960). "*A study of the reaction between calcium oxide and water.*" Washington National Lime Association.
- Milne, I., Ritchie, R. O. and Karihaloo, B. L., (2003). "*Comprehensive Structural Integrity.*" Elsevier Science and Technology.
- Mjörnell, K., (1997). "*Moisture conditions in high performance concrete.*" PhD Thesis, Chalmers University of Technology.
- Moffat, W. and Walmsley, M. R. W., (2006). "Understanding lime calcination kinetics for energy cost reduction." In: *59th Appita Conference*, 16-19 May 2006, Auckland, New Zeland. 210-218.

- Molins, S., Carrera, J., Ayora, C. and Saaltink, M. W., (2004). "A formulation for decoupling components in reactive transport problems." *Water Resources Research*, 40 (10), 1-13.
- Monteiro, P. J. M., (1995). "Mechanical Modeling of the Transition Zone, Chapter 4." In: J. C. Maso (ed.) *Interfacial Transition Zone in Concret*. E & FN SPON.
- Montes-Hernandez, G., Chiriach, R., Toche, F. and Renard, F., (2012). "Gas–solid carbonation of Ca(OH)₂ and CaO particles under non-isothermal and isothermal conditions by using a thermogravimetric analyzer: Implications for CO₂ capture." *International Journal of Greenhouse Gas Control*, 11 172-180.
- Montes-Hernandez, G., Daval, D., Chiriach, R. and Renard, F., (2010a). "Growth of Nanosized Calcite through Gas–Solid Carbonation of Nanosized Portlandite under Anisobaric Conditions." *Crystal Growth & Design*, 10 (11), 4823-4830.
- Montes-Hernandez, G., Pommerol, A., Renard, F., Beck, P., Quirico, E. and Brissaud, O., (2010b). "In situ kinetic measurements of gas–solid carbonation of Ca(OH)₂ by using an infrared microscope coupled to a reaction cell." *Chemical Engineering Journal*, 161 (1–2), 250-256.
- Montoya, C., Lanas, J., Arandigoyen, M., Navarro, I., García Casado, P. J. and Alvarez, J. I., (2003). "Study of ancient dolomitic mortars of the church of Santa María de Zamarce in Navarra (Spain): comparison with simulated standards." *Thermochimica Acta*, 398 (1–2), 107-122.
- Moorehead, D. R., (1986). "Cementation by the carbonation of hydrated lime." *Cement and Concrete Research*, 16 (5), 700-708.
- Morandea, A., Thiéry, M., Dangla, E. and Patrick, W. C., (2014). "Accelerated carbonation modelling of fly ash-blended cement paste." In: *RILEM International Symposium on Concrete Modelling*, 2014, 408-416.
- Moriconi, G., Castellano, M. G. and Collepardi, M., (1994). "Mortar deterioration of the masonry walls in historic buildings. A case history: Vanvitelli's Mole in Ancona." *Materials and Structures*, 27 (7), 408-414.
- Moropoulou, A., Bakolas, A. and Aggelakopoulou, E., (2001). "The effects of limestone characteristics and calcination temperature to the reactivity of the quicklime." *Cement and Concrete Research*, 31 (4), 633-639.
- Moropoulou, A., Bakolas, A. and Aggelakopoulou, E., (2004). "Evaluation of pozzolanic activity of natural and artificial pozzolans by thermal analysis." *Thermochimica Acta*, 420 (1–2), 135-140.
- Moropoulou, A., Bakolas, A. and Bisbikou, K., (1995). "Characterization of ancient – Byzantine and later historic mortars by thermal and X–ray diffraction techniques." *Thermochimica Acta*, 269-270 779–795.
- Moropoulou, A., Bakolas, A., Moundoulas, P., Aggelakopoulou, E. and Anagnostopoulou, S., (2005). "Strength development and lime reaction in mortars for repairing historic masonries." *Cement and Concrete Composites*, 27 (2), 289-294.

- Moropoulou, A., Tsiourva, T., Bisbikou, K., Biscontin, G., Bakolas, A. and Zendri, E., (1996). "Hot lime technology imparting high strength to historic mortars." *Construction and Building Materials*, 10 (2), 151-159.
- Mosquera, M. J., Silva, B., Prieto, B. and Ruiz-Herrera, E., (2006). "Addition of cement to lime-based mortars: Effect on pore structure and vapor transport." *Cement and Concrete Research*, 36 (9), 1635-1642.
- Muntean, A., Bohm, M. and Kropp, J., (2011). "Moving carbonation fronts in concrete: A moving-sharp-interface approach." *Chemical Engineering Science*, 66 538–547.
- Muntean, A., Meier, S. A., Peter, M. A., Bohm, M. and Kropp, J. (2005). "A note on limitations of the use of accelerated concrete-carbonation tests for service-life predictions." *Zentrum für Technomathematik*. Bremen, Germany: Centre for Industrial Mathematics, FB 3, University of Bremen.
- Mydin, M. A. O., (2013). "Modeling of Transient Heat Transfer in Foamed Concrete Slab." *Journal of Engineering Science and Technology*, 8 (3), 326 - 343
- Nakarai, K., Ishida, T. and K., M., (2006). "Modeling of calcium leaching from cement hydrates coupled with micro-pore formation." *The Journal of the Advanced Concrete Technology*, 4 (3), 395–407.
- Nehdi, M. and Hayek, M., (2005). "Behavior of blended cement mortars exposed to sulfate solutions cycling in relative humidity." *Cement and Concrete Research*, 35 (4), 731-742.
- Neville, A., (1995). "Properties of Concrete." Longman Group Limited, Essex.
- Ng, C. W. W., Xu, J. and Yung, S. Y., (2009). "Effects of imbibition-drainage and stress ratio on anisotropic stiffness of an unsaturated soil at very small strains." *Canadian Geotechnical Journal*, 46 (9), 1062-1076.
- Ngala, V. T. and Page, C. L., (1997). "Effects of carbonation on pore structure and diffusional properties of hydrated cement pastes." *Cement and Concrete Research*, 27 (7), 995-1007.
- Ngoma, A. M. K., (2009). "Characterisation and Consolidation of Historical Lime Mortars in Cultural Heritage Buildings and Associated Structures in East Africa." PhD Thesis, Royal Institute of Technology.
- Nikulshina, V., Gálvez, M. E. and Steinfeld, A., (2007). "Kinetic analysis of the carbonation reactions for the capture of CO₂ from air via the Ca(OH)₂–CaCO₃–CaO solar thermochemical cycle." *Chemical Engineering Journal*, 129 (1–3), 75-83.
- Nilsson, L.-O. (1980). "Hygroscopic Moisture in Concrete - Drying, measurements and related material properties." Lund, Sweden: Lund Institute of Technology, Division of Building materials.
- Nilsson, L. O., (2002). "Long-term moisture transport in high performance concrete." *Materials and Structures*, 35 (10), 641-649.

- Oates, J. A. H., (1998). *"Lime and Limestone: Chemistry and Technology, Production and Uses."* WILEY-VCH Verlag GmbH.
- Oh, B. H. and Jang, S. Y., (2007). "Effects of material and environmental parameters on chloride penetration profiles in concrete structures." *Cement and Concrete Research*, 37 (1), 47-53.
- Okonkwo, P. C. and Adefila, S. S., (2012). "The Kinetics of Calcination of High Calcium Limestone " *International Journal of Engineering Science and Technology (IJEST)* 4(2), 391-400.
- Oliveira, D. V. C., (2002). *"Experimental and Numerical analysis of blocky masonry structures under cyclic loading."* PhD thesis, University of Minho.
- Oliveira, M. A., Azenha, M. and Lourenço, P. B., (2015). "Simulation of Humidity Fields in Concrete: Experimental Validation and Parameter Estimation " *Journal of Advanced Concrete Technology - J-Stage*, 13 (4), 214-229.
- Özisik, M. N., (1993). *"Heat conduction."* 2nd edition. John Wiley & Sons.
- Özisik, M. N., (2002). *"Boundary Value Problems of Heat Conduction."* Courier Corporation. Dover Phoenix Editions, reprint originally published: Scranton, International Textbook Co., 1968.
- Paama, L., Pitkänen, I., Rönkkömäki, H. and Perämäki, P., (1998). "Thermal and infrared spectroscopic characterization of historical mortars." *Thermochimica Acta*, 320 (1-2), 127-133.
- Pacheco Torgal, F., Miraldo, S., Labrincha, J. A. and De Brito, J., (2012). "An overview on concrete carbonation in the context of eco-efficient construction: Evaluation, use of SCMs and/or RAC." *Construction and Building Materials*, 36 (0), 141-150.
- Padura, B. A., (2001). *"Estudio de las cimentaciones de edificios históricos en la provincia de Sevilla: siglo XII al XVI (in Spanish)."* PhD Dissertation, Universidad de Sevilla.
- Paiva, H., Marques, E., Velosa, A., Coroado, J., Labrincha, A. and Ferreira, V. M., (2006). "Preliminary studies on the development of lime based mortars for adobe masonry, Heritage." In: Monica Alvarez de Buergo Rafael Fort, Miguel Gomez-Heras, Carmen Vazquez-Calvo, ed. *Weathering and Conservation*, 21-24 June 2006, Madrid, Spain. 103-107.
- PANalytical. (2015). SuperQ - Analytical XRF software package. Available: <http://www.panalytical.com/Xray-fluorescence-software/SuperQ/Specifications.htm> [Accessed 09-09-2015].
- Papa, E., L., B. and Nappi, A., (1994). "A numerical approach for modelling the effect of persistent loads in masonry structures." In: *Proceedings 3rd International Masonry Conference*, 1994, 290-294.

- Papadakis, V., Vayenas, C. G. and Fardis, M. N., (1991a). "Fundamental modeling and experimental investigation of concrete carbonation." *ACI Materials Journal*, 88 (4), 363–373.
- Papadakis, V. G., Fardis, M. N. and Vayenas, C. G., (1992). "Effect of composition, environmental factors and cement-lime mortar coating on concrete carbonation." *Materials and Structures*, 25 (5), 293-304.
- Papadakis, V. G., Vayenas, C. G. and Fardis, M. N., (1989). "A reaction engineering approach to the problem of concrete carbonation." *AIChE Journal*, 35 (10), 1639-1650.
- Papadakis, V. G., Vayenas, C. G. and Fardis, M. N., (1991b). "Physical and chemical characteristics affecting the durability of concrete." *ACI Materials Journal*, 88 (2), 186–196.
- Park, J., Hasegawa, T., Senbu, O. and Park, D., (2012). "Study on Neutralization Progress Model of Concrete with Coating Finishing Materials in Outdoor Exposure Conditions Based on the Diffusion Reaction of Calcium Hydroxide." *International Journal of Concrete Structures and Materials*, 6 (3), 155-136.
- Park, W. K., Ko, S.-J., Lee, S. W., Cho, K.-H., Ahn, J.-W. and Han, C., (2008). "Effects of magnesium chloride and organic additives on the synthesis of aragonite precipitated calcium carbonate." *Journal of Crystal Growth*, 310 (10), 2593-2601.
- Parkhurst, D. (1995). "*User's guide to PHREEQC: a computer program for speciation, reaction-path, advective transport, and inverse geochemical calculations.*". US Geological Survey, Water Resources Investigations Report.
- Parrott, L. J., (1990). "Assessing carbonation in concrete structures." In: *Durability of building materials and components*, 1990, London, UK. E. & F.N. Spon, 575-586.
- Parrott, L. J. and Killoh, D. C., (1989). "Carbonation in a 36 year old, in-situ concrete." *Cement and Concrete Research*, 19 (4), 649-656.
- Parrott, P. J., (1994). "Design for avoiding damage due to carbonation–induced corrosion." *American Concrete Institute SP–145*, ACI, Detroit 283-298.
- Pavía, S., Fitzgerald, B. and Treacy, E., (2006). "An assessment of lime mortars for masonry repair." In: *Concrete Research in Ireland Colloquium*, 2006, Dublin. University College Dublin, 101-108.
- Pavía, S. and Treacy, E., (2006). "A comparative study of the durability and behaviour of fat lime and feebly-hydraulic lime mortars." *Materials and Structures*, 39 (3), 391-398.
- Pavlík, Z., Benešová, H., Matiašovský, P. and Pavlíková, M., (2012). "Study on Carbonation Process of Several Types of Advanced Lime-Based Plasters." *World Academy of Science, Engineering and Technology*, 6 (10), 10-29

- PCA (2012). *"Types and Causes of Concrete Deterioration."* PCA R&D, Serial No. 2617. Portland Cement Association.
- Pel, L., Landman, K. A. and Kaasschieter, E. F., (2002a). "Analytic solution for the nonlinear drying problem." *International Journal of Heat and Mass Transfer*, 45 (15), 3173–3180.
- Pel, L., Landman, K. A., Kaasschieter, E. F. and . (2002b). "International Journal of Heat and Mass Transfer." *Analytic solution for the nonlinear drying problem*, 45 (15), 3173-3180.
- Pereira, J., Figueiredo, N., Goufo, P., Carneiro, J., Morais, R., Carranca, C., Coutinho, J. and Trindade, H., (2013). "Effects of elevated temperature and atmospheric carbon dioxide concentration on the emissions of methane and nitrous oxide from Portuguese flooded rice fields." *Atmospheric Environment*, 80 (0), 464-471.
- Pérez Bernal, J. L. and Bello López, M. A., (2004). *"Dióxido de azufre. Química atmosférica y destrucción del patrimonio (in Spanish)."* Seville: Fundación El Monte.
- Persson, B., (1996). "Hydration and strength of high performance concrete." *Advanced Cement Based Materials*, 3 (3–4), 107-123.
- Persson, B., (1997). "Moisture in concrete subjected to different kinds of curing." *Materials and Structures*, 30 (9), 533-544.
- Pesce, G. L., (2014). *"Study of carbonation in novel lime based materials."* Doctor of Philosophy, PhD Thesis, University of Bath.
- Peter, M. A., Muntean, A., Meier, S. A. and Böhm, M., (2008). "Competition of several carbonation reactions in concrete: A parametric study." *Cement and Concrete Research*, 38 (12), 1385-1393.
- Pfeifer, G., (2001). *"Masonry Construction Manual."* illustrated edition. Princeton Architectural Press.
- Philippi, P. C., Yunes, P. R., Fernandes, C. P. and Magnani, F. S., (1994). "The microstructure of porous building materials: Study of a cement and lime mortar." *Transport in Porous Media*, 14 (3), 219-245.
- Philips (1993). *"Sample Charger, Philips Analytical PW1510 - Service Manual."* Second Edition ed.
- Poole, J. L., Riding, K. A., Folliard, K. J., Maria, C. G., Anton, J. and Schindler, K., (2007). "Methods for Calculating Activation Energy for Portland Cement." *Materials Journal*, 104 (1), 303-311.
- Powers, T. C. and Brownyard, T. L., (1948). "Studies of the Physical Properties of Hardened Portland Cement Paste." *Journal Proceedings*, 43 (9), 249-336.
- Price, C. A., (1996). *"Stone conservation: an overview of current research."* Los Angeles: The Getty Conservation Institute.

- Puatatsananon, W. and Saouma, V., (2005). "Nonlinear Coupling of Carbonation and Chloride Diffusion in Concrete." *Journal of Materials in Civil Engineering*, 17 (3), 264-275.
- Quincot, P. G., (2012). "*Measurement of internal moisture distribution in concrete with relative humidity sensors.*" Bachelor Thesis, University of Minho.
- Rabun, J. S., (2000). "*Structural Analysis of Historic Buildings: Restoration, Preservation, and Adaptive Reuse Applications for Architects and Engineers.*" 1st. Wiley.
- Rackley, S., (2009). "*Carbon Capture and Storage.*" Elsevier Science.
- Radonjic, M., Hallam, K. R., Allen, G. C. and Hayward, R., (2001a). "Mechanism of carbonation in lime-based materials." *Journal of the Building Limes Forum*, 8, 50-64.
- Radonjic, M., Hallam, K. R., Allen, G. C. and Hayward, R., (2001b). "Mechanism of carbonation in lime-based materials." In: *Proceedings of the 8th Euroseminar on Microscopy Applied to Building Materials*, 2001b, Athens, Greece. 465 – 475.
- Ramachandran, V. S., (1979). "Differential thermal method of estimating calcium hydroxide in calcium silicate and cement pastes." *Cement and Concrete Research*, 9 (6), 677-684.
- Randall, F. A., (1949). "*History of the development of building construction in Chicago.*" University of Illinois Press.
- Reinecke, S. A. and Sleep, B. E., (2002). "Knudsen diffusion, gas permeability, and water content in an unconsolidated porous medium." *Water Resources Research*, 38 (12), 16-1-16-15.
- Riccardi, M. P., Duminuco, P., Tomasi, C. and Ferloni, P., (1998). "Thermal, microscopic and X-ray diffraction studies on some ancient mortars." *Thermochimica Acta*, 321 (1–2), 207-214.
- Richards, G., (2002). "Tourism attraction systems: Exploring Cultural Behavior." *Annals of Tourism Research*, 29 (4), 1048-1064.
- Richardson, M., (1988). "*Carbonation of Reinforced Concrete: Its Causes and Management.*" Dublin: CITIS Ltd.
- Richardson, M. G., (2003). "*Fundamentals of Durable Reinforced Concrete.*" 1st edition. Taylor & Francis.
- RILEM, (1988). "CPC-18 Measurement of hardened concrete carbonation depth, TC 56-MHM." *Materials and Structures*, 21 (126), 453 - 455.
- Robertson, L. E. and Naka, T., (1980). "*Tall Building Criteria and Loading.*" American Society of Civil Engineers.
- Roca, P., (2001). "Studies on the structure of Gothic Cathedrals." In: P.B. Lourenço and P. Roca (Eds.), ed. *Historical Constructions*, 2001, Guimarães, Portugal. 71–90.

- Roca, P., Cervera, M., Pelà, L., Clemente, R. and Chiumenti, M., (2012). "Viscoelasticity and Damage Model for Creep Behavior of Historical Masonry Structures." *The Open Civil Engineering Journal*, 6 (Suppl 1–M7), 188–199.
- Rocha, J. A., (2013). "*Diagnósticos dos Procedimentos Executivos nos Canteiros de Obras de Alvenaria Estrutural (in Portuguese).*" Master Thesis, São Paulo State University - UNESP
- Rodriguez-Navarro, C., Cazalla, O., Elert, K. and Sebastian, E., (2002). "Liesegang pattern development in carbonating traditional lime mortars." *Proceeding of The Royal Society*, 458, 2261–2273.
- Rodriguez-Navarro, C., Hansen, E. and Ginell, W. S., (1998). "Calcium Hydroxide Crystal Evolution upon Aging of Lime Putty." *Journal of the American Ceramic Society*, 81 (11), 3032-3034.
- Roels, S., (2000). "*Modelling unsaturated moisture transport in heterogeneous limestone.*" PhD. Thesis, Katholieke Universiteit Leuven.
- Rogério-Candelera, M. A., Lazzari, M. and Cano, E., (2013). "*Science and Technology for the Conservation of Cultural Heritage.*" Taylor & Francis.
- Roncero, J., (2000). "*Effect of superplasticizers on the behavior of concrete in the fresh and hardened states: implications for high performance concretes.*" PhD Thesis, Universitat Politècnica de Catalunya.
- Roques, H. and Girou, A., (1974). "Kinetics of formation conditions of carbonate tartars." *Water Research*, 8 (11), 907–920.
- Rostásy, F., Gutsch, A. and Krauß, M. (2001). "*Computation of stresses and cracking criteria for early age concrete.*" *Methods of iBMB. IPACS.*
- Rouchon, L., Favregeon, L. and Pijolat, M., (2013). "Analysis of the kinetic slowing down during carbonation of CaO by CO₂." *Journal of Thermal Analysis and Calorimetry*, 113 (3), 1145-1155.
- Ruiz-Agudo, E. and Rodriguez-Navarro, C., (2010). "Microstructure and rheology of lime putty." *Langmuir*, 26 (6), 3868-3877.
- Sabbioni, C., Bonazza, A. and Zappia, G., (2002). "Damage on hydraulic mortars: the Venice Arsenal." *Journal of Cultural Heritage*, 3 (1), 83-88.
- Sabbioni, C., Zappia, G., Riontino, C., Blanco-Varela, M. T., Aguilera, J., Puertas, F., Balen, K. V. and Toumbakari, E. E., (2001). "Atmospheric deterioration of ancient and modern hydraulic mortars." *Atmospheric Environment*, 35 (3), 539-548.
- Sada, E., Kumazawa, H. and Butt, M. A., (1977). "Simultaneous absorption with reaction in a slurry containing fine particles." *Chemical Engineering Science*, 32 (12), 1499-1503.
- Sadouki, H. and van Mier, J. G. M., (1997). "Simulation of hygral crack growth in concrete repair systems." *Materials and Structures*, 30 (9), 518-526.

- Saeki, T., Ohga, H. and Nagataki, S., (1991). "Mechanisms of carbonation and prediction of the carbonation process of concrete." *JSCE*, 17, 23-36
- Saetta, A. V., (1992). "*Durabilità delle strutture di calcestruzzo armato e analisi dei fenomeni di diffusione dei materiali multifase (in Italian)*." PhD Thesis, University of Padova.
- Saetta, A. V., Schrefler, B. A. and Vitaliani, R. V., (1993a). "The carbonation of concrete and the mechanism of moisture, heat and carbon dioxide flow through porous materials." *Cement and Concrete Research*, 23 (4), 761-772.
- Saetta, A. V., Schrefler, B. A. and Vitaliani, R. V., (1995). "2 – D model for carbonation and moisture/heat flow in porous materials." *Cement and Concrete Research*, 25 (8), 1703-1712.
- Saetta, A. V., Scotta, R. V. and Vitaliani, R. V., (1993b). "Analysis of Chloride Diffusion into Partially Saturated Concrete." *Materials Journal*, 90 (5), 441-451.
- Saetta, A. V. and Vitaliani, R. V., (2004). "Experimental investigation and numerical modeling of carbonation process in reinforced concrete structures: Part I: Theoretical formulation." *Cement and Concrete Research*, 34 (4), 571-579.
- Saetta, A. V. and Vitaliani, R. V., (2005). "Experimental investigation and numerical modeling of carbonation process in reinforced concrete structures: Part II. Practical applications." *Cement and Concrete Research*, 35 (5), 958-967.
- Sakata, K., (1983). "A study on moisture diffusion in drying and drying shrinkage of concrete." *Cement and Concrete Research*, 13 (2), 216-224.
- Samson, E. and Marchand, J., (1999). "Numerical Solution of the Extended Nernst–Planck Model." *Journal of Colloid and Interface Science*, 215 (1), 1-8.
- Sanjuán, M. A., Andrade, C. and Cheyrezy, M., (2003). "Concrete carbonation tests in natural and accelerated conditions." *Advances in Cement Research*, 14 (5), 171-180.
- Sasse, H. R. and Snethlage, R., (1997). "Methods for the evaluation of stone conservation treatments." In: N. S. and Snethlage Baer, R., ed. *Saving our architectural heritage: the conservation of historic stone structures*, 1997, Chichester. John Wiley & Sons, 223-243.
- Scannell, S., Lawrence, M. and Walker, P., (2014). "Impact of Aggregate Type on Air Lime Mortar Properties." *Energy Procedia*, 62 (0), 81-90.
- Scheffler, G. and Plagge, R., (2011). "Application of instantaneous profile measurement of moisture content and moisture potential in porous materials." *Materials and Structures*, 44 (8), 1517-1536.
- Scherer, G. W., (2006). "Internal Stress and Cracking in Stone and Masonry." In: Marias Konsta-Gdoutos (ed.) *Measuring, Monitoring and Modeling Concrete Properties*. Springer Netherlands.

- Schick, H. L., (1960). "A Thermodynamic Analysis of the High-temperature Vaporization Properties of Silica." *Chemical Reviews*, 60 (4), 331-362.
- Schofield, J., (1997). "*Lime in building, a practical guide.*" 3rd Revised edition Crediton: Black Dog Press.
- Scholtès, L., Hicher, P. Y., Nicot, F., Chareyre, B. and Darve, F., (2009). "On the capillary stress tensor in wet granular materials." *International Journal for Numerical and Analytical Methods in Geomechanics*, 33 (10), 1289-1313.
- Schuettpeitz, C., Fratta, D. and Edil, T., (2010). "Mechanistic Corrections for Determining the Resilient Modulus of Base Course Materials Based on Elastic Wave Measurements." *Journal of Geotechnical and Geoenvironmental Engineering*, 136 (8), 1086-1094.
- Seabra, M. P., Paiva, H., Labrincha, J. A. and Ferreira, V. M., (2009). "Admixtures effect on fresh state properties of aerial lime based mortars." *Construction and Building Materials*, 23 (2), 1147-1153.
- Sear, F., (1983). "*Roman Architecture.*" Cornell University Press.
- Selih, J., Sousa, A. and Bremner, T., (1996). "Moisture transport in initially fully saturated concrete during drying." *Transport in Porous Media*, 24 (1), 81-106.
- Sensorium. (2015). Datasheet Evaluation Kit EK-H4 - SHT75 Version 4. Available: <http://www.sensirion.com/nc/en/products/humidity-temperature/download-center/?cid=879&did=62&sechash=e4106742> [Accessed 14/08/2015].
- Shackelford, J. F., (2009). "*Introduction to Materials Science for Engineers.*" Pearson Prentice Hall.
- Shackley, S. M., (2011). "An Introduction to X-Ray Fluorescence (XRF) Analysis in Archaeology " In: S. M. Shackley (ed.) *X-Ray Fluorescence Spectrometry (XRF) in Geoarchaeology*. Springer New York: Springer Science+Business Media, LLC.
- Shampine, L. F., (1994). "*Numerical Solution of Ordinary Differential Equations.*" Taylor & Francis.
- Shao, Y., Lynsdale, C. J., Lawrence, C. D. and Sharp, J. H., (1997). "Deterioration of heat-cured mortars due to the combined effect of delayed ettringite formation and freeze/thaw cycles." *Cement and Concrete Research*, 27 (11), 1761-1771.
- Sheng Han, Y., Hadiko, G., Fuji, M. and Takahashi, M., (2006). "Crystallization and transformation of vaterite at controlled pH." *Journal of Crystal Growth*, 289 (1), 269-274.
- Shih, S. M., Ho, C. S., Song, Y. S. and Lin, J. P., (1999). "Kinetics of the reaction of Ca(OH)₂ with CO₂ at low temperature." *Industrial and Engineering Chemistry Research*, 28 (4), 1316–1322.

- Shimomura, T. and Maekawa, K., (1997). "Analysis of the drying shrinkage behaviour of concrete using a micromechanical model based on the micropore structure of concrete." *Magazine of Concrete Research*, 49 (181), 303–322.
- Shin, H., (2009). "Effect of Reactivity of Quicklime on the properties of hydrated lime solvent for SO₂ removal." *Journal of Material Science and Technology*, 25 (3), 329-332.
- Shrive, N. G., Sayed–Ahmed, E. Y. and Tilleman, D., (1997). "Creep analysis of clay masonry assemblages." *Canadian Journal of Civil Engineering*, 24 (3), 367–379.
- Sickels, L. B., (1988). "*Mortars in Old buildings and in Masonry conservation: a historical and practical treatise.*" Doctoral Dissertation, University of Edinburgh, UK.
- Sickels Taves, L. B., (1995). "Creep, shrinkage and mortars in historic preservation." *Journal of Testing and Evaluation*, 23 (6), 447–452.
- Siddiqi, Z. A., (2012). "*Concrete Structures Part–II.*" 2nd Edition. Lahore: Help Civil Engineering Publishers.
- Silva, A. S., Ricardo, J. M., Salta, M., Adriano, P., Mirão, J., Candeias, A. E. and Macias, A., (2006). "Characterization of Roman mortars from the historical town of Mértola." In: Vasquez-Calvo Alvarez de Buergo; Gomes-Heras (ed.) *Heritage Weathering and Conservation*. Madrid, Spain: Taylor & Francis.
- Silva, D. A., Wenk, H. R. and Monteiro, P. J. M., (2005). "Comparative investigation of mortars from Roman Colosseum and cistern." *Thermochimica Acta*, 438 (1–2), 35-40.
- Sisomphon, K., (2004). "*Influence of Pozzolanic Material Additions on the Development of the Alkalinity and the Carbonation Behaviour of Composite Cement Pastes and Concretes.*" PhD thesis, Technische Universität Hamburg–Harburg.
- Slegers, P. A. and Rouxhet, P. G., (1976). "Carbonation of the hydration products of tricalcium silicate." *Cement and Concrete Research*, 6 (3), 381-388.
- Smith, J. W. L. (1994). "*A literature survey of electrical techniques for measuring concrete moisture profile, Study Report, SR 48.*" Building Research Association of New Zealand.
- Snow, J. and Torney, C. (2014). Lime Mortars in Traditional Buildings. (Short Guides, 6). Available: <http://conservation.historic-scotland.gov.uk/hs-short-guide-6.pdf> [Accessed 05-02-2015].
- Song, H. W., Kwon, S. J., Byun, K. J. and Park, C. K., (2006). "Predicting carbonation in early-aged cracked concrete." *Cement and Concrete Research*, 36 (5), 979-989.
- Steffens, A., Dinkler, D. and Ahrens, H., (2002). "Modeling carbonation for corrosion risk prediction of concrete structures." *Cement and Concrete Research*, 32 (6), 935-941.

- Stepkowska, E. T., (2005). "Hypothetical transformation of $\text{Ca}(\text{OH})_2$ into CaCO_3 in solid-state reactions of portland cement." *Journal of Thermal Analysis and Calorimetry*, 80 (3), 727-733.
- Stewart, J., (2007). "*Calculus*." 6th edition. Cengage Learning.
- Strydom, C. A., Roode, Q. I. and Potgieter, J. H., (1996). "Thermogravimetric and X-ray powder diffraction analysis of precipitator dust from a rotating lime kiln." *Cement and Concrete Research*, 26 (8), 1269-1276.
- Suwito, A., Ababneh, A., Xi, Y. and Willam, K., (2006). "The coupling effect of drying shrinkage and moisture diffusion in concrete." *Computers & Concrete*, 3 (2-3), 103-122.
- Swallow, P. and Carrington, D., (1995). "Limes and lime mortars - Part One." *Journal of Architectural Conservation* 1(3), 7-25.
- Swenson, E. G. and Sereda, P. J., (1968). "Mechanism of the carbonatation shrinkage of lime and hydrated cement." *Journal of Applied Chemistry*, 18 (4), 111-117.
- TA (1997). "*TA Instruments - Thermal Solutions - User Reference Guide - Vol 1*." In: Waters Corporation (ed.) New Castle, USA:
- Tai, C. Y. and Chen, F. B., (1998). "Polymorphism of CaCO_3 , precipitated in a constant-composition environment." *AIChE Journal*, 44 (8), 1790-1798.
- Talukdar, S., Bantia, N. and Grace, J. R., (2012). "Carbonation in concrete infrastructure in the context of global climate change – Part 1: Experimental results and model development." *Cement and Concrete Composites*, 34 (8), 924-930.
- Tanabe, T., Sakata, K., Mihashi, H., Sato, R., Maekawa, K. and Nakamura, H., (2008). "*Creep, Shrinkage and Durability Mechanics of Concrete and Concrete Structures, Two Volume Set: Proceedings of the CONCREEP 8* " First Edition. Taylor & Francis.
- Taylor, H. F. W., (1977). "*Cement Chemistry*." Second Edition. Thomas Telford.
- TecMinho. (2014). Laboratory of Chemical Analysis of TecMinho - Laboratório de Análises Químicas da TecMinho (in Portuguese). Available: <http://www.tecminho.pt/laq/> [Accessed 01-09-2014].
- Tanchev, R. and Purnell, P., (2005). "An application of a damage constitutive model to concrete at high temperature and prediction of spalling." *International Journal of Solids and Structures*, 42 (26), 6550-6565.
- Teutonico, J. M., McCaig, I., Burns, C. and Ashurst, J., (1993). "The Smeaton Project: Factors Affecting the Properties of Lime-Based Mortars." *APT Bulletin*, 25 (3/4), 32-49.
- Thiery, M., Dangla, P., Villain, G., Platret, G., Massieu, E., Druon, M. and Baroghel-Bouny, V. (2004). "*Atmospheric modelling of cement based materials*." Laboratoires des Ponts et Chaussées.

- Thiery, M., Villain, G., Dangla, P. and Platret, G., (2007). "Investigation of the carbonation front shape on cementitious materials: Effects of the chemical kinetics." *Cement and Concrete Research*, 37 (7), 1047-1058.
- Thirumalini, P. and Sekar, S. K., (2013). "Review on Herbs used as Admixture in Lime Mortar used in Ancient Structures." *Indian Journal of Applied Research*, 3 (8), 295-298.
- Thomas, J. W., (1995). *Numerical Partial Differential Equations: Finite Difference Methods.* Springer.
- Tian, S. and Jiang, J., (2012). "Sequestration of Flue Gas CO₂ by Direct Gas–Solid Carbonation of Air Pollution Control System Residues." *Environmental Science & Technology*, 46 (24), 13545-13551.
- TNO-DIANA-BV (2010). *"Diana User´s Manual."* Delft, The Netherlands: Release 9.4.
- Tobriner, S., (2003). "Building the cathedral of Noto." In: Madrid: I. Juan de Herrera S. Huerta, SEdHC, ETSAM, A. E. Benvenuto, COAM, F. Dragados,, ed. *Proceedings of the First International Congress on Construction History*, 20th–24th January 2003 2003, Madrid. 1979–1988.
- Topcu, B. and Ugurlo, A., (2007). "Elasticity theory of concrete and prediction of Static E-modulus for dam Concrete using composite models." *Digest*, 2007, 1115-1127.
- Torgal, F. P., Faria, J. and Jalali, S., (2012). "Some considerations about the use of lime–cement mortars for building conservation purposes in Portugal: A reprehensible option or a lesser evil?" *Construction and Building Materials*, 30, 488-494.
- Torney, C., Forster, A. M. and Szadurski, E. M., (2014). "Specialist ‘restoration mortars’ for stone elements: a comparison of the physical properties of two stone repair materials." *Heritage Science* 2(1), 1-12.
- Tracy, S. L., François, C. J. P. and Jennings, H. M., (1998a). "The growth of calcite spherulites from solution: I. Experimental design techniques." *Journal of Crystal Growth*, 193 (3), 374-381.
- Tracy, S. L., Williams, D. A. and Jennings, H. M., (1998b). "The growth of calcite spherulites from solution: II. Kinetics of formation." *Journal of Crystal Growth*, 193 (3), 382-388.
- Truc, O., Ollivier, J.-P. and Nilsson, L.-O., (2000a). "Numerical simulation of multi-species transport through saturated concrete during a migration test - MsDiff code." *Cement and Concrete Research*, 30 (10), 1581-1592.
- Truc, O., Ollivier, J. P. and Nilsson, L. O., (2000b). "Numerical simulation of multi-species diffusion." *Materials and Structures*, 33 (9), 566-573.
- Tucker, M. E. and Wright, P. V., (1991). *"Carbonate Sedimentology "* 1st edition. Wiley-Blackwell.

- Turcry, P., Oksri-Nelfia, L., Younsi, A. and Ait-Mokhtar, A., (2014). "Analysis of an accelerated carbonation test with severe preconditioning." *Cement and Concrete Research*, 57, 70-78.
- Ubbríaco, P. and Tasselli, F., (1998). "A Study of the Hydration of Lime-Pozzolan Binders." *Journal of Thermal Analysis and Calorimetry*, 52 (3), 1047-1054.
- Ukrainczyk, N., Ukrainczyk, M., Šipušić, J. and Matusinović, T., (2006). "XRD and TGA Investigation of Hardened Cement Paste Degradation." In: *11. Conference on Materials, Processes, Friction and Wear*, 2006, Vela Luka, Croatia. 242-249.
- Ulm, F. and Coussy, O., (1995). "Modeling of Thermochemomechanical Couplings of Concrete at Early Ages." *Journal of Engineering Mechanics*, 121 (7), 785-794.
- UNWTO, (2014). "*Tourism Highlights*." 2014 Edition. Available in <http://www.e-unwto.org/doi/pdf/10.18111/9789284416226>: The United Nations World Tourism Organization.
- Vágvölgyi, V., Frost, R. L., Hales, M., Locke, A., Kristóf, J. and Horváth, E., (2008). "Controlled rate thermal analysis of hydromagnesite." *Journal of Thermal Analysis and Calorimetry*, 92 (3), 893-897.
- Vaisala (2004). "*Operationg Manual*." *HMI41 Indicator and HMP42 Prove*. Helsinki, Finland: Vaisala Oyj.
- Valek, J., Hughes, J. J. and Groot, C. J. W. P., (2012). "*Historic Mortars: Characterisation, Assessment and Repair*." Springer Netherlands.
- Válek, J. and Matas, T., (2010). "Experimental study of hot mixed mortars in comparison with lime putty and hydrate mortars." In: C. Groot and J.J. Hughes J. Válek, ed. *2nd Conference on Historic Mortars - HMC 2010 and RILEM TC 203-RHM final workshop*, 2010, Prague. RILEM Publications SARL.,
- Válek, J. and Matas, T., (2012). "Experimental Study of Hot Mixed Mortars in Comparison with Lime Putty and Hydrate Mortars." In: Jan Válek, John J. Hughes and Caspar J. W. P. Groot (eds.) *Historic Mortars*. Springer Netherlands.
- Valenti, G. L. and Cioffi, R., (1985). "Quantitative determination of calcium hydroxide in the presence of calcium silicate hydrates. Comparison between chemical extraction and thermal analysis." *Journal of Materials Science Letters*, 4, 475-478.
- Valluzzi, M. R., Binda, L. and Modena, C., (2005). "Mechanical behaviour of historic masonry structures strengthened by bed joints structural repointing." *Construction and Building Materials*, 19 (1), 63-73.
- Van Balen, K., (2005). "Carbonation reaction of lime, kinetics at ambient temperature." *Cement and Concrete Research*, 35 (4), 647-657.
- Van Balen, K., Van den Brande, C., Toumbakari, E. E., Van Gemert, D. I. and Amarkai, A. B., (1997). "Influence of moisture content on the effective diffusion coefficient in lime mortars with different porosities. ." In: *10th International congress on the*

chemistry of cement and Congrex Goteborg AB, 1997, Gothenburg, Sweden. p. 4IV010.

- Van Balen, K. and Van Gemert, D., (1994). "Modelling lime mortar carbonation." *Materials and Structures*, 27 (27), 393-398.
- Van Gerven, T., Cizer, O., Mertens, G., Vandecasteele, C., Elsen, J. and Van Balen, K., (2009). "Mineral Carbonation at K.U.Leuven." In: *1st International Slag Valorisation Symposium*, 2009, Leuven, Belgium, 6-7/4/2009. 12 p.
- van Zijl, G. P. A. G., (2000). "*Computational modelling of masonry creep and shrinkage.*" PhD thesis, Delft University of Technology.
- van Zijl, G. P. A. G., de Borst, R. and Rots, J. G., (2001). "The role of crack rate dependence in the long-term behaviour of cementitious materials." *International Journal of Solids and Structures*, 38 (30–31), 5063-5079.
- Veiga, M. R., Fragata, A., Velosa, A. L., Magalhães, A. C. and Margalha, G., (2010a). "Lime-Based Mortars: Viability for Use as Substitution Renders in Historical Buildings." *International Journal of Architectural Heritage*, 4 (2), 177-195.
- Veiga, M. R. and Souza, R., (2004). "Metodologia de avaliação da retracção livre das argamassas desde a sua moldagem (in Portuguese)." *Revista de Engenharia Civil da Universidade do Minho*, 20, 45-56.
- Veiga, M. R., Valek, J., Groot, C. and Hughes, J., (2010b). "Conservation of historic renders and plasters: from lab to site." In: *Proceedings of the 2nd Historic Mortars Conference*, 2010b, Prague. RILEM Publications SARL, 1241–1256.
- Veiga, R., Fragata, A., Velosa, A., Magalhães, A. and Margalha, G., (2008). "Substitution mortars for application in historical buildings exposed to the sea environment. Analysis of the viability of several types of compositions." In: *Medachs - Construction Heritage in Coastal and Marine Environments: damage, diagnostics, maintenance and rehabilitation*, January 2008, Lisbon, Portugal. 9.
- Velosa, A. L. and Veiga, M. R., (2007). "Lime-metakaolin mortars – properties and applications." In: *Sustainable Construction, Materials and Practices: Challenge of the Industry for the New Millenium*, 2007, Lisbon, Portugal. 6.
- Venhuis, M. A. and Reardon, E. J., (2003). "Carbonation of cementitious wasteforms under supercritical and high pressure subcritical conditions." *Environmental Technology*, 24 (7), 877–887.
- Verstrynge, E., (2010). "*Long-term behaviour of monumental masonry constructions: modelling and probabilistic evaluation.*" PhD thesis, Katholieke Universiteit Leuven.
- Verstrynge, E., Schueremans, L. and Van Gemert, D., (2011). "Time-dependent mechanical behavior of lime-mortar masonry." *Materials and Structures*, 44 (1), 29-42.
- Vicat, L. J., (1997). "*Mortars and cements. Reprint of the 1837 edition.*" Donhead Publishing Ltd.

- Villain, G., Thierry, M. and Platret, G., (2007). "Measurement methods of carbonation profiles in concrete: Thermogravimetry, chemical analysis and gammadensimetry." *Cement and Concrete Research*, 37 (8), 1182-1192.
- Walton, J., Bin-Shafique, S. Smith, R., Gutierrez, N. and A., T., (1997). "Role of carbonation in transient leaching of cementitious waste forms." *Environmental Science and Technology*, 31 (8), 2345- 2349.
- Warren, M., (2000). "*Economic Analysis for Property and Business.*" First Edition. Butterworth-Heinemann, Routledge.
- Wedler, E. and Charola, A. E., (2008). "Water and its interaction with porous inorganic building materials." In: *Proceedings of Hydrophobe V – Fifth International Conference on Water Repellent Treatment of Building Materials*, 2008, Brussels. 57-73.
- Whitaker, S., (1977). "Simultaneous heat, mass, and momentum transfer in porous media: A Theory of Drying " *Advances in Heat Transfer*, 13, 119-203.
- Winfield, D. (ed.) (2006). *Military, and masonry developments*, London, UK: Routledge.
- Wood, R. C., (2015). "*Hospitality Management: A Brief Introduction.*" SAGE Publications Ltd.
- Xi, Y., Bažant, Z. P. and Jennings, H. M., (1994a). "Moisture diffusion in cementitious materials Adsorption isotherms." *Advanced Cement Based Materials*, 1 (6), 248–257.
- Xi, Y., Bažant, Z. P., Molina, L. and Jennings, H. M., (1994b). "Moisture diffusion in cementitious materials Moisture capacity and diffusivity." *Advanced Cement Based Materials*, 1 (6), 258-266.
- Yeh, G. and Tripathi, V. S., (1991). "A Model for Simulating Transport of Reactive Multispecies Components: Model Development and Demonstration." *Water Resources Research*, 27 (12), 3075–3094.
- Yiotis, A. G., Tsimpanogiannis, I. N., Stubos, A. K. and Yortsos, Y. C., (2007). "Coupling between external and internal mass transfer during drying of a porous medium." *Water Resources Research*, 43 (6), W06403.
- Yoshitake, I., Rajabipour, F., Mimura, Y. and Scanlon, A., (2012). "A Prediction Method of Tensile Young's Modulus of Concrete at Early Age." *Advances in Civil Engineering*, 2012 (Article ID 391214), 10.
- Yuan, Y. and Wan, Z. L., (2002). "Prediction of cracking within early-age concrete due to thermal, drying and creep behavior." *Cement and Concrete Research*, 32 (7), 1053-1059.
- Zacharopoulou, G., (2013). "The effects of limestone calcination heating rate on the yield, water rejection and strengths of high calcium lime putty binder." In: *3rd Historic Mortars Conference* 11-14 September 2013, Glasgow, Scotland.

- Zappia, G., Sabbioni, C., Pauri, M. G. and Gobbi, G., (1994). "Mortar damage due to airborne sulfur compounds in a simulation chamber." *Materials and Structures*, 27 (8), 469-473.
- Zawawi, R., (2010). "*Artificial hydraulic lime mortar obtained by calcining limestone and siliceous waste materials.*" PhD Thesis, Heriot Watt University.
- Zhang, J., Gao, Y., Han, Y. and Sun, W., (2012). "Shrinkage and Interior Humidity of Concrete under Dry–Wet Cycles." *Drying Technology*, 30 (6), 583-596.
- Zhang, J., Han, Y. and Gao, Y., (2014). "Effects of Water–Binder Ratio and Coarse Aggregate Content on Interior Humidity, Autogenous Shrinkage, and Drying Shrinkage of Concrete." *Journal of Materials in Civil Engineering*, 26 (1), 184–189.
- Zhang, J., Qi, K. and Huang, Y., (2009). "Calculation of Moisture Distribution in Early-Age Concrete." *Journal of Engineering Mechanics*, 135 (8), 871-880.
- Zhang, Z., (2014). "*Modelling of sorption hysteresis and its effect on moisture transport within cementitious materials.*" PhD, Paris Est, École Doctorale Sciences, Ingénierie et Environnement.
- Zhi, P., Xianyu, J. and Nanguo, J., (2010). "Theoretical Modeling of Concrete Moisture Diffusion Surface Factor." In: *Earth and Space 2010: Engineering, Science, Construction, and Operations in Challenging Environments*, 2010, 3610–3616.
- Zill, D. G., (2012). "*Differential Equations with Boundary–Value Problems.*" 8th edition. Brooks Cole.
- Zucchini, A. and Lourenço, P. B., (2004). "A coupled homogenisation–damage model for masonry cracking." *Computers & Structures*, 82 (11–12), 917-929.
- Zwillinger, D., (1998). "*Handbook of Differential Equations.*" 3rd Edition. Academic Press.

ANNEX A

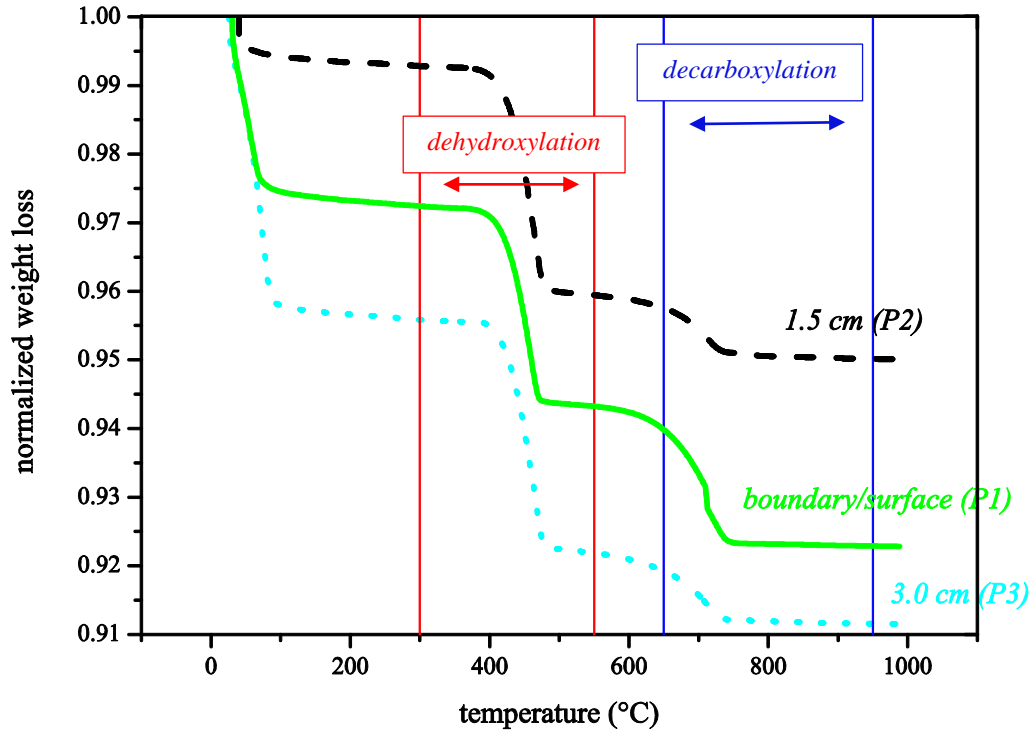


Figure A1 1 - TGA results for cylindrical specimen after 1 day in three depths (P1, P2 and P3)

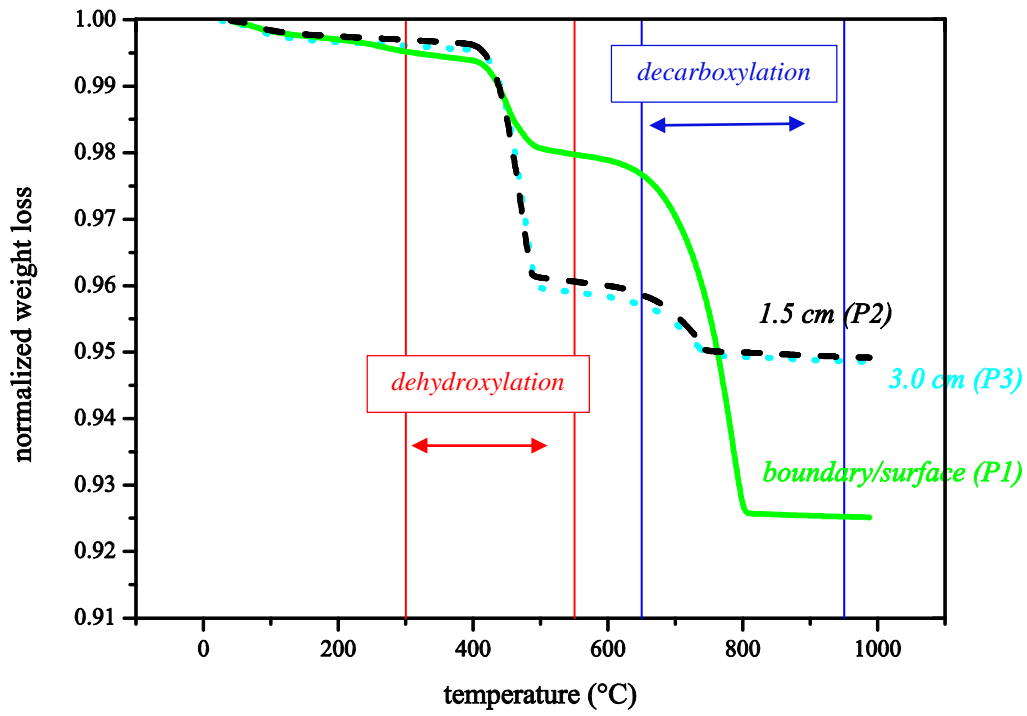


Figure A1 2 - TGA results for cylindrical specimen after 14 day in three depths (P1, P2 and P3)

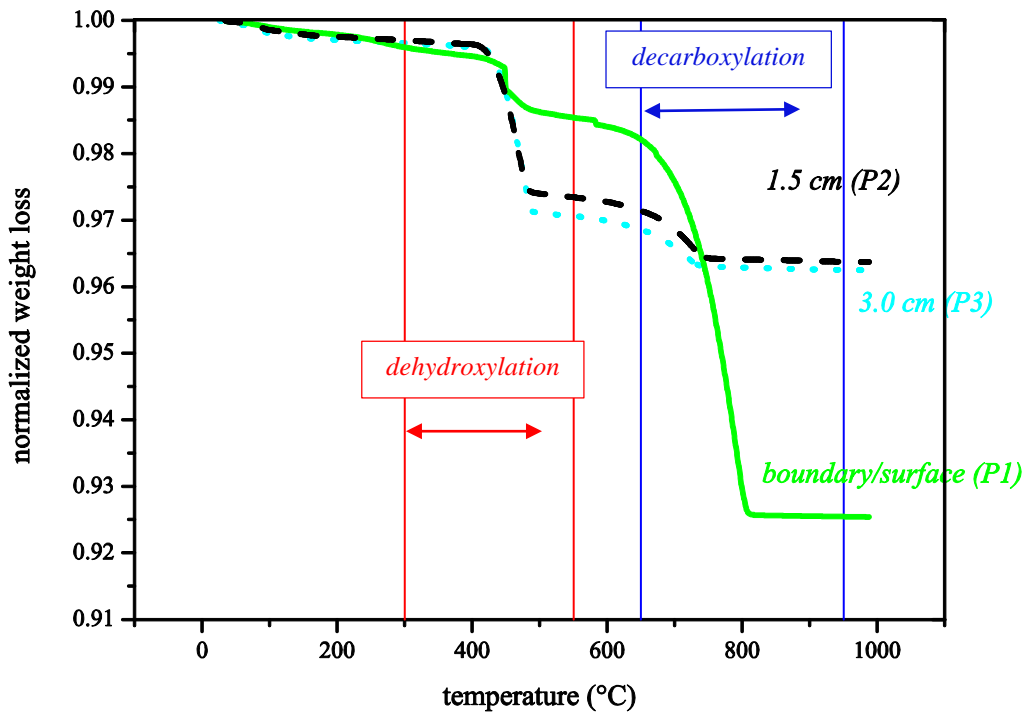


Figure A1 3 - TGA results for cylindrical specimen after 69 day in three depths (P1, P2 and P3)